Materials Science in Additive Manufacturing

eISSN: 2810-9635

Volume 3 Issue 2, June 2024

ACCSCIENCE
PUBLISHING

ACCSCIENCE
PUBLISHING

Materials Science in Additive Manufacturing

Online ISSN: 2810–9635

Materials Science in Additive Manufacturing aims to bridge the cutting-edge research between additive manufacturing and the entire spectrum of materials science. The journal covers all applied and fundamentals of processing, synthesis, structure, composition, properties and performance of materials designed or manipulated for additive manufacturing. The journal covers a wide scope of innovative techniques, processes, methods, and applications.

About the Publisher

AccScience Publishing is a publishing company based in Singapore. We publish a range of high-quality, open-access, peer-reviewed journals and books from a broad spectrum of disciplines.

Contact Us

Managing Editor
msam.office@accscience.sg

AccScience Publishing
8 Burn Road, #15-03 Trivex, Singapore 369977.

Volume 3 • Issue 2 • June 2024
ISSN 2810-9635 (online)

MATERIALS SCIENCE IN ADDITIVE MANUFACTURING

Editor-in-Chief

Chee Kai Chua

Singapore University of Technology and Design,
Singapore

ACCSCIENCE
PUBLISHING

Full issue copyright © 2024 AccScience Publishing
All rights reserved. Without permission in writing from the publisher, this full issue publication in its entirety may not be reproduced or transmitted for commercial purposes in any form or by any means, electronic or mechanical, including photocopying, recording, or any information storage and retrieval system. Permissions may be sought from msam.office@accscience.sg.

Article copyright © Respective Author(s)
See articles for copyright year. All articles in this full issue publication are open-access. There are no restrictions in the distribution and reproduction of individual articles, provided the original work is properly cited. However, permission to reuse copyrighted materials of an article for commercial purposes is applicable if the article is licensed under Creative Commons Attribution-NonCommercial License. Check the specific license before reusing.

MATERIALS SCIENCE IN ADDITIVE MANUFACTURING

ISSN: 2810-9635 (online)

Editorial and Production Credits

Publisher: AccScience Publishing
Managing Editor: Ginger Lv
Editorial Assistant: Flora Kang
Production Editor: Puva Ramakrishnan
Article Layout and Typeset: Sinjore Technologies (India)

For all advertising queries, contact msam.office@accscience.sg.

Supplementary file

Supplementary files of articles can be obtained at https://accscience.com/journal/MSAM/3/2.

Disclaimer

AccScience Publishing is not liable to the statements, perspectives, and opinions contained in the publications. The appearance of advertisements in the journal shall not be construed as a warranty, endorsement, or approval of the products or services advertised and/or the safety thereof. AccScience Publishing disclaims responsibility for any injury to persons or property resulting from any ideas or products referred to in the publications or advertisements. AccScience Publishing remains neutral with regard to jurisdictional claims in published maps and institutional affiliations.

Material Science in Additive Manufacturing

Editorial Board

Editor-in-Chief

Chee Kai Chua
Singapore University of Technology and Design, Singapore

Associate Editor

Swee Leong Sing
National University of Singapore, Singapore

*Editorial Board Members**

Shweta Agarwala, *Denmark*
Mohsen Akbari, *Canada*
Craig Banks, *UK*
Flávio Bartolomeu, *Portugal*
Filippo Berto, *Italy*
Mahdi Bodaghi, *UK*
Thomas Boland, *USA*
Paulo Jorge da Silva Bártolo, *Singapore*
Pasquale Daniele Cavalière, *Italy*
Ming-Wei Chang, *UK*
Zhangwei Chen, *China*
Dong-Woo Cho, *South Korea*
Luciano Feo, *Italy*
Antonio Gloria, *Italy*
Maling Gou, *China*
Dongdong Gu, *China*
Dong-Wook HAN, *Korea*
Charlotte Hauser, *Saudi Arabia*
Jingchao Jiang, *China*
Clodualdo Aranas Jr, *Canada*
Leong Kah Fai, *Singapore*
Lifeng Kang, *Australia*
Shanmugam Kumar, *UK*
Ming C Leu, *USA*
Xiaopeng Li, *Australia*
Xiaochun Li, *USA*
Peifeng Li, *UK*
Jikai Liu, *China*
Guoxing Lu, *Australia*
Guha Manogharan, *USA*
David K. Mills, *USA*
Mui Ling Sharon Nai, *USA*
Eujin Pei, *UK*
Mika Salmi, *Finland*
Jose M. San Juan, *Spain*
Jing Shi, *USA*
Cijun Shuai, *China*
Jonathan Phuong Tran, *Australia*
Dimitrios Tzetzis, *Greece*
Yiwei Weng, *China*
Chunze Yan, *China*
Wai Yee Yeong, *Singapore*
Ali Zamanian, *Iran*
Yicha Zhang, *France*
Jack G. Zhou, *USA*
Jie Zhou, *Netherlands*
Tuğrul Özel, *USA*

*Editorial Board Members as of March 1, 2024

ACCSCIENCE PUBLISHING

Volume 3 | Issue 2 | June 2024 |

Materials Science in Additive Manufacturing

https://accscience.com/journal/msam

CONTENTS

REVIEW ARTICLE

ORIGINAL RESEARCH ARTICLES

ACCSCIENCE PUBLISHING

Materials Science in
Additive Manufacturing

REVIEW ARTICLE

Recent progress on materials for functional additive manufacturing

Hayeol Kim[1], **Kyung-Hwan Kim**[1], **Jiyun Jeong**[1], **Yunsoo Lee**[1], **and Im Doo Jung**[1,2*]

[1]Department of Mechanical Engineering, Faculty of Mechanical Engineering, Ulsan National Institute of Science and Technology, Ulsan, Republic of Korea

[2]Artificial Intelligence Graduate School, Ulsan National Institute of Science and Technology, Ulsan, Republic of Korea

Abstract

Material science in additive manufacturing (AM) has experienced remarkable advancements in the development of functional materials. This review systematically investigates the state-of-the-art research on AM of functional materials, providing a comprehensive overview of AM systems and methodologies employed for functional materials and applications. The review delves into various functional materials, including magnetic, metal powder, perovskite, piezoelectric, thermoelectric, and carbon-based materials, exploring their fabrication and applications in creating multifunctional components and devices. Furthermore, it examines the integration of these functional materials, enabling manufacturing on curved surfaces, the development of flexible components, and the enhancement of functional properties. By analyzing the latest developments in this rapidly evolving field, this review offers insights into current challenges, future directions, and potential innovations, promoting a deeper understanding of AM technology and stimulating further advancements toward the realization of advanced functional devices and systems.

Keywords: Additive manufacturing; Functional materials; Polymer matrices; Multifunctional components

***Corresponding author:**
Im Doo Jung
(idjung@unist.ac.kr)

Citation: Kim H, Kim KH, Jeong J, Lee Y, Jung IM. Recent progress on materials for functional additive manufacturing. *Mater Sci Add Manuf.* 2024;3(2):3323. doi: 10.36922/msam.3323

Received: March 29, 2024

Accepted: May 16, 2024

1. Introduction

Additive manufacturing (AM), commonly referred to as three-dimensional (3D) printing, manufactures objects layer by layer. This process has revolutionized the manufacturing landscape by offering enhanced design flexibility and reduced production times. AM technology enables the fabrication of complex structures and allows for the manufacturing of creative and innovative designs.[1-3] It facilitates the customized production of each product, which offers significant advantages in prototype development and personalized product manufacturing.[4,5] Moreover, AM enables the fabrication of complex structures, contributing to light weighting and structural optimization in industries such as aerospace and automotive.[6-11] With these diverse arrays of advantages, AM technology is driving innovative changes in the manufacturing industry.

Polymer materials are widely utilized in AM due to their inherent advantages, such as lightweight, corrosion resistance, mechanical strength, and biocompatibility.[4]

These polymers, ranging from photo-curable resins to thermoplastics and viscous polymer inks, find applications across diverse areas, including medical, aerospace, automotive, electronics, soft robotics, energy, environmental, and industrial fields, depending on their specific characteristics.[12,13] Moreover, recent research is exploring the potential of polymers for 4D printing, where they can respond to stimuli such as temperature, light, electric fields, magnetic fields, and moisture, resulting in changes in shape or properties over time.[14,15] The versatility and adaptability of polymer materials render them highly desirable for AM, especially when integrated with functional materials to enable a wide range of applications.

AM using functional materials has emerged as a critical area of research in the manufacturing industry. The use of polymer-based functional materials in AM offers significant advantages due to ease of processing and low manufacturing temperatures. By combining various functional materials with polymer matrices, it becomes possible to enhance the characteristics and functionalities of polymers, facilitating the fabrication of components with properties such as magnetic, actuating, and electrical conductivity.[4] Furthermore, ongoing research is exploring the fabrication of parts with properties such as piezoelectric and thermoelectric behavior by leveraging multi-material manufacturing capabilities.[16,17] The development of AM technology using functional and high-performance materials unlocks diverse applications across various industries, ranging from electronics engineering to medical purposes such as artificial organs and medical robotics.[18,19] These research efforts underscore the innovative advancements driven by AM with functional materials in the manufacturing industry and are expected to contribute to enhancing manufacturing process efficiency and product performance.

This review aims to comprehensively investigate state-of-the-art research efforts on AM of functional materials integrated with polymer matrices. It systematically categorizes AM systems and methodologies used for polymer-based functional materials. Subsequently, it summarizes notable studies that fabricate various functional materials or structures, such as magnetic, metal powder, perovskite, piezoelectric, and thermoelectric materials, exploring their applications in fabricating multifunctional components and devices. Ultimately, by studying and analyzing the latest developments in polymer-based AM of functional materials, this review seeks to provide insights into current challenges, future directions, and potential innovations in the rapidly growing field of functional AM. Figure 1 provides an overview of functional materials for AM techniques and applications. Descriptions of key strategies, material selections, and application prospects are provided to foster a deeper understanding of AM technology and stimulate further innovation toward the realization of advanced functional devices and systems.

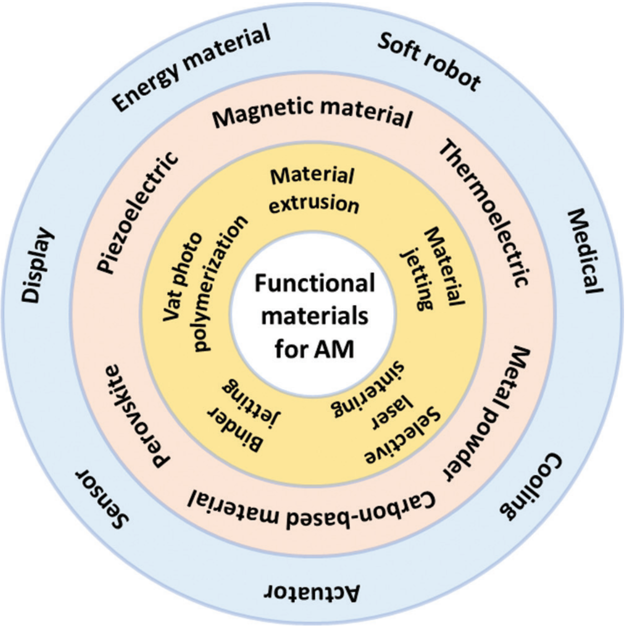

Figure 1. Overview of functional materials for additive manufacturing techniques and applications.

2. AM methods for functional materials

According to American Society for Testing and Materials standards, the AM of functional polymer materials can be classified into several categories: material extrusion, vat photopolymerization, binder jetting, powder bed fusion (PBF), and material jetting. Each AM technology has its unique manufacturing process and compatible materials, with the suitable technology varying depending on the required functional characteristics and polymer types. These classifications and characteristics are summarized in Table 1.

2.1. Material extrusion

Material extrusion is currently the most commonly used AM method, forming layers by extruding thermoplastic or liquid-state materials through small nozzles.[20] While this method may have relatively lower resolution and accuracy, its affordability and ability to mix with various materials make it widely utilized, especially in the manufacturing of functional polymers. An example of a material extrusion AM method commonly used for polymers is depicted in Figure 2A.

Fused deposition modeling (FDM) is a 3D printing technique in which molten thermoplastic material is

Table 1. Characteristics of each polymer AM process

AM process	Printing method	Raw materials	Fabrication mechanism	Resolution (xy [μm])	Resolution (thickness [μm])	Typical build size (mm^3)
Material extrusion	FDM	Thermoplastic filaments or pellets	Molten material extrusion	100 – 150	100 – 200	223×223×305
	DIW	Viscoelastic ink	Material extrusion and solidification	100 – 1200	100 – 400	260×220×70
	Meniscus printing	Viscous ink	Ink extrusion by meniscus contact	0.05 – 2	-	4×25
Vat photopolymerization	SLA	Photosensitive polymer resin	UV laser curing	6.5 – 25	25 – 300	145×145×175
	DLP	Photosensitive polymer resin	DLP projector curing	35 – 100	25 – 150	140×79×100
	CLIP	Photosensitive polymer resin	Continuous UV curing	75	0.4 – 100	150×80×300
Binder jetting	-	Powdered materials	Drop bonding liquid	100	260 – 380	1800×1000×700
Powder bed fusion	SLS	Polymer powder	Laser sintering	30 – 100	60 – 180	340×340×600
Material jetting	Polyjet	Thermoset photopolymers	Liquid material deposit and UV curing	42 – 85	16 – 28	294×192×148.6

Abbreviations: AM: Additive manufacturing; CLIP: Continuous liquid interface production; DIW: Direct ink writing; DLP: Digital light processing; FDM: Fused deposition modeling; SLA: Stereolithography; SLS: Selective laser sintering.

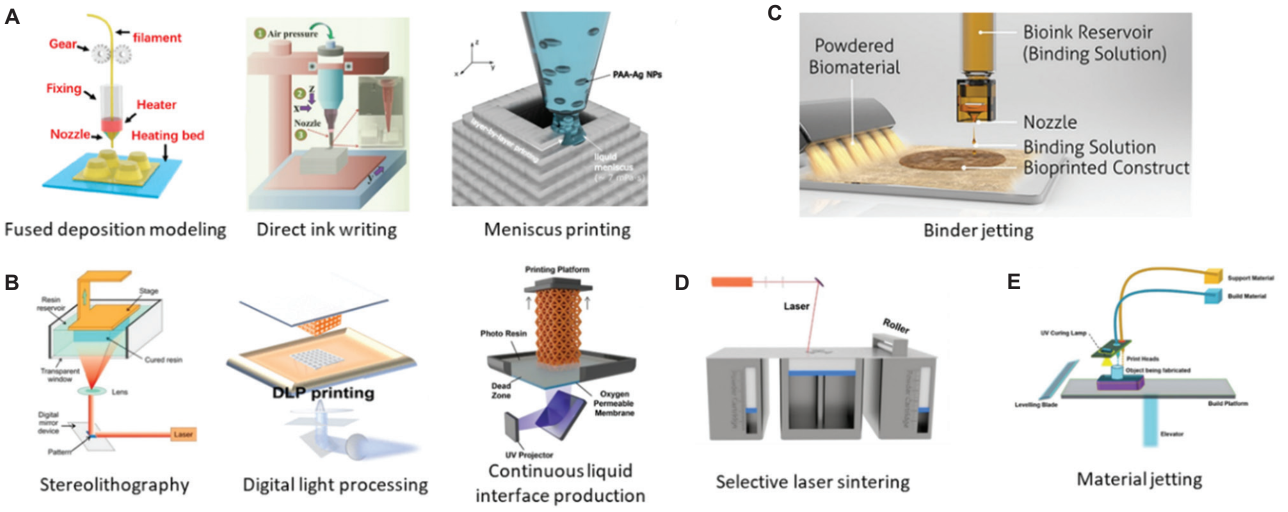

Figure 2. Schematic illustrations of the additive manufacturing process for functional materials. (A) Material extrusion 3D printing; left panel reproduced with permission from Liu *et al.*[16] (Copyright © 2022 American Chemical Society); center panel reproduced with permission from Hossain *et al.*[21] (Copyright © 2022 American Chemical Society); right panel reproduced with permission from Lee *et al.*[23] (Copyright © 2017 American Chemical Society). (B) Vat photopolymerization 3D printing; left panel reproduced with permission from Pagac *et al.*[25] (Copyright © 2018 American Chemical Society); center panel reproduced with permission from Chiappone *et al.*[27] (Copyright © 2021 American Chemical Society); and right panel reproduced with permission from Wang *et al.*[28] (Copyright © 2023 American Chemical Society). (C) Binder jetting; reproduced with permission from Jose *et al.*[29] (Copyright © 2016 American Chemical Society). (D) Selective laser sintering; reproduced with permission from Ouyang *et al.*[30] (Copyright © 2022 American Chemical Society). (E) Material jetting; reproduced with permission from Sireesha *et al.*[31] (Copyright © 2018 RSC Advances).

extruded through a movable nozzle controlled by software to create layers.[16] This process typically involves heating the thermoplastic filament to its melting point within the printer's extruder assembly. The melted filament is then precisely deposited onto the build platform layer by layer, where it quickly solidifies to form the desired object. The movement of the nozzle is directed by computer-aided design software, allowing for the production of intricate and precise shapes. Recent advancements include screw-based systems capable of using pellets, enabling the processing of a wider range of thermoplastic materials in large sizes. This expansion of capabilities has increased the scope of FDM applications in both research and industry.

Direct ink writing (DIW) is a 3D printing technique that enables the precise deposition of liquid-state materials through small nozzles to create desired shapes. This process involves the extrusion of material in a continuous stream rather than layer-by-layer deposition typical of other 3D printing methods. DIW allows for the use of various materials, including non-thermoplastic polymers, hydrogels, ceramics, and even living cells, in bio-printing applications. The ability to print with liquid materials provides flexibility in material composition and properties, making DIW suitable for a wide range of applications in fields such as biomedicine, soft robotics, and electronics.[21,22]

Meniscus printing is a 3D printing technology wherein liquid polymers are dispensed onto a flat surface and shaped using surface tension to achieve the desired form. This method typically involves the controlled deposition of droplets of liquid polymer onto a substrate. The surface tension of the liquid causes it to form a meniscus, which can be controlled to create precise shapes and structures.[23,24] Meniscus printing offers advantages in producing complex geometries and structures with high resolution and precision. It finds applications in various fields, including biomedicine, where it can be used to create biomaterials for tissue engineering and drug delivery systems.

2.2. Vat photopolymerization

Vat photopolymerization is an AM technology that selectively solidifies liquid resin contained in a vat using a curing device. The liquid resin typically consists of oligomers and monomers. When exposed to the curing light, the oligomers and monomers undergo polymerization, forming polymer chains that harden to create the desired object. The curing process occurs layer by layer, with each layer solidified before the next layer is added, resulting in precise and detailed models. Vat photopolymerization utilizes various curing devices such as UV beams, digital light, and light-emitting diodes (LEDs), offering advantages in high resolution and accuracy for the resulting products.[25]

Stereolithography (SLA) is a high-resolution AM technology that employs rastering lasers to photopolymerize liquid resin, forming 3D models. The process involves sequentially exposing the resin surface to the laser to create layers, with each layer cured by UV light.[26] A schematic diagram of the SLA process is illustrated on the left in Figure 2B. SLA is capable of producing intricate and complex models with high precision. It finds extensive applications in industries such as advanced medical, automotive, and aerospace due to its ability to fabricate precise and complex prototypes and functional parts.

Digital light processing (DLP) stands out in the realm of AM as a technology that precisely photopolymerizes liquid resin using a projector light source. Its significant difference from SLA lies in the light source. While SLA employs rastering lasers, DLP utilizes a projector light source, enabling a different approach to layer creation. A defining advantage of DLP is its capability to print an entire 2D layer simultaneously, thanks to the digital micro-mirror device generating a digital image to illuminate each layer's shape in one go.[27] This simultaneous curing process contributes to the rapid production of high-resolution models, distinguishing DLP for its speed in manufacturing. This speed advantage positions DLP as a viable choice for applications where time-to-market is crucial, such as precision parts manufacturing and medical modeling. However, it is worth noting that compared to SLA, DLP may exhibit slightly lower resolution due to the nature of its projection method. Despite this minor drawback, DLP's efficiency in printing speed makes it an attractive option for various industries seeking to balance between speed and resolution in their AM processes.

Continuous liquid interface production (CLIP) 3D printing is an AM technology that addresses the slow production speed of SLA and DLP by fundamentally changing the manufacturing process. Instead of layer-by-layer manufacturing using photo-curable resin, CLIP continuously lowers a liquid resin pool to manufacture objects.[28] This continuous process offers significantly faster production speeds, up to 100 times faster than conventional layer-by-layer methods, while maintaining high accuracy. CLIP holds promise for manufacturing innovation due to its speed and precision, opening up new possibilities for various industries. The primary distinction between DLP and CLIP lies in their manufacturing processes: CLIP utilizes a continuous manufacturing process, whereas DLP employs a layer-by-layer approach, as illustrated in Figure 2B.

2.3. Binder jetting

Binder jetting is an AM process that begins by evenly spreading powder material across a build platform. Subsequently, a binder, typically in liquid form, is precisely jetted onto the powder layer, selectively solidifying it. This process is repeated for each layer until the desired object is formed. The schematic of the binder jetting process is depicted in Figure 2C. Post-processing techniques such as sintering or infiltrating can, further, enhance the precision and strength of the final product. Binder jetting is known for its relatively high production speeds and cost-effectiveness, making it suitable for mass production. In addition, its ability to mix various materials provides versatility for manufacturing functional components across different industries.[26]

2.4. PBF

Polymer materials are primarily utilized in the PBF process, predominantly through selective laser sintering (SLS).

SLS involves laying down a flat layer of polymer powder particles and selectively sintering them with a laser into the desired shape. After each layer is sintered, the powder bed is lowered, and another flat powder layer is laid on top, repeating the process until the entire object is fabricated. It is important to note that SLS differs distinctly from selective laser melting (SLM), as SLS does not fully melt the powder into a liquid state. The schematic of the SLS process is shown in Figure 2D. SLS technology offers the capability to manufacture complex 3D shapes, enabling its application across a wide range of fields. In addition, its ability to mix various materials further extends its versatility.[30] Particularly, noteworthy is the role of polymer powder in serving as support, enhancing design flexibility. From prototype fabrication to final product manufacturing, SLS emerges as a promising manufacturing method extensively used across diverse industries.

2.5. Material jetting

Material jetting is a manufacturing method where liquid materials are precisely sprayed through small nozzles to form layers. This technology offers exceptional fabrication speed, making it suitable for various industries and applications.[31] In material jetting, materials are deposited at precise locations through small nozzles and then cured either by UV light or heat to form and bond layers. The referenced process schematic is shown in Figure 2E. This process allows for the creation of models with complex shapes and intricate details, providing high material selectivity and enabling the fabrication of parts with specific material properties tailored to the application's requirements.

3. AM with functional materials and their applications

3.1. Magnetic powders

Recently, there has been active research on magnetically responsive soft materials among various types of polymer-based stimuli-responsive soft materials. This interest primarily stems from their advantage of faster response compared to other operating modes, such as heat, light, and electric fields.[32] The magnetic field, which serves as the actuating source for these magnetically responsive soft materials, is non-contact and relatively easy to control, as its magnitude, phase, and frequency can be modulated quickly and accurately, and the magnetic field is transparent to most materials.[32-34]

Magnetic filler particles generally consist of ferromagnetic materials that exhibit significant magnetization under an external magnetic field. These ferromagnetic materials can be classified according to their magnetization properties into hard magnetic materials, soft magnetic materials, and superparamagnetic materials. Hard magnetic materials have high remanence and coercivity. Remanence (or residual magnetization) refers to the magnetization remaining in a material after the external magnetic field has been removed. This property renders hard magnetic materials to be considered permanent magnets. Coercivity is the strength of the external magnetic field required to demagnetize the magnetized material. Hard magnetic materials can maintain significant residual magnetization even after the removal of the magnetic field following saturation, and they can also retain notable residual magnetization when subjected to magnetic fields below their coercive strength.[35,36] Due to these characteristics, hard magnetic materials exhibit large hysteresis (Figure 3A). Hence, composites containing hard magnetic particles embedded in a polymer matrix retain high residual properties after magnetization and exhibit independent behavior in response to applied magnetic fields below the coercive fields. Hard magnetic materials include ferrite-based substances such as barium ferrite ($BaFe_{12}O_{19}$), strontium ferrite ($SrFe_{12}O_{19}$), or neodymium iron boron ($Nd_2Fe_{14}B$) and samarium cobalt ($SmCo_5$, Sm_2Co_{17}) known as rare-earth magnets.

Soft magnetic materials, such as pure iron (Fe), nickel-iron alloy, and silicon-iron alloy, are known for their strong response to magnetic fields, characterized by high saturation magnetization. However, they tend to retain a low residual magnetization after saturation and are easily demagnetized due to their low coercivity. That is, soft magnetic materials have narrow hysteresis (Figure 3B). In addition, these materials, utilized as fillers, possess high relative permeability and swift responsiveness, making them widely utilized in the fabrication of magnetic alignment composites.[35] Ferromagnetic particles smaller than a certain critical size are referred to as superparamagnetic materials, behaving somewhat similarly to non-magnetic substances in the absence of an external magnetic field, despite maintaining relatively high magnetization (Figure 3C). Superparamagnetism is a property exhibited by nanometer-sized magnetic particles, where the continual thermal motion and Brownian motion cause their magnetic structure to fluctuate, rendering them essentially unaligned in the absence of an external magnetic field. Notably, Fe_3O_4 nanoparticles are widely utilized in various fields, including biomedical applications and micro-robotics, due to their biocompatibility and relatively high magnetization.[37-39] Typically, Fe_3O_4 undergoes a transition from a soft magnetic phase to a superparamagnetic phase at a critical size of around 20 nm.[40]

3.1.1. Magnetically responsive soft robots

Due to recent advances in 3D printing technology for soft materials, current research is focused on developing soft robots capable of achieving complex behaviors through the use of 3D-printed magnetically responsive soft materials (Table 2). Embedded magnetic filler particles generate internal stress as they attempt to align with the magnetic field under external magnetic influence, resulting in macroscopic deformation and exhibiting intricate behavior.[41-43]

A method has been developed to program complex non-uniform magnetic domain patterns using permanent magnets or electromagnets on hard magnetic particles

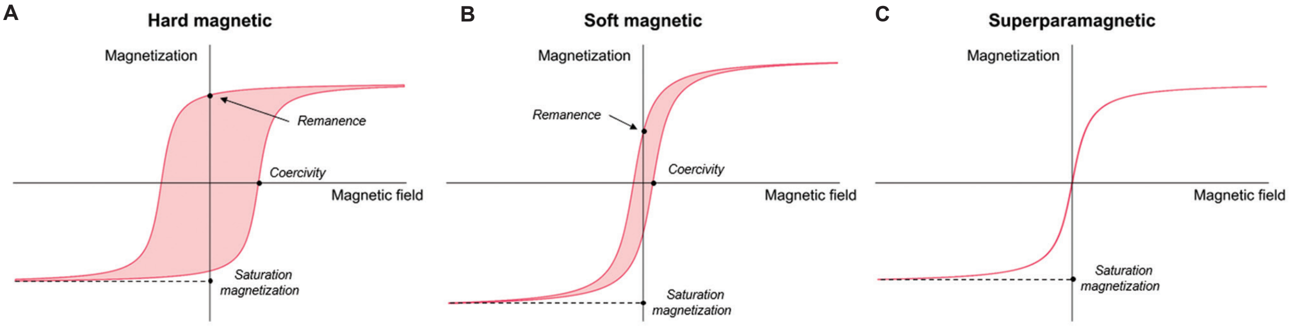

Figure 3. Comparison of magnetization characteristics under magnetic field. (A) Hard magnetic materials. (B) Soft magnetic materials. (C) Superparamagnetic materials.

Table 2. Comparison of materials and fabrication methods for magnetically responsive soft robots

3D printing method	Material composition	Description	References
Material extrusion (DIW)	NdFeB microparticles+thermoplastic elastomers (styrene-isoprene block copolymers)	NdFeB-SIS composite ink is developed to provide high elasticity (>1000%), and an origami-inspired printing method is introduced for reprogramming.	41
Material extrusion (DIW)	NdFeB microparticles+silicone elastomers (SE1700 and Ecoflex 00-30 Part B)	The evolutionary algorithm-guided voxel encoding is proposed to design tailored magnetic density and direction, leading to functional biomimetic soft robots and expanded applications.	42
Material extrusion (DIW)	NdFeB microparticles+silicone elastomers (SE1700 and Ecoflex 00-30 Part B)	A new 3D printing technology is proposed for shape-programmable soft materials utilizing magnetic fields for untethered actuation and delivering potential for biomedical devices, and soft robotics via customized domain patterns and magnetization strength.	44
Material extrusion (DIW)	NdFeB microparticles+silicone elastomers (Sylgard 184)	A 4D printing method utilizing an origami-based magnetization technique is proposed. This method enables the fabrication of complex objects with the ability to reprogram their magnetization. Bionic hands serve as an example of this capability.	43
Material extrusion (DIW)	NdFeB microparticles+thermoplastic elastomers (thermoplastic urethane) NdFeB microparticles+silicone elastomers (Sylgard 184)	A continuum soft robot with omnidirectional steering capabilities, miniaturized ferromagnetic domains, and hydrogel skin for navigation in complex environments and steerable laser delivery was presented for minimally invasive robotics surgery.	45
Material extrusion (DIW)	NdFeB microparticles+silicone elastomers (SE 1700)	A coaxial printing method for creating soft-magnetic-electrical fibers is presented, enabling hybrid functions issues in soft robotics and biomedical applications, demonstrated by catheter-based electro-ablation, somatosensory gripper.	47
Vat photopolymerization (DLP)	NdFeB microparticles+photocurable elastomers	A UV lithography-based method is presented for patterning magnetic particles in elastomer matrices, enabling custom 3D magnetization profiles for higher-order microrobots, leading to locomotion with multi-arm grasping and multi-legged crawling.	49
Vat photopolymerization (CLIP)	Fe_3O_4 nanoparticles+photocurable elastomers	A comprehensive solution for designing and fabricating a 3D micro-robotic gripper using a high-resolution CLIP process for untethered operation in both dry and aqueous environments has been presented, resulting in a monolithic gripper design.	50

Abbreviations: CLIP: Continuous liquid interface production; DIW: Direct ink writing; DLP: Digital light processing; NdFeB: Neodymium magnet.

inside soft materials utilized in extrusion-based 3D printing, such as DIW.[44] Soft materials embedded with neodymium magnet (NdFeB) particles, programmed through this method, can undergo rapid transformations of complex shapes under the influence of an external magnetic field. Building on this capability, a soft robot capable of crawling and jumping was developed. Similarly, a method has been developed that can program not only the direction but also the density of the magnetic domain on a voxel basis in the printed filament using an evolutionary algorithm.[42] Through this approach, a four-legged soft robot mimicking a trot (dog gaits) was developed from a soft material embedded with NdFeB particles under an alternating magnetic field. This demonstration highlights the potential for greatly expanding application possibilities beyond the brute-force approach used to program the magnetization domain of existing magnetically responsive soft materials.

A mechanism was proposed to reprogram the magnetization profile by folding a hinge-designed magnetically responsive material into a desired shape and applying an impulse magnetic field exceeding the coercivity. Using this mechanism, a multi-finger soft robotic gripper exhibiting precise operation was demonstrated (Figure 4A).[41] A rock-paper-scissors gesture was demonstrated by re-magnetizing a magnetically responsive NdFeB material that mimics the human hand.[45] For hard magnetic materials that are already saturated, the remanence can be initialized by heating and cooling above the Curie point of the material in addition to applying an impulse magnetic field greater than the coercive force.

The self-responsive soft material is soft and flexible while exhibiting excellent responsiveness, enabling expansion into a core-sheath structure through integration with a functional core. Several studies have explored its application in biomedical contexts. For instance, a soft robotic catheter was developed using a polymer matrix embedded with NdFeB particles as a sheath and inserting other functional materials coaxially into the core.[46] This catheter robot, featuring an optical fiber as its functional core and a magnetically responsive soft material coated with hydrogel as its sheath, demonstrated laser delivery by reaching the target point within a 3D cerebrovascular phantom through flexible motion. Similarly, a coaxial printing method has been developed, enabling the simultaneous printing of the core and sheath to yield structures with excellent magnetic reactivity and conductivity. This method involves using a conductive liquid metal core and a magnetically responsive soft material sheath structure embedded with NdFeB particles.[47] Employing this coaxial printing method, a soft robot gripper has been developed, capable of grabing objects of various sizes by transforming under the influence of a magnetic field. In addition, a soft robot gripper capable of detecting the size of the captured object by analyzing the changing induced magnetic field was demonstrated.

In addition to extrusion-based 3D printing methods, the design and fabrication of magnetically responsive soft materials using light-based 3D printing methods have been reported. Compared to extrusion-based 3D printing, which typically has relatively lower resolution, light-based 3D printing generally has high resolution.[48] By utilizing this technology, an eight-legged paddle-crawling robot was developed by programming magnetic domains into NdFeB particles embedded within a magnetically responsive soft material.[49] Demonstrations of the robot's crawling motion on silicone oil were achieved by applying an alternating magnetic field. Furthermore, a micro-scale robotic gripper was developed using the CLIP approach instead of the slower SLA approach, which exhibits clear boundaries between layers.[50] This gripper utilizes Fe_3O_4 with a diameter of 20 – 30 nm, considered a superparamagnetic material, as a filler for achieving fast closing motion.[40] The low residual magnetization enables rapid closing of the gripper by its elasticity.

3D printing technology has revolutionized the field of magnetically responsive soft robots, enabling the creation of complex designs and sophisticated functionalities that were previously unattainable through traditional manufacturing methods. Material extrusion 3D printing offers the ability to program the magnetization direction of the printed filament by applying an external magnetic field, allowing for customized designs. This technique has proven particularly useful for fabricating soft robots with intricate structures and tailored properties. Vat photopolymerization 3D printing also provides the capability for localized magnetization programming during layer-by-layer printing. Light-based 3D printing generally offers higher resolution and faster printing speeds compared to extrusion-based methods. However, the use of dark magnetic materials can lead to reduced curing speeds, limiting the incorporation of high magnetic particle contents.

Despite the rapid advancements in 3D-printed magnetically responsive soft robots, several areas still require improvement:

(i) Real-time feedback-based autonomous control: In soft robotic applications, such as navigating through blood vessels, real-time feedback is crucial for obstacle avoidance and path planning. Vision-based feedback systems can be integrated with electromagnetic actuation systems to enable intelligent control and maneuverability.

(ii) Multi-material printing: The combination of materials with different magnetic properties using multi-nozzle printers opens up possibilities for creating

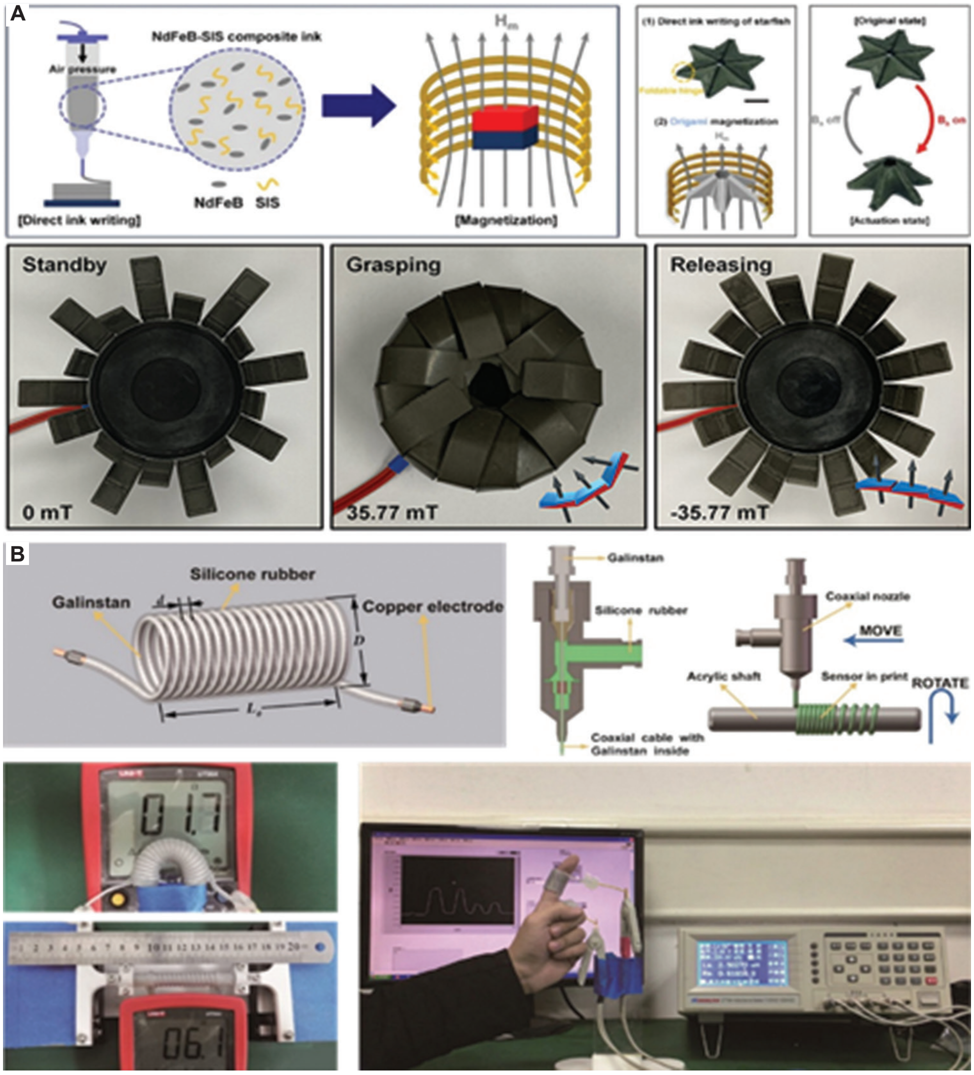

Figure 4. Polymer-based applications of magnetic powder- and metallic powder-embedded materials. (A) Origami-based programming magnetization profile method and soft robots based on magnetically responsive soft materials. Images reproduced with permission from Wajahat *et al.*[41] Copyright © 2023 American Chemical Society. (B) Soft wearable inductance sensor fabricated with a liquid metal core-polymer sheath structure. Images reproduced with permission from Zhou *et al.*[74] Copyright © 2018 American Chemical Society.

multifunctional soft robots. Integrating magnetic materials with other functional materials, such as biocompatible or conductive materials, can expand the capabilities and applications of these robots.

(iii) High magnetic particle content limitations in vat photopolymerization: While vat photopolymerization offers advantages like high resolution, it presents a challenge when using dark magnetic particles. These particles can hinder the curing process due to light absorption, making it difficult to achieve high magnetic particle content within the printed structures. This limitation can restrict the overall magnetic strength and functionality of the soft robots produced using this method.

3.2. Metal powders

In recent years, there has been remarkable progress in the field of electronic devices, especially with the emergence of soft electronics based on polymer matrices, which have seen significant advancements following the recent strides in 3D printing technology. Nanoparticle fillers can be added to polymers to impart various properties.[51] Among these, metal nanoparticle inks are readily available and exhibit relatively high electrical conductivity compared to inks containing other types of nanofillers.[52] These metal nanoparticles are used to develop a variety of flexible or stretchable soft electronics by combining embedded polymer composite ink, conformal printing, and 3D printer technology, which allows for on-demand production.

Metal nanoparticle fillers have a direct impact on the electrical and mechanical characteristics of the printed products.[52-54] To determine the suitability of metal nanoparticles, factors such as electrical conductivity, oxidation stability, and electrical properties can be considered based on the required performance of individual soft electronics. The most commonly used metal nanoparticles are those of single elements, such as silver, gold, and copper nanoparticles.[52-56] Among them, silver is the most widely used conductive filler due to its outstanding electrical conductivity, mechanical rigidity, and high corrosion resistance among metals.[55-59] Moreover, silver nanoparticles find extensive use in medical applications, as they can be employed for selective laser photothermal treatment, leveraging the surface plasmon resonance effect and the ability to convert strongly absorbed light into local heat.[60-62] Copper nanoparticles are relatively inexpensive compared to silver and gold and possess similar electrical conductivity and a low electron transfer effect as silver.[53,54] However, when forming copper nanoparticles in air, an oxide layer is generated on the surface for thermodynamic stability, leading to a reduction in electrical conductivity and an increase in sintering temperature.[63-66] The formation of an oxide layer renders the sintering of copper nanoparticle inks technically challenging, which is one of the main reasons why copper nanoparticles are used less frequently than the relatively more expensive silver nanoparticles as conductive fillers.

3.2.1. Soft sensors embedded with metallic nanoparticles

Polymer-based sensors printed using 3D printing technology can achieve excellent shape restoration and perform various functions depending on the embedded conductive material. Particularly, polymer composites embedded with conductive nanoparticles are known to exhibit a sensitive resistance response to strain and possess excellent electrical conductivity.[67-69] An ideal elastic conductor maintains constant high conductivity over a wide range of strain rates.[70] In particular, strain and tactile sensors made of metals with excellent conductivity are actively being researched. The material, fabrication method, and performance of the polymer-based sensor embedded with metallic particles are summarized in Table 3.

Taking advantage of the fact that extrusion-based DIW 3D printing allows for multi-material printing, a tactile sensor was demonstrated through a single process with four different independently addressable nozzles.[71] The tactile sensor comprises two electrode layers, one insulating layer, a support layer, a sensor layer, and a base layer. The sensor layer and electrode layer contained silver nanoparticles embedded in silicone elastomer, and the completed sensor exhibited high flexibility, electrical conductivity, and sensitivity. It is also possible to expand it into an array form.

Strain sensors and capacitive sensors fabricated using a new method called hybrid 3D printing have been reported.[72] Advanced soft sensors are accomplished

Table 3. Comparison of materials, fabrication methods, and performance of soft sensors embedded with metallic nanoparticles

3D printing method	Material composition	Applications	Performances	References
Multi-material extrusion (DIW)	Submicrometer-sized silver particles+silicone elastomers (Dragon Skin 10)	Tactile sensor	As the pressure applied rose from 100 to 500 kPa, the device's resistance decreased approximately twelvefold, dropping from 1.14 kΩ to 95 Ω; gauge factor: about 180	71
Material extrusion (DIW) with automated pick-and-place	Silver micro-flakes+thermoplastic elastomers (thermoplastic urethane)	Microcontroller device and wearable device	Electrical conductivity; initial: 10^4×S/cm; at strain of 240%: 0.1 S/cm; gauge factor 13.3	72
Feedback-controlled material extrusion (DIW)	Silver micro-flakes+poly (ethylene oxide) (PEO)	Inductive coil (also suitable for moisture sensing), wearable device	Electrical conductivity $(1.38\pm0.0814) \times 10^4$ S/cm (one order of magnitude lower than bulk silver)	73
Coaxially material extrusion (DIW)	Galinstan+silicone elastomers (737 neutral cure sealant)	Strain sensor	Maximum tensile strain of 100%; can be bent up to 180 degrees	74
Integrating vat photopolymerization (DLP) and material extrusion (DIW)	(i) DLP elastomer: acrylate-based (ii) DLP plastic: acrylate-thiol based (iii) DIW ink: photosensitive ink, conductive silver ink, and LCE ink	Strain gauge	Gauge factor: 251	75

Abbreviations: DIW: Direct ink writing; DLP: Digital light processing; LCE: Liquid crystal elastomers.

through the integration of DIW printing and automated pick-and-place of electronic components within a unified manufacturing platform. Ink using silver flakes as filler in a thermoplastic polyurethane (TPU) matrix is printed as a strain gauge, along with a pick-and-place microcontroller and LED, resulting in the development of a large-area wearable strain gauge. The developed strain gauge outputs LED readings according to joint bending. Similarly, a moisture sensor was developed through a pick-and-place hybrid procedure of DIW 3D printing and surface-mount electronic components (LEDs).[73] Polyethylene oxide (PEO) composite with silver flakes as conductive filler was extruded and printed in the form of an induction coil. When immersed in water, the printed conductive traces undergo a reverse drying process and exhibit higher impedance. Under controlled moisture, the ink maintains its printed shape and recovers to its initial impedance level after drying.

In addition, a flexible sensor was developed to detect the deformation and posture of a snake-like soft robot based on liquid metal (Figure 4B).[74] Liquid metal-based sensors have the advantage of measuring large deformations by remaining connected even after experiencing large deformations due to their stable electrical properties. Since liquid metal has low printability, silicon and liquid metal are printed together coaxially. The sensor is printed in the shape of a solenoid and can be installed on a soft robot, such as a snake, to distinguish tensile and bending deformations.

Extrusion-based 3D printing has been considered the predominant approach for fabricating soft sensors embedded with metallic powder. However, a limited but notable alternative has been reported: vat photopolymerization printing. Photopolymerization-based printing is only applicable to photosensitive resins, and metallic powders may absorb and reflect light, potentially impeding sufficient light penetration into the material. These limitations can result in incomplete curing of the material and degradation of mechanical properties. In addition, metallic powders have high thermal conductivity, which can concentrate heat energy generated during the photopolymerization process onto the soft material, leading to thermal damage or deformation of the material.

To circumvent these limitations, hybrid 3D printing that integrates the advantages of vat photopolymerization and extrusion-based 3D printing was developed. This approach has demonstrated strain gauge fabrication.[75] The hybrid 3D printer combines DLP for high-resolution printing of a photosensitive matrix and DIW for printing conductive silver nanoparticle ink. Through optimization of printing parameters, strong interfacial bonding between the DLP-printed matrix and DIW-printed functional materials was achieved. The developed strain gauge exhibited a gauge factor of 251, indicating relatively excellent sensitivity.

Advanced 3D printing techniques, such as multi-material extrusion, hybrid printing, and coaxial printing, have emerged as powerful tools for fabricating soft sensors. These 3D printing methods have particularly facilitated soft sensors embedded with metallic nanoparticles, enabling immediate fabrication on request. The integration of metal particles into non-conductive polymer matrices imparts electrical conductivity, while the inherent flexibility of polymers facilitates their applications in various fields, such as strain sensors and wearable sensors. Despite their advantages, metal particle-embedded soft materials face several challenges:

(i) High-temperature sintering: Metal nanoparticles often require high-temperature sintering (typically above 100°C) to enhance electrical conductivity, hindering *in situ* fabrication within the human body.
(ii) Cost limitations: Silver nanoparticles, the most commonly used, are expensive, thereby limiting their suitability for mass production. Although copper nanoparticles are cheaper than silver nanoparticles, they are less commonly used due to the aforementioned manufacturing difficulties.
(iii) Oxidation: The large surface area of nanoparticles makes them susceptible to oxidation, potentially compromising their long-term performance.

3.3. Perovskites

Perovskite materials have attracted considerable interest in the semiconductor field due to their unique characteristics, such as strong absorption coefficients, excellent tolerance to defects, and high charge carrier mobility.[76-78] Perovskites generally possess ABX_3 structure, where A and B represent cations, and X represents an anion (A: MA^+ or FA^+ or Cs^+, B: Pb^{2+} or Sn^{2+}, X: Cl^- or Br^- or I^-). The enhanced photoluminescence quantum yield (PLQY) and superior color purity inherent to perovskites significantly enhance the power conversion efficiency (PCE) in solar cells.[79-83] Furthermore, their broad wavelength spectrum facilitates the generation of diverse light colors in LEDs, which plays a critical role in achieving high-resolution display technologies.[84,85] Moreover, these properties are critically harnessed in engineering highly sensitive sensors capable of detecting subtle environmental alterations.[86] Conventional fabrication methods of perovskite devices include spin coating,[87] spray coating,[88] and blade coating.[89] However, spin coating often leads to substantial material loss, spray coating poses challenges in controlling the uniformity of perovskite layer thickness, and blade coating encounters difficulties in fabricating ultrathin films.

3D printing technology has emerged as an alternative that overcomes the limitations of conventional fabrication methods. It enables the fabrication of complex structures, optimization of material usage, and cost-effective production. In particular, it has been employed for fabricating perovskite layers using inkjet printing,[90] meniscus printing,[91] electrohydrodynamic (EHD) printing,[92] FDM,[93] and DIW.[94] However, securing high-quality and stable inks remains a significant challenge. Technological advancements in the fabrication and performance of perovskite materials using 3D printing technology are detailed in Table 4, highlighting their application in devices such as solar cells, sensors, and LEDs.

3.3.1. Photovoltaic effect

Perovskite solar cells (PSCs) and photodetectors both leverage the light absorption properties of perovskites to generate electrical signals from light energy. In PSCs, light induces the generation of electron-hole pairs within the active perovskite layer, which are, then, transported through the hole transport layer (HTL) and electron transport layer (ETL) to electrodes, thereby transforming light into electricity. Similarly, perovskite photodetectors generate electron-hole pairs on exposure to light, guiding them toward electrodes to produce electrical signals for detecting light intensity and wavelength. These applications are pivotal in various fields, such as environmental monitoring, image sensing, and optical communication, requiring high sensitivity and rapid response times. These technologies underscore the versatility and efficiency of perovskites in converting light into electrical energy for various practical applications.

Inkjet printing achieves a high PCE of more than 21%, replacing the conventional spin coating method due to difficulties in scaling up to large areas. This advancement was facilitated by utilizing a high-concentration precursor to effectively form absorption layers thicker than 1 μm, and by streamlining the manufacturing process through a single-ink approach.[95] Perovskite photodetectors with high resolution, flexibility, and wide color range have been fabricated using EHD printing, overcoming the limitations of fabricating multi-spectral semiconductors. This printing technique successfully produced high-quality perovskite dot arrays with 1 μm precision, presenting the potential for future wide-color photodetector and artificial vision systems.[96]

3.3.2. Perovskite displays

In perovskite LEDs and through photoluminescence in perovskites, the interplay of electrons and holes is crucial for the conversion of electrical and absorbed light energy into emitted light of various wavelengths. Electron-hole recombination within the perovskite layer is key to the efficiency of light emission in LEDs, where the introduction of various nanoparticles allows for a spectrum of colors with high purity. Photoluminescence, on the other hand, involves the absorption of photons that excite electrons to higher energy states. Following this excitation, some energy is lost, and the remaining energy is emitted as light when the

Table 4. Fabrication methods and applications using perovskite

3D printing method	Structure	Applications	Description	References
Inkjet	$Cs_{0.1}MA_{0.15}FA_{0.75}$, Pb $(I_{0.85}Br_{0.15})_3$	Solar cells	Inkjet-printed micrometer-thick perovskite solar cells achieve high power conversion efficiencies (PCEs) exceeding 21% and are promising for scalable applications in photovoltaic technologies.	95
Electrohydrodynamic (EHD)	$MAPbX_3$	Photodetector	The high-resolution perovskite full-colored photodetector achieves a responsivity of 14.97 A W^{-1}, a detectivity of 1.41×10^{12} Jones and features 1 μm diameter dot arrays.	96
Inkjet	$CsPbBr_3$	Displays (LEDs)	The inkjet-printed perovskite photodetector reported a PLQY of 61.8% and an external quantum efficiency (EQE) of 5.9%.	97
Inkjet	$FA_{0.8}Cs_{0.2}PbI_3$, $CsPbBr_3$, $Cs_{0.75}EA_{0.25}PbBr_3$	Displays (LEDs)	Perovskite light-emitting diodes (PeLEDs) exhibit a PLQY of 14.3% and are used in flexible, large-area panel lighting and displays, offering high resolution.	98
Inkjet	$CsPbBr_3$-PVP	Displays	Inkjet-printed perovskite nanocomposites achieve a 64.3% PLQY and are used for detailed, high-resolution patterning in applications like anticounterfeiting labels.	99
Meniscus	$MAPbX_3$	Displays	The meniscus-guided 3D printing technique enables the creation of perovskite nanowire heterostructures with nano-pixel resolution, facilitating innovative applications in high-resolution optoelectronics.	91

Abbreviations: PLQY: Photoluminescence quantum yield; LEDs: Light-emitting diode.

electrons return to lower energy states. This process enables perovskites to emit light at wavelengths different from the absorbed light, showcasing their potential to produce diverse and pure colors in lighting and display technologies.

LEDs were fabricated using $CsPbBr_3$ nanocrystals that maintain their crystalline structure and exhibit high PLQY even under high-temperature annealing. A novel inkjet printing technique utilizing high-boiling decalin and octane-mixed solvents was developed. This method demonstrated a six-fold increase in efficiency compared to LEDs fabricated using conventional spin coating.[97] Perovskite LEDs (PeLEDs) have garnered attention due to their characteristics, such as solution processing, large-area fabrication, and flexibility, which contrast with those of conventional inorganic LEDs. However, challenges arise when applying blade or slot-die coating to flexible substrates. In a separate study, large-area fabrication was achieved through inkjet printing technology. The fabricated PeLEDs exhibited an external quantum efficiency (EQE) of 14.3% at an area of 0.04 cm², suggesting the feasibility of future wide-color displays.[98]

Inkjet printing capable of precision control was implemented by adding polyvinylpyrrolidone (PVP) to perovskite. This technology is activated by light, exhibiting a fluorescent effect. The patterns created are composed of dot microarrays, exhibiting homogeneity at a macroscopic level and high reproducibility at a microscopic level. In the pertinent study, the arrangement of these dots enabled the creation of complex images such as barcodes, the logo of Fuzhou University, and honeybee illustrations. Perovskite exhibits nearly invisible characteristics in ambient conditions and can be applied to flexible substrates, indicating its potential for use in anticounterfeiting labels (Figure 5A).[99] Furthermore, complex-shaped and compositionally diverse perovskite heterostructures were fabricated using meniscus-guided printing. A study demonstrated the capability to program various emission colors, achieving color mixing and encryption at the single nanopixel level.[91]

Perovskite printing technology is garnering attention for its potential applications in flexible electronics and wearable devices due to its high material utilization efficiency and cost-effectiveness. This technology enables direct printing on flexible substrates, offering significant design flexibility and the ability to create precise patterns through fine nozzles, making it ideal for producing high-resolution displays. However, devices such as PSCs and photodetectors face challenges in maintaining long-term performance stability due to their sensitivity to environmental factors such as humidity and temperature. To overcome these challenges, further research emphasizes optimizing the chemical and physical properties of the ink, as well as exploring encapsulation and specialized coating techniques. Such advancements are expected to enhance the commercial viability of perovskite inkjet printing technology. In addition, ongoing studies focusing on optimizing ink viscosity, surface tension, and chemical properties are crucial for advancing this field.

3.4. Piezoelectrics

Piezoelectric technology possesses the capability to convert mechanical energy, such as vibrations or impacts, into electrical energy, and vice versa. The piezoelectric and converse piezoelectric effects are mathematically described by **Equations I and II**, respectively.

$$D = dT + \in^{T} E \qquad \text{(Piezoelectric effect)} \qquad \text{(I)}$$

$$S = s^{E}T + dE \qquad \text{(Converse piezoelectric effect)} \qquad \text{(II)}$$

In these equations, D represents electric displacement, d the piezoelectric charge coefficient, T mechanical stress, $\in^{T}$ permittivity of the material (for T = constant), E electrical field, S mechanical strain, and s^{E} mechanical compliance (for E = constant). The piezoelectric charge coefficient, d, varies depending on the material and its orientation, reflecting the material's effectiveness in converting mechanical energy into electrical energy and vice versa. This technology is crucial in the development of compact electronic devices, such as portable gadgets, medical technologies, and Internet of Things devices.[100,101] It enables continuous operation without the need for recharging, thereby gaining recognition as an environmentally friendly material.

Piezoelectric materials are categorized into ceramics and polymers. Ceramic materials include lead zirconate titanate (PZT)-based compounds, which possess high piezoelectric constants and ferroelectric properties,[102] as well as lead-free materials, such as $BaTiO_3$, known for their environmental friendliness.[103] On the polymer side, materials such as polyvinylidene fluoride (PVDF) and P(VDF-TrFE) are prominent, particularly in wearable technologies, due to their flexibility and ease of processing.[104,105]

Conventional manufacturing methods for piezoelectric devices, including sintering, etching, and cutting,[106-108] exhibit limitations in creating complex geometries. These methods often result in issues such as mechanical stress, loss of grain structure, reduction in strength, and near-surface depolarization.[109]

The introduction of 3D printing technology has addressed these challenges, offering advantages over traditional manufacturing methods as follows: (i) the capability to fabricate complex structures, (ii) precise

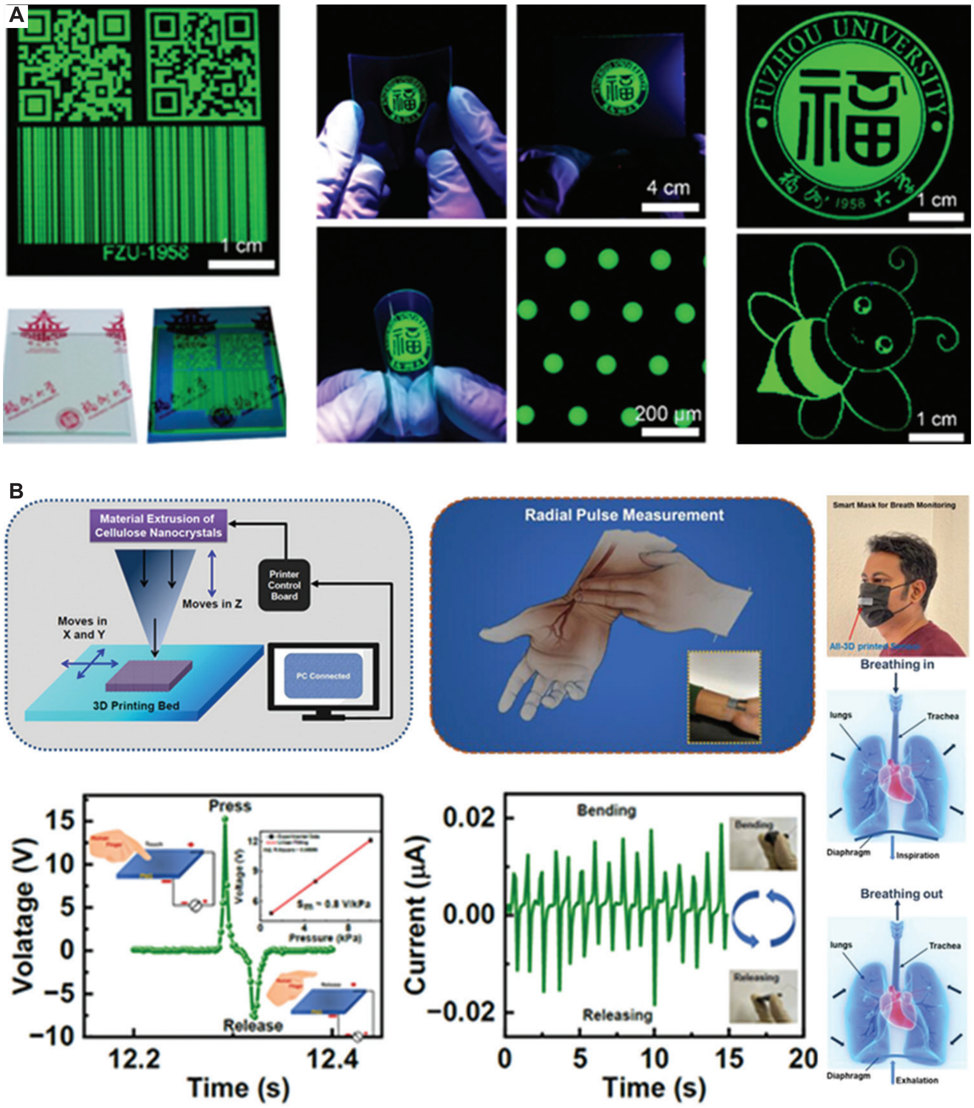

Figure 5. Applications of perovskite and piezoelectric materials. (A) Microarrays of anticounterfeiting labels made from perovskites with polyvinylpyrrolidone. Images reproduced with permission from Liu *et al.*[99] Copyright © 2019 American Chemical Society. (B) All-3D-printed pyroelectric NG (PyNG) applications, such as self-powered sensors and energy harvesting. Images reproduced with permission from Maity *et al.*[115] Copyright © 2023 American Chemical Society.

control over microscale components, (iii) simplification of device assembly and packaging stages, and (iv) enhanced electromechanical responses and piezoelectric output.[109] Piezoelectric devices are primarily manufactured using 3D printing methods such as SLA,[110] FDM,[111] DIW,[112] DLP,[113] and inkjet printing.[114] These techniques provide the potential for precise and efficient fabrication of complex 3D piezoelectric structures. Recent advances in 3D printing technology for piezoelectric materials are summarized in Table 5, highlighting their improved performance and applications in sensors, pressure detectors, and energy harvesting devices.

3.4.1. Energy harvester and sensors

Piezoelectric materials can convert mechanical stress or vibrations into electrical energy through structural deformation, leading to charge separation and accumulation. This process generates a potential difference, aiding in the transformation of mechanical to electrical energy, which can power devices immediately or be stored for future use. Widely adopted in the industrial sector for its accuracy and quick response, piezoelectric materials enable precise measurements of vibrations, pressure, and force, converting mechanical energy changes into electrical signals for application in various technologies.

Table 5. Comparison of materials and fabrication methods for piezoelectrics

3D printing method	Material composition	Applications	Description	References
FDM	Cellulose nanocrystal, CNT	Energy Harvester and sensors	An all-3D-printed pyro-piezoelectric nanogenerator using cellulose nanocrystals is introduced for self-powered cardiorespiratory monitoring, facilitating non-invasive health tracking.	115
DIW	PVDF, MoS_2	Energy Harvester and sensors	3D printing and 2D MoS2 nanofillers enhanced PVDF-based sensors, achieving a piezoelectric coefficient of 48.4 pC N^{-1}, approximately 8.2 times higher than as-cast PVDF for advanced precision applications.	116
DIW	P (VDF-TrFE), $BaTiO_3$	Sensors	A fully printed piezoelectric pressure sensor demonstrated in this work achieves a stable output of approximately 2.5 V at 30 kPa over 2000 seconds with minimal variation and is effectively employed in a prosthetic hand to discern the tactile hardness of various objects.	117
DLP	PZT, SiOC	Piezo actuators	The described multi-material additive manufacturing technique crafts intricate 3D robotic metamaterials with piezoceramic, metallic, and structural elements, enabling small-scale devices capable of complex motions and integrated sensing for advanced robotic and transducer applications.	118

Abbreviations: CNT: Carbon nanotube; DIW: Direct ink writing; DLP: Digital light processing; FDM: Fused deposition modeling; PZT: Lead zirconate titanate; PVDF: Polyvinylidene fluoride; SLA: Stereolithography; SLS: Selective laser sintering.

A hybrid thermoelectric-piezoelectric nanogenerator, utilizing cellulose nanocrystals to harvest mechanical and thermal energy, was fabricated using FDM. This 3D printing methodology reduces the number of processing steps required for multilayer fabrication while maintaining excellent stability and performance. The fabricated sensor exhibits superior mechanical energy harvesting and can accurately detect heartbeats and respiration regardless of time and location without an external power source. Furthermore, the device facilitates noninvasive monitoring of cardiorespiratory status, representing an advancement in the development of human-machine interfaces through its self-powered operation (Figure 5B).[115] Sensors fabricated using DIW with MoS_2-enhanced PVDF demonstrated a piezoelectric coefficient (d_{33}) of 48.4 pC N^{-1}, which is approximately eight times higher than that of sensors produced through casting.[116] In addition, a fully printed and PDMS-packaged piezoelectric sensor using P(VDF-TrFE)-$BaTiO_3$ was fabricated through DIW. The fabricated sensor was successfully attached to a prosthetic hand, enabling it to detect dynamic tactile data and identify objects.[117]

3.4.2. *Piezo actuators*

The inverse piezoelectric effect converts external electrical signals into mechanical energy, leading to the physical deformation of piezoelectric materials. When voltage is applied, the material's crystal structure deforms, slightly changing its dimensions. The extent of this expansion or contraction is influenced by the magnitude and direction of the applied voltage and the type of material. This precise control over deformation is utilized in applications such as precision positioning, vibration generation, and fluid control. These capabilities underline the significance of the inverse piezoelectric effect in various technological fields.

A robotic metamaterial utilizing DLP technology has been fabricated, featuring multi-degree-of-freedom movements. This robotic metamaterial is designed as a micro 3D lattice structure that integrates piezoelectric, conductive, and structural elements. It can undergo numerous deformation modes, including twisting, shear, normal deformation, and combinations and amplifications of these modes. Such robotic metamaterials surpass the limitations of natural piezoelectric crystals and are expected to directly influence the development of future micro-robots and transducers.[118]

3D printing of piezoelectric materials allows for the precise fabrication of complex shapes and structures, applicable in various fields such as energy harvesters and sensors. This technology enables the design of multifunctional sensors with integrated capabilities. In addition, 3D printing facilitates the structural optimization of lightweight actuators. However, products manufactured through this method may have reduced durability compared to those produced by traditional methods, and minor defects that occur during the printing process can lead to performance degradation. Consequently, further research and development are needed to enhance the piezoelectric efficiency and durability of these materials, addressing the challenges inherent in the 3D printing process to ensure reliable and robust performance in practical applications.

3.5. Thermoelectrics

Thermoelectrics directly transform the temperature difference into electric current and vice versa using the

Peltier and Seebeck effects. This feature can be utilized in various fields, such as energy harvesting, cooling systems, and sensors.[119] As the potential difference generated within a single p-n semiconductor remains at the millivolt scale, thermoelectric devices achieve higher voltages by linking multiple p-n semiconductors in series.[120] For the n-type component, cationic materials such as TiO_{2-x} and $BixSb_{2-x}Te_{3-y}$, while for the p-type component, anionic materials such as Ni and $Bi_2(SeyTe_{1-y})_3$ are used.

The inefficiency in utilizing thermal energy stems from the limitation of traditional thermoelectric device manufacturing, which is confined to a 2D plane. Therefore, 3D printing technology, which can overcome these limitations, is gaining attention. There are various thermoelectric manufacturing technologies utilizing the 3D printing method, including material jetting, vat photopolymerization, materials extrusion, PBF (SLS), screen printing, dispenser printing, and inkjet printing.[17,120-124] These techniques offer benefits, including the capability to create precise structures, reduce material wastage, apply diverse materials, and expedite the prototyping process.[119] Recent advances in 3D printing technology for thermoelectric materials are summarized in Table 6, highlighting their improved performance and applications in thermoelectric cooler and generator.

3.5.1. Thermoelectric coolers

Thermoelectric coolers (TECs), which function based on the Peltier effect, offer various advantages. TECs enable precise temperature control by directly adjusting power through variations in input current. Furthermore, they have the benefits of low noise and minimized size due to the absence of compressors.[125] Therefore, numerous studies have been conducted to enhance stability and increase cooling efficiency.

Li *et al.*[126] fabricated flexible thermoelectric thick films using screen printing on a polyimide substrate with a $Bi_{0.5}Sb_{1.5}Te_3$/epoxy composite. These films created a temperature difference from 4.2 to 7.8 K when the current was between 0.01 and 0.05 A, with a power factor (PF) of 1.12 mW/m·K^{-2}. This achievement expands the potential of the flexible TECs with better cooling performance based on the higher PF value. Lu *et al.*[127] utilized inkjet printing to fabricate thin film TECs using nanoparticle materials: p-type $Sb_{1.5}Bi_{0.5}Te_3$ size of 9.8 ±2.7 nm and n-type $Bi_2Te_{2.7}Se_{0.3}$ size of 7.6 ± 1.9 nm on a polyimide (PI) substrate. The maximum PF was approximately 77 μW/m·K^{-2} at 75°C. This finding suggests the potential for improving the drawbacks of conventional nanoparticle thin-film manufacturing processes, such as complex manufacturing processes and material wastage. Since thin films are superior in localizing cooling and heating compared to bulk devices,[128] they will lead to advancements in fields such as microelectronics and thermochemistry-on-a-chip.

3.5.2. Thermoelectric generators (TEGs)

The Seebeck effect is an electrical phenomenon observed between two semiconductors due to a temperature difference, where electrons migrate from one material to another in response to the temperature gradient. TEGs function based on the Seebeck effect, and they can generate electricity from small temperature differences, with the advantages of minimal size and lightweight. Therefore, numerous studies have been conducted to enhance stability and broaden the scalability of application areas. A state-of-the-art, flexible TEG with metal chalcogenide nanowires was developed through inkjet printing. The printed films achieved a PF of 493.8 μW/m·K^{-2} at 400 K and a power density of 0.9 μW/m·K^{-2} using materials such as Ag_2Te, Cu_7Te_4, and $Bi_2Te_{2.7}Se_{0.3}$.[129] This development enhanced both parameters and demonstrated promising scalability for novel materials. Moreover, a flexible TEG on a paper substrate was developed through dispenser printing. Materials such as $Bi_{0.5}Sb_{1.5}Te_3$ and $Bi_2Se_{0.3}Te_{2.7}$ were used, achieving an output power and voltage

Table 6. Comparison of materials and fabrication methods for thermoelectric

Printing Method	Composition	Application	Performance	Reference
Screen	Bi0.5Sb1.5Te3/epoxy composite	TEC	Temperature difference from 4.2 to 7.8 K with current 0.01 to 0.05 A, at PF of 1.12 mW/m·K^{-2}	126
Inkjet	p-type $Sb_{1.5}Bi_{0.5}Te_3$ n-type $Bi_2Te_{2.7}Se_{0.3}$	TEC	PF of 77 μW/m·K^{-2} at 75°C	127
Inkjet	Ag_2Te, Cu_7Te_4, $Bi_2Te_{2.7}Se_{0.3}$	TEG	PF of 493.8 μW/m·K^{-2} at 400 K and power density of 0.9 μW/m·K^{-2}	129
Dispenser	$Bi_{0.5}Sb_{1.5}Te_3$, Bi2Se$_{0.3}$Te$_{2.7}$	TEG	Output power and voltage of 10 nW and 8.3 mV, respectively, with a thousand bending cycles at 35K	124
Ink dispensing	SWCNTs/SDBS, SWCNTs/CTAB	TEG	PF values of 308 μW/m·K^{-2} and 258 μW/m·K^{-2} for the p-type and n-type film, respectively	130

Abbreviations: PF: Power factor; SWCNTs/CTAB: Single-walled carbon nanotubes/cetyltrimethylammonium bromide; SWCNTs/SDBS: Single-walled carbon nanotubes/sodium dodecylbenzene sulfonate; TEC: Thermoelectric cooler; TEG: Thermoelectric generator.

of 10 nW and 8.3 mV, respectively, after a thousand bending cycles at 35 K.[124] Figure 6B illustrates the manufacturing process and the complete structure of the flexible TEG. This research indicates the potential for printing TEGs on paper, which is widely used in various industries, thus enhancing the scalability of TEGs. Furthermore, Mytafides *et al.*[130] fabricated TEGs using ink dispensing with single-walled carbon nanotube (SWCNT) material. The resulting TEGs achieved high flexibility and PF values of 308 μW/m·K^{-2} and 258 μW/m·K^{-2} for the p-type and n-type film, respectively. The materials used were SWCNTs/sodium dodecylbenzene sulfonate and SWCNTs/cetyltrimethylammonium bromide. These TEGs maintained stability even in encapsulated conditions, demonstrating the potential for advancing TEG technology by adopting new materials and producing durable TEGs for applications in extreme conditions. Figure 6A depicts the structural composition, flexibility, and overall construction of the fabricated TEGs.

3.6. Carbon-based materials

Carbon-based materials are compounds consisting of carbon atoms, with properties varying according to their chemical structure. They generally exhibit lightweight, high strength, electrical and thermal conductivity, and chemical stability. Examples of carbon-based materials include graphene, which consists of widely spread carbon atoms, carbon nanotubes (CNTs) with a cylindrical structure, and fullerenes with a spherical shape. These materials find wide applications in various fields, such as microelectronics, electrochemical biosensors, strain sensors, and chemical sensors.[131,132] At present, the general manufacturing methods for carbon-based materials are chemical vapor deposition (CVD) and arc discharge. However, CVD has disadvantages, such as the use of numerous solvents, complex manufacturing processes, and high costs. The arc discharge method may also be susceptible to impurities and material wastage.[133] Therefore, various printing techniques such as DIW, binder jetting, inkjet printing, spray coating, FDM, and SLS have been developed to address these problems. These methods offer advantages such as simplification of processes, precise structure printing, minimal material wastage, and rapid prototyping. However, challenges remain, including high porosity, weak connections between layers, and ensuring the production of high-quality materials.[134] Recent advances in 3D printing technology for carbon-based materials are summarized in Table 7, with improved performance and applications in sensor and battery.

3.6.1. Carbon-based sensors

Carbon-based chemical and strain sensors have revolutionized modern sensing technology. Chemical

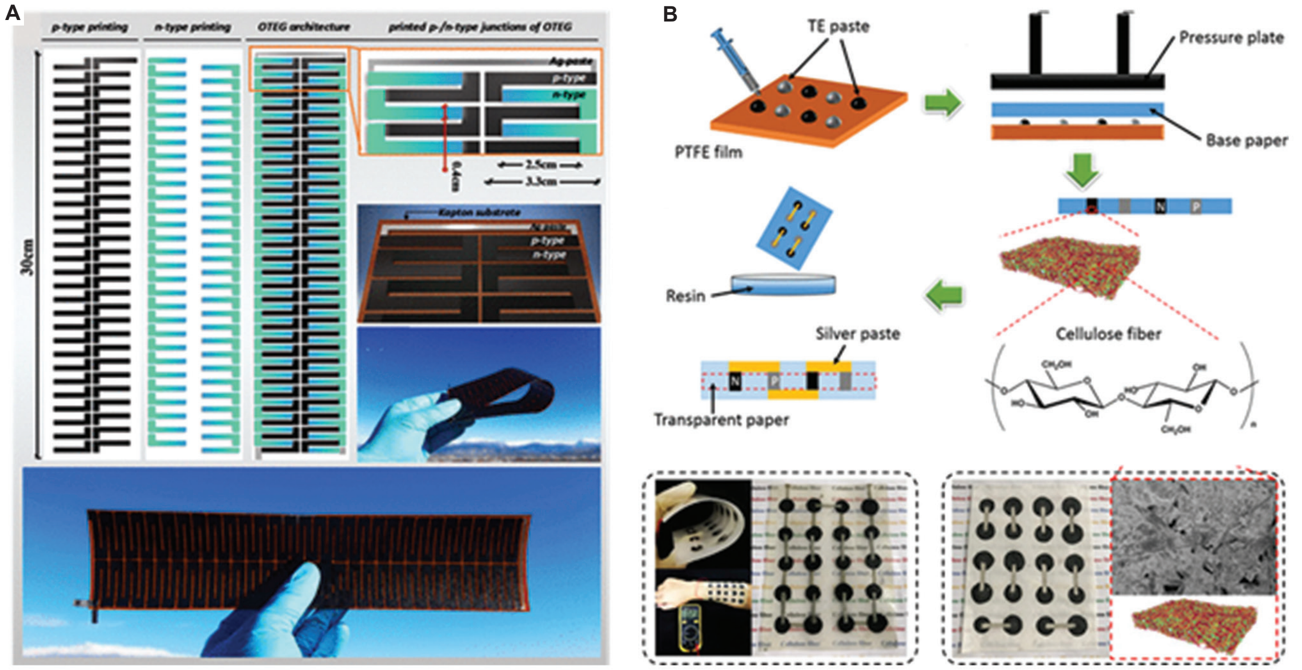

Figure 6. Applications of thermoelectric materials. (A) Fabrication of an all-carbon, fully printed, and flexible thermoelectric generator, including its structure, flexibility, and overall composition. Images reproduced with permission from Mytafides *et al.*[130] Copyright 2021 © American Chemical Society. (B) Schematic diagram illustrating the fabrication process and the resulting transparent paper-based flexible thermoelectric generator. Images reproduced with permission from Zhao *et al.*[124] Copyright © 2019 American Chemical Society. Abbreviations: OTEG: Organic thermoelectric generator; PTFE: Polytetrafluoroethylene; TE: Thermoelectric.

Table 7. Comparison of materials and fabrication methods for carbon-based materials

Printing method	Composition	Application	Performance	References
Inkjet	Poly (3,4ethylenedioxythiophene), COOH, PEDOT: PSS, CNT	Chemical sensor	Sensitivity (ΔS/ΔC) of 24.4×10^{-4} and short response/recovery times of 13/60 at 1000 ppm	135
Screen	Graphene-carbon ink	Humidity sensor	resistance-humidity gradient was~12.4 Ω/%RH (room humidity) on 25%RH to 91.7%RH	136
Extrusion	Pristine graphene formulated from ethyl cellulose, toluene/ethanol	VOC sensor	Detect chemical substances - ethanol, methanol, and acetone within the range of 5 to 100 ppm.	142
Laser-induced forward transfer	SWCNTs/SnO2 NPs	Chemical sensor (NH_3)	At room temperature, NH_3 response time of 13 s for 25 ppm	144
Meniscus	MWNTs, PVP	Strain sensor	Gauge factors of 12.87 at compressive strain and 13.07 at tensile strain at over 1500 bending cycles	137
FDM	Graphene-based polylactic acid, TPU	Strain sensor	High level of sensitivity	138
Inkjet	Graphene nano-sheets, green solvent: ethanol, stabilizer: 1 wt% ethyl-cellulose	Battery	~942 mAh/g at 0.1 C. With the 100 cycles of bending, 87% capacity remained.	140
Inkjet	$LiFePO_4$/AB/CNT	Battery	150 mAh/g at 0.1 C with 150 cycles	141
Vat photopolymerization (SLA)	PEGDA, Sudan I, GPE, PC, EC, Carbon black	Battery	Capacity of 1.4 μAh/cm^2 after 2 cycles.	143

Abbreviations: AB: Acetylene Black; CNT: Carbon nanotube; EC: Ethylene Carbonate; FDM: Fused deposition modeling; GPE: Gel Polymer Electrolyte; MWNTs: Multiwall nanotubes; NPs: Nanoparticles; PC: Propylene Carbonate; PEDOT: PSS: Poly (3,4-ethylenedioxythiophene) polystyrene sulfonate; PVP: Polyvinylpyrrolidone; SLA: Stereolithography; SWCNTs: Single-walled carbon nanotube; TPU: Thermoplastic polyurethane; VOC: Volatile organic compound.

sensors exhibit notable sensitivity to various compounds, with short response and recovery times. Similarly, strain sensors can sensitively detect structural deformations and stresses. Consequently, carbon-based chemical and strain sensors demonstrate innovative application potentials across various industries.

(a) Chemical sensors

Chemical sensors rely on chemical reactions altering the material's properties, forming the fundamental principle of their operation. Due to the durability and outstanding properties of carbon-based materials, they are often utilized in chemical sensors. For instance, a highly sensitive flexible ethanol sensor was developed using inkjet printing, functionalized with poly(3,4-ethylenedioxythiophene) and carboxylic acid (COOH) poly (styrenesulfonate) (PEDOT: PSS) CNT. It exhibits a sensitivity (ΔS/ΔC) of 24.4×10^{-4} and short response/recovery times of 13/60 at 1000 ppm.[135] Its high sensitivity is anticipated to lead to the development of precise ethanol sensors. In addition, a humidity sensor was developed using graphene-carbon ink through screen printing on substrates such as glossy paper, matt paper, and sylvicta. The sensor resistance-humidity gradient was approximately 12.4 Ω/%RH (room humidity) from 25% RH to 91.7% RH. It displayed flexibility, stability, repeatability, durability, and short response/recovery time.[136] Detecting humidity is essential across diverse industries, environmental monitoring, and health-care sectors, making it applicable in various fields. Furthermore, a volatile organic compound sensor was developed using pristine graphene formulated from ethyl cellulose and toluene/ethanol through extrusion printing.[137] Sized approximately 12 μm, it demonstrated the capability to detect chemical substances such as ethanol, methanol, and acetone within the range of 5 – 100 ppm. A formula relating concentration in ppm and resistance variation was derived, enabling current concentration measurements. The miniaturization of existing sensors suggests the potential to advance portable chemical sensor technology, thereby leading to the development of portable chemical sensors. Furthermore, Anca *et al.*[138] fabricated NH_3 detectable chemical sensors using laser-induced forward transfer printing. The minimum detectable NH_3 value was 25 ppm, with a response time of 13 s, showcasing an expansion of the manufacturing process.

(b) Strain sensors

The strain-sensitive property of an object, influenced by its structure, undergoes changes when subjected to mechanical forces such as tension or compression. This alteration in the property enables accurate measurement of strain experienced by the object.

Flexible strain sensors were developed using CNT ink with multiwall nanotubes and PVP through meniscus-guided printing based on the principle of piezoresistivity. This sensor achieved gauge factors of 12.87 at compressive strain and 13.07 at tensile strain and maintained its performance over approximately 1500 bending cycles (Figure 7A and B).[139] This research, by enhancing the gauge factor, has improved precision and shown new potential in fields such as robotics engineering and wearable sensors, which demand precise measurements. In addition, a strain sensor using graphene-based polylactic acid with TPU was developed through FDM. It operates on the principle of piezoresistivity, calculating variations in resistance induced by applied tensile and compressive strain.[140] The study demonstrated the possibility of enhancing flexibility by more than fourfold while maintaining a high level of sensitivity comparable to that of a typical graphene sensor.

3.6.2. Batteries

Most lithium-ion batteries share similar shapes and solid properties. However, since the majority of electronic devices use batteries and their design must accommodate the battery, it hinders the free design of electric devices. To overcome these drawbacks, there is increasing attention on 3D printing technology, which enables free control of shapes and the fabrication of precise structures, including flexible batteries. Consequently, research is progressing on 3D printing carbon-based materials, which constitute the major parts of a battery, to address these problems.

A state-of-the-art flexible battery was developed with a CNT: MnO$_2$ anode. It achieved a capacity of 63 µAh cm^{-2} at 0.4 mA cm^{-2} and experienced only a 2.72% loss in capacity when the battery was bent.[141] This advancement holds promise for the development of wearable electronic devices, medical devices, and smart clothing. Furthermore, a lithium-ion battery utilizing graphene nanosheets with solvent exfoliation using green solvent (ethanol) and stabilizer (1 wt% ethyl-cellulose) was developed through inkjet printing. The battery achieved a capacity of approximately 942 mAh/g at 0.1 C. Even after 100 cycles of bending, the electrode retained approximately 87% of its initial capacity, as shown in Figure 7C.[142] It demonstrated outstanding battery performance and scalability in industries such as smartphones and automobiles. Furthermore, a lithium-ion

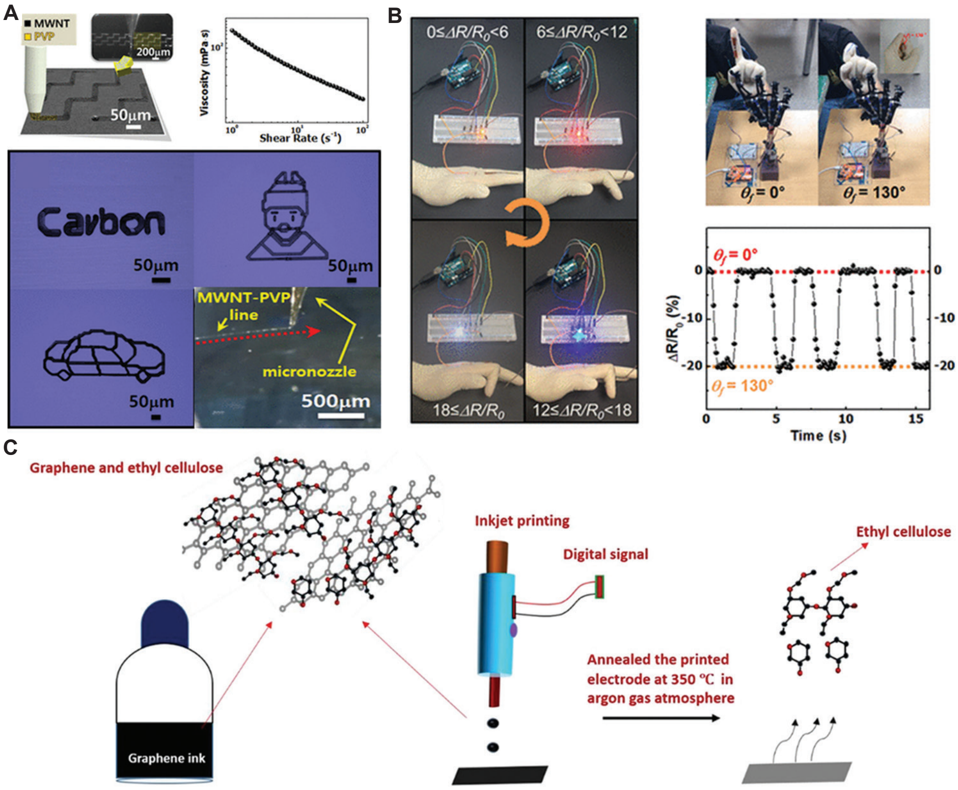

Figure 7. Fabrication and application of carbon-based materials. (A) Schematic diagram illustrating the meniscus-guided printing process for fabricating a transparent paper-based flexible thermoelectric generator (TEG), along with its resulting structure. (B) The fabrication process of an all-carbon fully printed and flexible TEG, including its structure, flexibility, and overall composition. Images in (A) and (B) reproduced with permission from Wajahat *et al.*[137] Copyright © 2018 American Chemical Society. (C) A schematic depiction of the graphene ink, inkjet-printing process, and annealing of printed samples in the production of graphene thin-film electrodes for use in lithium-ion batteries. Images reproduced with permission from Kushwaha *et al.*[142] Copyright © 2021 American Chemical Society.

battery using $LiFePO_4$/AB/CNT was developed through inkjet printing. It demonstrated a specific capacity of 150 mAh/g at 0.1 C with 150 cycles.[143] This study represents the fabrication of thick electrodes with high-power density and energy density, revealing the potential for high-performance energy storage devices. Furthermore, Chen *et al.*[144] developed a lithium-ion micro-battery using carbon black through SLA. The battery exhibited a capacity of 1.4 μAh/cm^2 after two cycles of charging. This study signifies the expansion of existing manufacturing methods.

4. Conclusion and future perspectives

The promising and essential AM technology, pivotal for the Fourth Industrial Revolution, offers tremendous utility in manufacturing, spanning from product development to efficient production and small-batch manufacturing of diverse products. The advancement of AM technology has led to the development of materials with enhanced performance and novel characteristics, alongside the introduction of efficient and precise manufacturing systems to the market. Particularly, intensive research on functional materials based on polymer substrates and their applications is currently underway, showcasing their immense potential value.

In this review, we categorize the AM technologies primarily used for manufacturing functional polymer materials based on their manufacturing methods and operational principles. Subsequently, we examine the AM processes based on the characteristics of functional materials. By emphasizing the key features of each material, we support an upward approach to functional polymer design, enabling not only optimal process ability but also the achievement of multifunctional and complex shape manufacturing.

Next, we investigate the functional properties primarily utilized in current polymer-based functional materials. The development of functional materials based on polymers is predominantly focused on photosensitive resins. Extensive research has been conducted on the development of functional resins with properties such as biocompatibility, electrical conductivity, and magnetism. For instance, research on biocompatible resins is progressing for the optimal design of artificial organs and internal implants. In addition, research on functional materials for various applications, such as sensors, actuators, and soft robots, utilizing electrical conductivity and magnetism, is ongoing. Studies showcasing the achievement of special functionalities through the utilization of the unique 3D manufacturing capabilities and mixed production characteristics of AM technologies have also been examined.

Furthermore, we explore the development of functional components with various structures utilizing AM technologies, such as piezoelectric, thermoelectric, and perovskite materials. The advancement of functional components usable in diverse applications such as energy harvesting, displays, and sensors has been facilitated by the development of AM technologies. Integration with polymer materials has enabled manufacturing on curved surfaces, the development of flexible components, and the enhancement of functional properties, maximizing the utilization methods and fields of AM technologies.

This review emphasizes the importance of functional polymer materials in expanding the scope and capabilities of AM processes. Active participation in diversifying material options to meet the varied requirements of modern manufacturing, ranging from photosensitive resins to polymer powders, filaments, and viscous inks, is evident in recent research. Novel functional polymer materials with enhanced conductivity, actuation, and other functionalities hold huge potential across various application domains, from biocompatible implants to smart robots.

Overall, the rapid growth of research environments and technological advancements in polymer materials for AM signify a promising future where AM becomes an essential and complementary component of the modern manufacturing ecosystem. Through continuous interdisciplinary collaboration and innovation, the vision of realizing fully functional custom products through AM will be achieved.

Acknowledgments

None.

Funding

This work was supported by the Technology Development Program (Grant No. S3248116) funded by the Ministry of SMEs and Startups (MSS, Korea), and the National Research Foundation of Korea (NRF) grant under the Korea government (MSIT) (no. RS-2023-00211636).

Conflicts of interest

The authors declare that they have no competing interests.

Authors' contributions

Conceptualization: Im Doo Jung, Hayeol Kim
Investigation: All authors
Writing – original draft: All authors
Writing – review and *editing:* Im Doo Jung, Hayeol Kim

Ethics approval and consent to participate

Not applicable.

Consent for publication

Not applicable.

Availability of data

Not applicable.

References

1. Madhavadas V, Srivastava D, Chadha U, *et al*. A review on metal additive manufacturing for intricately shaped aerospace components. *CIRP J Manuf Sci Technol*. 2022;39:18-36.

   doi: 10.1016/j.cirpj.2022.07.005

2. Park JW, Shin YC, Kang HG, *et al*. *In vivo* analysis of post-joint-peserving surgery fracture of 3D-printed Ti-6Al-4V implant to treat bone cancer. *Bio Des Manuf*. 2021;4:879-888.

   doi: 10.1007/s42242-021-00147-2

3. Kim T, Kim JG, Park S, *et al*. Virtual surface morphology generation of Ti-6Al-4V directed energy deposition via conditional generative adversarial network. *Virtual Phys Prototyp*. 2023;18(1):e2124921.

   doi: 10.1080/17452759.2022.2124921

4. Tan LJ, Zhu W, Zhou K. Recent progress on polymer materials for additive manufacturing. *Adv Funct Mater*. 2020;30(43):2003062.

   doi: 10.1002/adfm.202003062

5. Wu H, Fahy WP, Kim S, *et al*. Recent developments in polymers/polymer nanocomposites for additive manufacturing. *Prog Mater Sci*. 2020;111:100638.

   doi: 10.1016/j.pmatsci.2020.100638

6. Li J, Lin X, Kang N, Lu J, Wang Q, Huang W. Microstructure, tensile and wear poperties of a novel graded al matrix composite pepared by direct energy deposition. *J Alloy Compd*. 2020;826:154077.

   doi: 10.1016/j.jallcom.2020.154077

7. Seo E, Sung H, Jeon H, *et al*. Laser powder bed fusion for AI assisted digital metal components. *Virtual Phys Prototyp*. 2022;17(4):806-820.

   doi: 10.1080/17452759.2022.2068804

8. Hotz H, Zimmermann M, Greco S, Kirsch B, Aurich JC. Additive manufacturing of functionally graded Ti-Al structures by laser-based direct energy deposition. *J Manuf Process*. 2021;68:1524-1534.

   doi: 10.1016/j.jmapro.2021.06.068

9. Jung ID, Lee MS, Lee J, *et al*. Embedding sensors using selective laser melting for self-cognitive metal parts. *Addit Manuf*. 2020;33:101151.

   doi: 10.1016/j.addma.2020.101151

10. Lee MS, Kim H, Koo YT, *et al*. Selective laser melting process for sensor embedding into SUS316L with heat dissipative inner cavity design. *Met Mater Int*. 2022;28:1-9.

    doi: 10.1007/s12540-021-01106-3

11. Lee J, Choe J, Park J, Yu JH, Kim S, Sung H. Microstructural effects on the tensile and fracture behavior of selective laser melted H13 tool steel under varying conditions. *Mater Charact*. 2019;55:109817.

    doi: 10.1016/j.matchar.2019.109817

12. Verma S, Yang CK, Lin CH, Jeng JY. Additive manufacturing of lattice structures for high strength mechanical interlocking of metal and resin during injection molding. *Addit Manuf*. 2022;49:102463.

    doi: 10.1016/j.addma.2021.102463

13. Joyee EB, Pan Y. Additive manufacturing of multi-material soft robot for on-demand drug delivery applications. *J Manuf Process*. 2020;56:1178-1184.

    doi: 10.1016/j.jmapro.2020.03.059

14. Rafiee M, Farahani RD, Therriault D. Multi-material 3D and 4D printing: A survey. *Adv Sci*. 2020;7(12):1902307.

    doi: 10.1002/advs.201902307

15. Champeau M, Heinze DA, Viana TN, de Souza ER, Chinellato AC, Titotto S. 4D printing of hydrogels: A review. *Adv Funct Mater*. 2020;30(31):1910606.

    doi: 10.1002/adfm.201910606

16. Liu J, Shang Y, Shao Z, Liu X, Zhang C. Three-dimensional printing to translate simulation to architecting for three-dimensional high performance piezoelectric Energy harvester. *Ind Eng Chem Res*. 2021;61(1):433-440.

    doi: 10.1021/acs.iecr.1c04433

17. Zhang D, Lim WYS, Duran SSF, Loh XJ, Suwardi A. Additive manufacturing of thermoelectrics: Emerging trends and outlook. *ACS Energy Lett*. 2022;7(2):720-735.

    doi: 10.1021/acsenergylett.1c02553

18. Park JW, Seo E, Park H, *et al*. Hybrid solid mesh structure for electron beam melting customized implant to treat bone cancer. *Int J Bioprinting*. 2023;9(4):716.

    doi: 10.18063/ijb.716

19. Culmone C, Smit G, Breedveld P. Additive manufacturing of medical instruments: A state-of-the-art review. *Addit Manuf*. 2019;27:461-473.

    doi: 10.1016/j.addma.2019.03.015

20. Huang J, Chen Q, Jiang H, *et al*. A survey of design methods for material extrusion polymer 3D printing. *Virtual Phys Prototyp*. 2020;15(2):148-162.

    doi: 10.1080/17452759.2019.1708027

21. Hossain SS, Gao B, Park S, Bae CJ. Incorporating nanoparticles in alumina ink for improved solid-loading

and sinterability of extrusion-based 3D printing. *ACS Appl Nano Mater*. 2022;5(12):17828-17838.

doi: 10.1021/acsanm.2c03792

22. Kim JH, Park S, Ahn J, *et al*. Meniscus-guided micro-printing of prussian blue for smart electrochromic display. *Adv Sci*. 2023;10(3):2205588.

    doi: 10.1002/advs.202205588

23. Lee S, Kim JH, Wajahat M, *et al*. Three-dimensional printing of silver microarchitectures using newtonian nanoparticle inks. *ACS Appl Mater Interfaces*. 2017;9(22):18918-18924.

    doi: 10.1021/acsami.7b02581

24. Gu X, Shaw L, Gu K, Toney MF, Bao Z. The meniscus-guided deposition of semiconducting polymers. *Nat Commun*. 2018;9(1):534.

    doi: 10.1038/s41467-018-02833-9

25. Pagac M, Hajnys J, Ma QP, *et al*. A review of vat photopolymerization technology: Materials, applications, challenges, and future trends of 3D printing. *Polymers*. 2021;13(4):598.

    doi: 10.3390/polym13040598

26. Gross B, Lockwood SY, Spence DM. Recent advances in analytical chemistry by 3D printing. *Anal Chem*. 2017;89(1):57-70.

    doi: 10.1021/acs.analchem.6b04344

27. Chiappone A, Fantino E, Roppolo I, *et al*. 3D printed PEG-based hybrid nanocomposites obtained by sol-gel technique. *ACS Appl Mater Interfaces*. 2016;8(8):5627-5633.

    doi: 10.1021/acsami.5b12578

28. Wang W, Liu S, Liu L, Alfarhan S, Jin K, Chen X. High-speed and high-resolution 3D printing of self-healing and ion-conductive hydrogels via μCLIP. *ACS Mater Lett*. 2023;5(6):1727-1737.

    doi: 10.1021/acsmaterialslett.3c00439

29. Jose RR, Rodriguez MJ, Dixon TA, Omenetto F, Kaplan DL. Evolution of bioinks and additive manufacturing technologies for 3D bioprinting. *ACS Biomater Sci Eng*. 2016;2(10):1662-1678.

    doi: 10.1021/acsbiomaterials.6b00088

30. Ouyang H, Li X, Lu X, Xia H. Selective laser sintering 4D printing of dynamic cross-linked polyurethane containing diels-alder bonds. *ACS Appl Polym Mater*. 2022;4(5):4035-4046.

    doi: 10.1021/acsapm.2c00565

31. Sireesha M, Lee J, Kiran ASK, Babu VJ, Kee BBT, Ramakrishna S. A review on additive manufacturing and its way into the oil and gas industry. *RSC Adv*. 2018;8(40):22460-22468.

    doi: 10.1039/C8RA03194K

32. Hines L, Petersen K, Lum GZ, Sitti M. Soft actuators for small-scale robotics. *Adv Mater*. 2017;29(13):1603483.

    doi: 10.1002/adma.201603483

33. Ju Y, Hu R, Xie Y, *et al*. Reconfigurable magnetic soft robots with multimodal locomotion. *Nano Energy*. 2021;87:106169.

    doi: 10.1016/j.nanoen.2021.106169

34. Kim Y, Zhao X. Magnetic soft materials and robots. *Chem Rev*. 2022;122(5):5317-5364.

    doi: 10.1021/acs.chemrev.1c00481

35. Zhang C, Li X, Jiang L, *et al*. 3D pinting of functional magnetic materials: From design to applications. *Adv Funct Mater*. 2021;31(34):2102777.

    doi: 10.1002/adfm.20210277

36. Zhao R, Kim Y, Chester SA, Sharma P, Zhao X. Mechanics of hard-magnetic soft materials. *J Mech Phys Solids*. 2019;124:244-263.

    doi: 10.1016/j.jmps.2018.10.008

37. Lantean S, Barrera G, Pirri CF, *et al*. 3D printing of magnetoresponsive polymeric materials with tunable mechanical and magnetic properties by digital light processing. *Adv Mater Technol*. 2019;4(11):1900505.

    doi: 10.1002/admt.201900505

38. Shasha C, Krishnan KM. Nonequilibrium dynamics of magnetic nanoparticles with applications in biomedicine. *Adv Mater*. 2021;33(23):1904131.

    doi: 10.1002/adma.201904131

39. Xiao Y, Du J. Superparamagnetic nanoparticles for biomedical applications. *J Mater Chem B*. 2020;8(3):354-367.

    doi: 10.1039/C9TB01955C

40. Ghazanfari MR, Kashefi M, Shams SF, Jaafari MR. Perspective of Fe3O4 nanoparticles role in biomedical applications. *Biochem Res Int*. 2016;2016:7840161.

    doi: 10.1155/2016/7840161

41. Wajahat M, Kim JH, Kim JH, Jung ID, Pyo J, Seol SK. 4D printing of ultrastretchable magnetoactive soft material architectures for soft actuators. *ACS Appl Mater Interfaces*. 2023;15(51):59582-59591.

    doi: 10.1021/acsami.3c12173

42. Wu S, Hamel CM, Ze Q, Yang F, Qi HJ, Zhao R. Evolutionary algorithm-guided voxel-encoding printing of functional hard-magnetic soft active materials. *Adv Intell Syst*. 2020;2(8):2000060.

    doi: 10.1002/aisy.202000060

43. Ren Z, Hu W, Dong X, Sitti M. Multi-functional soft-bodied jellyfish-like swimming. *Nat Commun*. 2019;10(1):2703.

    doi: 10.1038/s41467-019-10549-7

44. Kim Y, Yuk H, Zhao R, Chester SA, Zhao X. Printing ferromagnetic domains for untethered fast-transforming soft materials. *Nature*. 2018;558(7709):274-279.

doi: 10.1038/s41586-018-0185-0

45. Zhang Y, Wang Q, Yi S, *et al*. 4D printing of magnetoactive soft materials for on-demand magnetic aactuation transformation. *ACS Appl Mater Interfaces*. 2021;13(3):4174-4184.

    doi: 10.1021/acsami.0c19280

46. Kim Y, Parada GA, Liu S, Zhao X. Ferromagnetic soft continuum robots. *Sci Robot*. 2019;4(33):eaax7329.

    doi: 10.1126/scirobotics.aax7329

47. Zhang Y, Pan C, Liu P, *et al*. Coaxially printed magnetic mechanical electrical hybrid structures with actuation and sensing functionalities. *Nat Commun*. 2023;14(1):4428.

    doi: 10.1038/s41467-023-40109-z

48. Hofmann M. 3D printing gets a boost and opportunities with polymer materials. *ACS Macro Lett*. 2014;3(4):295-397.

    doi: 10.1021/mz4006556

49. Xu T, Zhang J, Salehizadeh M, Onaizah O, Diller E. Millimeter-scale flexible robots with programmable three-dimensional magnetization and motions. *Sci Robot*. 2019;4(29):eaav4494.

    doi: 10.1126/scirobotics.aav4494

50. Shao G, Ware HOT, Huang J, Hai R, Li L, Sun C. 3D printed magnetically-actuating micro-gripper operates in air and water. *Addit Manuf*. 2021;38:101834.

    doi: 10.1016/j.addma.2020.101834

51. Siripongpreda T, Hoven VP, Narupai B, Rodthongkum N. Emerging 3D printing based on polymers and nanomaterial additives: Enhancement of properties and potential applications. *Eur Polym J*. 2021;184:111806.

    doi: 10.1016/j.eurpolymj.2022.111806

52. Tan HW, An J, Chua CK, Tran T. Metallic nanoparticle inks for 3D printing of electronics. *Adv Electron Mater*. 2019;5(5):1800831.

    doi: 10.1002/aelm.201800831

53. Huang Q, Zhu Y. Printing conductive nanomaterials for flexible and stretchable electronics: A review of materials, processes, and applications. *Adv Mater Technol*. 2019;4(5):1800546.

    doi: 10.1002/admt.201800546

54. Tan HW, Choong YYC, Kuo CN, Low HY, Chua CK. 3D printed electronics: Processes, materials and future trends. *Prog Mater Sci*. 2022;127:100945.

    doi: 10.1016/j.pmatsci.2022.100945

55. Yang C, Gu H, Lin W, *et al*. Silver nanowires: From scalable synthesis to recyclable foldable electronics. *Adv Mater*. 2011;23(27):3052-3056.

    doi: 10.1002/adma.201100530

56. Fu D, Yang R, Wang Y, Wang R, Hua F. Silver nanowire synthesis and applications in composites: Progress and prospects. *Adv Mater Technol*. 2022;7(11):2200027.

    doi: 10.1002/admt.202200027

57. Kim J, Kim WS. Stretching silver: Printed metallic nano inks in stretchable conductor applications. *IEEE Nanotechnol Mag*. 2014,8(4):6-13.

    doi: 10.1109/MNANO.2014.2355274

58. Jo H, Park JS, Lim HY, Lee GY. Laser sintered silver nanoparticles on the PDMS for a wearable strain sensor capable of detecting finger motion. *ACS Appl Nano Mater*. 2023;6(24):22998-23011.

    doi: 10.1021/acsanm.3c04386

59. Lee GY, Kim MS, Min SH, *et al*. Highly sensitive solvent-free silver nanoparticle strain sensors with tunable sensitivity created using an aerodynamically focused nanoparticle printer. *ACS Appl Mater Interfaces*. 2019;11(29):26421-26432.

    doi: 10.1021/acsami.9b00943

60. Jain PK, El-Sayed IH, El-Sayed MA. Au nanoparticles target cancer. *Nano Today*. 2007;2(1):18-29.

    doi: 10.1016/S1748-0132(07)70016-6

61. Boisselier E, Astruc D. Gold nanoparticles in nanomedicine: Preparations, imaging, diagnostics, therapies and toxicity. *Chem Soc Rev*. 2009;6:1759-1782.

    doi: 10.1039/B806051G

62. Dykman L, Khlebtsov N. Gold nanoparticles in biomedical applications: Recent advances and perspectives. *Chem Soc Rev*. 2012;41:2256-2282.

    doi: 10.1039/C1CS15166E

63. Park BK, Kim D, Jeong S, Moon J, Kim JS. Direct writing of copper conductive patterns by ink-jet printing. *Thin Solid Films*. 2007;515(19):7706-7711.

    doi: 10.1016/j.tsf.2006.11.142

64. Jeong S, Woo K, Kim D, *et al*. Controlling the thickness of the surface oxide layer on Cu nanoparticles for the fabrication of conductive structures by ink-jet printing. *Adv Funct Mater*. 2008;18(5):671-830.

    doi: 10.1002/adfm.200700902

65. Kim YJ, Ryu CH, Park SH, Kim HS. The effect of poly (N-vinylpyrrolidone) molecular weight on flash light sintering of copper nanopaste. *Thin Solid Films*. 2014;570:114-122.

    doi: 10.1016/j.tsf.2014.09.035

66. Dharmadasa R, Jha M, Amos DA, Druffel T. Room temperature synthesis of a copper ink for the intense pulsed light sintering of conductive copper films. *ACS Appl Mater Interfaces*. 2013;5(24):12773-13484.

    doi: 10.1021/am404226e

67. Zhan P, Jia Y, Zhai W, *et al*. A fibrous flexible strain sensor

with Ag nanoparticles and carbon nanotubes for synergetic high sensitivity and large response range. *Compos A Appl Sci Manuf*. 2023;167:107431.

doi: 10.1016/j.compositesa.2023.107431

68. Aslanidis E, Skotadis E, Tsoukalas D. Resistive crack-based nanoparticle strain sensors with extreme sensitivity and adjustable gauge factor, made on flexible substrates. *Nanoscale*. 2021;13(5):3263-3274.

    doi: 10.1039/d0nr07002e

69. Soe HM, Manaf AA, Matsuda A, Jaafar M. Development and fabrication of highly flexible, stretchable, and sensitive strain sensor for long durability based on silver nanoparticles-polydimethylsiloxane composite. *J Mater Sci Mater Electron*. 2020;31:11897-11910.

    doi: 10.1007/s10854-020-03744-6

70. Hammock ML, Chortos A, Tee BCK, Tok JBH, Bao Z. 25th Anniversary article: The evolution of electronic skin (E-Skin): A brief history, design considerations, and recent progress. *Adv Mater*. 2013;25(42):5997-6038.

    doi: 10.1002/adma.201302240

71. Guo SZ, Qiu K, Meng F, Park SH, McAlpine MC. 3D printed stretchable tactile sensors. *Adv Mater*. 2017;29(27):1701218.

    doi: 10.1002/adma.201701218

72. Valentine AD, Busbee TA, Boley JW, *et al*. Hybrid 3D printing of soft electronics. *Adv Mater*. 2017;29(40):1703817.

    doi: 10.1002/adma.201703817

73. Zhu Z, Guo SZ, Hirdler T, *et al*. 3D printed functional and biological materials on moving freeform surfaces. *Adv Mater*. 2018;30(23):1707495.

    doi: 10.1002/adma.201707495

74. Zhou LY, Gao Q, Zhan JF, Xie CQ, Fu JZ, He Y. Three-dimensional printed wearable sensors with liquid metals for detecting the pose of snakelike soft robots. *ACS Appl Mater Interfaces*. 2018;10(27):23208-23217.

    doi: 10.1021/acsami.8b06903

75. Peng X, Kuang X, Roach DJ, *et al*. Integrating digital light processing with direct ink writing for hybrid 3D printing of functional structures and devices. *Addit Manuf*. 2021;40:101911.

    doi: 10.1016/j.addma.2021.101911

76. Park NG. Perovskite solar cells: An emerging photovoltaic technology. *Mater Today*. 2015;18(2):65-72.

    doi: 10.1016/j.mattod.2014.07.007

77. Zhang X, Turiansky ME, Shen JX, Van de Walle CG. Defect tolerance in halide perovskites: A first-principles perspective. *J Appl Phys*. 2022;131(9):090901.

    doi: 10.1063/5.0083686

78. Motta C, El-Mellouhi F, Sanvito S. Charge carrier mobility in hybrid halide perovskites. *Sci Rep*. 2015;5(1):12746.

    doi: 10.1038/srep12746

79. Wei Z, Chen H, Yan K, Yang S. Inkjet printing and instant chemical transformation of a CH3NH3PbI3/nanocarbon electrode and interface for planar perovskite solar cells. *Angew Chem Int Ed Engl*. 2014;53(48):13239-13243.

    doi: 10.1002/anie.201408638

80. Mathies F, Abzieher T, Hochstuhl A, *et al*. Multipass inkjet printed planar methylammonium lead iodide perovskite solar cells. *J Mater Chem A*. 2016;4(48):19207-19213.

    doi: 10.1039/c6ta07972e

81. Choi JW, Woo HC, Huang X, *et al*. Organic-inorganic hybrid perovskite quantum dots with high PLQY and enhanced carrier mobility through crystallinity control by solvent engineering and solid-state ligand exchange. *Nanoscale*. 2018;10(28):13356-13367.

    doi: 10.1039/c8nr00806j

82. Liang H, Yuan F, Johnston A, *et al*. High color purity lead-free perovskite light-emitting diodes via sn stabilization. *Adv Sci* (*Weinh*). 2020;7(8):1903213.

    doi: 10.1002/advs.201903213

83. Bak T, Kim K, Seo E, *et al*. Accelerated design of high-efficiency lead-free tin perovskite solar cells via machine learning. *Int J Precis Eng Manuf Green Technol*. 2023;10(1):109-121.

    doi: 10.1007/s40684-022-00417-z

84. Ahmed T, Seth S, Samanta A. Boosting the photoluminescence of CsPbX3 (X=Cl, Br, I) perovskite nanocrystals covering a wide wavelength range by postsynthetic treatment with tetrafluoroborate salts. *Chem Mat*. 2018;30(11):3633-3637.

    doi: 10.1021/acs.chemmater.8b01235

85. Li F, Liu SF, Liu W, *et al*. 3D printing of inorganic nanomaterials by photochemically bonding colloidal nanocrystals. *Science*. 2023;381(6665):1468-1474.

    doi: 10.1126/science.adg6681

86. Liu J, Shabbir B, Wang C, *et al*. Flexible, printable soft-X-ray detectors based on all-inorganic perovskite quantum dots. *Adv Mater*. 2019;31(30):1901644.

    doi: 10.1002/adma.201901644

87. Zheng J, Zhang M, Lau CFJ, *et al*. Spin-coating free fabrication for highly efficient perovskite solar cells. *Sol Energy Mater Sol Cells*. 2017;168:165-171.

    doi: 10.1016/j.solmat.2017.04.029

88. Bishop JE, Smith JA, Lidzey DG. Development of spray-coated perovskite solar cells. *ACS Appl Mater Interfaces*. 2020;12(43):48237-48245.

    doi: 10.1021/acsami.0c14540

89. Kim JH, Williams ST, Cho N, Chueh CC, Jen AKY. Enhanced environmental stability of planar heterojunction perovskite solar cells based on blade-coating. *Adv Energy Mater*. 2014;5(4):1401229.

doi: 10.1002/aenm.201401229

90. Zhang L, Chen S, Wang X, *et al*. Ambient inkjet-printed high-efficiency perovskite solar cells: Manipulating the spreading and crystallization behaviors of picoliter perovskite droplets. *Sol RRL*. 2021;5(5):2100106.

doi: 10.1002/solr.202100106

91. Chen M, Zhou Z, Hu S, *et al*. 3D printing of arbitrary perovskite nanowire heterostructures. *Adv Funct Mater*. 2023;33(15):2212146.

doi: 10.1002/adfm.202212146

92. Zhu M, Duan Y, Liu N, *et al*. Electrohydrodynamically printed high-resolution full-color hybrid perovskites. *Adv Funct Mater*. 2019;29(35):1903294.

doi: 10.1002/adfm.201903294

93. Tang Y, Liu B, Yuan H, *et al*. *In situ* synthesis of MAPbX3 perovskite quantum dot-polycaprolactone composites for fluorescent 3D printing filament. *J Alloy Compd*. 2022;916:164961.

doi: 10.1016/j.jallcom.2022.164961

94. Jeon H, Wajahat M, Park S, *et al*. 3D Printing of luminescent perovskite quantum dot-polymer architectures. *Adv Funct Mater*. 2024;2024:2400594.

doi: 10.1002/adfm.202400594

95. Eggers H, Schackmar F, Abzieher T, *et al*. Inkjet-printed micrometer-thick perovskite solar cells with large columnar grains. *Adv Energy Mater*. 2019;10(6):1903184.

doi: 10.1002/aenm.201903184

96. Wang Q, Zhang G, Zhang H, Duan Y, Yin Z, Huang Y. High-resolution, flexible, and full-color perovskite image photodetector via electrohydrodynamic printing of ionic-liquid-based ink. *Adv Funct Mater*. 2021;31(28):2100857.

doi: 10.1002/adfm.202100857

97. Satake K, Sato Y, Narazaki K, *et al*. Fabrication of perovskite nanocrystal light-emitting diodes via inkjet printing with high-temperature annealing. *ACS Appl Opti Mater*. 2022;1(1):282-288.

doi: 10.1021/acsaom.2c00053

98. Liu H, Shi G, Khan R, *et al*. Large-area flexible perovskite light-emitting diodes enabled by inkjet printing. *Adv Mater*. 2024;36(8):2309921.

doi: 10.1002/adma.202309921

99. Liu Y, Li F, Qiu L, *et al*. Fluorescent Microarrays of in situ crystallized perovskite nanocomposites fabricated for patterned applications by using inkjet printing. *ACS Nano*. 2019;13(2):2042-2049.

doi: 10.1021/acsnano.8b08582

100. Yang Z, Zhou S, Zu J, Inman D. High-performance piezoelectric energy harvesters and their applications. *Joule*. 2018;2(4):642-697.

doi: 10.1016/j.joule.2018.03.011

101. Wu Y, Ma Y, Zheng H, Ramakrishna S. Piezoelectric materials for flexible and wearable electronics: A review. *Mater Des*. 2021;211:110164.

doi: 10.1016/j.matdes.2021.110164

102. Smith GL, Pulskamp JS, Sanchez LM, *et al*. PZT-based piezoelectric MEMS technology. *J Am Ceram Soc*. 2012;95(6):1777-1792.

doi: 10.1111/j.1551-2916.2012.05155.x

103. Park KI, Xu S, Liu Y, *et al*. Piezoelectric BaTiO(3) thin film nanogenerator on plastic substrates. *Nano Lett*. 2010;10(12):4939-4943.

doi: 10.1021/nl102959k

104. Ueberschlag P. PVDF piezoelectric polymer. *Sens Rev*. 2001;21(2):118-126.

doi: 10.1108/02602280110388315

105. Bhavanasi V, Kumar V, Parida K, Wang J, Lee PS. Enhanced piezoelectric energy harvesting performance of flexible PVDF-TrFE bilayer films with graphene oxide. *ACS Appl Mater Interfaces*. 2016;8(1):521-529.

doi: 10.1021/acsami.5b09502

106. Zhilun G, Longtu L, Suhua G, Xiaowen Z. Low-temperature sintering of lead-based piezoelectric ceramics. *J Am Ceram Soc*. 1989;72(3):486-491.

doi: 10.1111/j.1151-2916.1989.tb06160.x

107. Wang H, Godara M, Chen Z, Xie H. A one-step residue-free wet etching process of ceramic PZT for piezoelectric transducers. *Sens Actuator A Phys*. 2019;290:130-136.

doi: 10.1016/j.sna.2019.03.028

108. Amagata Y, Mihara S, Nishioki N, Higuchi T. *A New Fabrication Method for Microactuators with Piezoelectric Thin Film Using Precision Cutting Technique*. United States: IEEE; 1996. p. 307-311.

doi: 10.1109/MEMSYS.1996.493999

109. Megdich A, Habibi M, Laperrière L. A review on 3D printed piezoelectric energy harvesters: Materials, 3D printing techniques, and applications. *Mater Today Commun*. 2023;35:105541.

doi: 10.1016/j.mtcomm.2023.105541

110. Zhang J, Ye S, Liu H, *et al*. 3D printed piezoelectric BNNTs nanocomposites with tunable interface and microarchitectures for self-powered conformal sensors. *Nano Energy*. 2020;77:105300.

doi: 10.1016/j.nanoen.2020.105300

111. Song L, Dai R, Li Y, Wang Q, Zhang C. Polyvinylidene fluoride energy harvester with boosting piezoelectric performance through 3D printed biomimetic bone structures. *ACS Sustain Chem Eng*. 2021;9(22):7561-7568.

     doi: 10.1021/acssuschemeng.1c01305

112. Malakooti MH, Julé F, Sodano HA. Printed nanocomposite energy harvesters with controlled alignment of barium titanate nanowires. *ACS Appl Mater Interfaces*. 2018;10(44):38359-38367.

     doi: 10.1021/acsami.8b13643

113. Liu CL, Du Q, Zhang C, Wu JM, Zhang G, Shi YS. Fabrication and properties of BaTiO3 ceramics via digital light processing for piezoelectric energy harvesters. *Addit Manuf*. 2022;56:102940.

     doi: 10.1016/j.addma.2022.102940

114. Pabst O, Perelaer J, Beckert E, Schubert US, Eberhardt R, Tünnermann A. All inkjet-printed piezoelectric polymer actuators: Characterization and applications for micropumps in lab-on-a-chip systems. *Org Electron*. 2013;14(12):3423-3429.

     doi: 10.1016/j.orgel.2013.09.009

115. Maity K, Mondal A, Saha MC. Cellulose nanocrystal-based all-3D-printed pyro-piezoelectric nanogenerator for hybrid energy harvesting and self-powered cardiorespiratory monitoring toward the human-machine interface. *ACS Appl Mater Interfaces*. 2023;15(11):13956-13970.

     doi: 10.1021/acsami.2c21680

116. Islam MN, Rupom RH, Adhikari PR, *et al*. Boosting piezoelectricity by 3D printing PVDF-MoS2 composite as a conformal and high-sensitivity piezoelectric sensor. *Adv Funct Mater*. 2023;33(42):2302946.

     doi: 10.1002/adfm.202302946

117. Nassar H, Khandelwal G, Chirila R, *et al*. Fully 3D printed piezoelectric pressure sensor for dynamic tactile sensing. *Addit Manuf*. 2023;71:103601.

     doi: 10.1016/j.addma.2023.103601

118. Cui H, Yao D, Hensleigh R, *et al*. Design and printing of proprioceptive three-dimensional architected robotic metamaterials. *Science*. 2022;376(6599):1287-1293.

     doi: 10.1126/science.abn0090

119. Burton M, Howells G, Atoyo J, Carnie M. Printed thermoelectrics. *Adv Mater*. 2022;34(18):e2108183.

     doi: 10.1002/adma.202108183

120. Lee H, Chidambaram Seshadri R, Han SJ, Sampath S. TiO 2-X based thermoelectric generators enabled by additive and layered manufacturing. *Appl Energy*. 2017;192:24-32.

     doi: 10.1016/j.apenergy.2017.02.001

121. Shin S, Kumar R, Roh JW, *et al*. High-performance screen-printed thermoelectric films on fabrics. *Sci Rep*. 2017;7(1):7317.

     doi: 10.1038/s41598-017-07654-2

122. Juntunen T, Jussila H, Ruoho M, *et al*. Inkjet printed large-area flexible few-layer graphene thermoelectrics. *Adv Funct Mater*. 2018;28(22):1800480.

     doi: 10.1002/adfm.201800480

123. Bulman G, Barletta P, Lewis J, *et al*. Superlattice-bsed thin-film thermoelectric modules with high cooling fluxes. *Nat Commun*. 2016;7:10302.

     doi: 10.1038/ncomms10302

124. Zhao X, Han W, Zhao C, *et al*. Fabrication of transparent paper-based flexible thermoelectric generator for wearable energy harvester using modified distributor printing technology. *ACS Appl Mater Interfaces*. 2019;11(10):10301-10309.

     doi: 10.1021/acsami.8b21716

125. Liu H, Li G, Zhao X, Ma X, Shen C. Investigation of the impact of the thermoelectric geometry on the cooling performance and thermal-mechanic characteristics in a thermoelectric cooler. *Energy*. 2023;267:126471.

     doi: 10.1016/j.energy.2022.126471

126. Li P, Nie XL, Fang WB, *et al.* Fabrication and planar cooling performance of flexible Bi0.5Sb1.5Te3/epoxy composite thermoelectric films. *J Inorg Mater*. 2019;34(6):679.

     doi: 10.15541/jim20180528

127. Lu Z, Layani M, Zhao X, *et al*. Fabrication of flexible thermoelectric thin film devices by inkjet printing. *Small*. 2014;10(17):3551-3554.

     doi: 10.1002/smll.201303126

128. Venkatasubramanin R, Siivola E, Colpitts T, O'Quinn B. Thin-film thermoelectric devices with high room-temperature figures of merit. *Nature*. 2001;413:597-602.

     doi: 10.1038/35098012

129. Du J, Zhang B, Jiang M, *et al*. Inkjet printing flexible thermoelectric devices using metal chalcogenide nanowires. *Adv Funct Mater*. 2023;33(26):2213564.

     doi: 10.1002/adfm.202213564

130. Mytafides CK, Tzounis L, Karalis G, Formanek P, Paipetis AS. High-power all-carbon fully printed and wearable SWCNT-based organic thermoelectric generator. *ACS Appl Mater Interfaces*. 2021;13(9):11151-11165.

     doi: 10.1021/acsami.1c00414

131. Schroeder V, Savagatrup S, He M, Lin S, Swager TM. Carbon nanotube chemical sensors. *Chem Rev*. 2019;119(1):599-663.

     doi: 10.1021/acs.chemrev.8b00340

132. Jung ID, Kim M, Gao C, *et al*. Selective ion sweeping on prussian blue analogue nanoparticles and activated carbon

for electrochemical kinetic energy harvesting. *Nano Letters*. 2020;20(3):1800-1807.

doi: 10.1021/acs.nanolett.9b05029

133. Sidhu JS, Misra A, Bhardwaj A. Fabrication of Carbon Nanotube Components Using 3D Printing: Review. In: *Mater Today Proceedings*; 2023.

doi: 10.1016/j.matpr.2023.08.040

134. Lawes S, Riese A, Sun Q, Cheng N, Sun X. Printing nanostructured carbon for energy storage and conversion applications. *Carbon*. 2015;92:150-176.

doi: 10.1016/j.carbon.2015.04.008

135. Alshammari AS, Alenezi MR, Lai KT, Silva SRP. Inkjet printing of polymer functionalized CNT gas sensor with enhanced sensing properties. *Mater Lett*. 2017;189:299-302.

doi: 10.1016/j.matlet.2016.11.033

136. Beniwal A, Ganguly P, Aliyana AK, Khandelwal G, Dahiya R. Screen-printed graphene-carbon ink based disposable humidity sensor with wireless communication. *Sens Actuators B Chem*. 2023;374:132731.

doi: 10.1016/j.snb.2022.132731

137. Hassan K, Tung TT, Stanley N, *et al*. Graphene ink for 3D extrusion micro printing of chemo-resistive sensing devices for volatile organic compound detection. *Nanoscale*. 2021;13(10):5356-5368.

doi: 10.1039/d1nr00150g

138. Anca FB, Filipescu M, Voicu SI, Lippert T, Palla-Papavlu A. Facile fabrication of hybrid carbon nanotube sensors by laser direct transfer. *Nanomaterials* (*Basel*). 2021;11(10):2604.

doi: 10.3390/nano11102604

139. Wajahat M, Lee S, Kim JH, *et al*. Flexible strain sensors fabricated by meniscus-guided printing of carbon nanotube-polymer composites. *ACS Appl Mater Interfaces*. 2018;10(23):19999-20005.

doi: 10.1021/acsami.8b04073

140. Alsharari M, Chen B, Shu W. 3D printing of highly stretchable and sensitive strain sensors using graphene based composites. *Proceedings*. 2018;2:792.

doi: 10.3390/proceedings2130792

141. Ren Y, Meng F, Zhang S, *et al*. CNT@MnO2 composite ink toward a flexible 3D printed micro-zinc-ion battery. *Carbon Energy*. 2022;4(3):446-457.

doi: 10.1002/cey2.177

142. Kushwaha A, Jangid MK, Bhatt BB, Mukhopadhyay A, Gupta D. Inkjet-printed environmentally friendly graphene film for application as a high-performance anode in Li-Ion batteries. *ACS Appl Energy Mater*. 2021;4(8):7911-7921.

doi: 10.1021/acsaem.1c01249

143. Wang J, Sun Q, Gao X, *et al*. Toward high areal energy and power density electrode for Li-Ion batteries via optimized 3D printing approach. *ACS Appl Mater Interfaces*. 2018;10(46):39794-39801.

doi: 10.1021/acsami.8b14797

144. Chen Q, Xu R, He Z, Zhao K, Pan L. Printing 3D gel polymer electrolyte in lithium-ion microbattery using stereolithography. *J Electrochem Soc*. 2017;164:X18.

doi: 10.1149/2.0651709jes

ACCSCIENCE PUBLISHING

Materials Science in Additive Manufacturing

ORIGINAL RESEARCH ARTICLE

The role of graded layers in interfacial characteristics and mechanical properties of Ti6Al4V/AlMgScZr-graded multi-material parts fabricated using laser powder bed fusion

Guangjing Huang, Dongdong Gu*, Hong Liu, Kaijie Lin, Rui Wang, and He Sun

Jiangsu Provincial Engineering Research Center for Laser Additive Manufacturing of High-Performance Metallic Components, College of Materials Science and Technology, Nanjing University of Aeronautics and Astronautics, Nanjing, Jiangsu, China

Abstract

Graded multi-material parts achieve a compositionally graded transition between two different materials, mitigating undesirable consequences such as cracking and delamination due to property mismatch and significantly improving the comprehensive performance of parts. In this study, the Ti6Al4V/AlMgScZr-graded multi-material parts were fabricated using laser powder bed fusion technology, introducing a composition-graded layer with 25 wt.% Ti6Al4V and 75 wt.% AlMgScZr at the interface to reduce the mismatch between the two materials. The effect of the graded layer's laser scanning speed on the densification behavior, microstructure evolution, and mechanical properties of the Ti6Al4V/AlMgScZr-graded multi-material parts was investigated. It was revealed that the crack area at the interface reduced from 0.325 to 0.067 mm^2 as the scanning speed increased from 2400 to 2800 mm/s and then increased to 0.161 mm^2 at 3000 mm/s. A smooth, continuous-graded layer with good metallurgical bonding was fabricated at 2800 mm/s. The $TiAl_3$ intermetallic compound was formed at the interface and underwent a transition from rod-like to coarse dendritic and finally to finer dendritic structure along the building direction. The Ti6Al4V/AlMgScZr-graded multi-material parts exhibited a graded decrease in microhardness from 374 $HV_{0.2}$ on the Ti6Al4V side to 122 $HV_{0.2}$ on the AlMgScZr side, and an excellent compressive strength of 1531 MPa was obtained at the optimal parameter of 2800 mm/s.

Keywords: Laser powder bed fusion; Graded multi-material parts; Interface; Intermetallic compound

1. Introduction

Graded multi-material parts consist of at least two different materials in the three-dimensional (3D) space.[1] By integrating the exceptional properties of various materials, multi-material parts can overcome the limitations of single-material parts and thus effectively fulfill the functional and performance requirements of engineering applications.[2,3] For instance, in the construction of aircraft wings, connections between Ti alloy longeron components and Al alloy rudder connectors are typically achieved

***Corresponding author:**
Dongdong Gu
(dongdonggu@nuaa.edu.cn)

Citation: Huang G, Gu D, Liu H, Lin K, Wang R, Sun H, 2024, The role of graded layers in interfacial characteristics and mechanical properties of Ti6Al4V/AlMgScZr-graded multi-material parts fabricated using laser powder bed fusion. *Mater Sci Add Manuf.* 2024;3(2):3088.
doi: 10.36922/msam.3088

Received: March 5, 2024

Accepted: April 17, 2024

through traditional fabrication methods such as bolting and welding. However, these methods are susceptible to issues such as fatigue and looseness under high-frequency vibrational environments, imposing substantial limitations on the geometric shapes of the parts and leading to interface defects and brittle phase issues that severely compromise the reliability of the parts, ultimately affecting their service life.[4,5] Employing graded multi-material design is expected to achieve integrated fabrication of "material-structure-performance" in Ti6Al4V/AlMgScZr frame girder to achieve excellent interfacial metallurgical bonding and comprehensive mechanical properties.[6]

Laser directed energy deposition (LDED) and laser powder bed fusion (LPBF), as two near-net shape manufacturing techniques, offer greater design freedom in fabricating graded multi-material parts, enabling the production of parts with more complex geometric shapes compared to traditional manufacturing methods.[7] These techniques have been applied in fabricating at least two distinct metals in both vertical and horizontal directions within a part.[8,9] LPBF utilizes a discrete-to-accumulative approach to fabricate solid parts. Based on a computer-generated 3D model, it employs a high-energy laser beam to selectively melt and solidify the pre-laid metal layer by layer to fabricate multi-material parts.[10] With a smaller laser spot size and thinner layer thickness, LPBF enables the fabrication of more complex structures compared to LDED.[11] In laser additive manufacturing of multi-material parts, the main challenge is the mismatching of mechanical and thermal properties among different materials. During both the manufacturing and utilization processes, the unavoidable sharp interfaces can result in steep gradients in performance, which may become focal points for residual stress concentration and lead to premature failure. In certain extreme cases, property mismatches, such as thermal conductivity and melting temperature between materials, can render the forming process entirely unsuccessful.[12] At present, multi-material connections typically present three common joining methods.[12]: direct joining,[13,14] graded path method,[15,16] and intermediate section method.[17,18] Graded multi-material parts can achieve a graded transition between two materials along the building direction, thus addressing the issue of mismatched interface performance in multi-material systems. For example, 316L/CuSn10 multi-material parts possess excellent electrical and thermal conductivity, along with high specific strength and cost-effectiveness, making them widely applicable in industries such as power generation and heat transfer. However, the notable difference in thermal expansion coefficients between Cu and Fe, as well as the high thermal conductivity of Cu, results in an increased temperature gradient at the interface. Consequently, the rapid solidification process in LPBF induces the development of thermal stress and microcracks at the interface.[19] Wei *et al.*[20] successfully utilized a composition-graded layer to fabricate 316L/CuSn10-graded multi-material parts with excellent metallurgical bonding. They discovered that elements at the interface exhibited good mutual diffusion, and microhardness showed a graded change along the building direction. The results indicated that a composition-graded layer could help reduce the temperature gradient between 316L and CuSn10, alleviate thermal stress, significantly inhibit interfacial cracks, and enhance interfacial bonding strength. Demir *et al.*[21] utilized the multi-material LPBF system to fabricate 316L/Fe35Mn-graded multi-material parts with a tensile strength of 600 MPa. They have discovered that due to the deliberate mixing of the graded powder within the multi-material LPBF system and sufficient melting of each layer, elements such as Cr, Ni, and Mo in the 316L were gradually replaced by Mn, resulting in a continuous-graded transition. Consequently, the method of graded joining in the fabrication of multi-material parts could be expected to achieve good metallurgical bonding at the interface.

Ti alloys possess high specific strength, excellent fatigue characteristics, and good high-temperature behavior, while Al alloys exhibit good ductility and heat conduction alongside low density.[22,23] These properties render them widely used in aerospace, automotive, and medical applications as lightweight and high-strength materials. The integration of both alloys in Ti/Al multi-material parts holds promise for significantly enhancing the lightweighting efforts and overall performance of metal components.[8] However, the distinct physical properties of Ti and Al alloys present challenges when combining them for specific applications. During laser irradiation, as the molten pool approaches the melting point of Ti alloys, Al alloys are susceptible to elemental depletion, resulting in gas entrapment and pore formation.[24] In addition, the formation of intermetallic compounds (IMCs) poses a major obstacle for Ti/Al multi-material systems. The limited solubility between the two materials increases the likelihood of IMCs formation in Ti-Al system such as Ti_3Al, TiAl, and $TiAl_3$ during metallurgical reactions, thereby resulting in decreased interfacial bonding strength of multi-material parts.[25]

Jing *et al.*[26] investigated Ti6Al4V/AlSi12 multi-material parts prepared through LDED, resulting in a transition layer approximately 0.8 mm wide. They observed that the presence of Si elements caused more complex metallurgical reactions at the interface and the uneven distribution of microhardness. Cracks were identified at the interface, thereby weakening the bonding strength of the Ti6Al4V/AlSi12 multi-material parts, which exhibited a tensile strength of approximately 110 MPa. In a separate study, Wu *et al.*[27] utilized LPBF to fabricate Ti6Al4V/AlSi10Mg multi-material parts, achieving a good metallurgical bonding with a transition zone width of only 0.1 mm. The *in situ* generated nanoparticles Ti_5Si_3 during interfacial reactions improved interfacial bonding, resulting in a tensile strength of 264.8 MPa. However, a large lattice distortion at the interface was observed, attributed to the absence of heat treatment.

It has been reported that the direct joining strategy for fabricating multi-material parts consisting of Ti alloy and Al alloys often leads to the formation of cracks. These cracks primarily arise from the abrupt change in the composition at the interface and the mismatches in properties between the two materials. Therefore, Liu *et al.*[28] fabricated Ti6Al4V/AlSi10Mg-graded multi-material parts using LDED. In their study, the composition gradually changed from 100 vol.% Ti6Al4V to 100 vol.% AlSi10Mg, effectively mitigating interface properties mismatch at the interface. Their results indicated a gradual variation in microstructure and phase constitution with the increasing proportion of AlSi10Mg, leading to the formation of a graded reaction transition layer approximately 2-mm thick along the building direction. This transition layer comprised $\alpha\text{-Ti} \rightarrow AlTi_3 \rightarrow Al_3Ti + Ti_5Si_3 + Al_5Ti_2 \rightarrow Al_3Ti + Ti_5Si_3 + Al_5Ti_2 + Al \rightarrow Al_3Ti + Al$. Despite the increased thickness of IMCs, the systematic gradient variation of these compounds also resulted in a gradual change in microhardness along the building direction, culminating in a tensile strength of approximately 417 MPa. These results underscore the effectiveness of Ti/Al-graded multi-material parts in alleviating issues such as cracking deformation and inferior performance caused by differences in properties between Ti and Al at the interface.

In this study, a graded joining method was employed, which added a composition-graded layer (25 wt.% Ti6Al4V + 75 wt.% AlMgScZr) to avoid excessive formation of brittle IMCs and consequent property mismatch. This method facilitated a gradient transformation from the interface composition while ensuring good metallurgical bonding. The Ti6Al4V/AlMgScZr-graded multi-material parts were fabricated using LPBF technology. Detailed investigations were conducted on the relationships between process parameters, densification behavior, microstructure evolution, and mechanical properties. In addition, the mechanisms underlying the IMC generation and crack formation were elucidated, providing a fundamental understanding of LPBF-processed Ti6Al4V/AlMgScZr-graded multi-material parts.

2. Materials and methods

2.1. Materials

In this study, Ti6Al4V/AlMgScZr-graded multi-material parts were fabricated using gas-atomized Ti-6Al-4V powders (TLS Technology Co. LTD, Germany) and Al-4.2Mg-0.6Sc-0.2Zr powders (Heraeus Materials Technology, Taiwan, China) with particle sizes distribution of 20 – 67 μm (Figure 1A) and 22 – 67 μm (Figure 1B), respectively, were used. Ti6Al4V powder and AlMgScZr

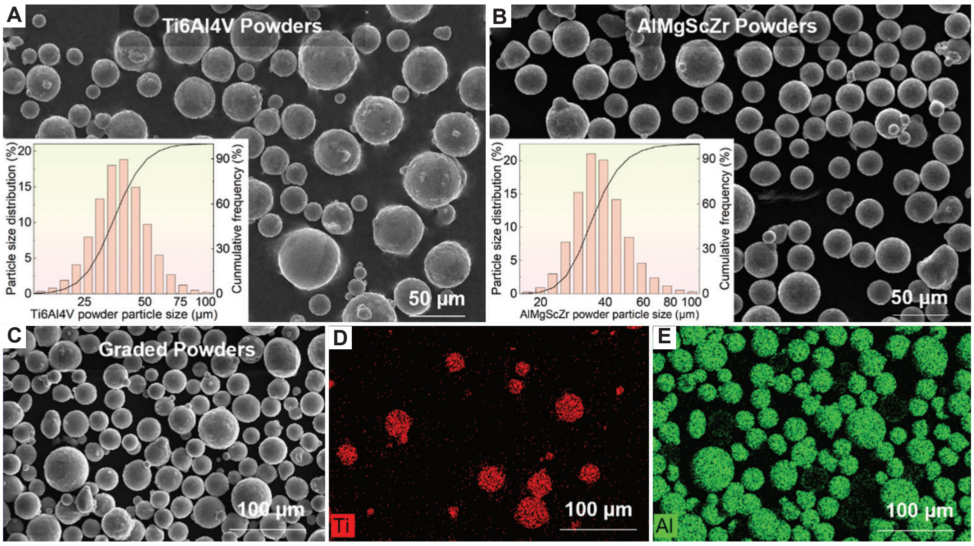

Figure 1. The raw materials for laser powder bed fusion-processed Ti6Al4V/AlMgScZr-graded multi-material parts. (A) The particle size distribution and morphology of Ti6Al4V powders. (B) The particle size distribution and morphology of AlMgScZr powders. (C) The morphology of graded powder, (D) the Ti element distribution of graded powder. (E) The Al element distribution of graded powder. Scale bars: (A and B) 50 μm, magnification ×500; (C-E) 100 μm, magnification ×1000.

powder were homogeneously mixed in a weight ratio of 25 to 75 (Figure 1C-E). Mixing was performed using a V-10L V-shaped mixer (Changsha Miqi instrument equipment Co., LTD, China) under an argon atmosphere, with a mixing time of 0.3 h and a mixing speed of 50 r/min.

2.2. Graded multi-material parts LPBF process

A self-developed LPBF-80 apparatus was used to fabricate the Ti6Al4V/AlMgScZr-graded multi-material parts. The apparatus consists of a 200 W fiber laser with a spot size of 70 μm, an automatic powder spreading system, a process control system, and a protective atmosphere system. The schematic of graded multi-material parts for the LPBF process is illustrated in Figure 2A. Initially, Ti6Al4V powder was spread onto a room-temperature Ti6Al4V substrate at oxygen concentration below 50 ppm, employing a flexible rubber recoater blade to fabricate the Ti6Al4V layer. Subsequently, the powder cylinder and recycled product were cleaned, and the graded powder and AlMgScZr powder were added to two separate powder cylinders to process the subsequent layers. The Ti6Al4V/AlMgScZr-graded multi-material samples were fabricated using the parameters listed in Table 1, with both Ti6Al4V and AlMgScZr adopting their respective optimized laser process parameters. However, the graded layer exhibited a high propensity to crack under the same heat input as Ti6Al4V and AlMgScZr, which could be reduced by appropriately increasing the scanning speed of the graded layer. An island scanning strategy with a rotation angle of 37° between layer N and layer N+1 was applied to mitigate the effect of thermal stress (Figure 2B). For microstructure analysis of the interface, cubic samples with two different building heights were used, as shown in Figure 2C. In addition, cylindrical samples with a length-to-diameter ratio of 1.5:1 were processed for compression testing. The parts produced using LPBF are presented in Figure 2D.

2.3. Physical characterization of the samples

The LPBF processed samples were ground and polished following standard metallographic procedures, followed by etching using Kroll reagent (1 mL HF, 2 mL HNO_3, 47 mL H_2O, Sinopharm Chemical Reagent Co., Ltd., China) for 30 s. The density of the LPBF processed parts was measured according to Archimedes' principle. The crack area was observed using an optical microscope (OM) (BX53M, OLYMPUS, Japan) and calculated using Image J software (National Institutes of Health, USA). The surface roughness of the graded layer was examined using a LEXT OLS5000 laser confocal scanning microscope (OLYMPUS, Japan). The microstructure of the Ti6Al4V/AlMgScZr-graded multi-material parts at the interface was observed using a scanning electron microscope (SEM) (LYRA3, TESCAN, Czech Republic), and the XFlash 6130 EDS system (BRUKER, YYY) was used for characterizations to identify the parts and element distributions around the interface. Phase constitution was measured using a D8 Advance X-ray diffractometer (XRD) (Germany) with Cu Kα radiation at 40 kV and 45 mA, in the 2θ range of 30° – 90° and a scan rate of 4°/min.

2.4. Characterization of mechanical properties of the samples

Microhardness tests were performed using a Micromet

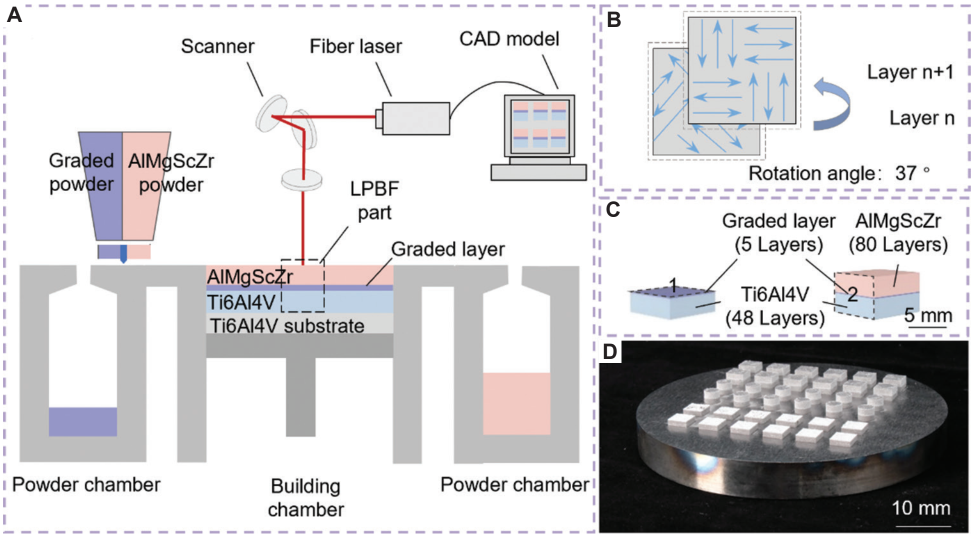

Figure 2. Schematic and experiments of LPBF-processed Ti6Al4V/AlMgScZr-graded multi-material parts. (A) Schematic of graded multi-material parts LPBF process. (B) The chessboard scanning strategy applied in LPBF. (C) The graded multi-material block model. (D) The laser-processed parts. Abbreviations: CAD: Computer aided design; LPBF: Laser powder bed fusion.

5101 micro-sclerometer (Bang Yi Precision measuring Instrument (Shanghai) Co., LTD, China), applying a load of 200 g and a dwell time of 10 s. Fourteen points, with a step size of 0.2 mm symmetrically positioned about the interface, were measured. Compression tests at room temperature were conducted using a CMT5205 testing machine (MTS, America). The ultimate compressive strength and strain of Ti6Al4V/AlMgScZr-graded multi-material samples were determined from the engineering stress-strain curves. Fracture morphologies of samples were characterized using SEM.

3. Results and discussion

3.1. Surface morphology and densification behavior

Figure 3 demonstrates the surface morphology and roughness of the graded layer of LPBF-processed Ti6Al4V/AlMgScZr-graded multi-material parts at different scanning speeds (Figure 2C-1). The samples were oriented vertically, with the Ti6Al4V layer at the bottom and the graded layer at the top.

Various issues, such as overlapping of the molten pool, pores, balling, protrusions, and cracks, can impact surface roughness, thereby influencing the subsequent LPBF process. At a scanning speed of 2400 mm/s, a rough surface with a Ra value up to 33.35 μm was observed, with cracks, pores, and protrusions evident in Figure 3A. During the LPBF process, excessive laser energy input led to significant heat accumulation in the molten pool, resulting in excessive residual thermal stress. Consequently, the concentration of residual thermal stress induced crack formation at the interface. The protrusions might be caused by partially melted powder particles or local disturbances in the molten pool. Increasing the scanning speed to 2600 mm/s still resulted in the presence of pores and protrusions (Figure 3B), albeit with a reduced Ra value of 29.78 μm. The higher scanning speed helped decrease residual thermal stress in the graded layer. Samples processed at 2800 mm/s exhibited a further reduction in Ra value to 24.18 μm, although some protrusions were still observed. This reduction in surface roughness may be attributed to decreased cracking and warping, which were beneficial for subsequent LPBF processes. However, when the scanning speed reached 3000 mm/s, the insufficient laser energy input prevented the complete melting of the powder in the molten pool. As a result, a roughened-graded layer with a Ra value

Table 1. The process parameters applied in the fabrication of Ti6Al4V/AlMgScZr-graded multi-material parts using laser powder bed fusion process

Parameters	Materials					
	Ti6Al4V	AlMgScZr	Graded 1	Graded 2	Graded 3	Graded 4
Laser power (W)	175	200	200	200	200	200
Scanning speed (mm/s)	950	1500	2400	2600	2800	3000
Laser thickness (mm)	0.05	0.03	0.03	0.03	0.03	0.03
Hatch distance (mm)	0.05	0.06	0.06	0.06	0.06	0.06

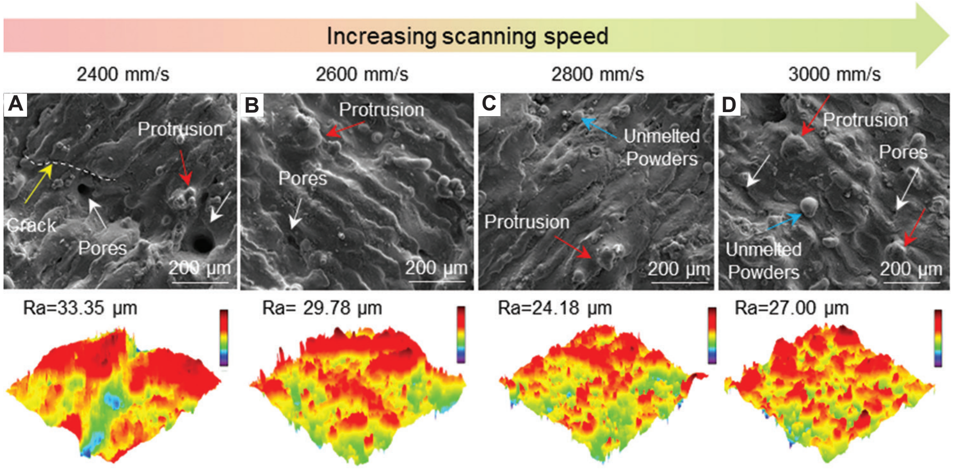

Figure 3. The surface morphology and surface roughness of Ti6Al4V/AlMgScZr-graded multi-material-graded layer at different scanning speeds. (A) 2400 mm/s. (B) 2600 mm/s. (C) 2800 mm/s. (D) 3000 mm/s. Scale bars: 200 μm, magnification ×250.

of approximately 27.00 μm was observed.

The densification behavior of Ti6Al4V/AlMgScZr-graded multi-material parts was examined by measuring the density of the whole parts and the crack area at the interfaces across different scanning speeds. The archimedes' method was employed for density measurement, while image analysis was utilized for crack area assessment. The OM images in Figure 4 vividly illustrate the interface between Ti6Al4V and the graded layer, revealing cracks along the interface attributed to differences in expansion coefficient, thermal conductivity between the two materials, and the high content of AlMgScZr in the graded layer. Overall, the density of Ti6Al4V/AlMgScZr-graded multi-material parts exhibited an initial increase followed by a decrease, with the transition point observed at a scanning speed of 2800 mm/s as the scan speed increased from 2400 to 3000 mm/s. In contrast, the crack area exhibited an opposite trend, initially declining before increasing. At a scanning speed of 2400 mm/s, the lowest density and highest crack area were recorded at 3.17 g/cm^3 and 0.325 mm^2, respectively. Conversely, the maximum density and minimum crack area were observed at 3.24 g/cm^3 and 0.067 mm^2, respectively, at the scanning speed of 2800 mm/s. However, at the scanning speed of 3000 mm/s, a significant reduction in density and an increase in crack area were noted, attributed to the presence of unmelted powders. In conclusion, the lowest crack area of Ti6Al4V/AlMgScZr-graded multi-material parts was observed at scanning speeds below 2800 mm/s, corresponding to the highest density. We posit that the primary cause of cracking in Ti6Al4V/AlMgScZr-graded multi-material parts is the formation of IMCs and the thermal stress at the interface. At higher laser energy densities, increased molten pool temperatures lead to a more severe remelting degree of Ti6Al4V that promoted element diffusion and reaction, thus generating more IMCs. Samples processed at a scanning speed of 2800 mm/s may exhibit fewer IMCs compared to those processed at lower scanning speeds, thus exhibiting a lower cracking propensity. However, further reductions in scanning speed may result in the formation of lack of fusion and the presence of unmelted powders at the interface. Therefore, samples at 3000 mm/s should have fewer IMCs, but poorer interface bonding exacerbates cracking propensity. In addition, the graded layer with a smooth and flat surface had enhanced forming quality, and the smooth-graded layer surface also provided an enhanced forming basis for subsequent powder laying and laser processing of AlMgScZr, which was conducive to improving the overall density of LPBF-processed multi-material parts.

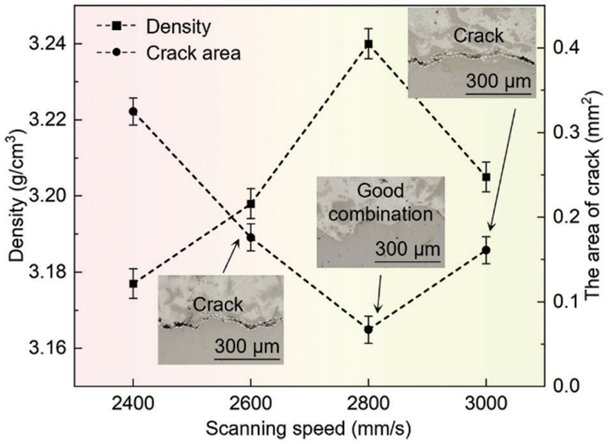

Figure 4. Density and the crack area of laser powder bed fusion-processed Ti6Al4V/AlMgScZr-graded multi-material parts at different scanning speeds.

3.2. Phase constitution of Ti6Al4V/AlMgScZr-graded multi-material parts

The results of the XRD pattern of Ti6Al4V/AlMgScZr-graded multi-material samples at the cross-section (Figure 2C-2) under 2800 mm/s and at graded layer

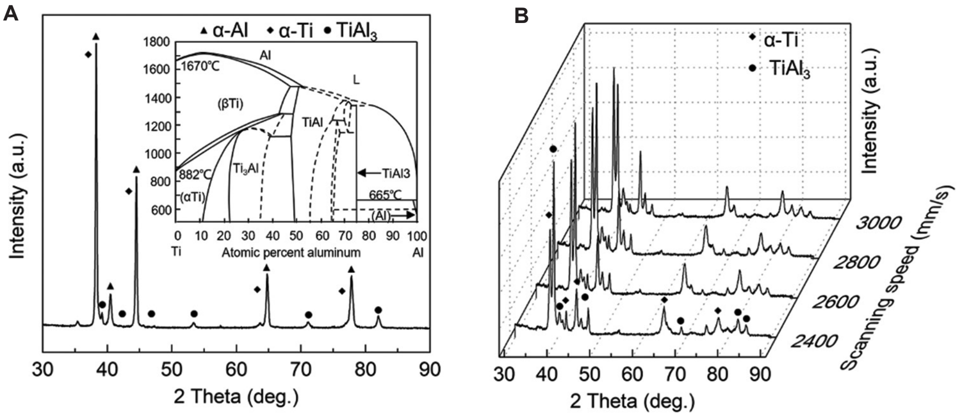

Figure 5. X-ray diffractometer spectra for laser powder bed fusion-processed Ti6Al4V/AlMgScZr-graded multi-material parts. (A) The cross-section of the sample (Inset: Ti-Al phase diagram[28]). (B) Surface of the graded layer of the samples at different scanning speeds.

surface (Figure 2C-1) under different scanning speeds are presented in Figure 5. The examination of the cross-section sample revealed the presence of three phases: α-Al, α-Ti, and TiAl$_3$. In addition, other phases composed of elements such as Mg, V, Sc, and Zr may exist in the microstructure but cannot be detected by XRD due to their low volume fraction or small size. Meanwhile, α-Ti and TiAl$_3$ were detected at the graded layer surface. Based on the Ti-Al phase diagram displayed in Figure 5A, several IMCs, including Ti$_3$Al, TiAl, TiAl$_3$, TiAl$_2$, and Ti$_2$Al$_{5,}$ were expected to form during the metallurgical reaction between Ti and Al.[29] The Gibbs free energy for the formation of the Ti-Al IMC was calculated using the formula proposed by Kattner *et al.*[30] The formation of TiAl$_2$ and Ti$_2$Al$_5$ entails a series of reactions with TiAl as the initial phase, which were not thermodynamically considered, indicating that TiAl$_3$ has the lowest free energy of formation among phases. Consequently, as the laser irradiated, the graded powder underwent melting and reacted to form TiAl$_3$ through the $Ti+3Al \rightarrow TiAl_3$ reaction.[31] When the scanning speed of the graded layer was increased from 2400 mm/s to 2800 mm/s, the intensities of the Ti and TiAl$_3$ diffraction peaks changed from 6307 and 10992 to 8655 and 10211, respectively. As the scanning speed further increased to 3000 mm/s, the intensity of the Ti peak surpassed that of the TiAl$_3$ peak as the dominant phase. This phenomenon can be attributed to the decreased interaction time between the laser and the powder as well as the lower melting pool temperature. As a result, the Ti6Al4V powders incompletely melted and retained in the molten pool, leading to a reduced formation of TiAl$_3$. Therefore, for samples processed with lower scanning speeds, due to the formation of a greater number of brittle IMCs at the interface, there is a poorer resistance to crack propagation, resulting in larger areas of cracks. In contrast, the sample scanned at 2800 mm/s exhibited fewer brittle phases at the interface, hence demonstrating a stronger resistance to crack propagation and a reduction in crack area. However, when the scanning speed increased to 3000 mm/s, despite the reduced quantity of brittle phases formed, the lower thermal input led to the occurrence of defects, such as unmelted powders at the interface, resulting in the formation of cracks under thermal stress. Therefore, at a scanning speed of 2800 mm/s, the sample exhibited the optimal behavior of densification.

3.3. Microstructure evolution of Ti6Al4V/AlMgScZr-graded multi-material parts

Figure 6 illustrates the cross-section microstructure evolution of Ti6Al4V/AlMgScZr-graded multi-material parts at the interface. In Figure A, several unmelted Ti6Al4V powder particles are visible at the interface, attributed to the significant difference in melting point between Ti6Al4V and AlMgScZr, and the lower laser absorptivity of mixed powders caused by highly reflective AlMgScZr powders. The insufficient absorption of laser energy of the mixed powder bed led to a lower temperature of the molten pool and the inadequate melting of Ti6Al4V powders.[32,33] To further characterize the microstructure and chemical composition, the cross-section SEM images of the sample were amplified, as shown in Figure 6B-D. In Figure 6D, rod-like structures are observed at the bottom region of the graded layer, where the Al/Ti atomic ratio is approximately 2.48. Based on the results of the XRD pattern and the Ti-Al phase diagram, it can be inferred that these rod-like structures are TiAl$_3$. The rod-like TiAl$_3$ precipitated along the interface between Ti6Al4V and the graded layer and grew in the direction of the temperature gradient. In addition, several finer dendrites precipitated above the rod-like TiAl3. In Figure 6C, corresponding to the middle region of the interface, a significant number of dendritic precipitates is presented. The atomic percentages of Al and Ti were 76.36% and 23.64%, respectively, with an atomic ratio of 3.2. It could be inferred that these dendritic structures were also composed of TiAl3. Figure 6B depicts TiAl$_3$ fine dendrites with Al and Ti atomic percentages of

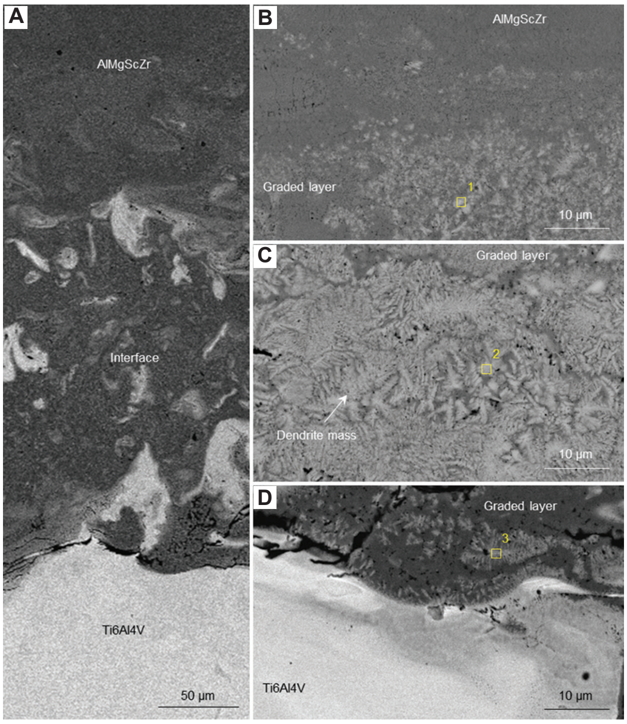

Figure 6. The scanning electron microscopic images of the cross-section microstructure evolution at the interface of Ti6Al4V/AlMgScZr-graded multi-material parts. (A) Low-magnification image of the interface. (B) The top region of the interface. (C) The middle region of the interface. (D) The bottom region of the interface. Scale bars: (A) 50 µm, magnification ×400; (B-D) 10 µm, magnification ×8000.

79.30% and 20.70%, respectively, and an Al to Ti atomic ratio of 3.8 found under the AlMgScZr molten pool. During the LPBF fabrication of AlMgScZr, the graded layer underwent remelting, and Ti atoms diffused toward the low concentration region under the influence of chemical potential graded, reacting with Al atoms to form $TiAl_3$.[34] At this stage, the acquisition of Ti atoms in the AlMgScZr layer relied solely on the diffusion mechanism, leading to insufficient Ti content and unfavorable growth for $TiAl_3$ dendrites.

Figure 7 illustrates the distribution of Ti, Al, V, and Mg elements at the interface between the Ti6Al4V layer and the graded layer. A curved boundary line delineating the molten pool can be observed, along which $TiAl_3$ precipitated and formed short rod-like structures extending toward the center. Based on the distribution of Ti and V elements, it can be inferred that Ti6Al4V exhibited island-like segregations at the interface. During the LPBF process for forming the Ti6Al4V/AlMgScZr-graded layer, partial melting of Ti6Al4V under the graded layer occurred through thermal conduction, with subsequent introduction into the graded layer through Marangoni convection. The higher melting point of Ti6Al4V led to rapid solidification of the molten Ti6Al4V.[35] Furthermore, the presence of Al and Mg elements on both sides of the interface indicated their diffusion across the interface. As the laser irradiated graded layer, the rapid melting of AlMgScZr powders facilitated the diffusion of elements such as Al and Mg into the remelted Ti6Al4V layer. The elevated temperature of the molten pool, induced by laser irradiation, enhanced the thermal motion of Ti and Al elements, thereby accelerating the reaction between Ti and Al.

Based on the results of the XRD pattern and SEM analysis, Figure 8 illustrates the mechanism of microstructure evolution at the interface of LPBF-processed Ti6Al4V/AlMgScZr-graded multi-material parts. When the graded layer was formed on top of the Ti6Al4V substrate, the previously solidified Ti6Al4V layer was remelted to achieve the metallurgical bonding. Subsequently, the remelted Ti6Al4V was mixed into the molten pool of the graded layer through Marangoni convection.[36] Due to the lower temperature and higher liquid viscosity of the molten pool, the remelted Ti6Al4V solidified rapidly, resulting in the formation of island-like segregations of Ti6Al4V. The higher melting point of Ti6Al4V powders and the lower laser absorption rate of AlMgScZr in the molten pool resulted in insufficient melting of Ti6Al4V powders within the graded layer. In addition, the Al elements in the graded layer reacted with Ti to form rod-like $TiAl_3$ along the boundary of the molten pool, which grew toward the center of the molten pool. With increasing Al content, a small number of $TiAl_3$ fine dendrites precipitated above the rod-shaped $TiAl_3$ structures. As the deposition of the graded layer continued, the elevated temperature of the molten pool facilitated the complete melting of Ti6Al4V powders and the mixing of the Ti and Al elements under the influence of Marangoni convection. As a result, numerous $TiAl_3$ dendrites were formed in the graded layer with a Ti-to-Al atom ratio of approximately 3. During the fabrication

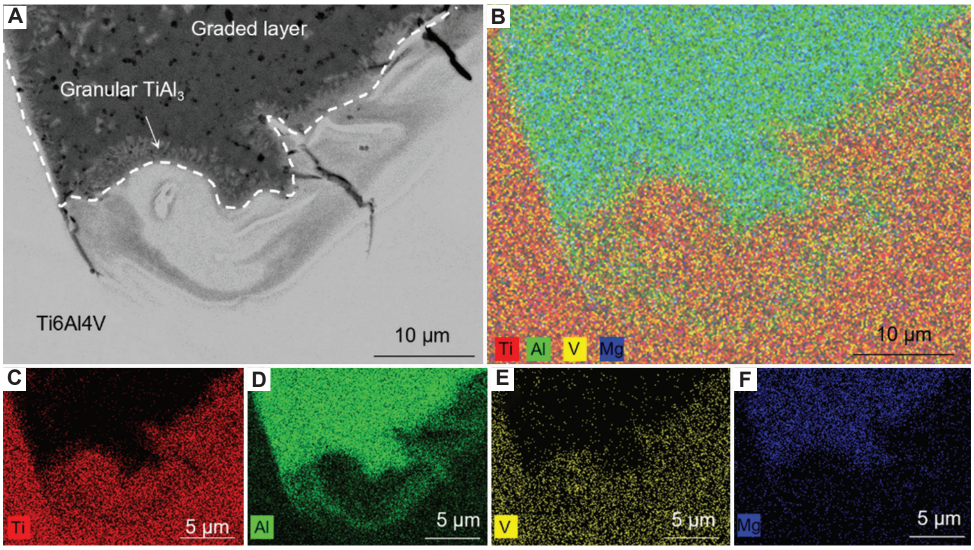

Figure 7. Element distribution of laser powder bed fusion-processed Ti6Al4V/AlMgScZr-graded multi-material parts at the interfacial molten pool. (A) Scanning electron microscopic images of the interface. (B-F) Distribution of Ti, Al, V, and Mg elements. Scale bars: (A and B) 10 µm, magnification ×8000; (C-F) 5 µm, magnification ×4000.

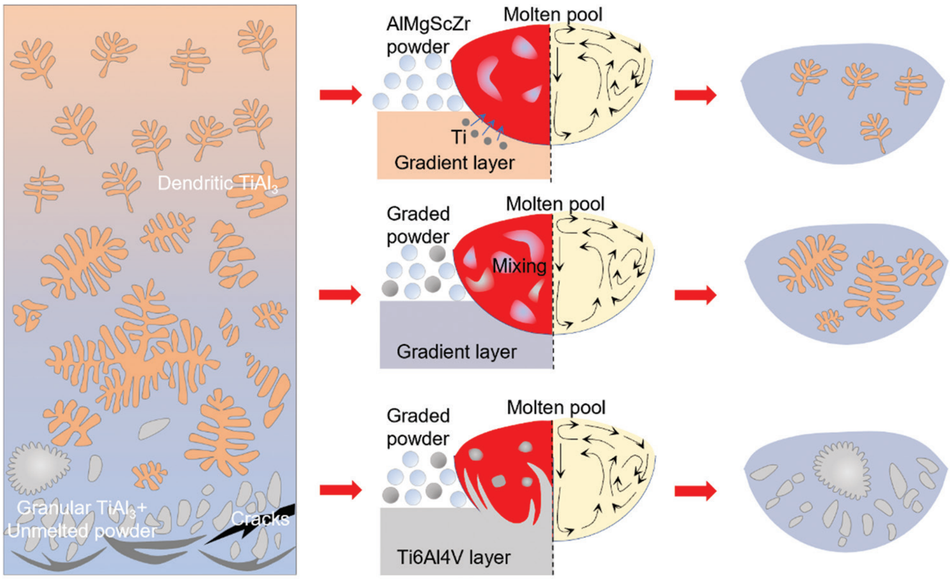

Figure 8. The illustration of the formation mechanism of $TiAl_3$ intermetallic compound.

of the AlMgScZr layer, the graded layer underwent remelting. Higher energy input accelerated the diffusion of Ti from the high-concentration region in the graded layer to the low-concentration region in the AlMgScZr layer. Finer $TiAl_3$ dendrites precipitated in the AlMgScZr layer through the Ti-Al reaction. Research indicates that the nucleation and growth dynamics of $TiAl_3$ strongly depended on the concentration distributions of Ti and Al, influencing the morphology of the $TiAl_3$ IMC. In regions with insufficient Ti or Al, $TiAl_3$ tends to precipitate finer dendrites or rod-like structures. With a moderate concentration distribution (Al-to-Ti atomic ratio of approximately 3), a large number of $TiAl_3$ dendrites are formed.[37] In addition, cracks form at the interface between the graded layer and Ti6Al4 due to the lattice type mismatch between Ti and Al and the significant difference in thermal properties between the two materials.

3.4. Mechanical properties of Ti6Al4V/AlMgScZr-graded multi-material parts

Figure 9 demonstrates the variation in microhardness across the interface of Ti6Al4V/AlMgScZr-graded multi-material parts at different laser scanning speeds. The average microhardness value of the Ti6Al4V was approximately 374 $HV_{0.2}$, consistent with values reported by Liu *et al.*[38] Similarly, the average microhardness value of AlMgScZr was 122 $HV_{0.2}$, aligning closely with values reported by Xi *et al.*[39] Overall, microhardness exhibited a gradual decrease from Ti6Al4V to the interface as the Ti6Al4V content diminished and $TiAl_3$ precipitated along the interface. Moreover, the variation in microhardness remained relatively stable without significant increase, suggesting the absence of IMCs with high microhardness values at the interface. As the amount and size of $TiAl_3$ decreased, microhardness consistently declined until reaching the AlMgScZr region. At a lower scanning speed of the graded layer (2400 mm/s), the average microhardness at the interface was the lowest (226 $HV_{0.2}$) due to the presence of cracks resulting from thermal stress. Increasing the scanning speed to 2800 mm/s led to the highest average microhardness at the interface, reaching 263 $HV_{0.2}$. However, with a further increase in scanning speed to

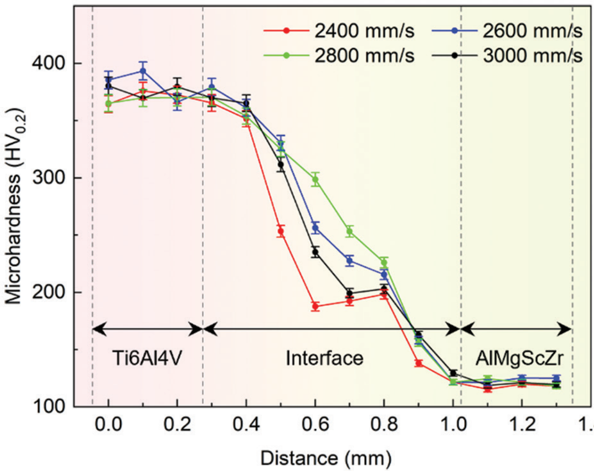

Figure 9. The microhardness curves of laser powder bed fusion-processed Ti6Al4V/AlMgScZr-graded multi-material parts at different scanning speeds.

3000 mm/s, the average microhardness at the interface decreased to 247 $HV_{0.2}$. This reduction in microhardness was attributed to cracks caused by insufficient powder melting under conditions of excessive scanning speed and reduced heat input.

To further investigate the mechanical properties of Ti6Al4V/AlMgScZr-graded multi-material parts, each sample underwent compressive testing. Figure 10A depicts the compressive stress-strain curves for the LPBF-processed Ti6Al4V/AlMgScZr-graded multi-material parts at different scanning speeds. The compressive load was applied vertically to the interface between Ti6Al4V and AlMgScZr. It is important to note that any cracks or pores existing at the interface would close during the compression process, which might not fully describe the relationship between cracks and compression properties.[40] However, some quantitative relationships exist between the compressive mechanical properties and the forming process or forming quality of the samples. Figure 10B illustrates the resultant ultimate compressive strengths (σ_{bc}) and strains (δ) of the compressive samples. Analysis of the compressive stress-strain curves reveals two distinct stages. The first stage occurred within the deformation range of 22 – 30%, mainly involving the compression of AlMgScZr. The second stage occurred within the deformation range of 45 – 50% and primarily involved compression of the graded layer and Ti6Al4V. With an increase in scanning speed from 2400 – 2800 mm/s, the compressive strength and strain increased from 1359 MPa and 46.7% to 1531 MPa and 49.8%, respectively. However, at a scanning speed of 3000 mm/s, the unmelted powders were observed at the interface, rendering the interface susceptible to cracks and resulting in a decrease in compressive strength and strain to 1461 MPa and 47.9%, respectively. The observed compressive performance is

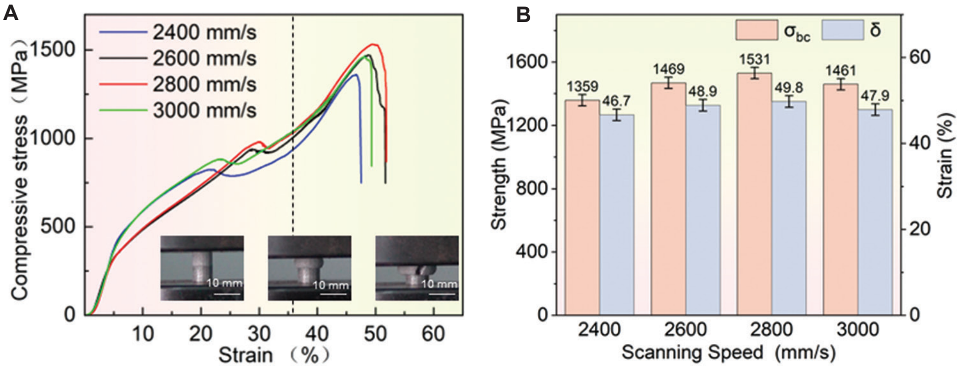

Figure 10. The compressive properties of laser powder bed fusion-processed Ti6Al4V/AlMgScZr-graded multi-material parts. (A) Compressive stress-strain curves for Ti6Al4V/AlMgScZr-graded multi-material parts at different scanning speeds (Insets: The compression process of the sample at 2800 mm/s. Scale bars: 10 mm, magnification ×2.5;). (B) Comparison of the scanning speed on ultimate compressive strength (σ_{bc}) and failure strain (δ) of the compressive samples.

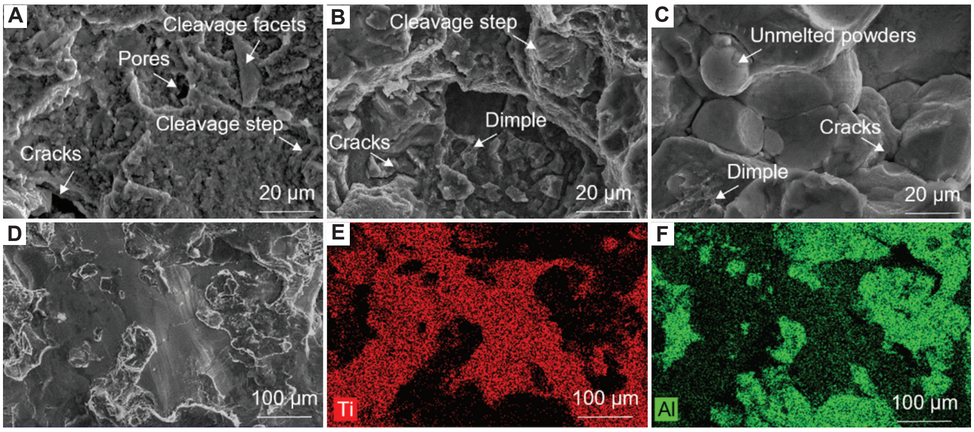

Figure 11. Scanning electron microscopic images showing the fracture morphologies of the laser powder bed fusion-processed Ti6Al4V/AlMgScZr-graded multi-material parts at different scanning speeds. (A) 2600 mm/s on AlMgScZr side. (B) 2800 mm/s on AlMgScZr side. (C) 3000 mm/s on AlMgScZr side, (D) 2800 mm/s on Ti6Al4V side. (E) Ti element distribution of (D). (F) Al element distribution of (D). Scale bars: (A-C) 20 μm, magnification ×3500; (D-F) 100 μm, magnification ×400.

consistent with the density data for Ti6Al4V/AlMgScZr-graded multi-material. As interface cracks reduced, both the ultimate compressive strength and strain of the samples improved, indicating that the compression performance of the samples primarily depended on the quality of the formation.

The fracture mechanism of the Ti6Al4V/AlMgScZr-graded multi-material was further elucidated through additional analyses conducted on the fracture morphologies of the corresponding samples. Figure 11 presents the morphologies of the fractures on both sides (AlMgScZr and Ti6Al4V) of the samples at different laser scanning speeds. At a laser scanning speed of 2600 mm/s, distinct cleavage steps and cleavage facets were observed on the AlMgScZr side (Figure 11A), indicative of a brittle fracture mechanism. The excessive energy input resulted in the formation of porosities and cracks on the fracture surface, which could serve as the initiation points for fracture and lead to reduced compressive strength. With an increase in scanning speed to 2800 mm/s, the fracture exhibited features of cleavage steps, cleavage planes, and a few dimples (Figure 11B), suggesting a combination of ductile and brittle behavior in the fracture mechanism. Further increase in scanning speed to 3000 mm/s resulted in the presence of unmelted Ti6Al4V powders on the fracture surface, with cracks originating and propagating from these unmelted powders. This observation indicates that unmelted powders in the graded layer induced the formation of cracks under higher laser scanning speeds of 3000 mm/s during the compression process, thereby weakening the mechanical properties of the samples (Figure 11C). Analysis of the distribution of Ti and Al elements on the fracture surface of the Ti6Al4V side (Figure 11D-F) revealed that cracks occurred at the interface between the graded layer and Ti6Al4V.

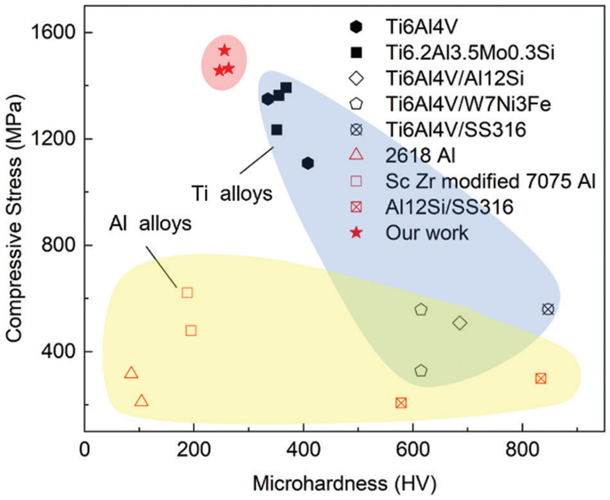

Figure 12. The hardness and compressive stress of Ti alloys, Al alloys, and their multi-materials.[40-48]

Figure 12 summarizes the microhardness and compressive strength of Ti alloys, Al alloys, and multi-material parts consisting of Ti alloys or Al alloys. Ti alloys exhibit higher microhardness values (approximately 380 HV) and compressive strengths ranging from 1109 MPa to 1393.8 MPa,[41,42] whereas Al alloys demonstrate lower microhardness values (≤200 HV) and compressive strengths ranging from 211 – 621 MPa.[43,44] The significant discrepancy in microhardness between these two materials results in a performance mismatch at the interface, which is a key factor contributing to interface susceptibility to crack. In this study, the microhardness value of TiAl$_3$ fell between that of Ti6Al4V and AlMgScZr, and the interface microhardness exhibited a graded decrease along the building direction, promoting favorable metallurgical bonding at the interface. This microhardness profile significantly improved the interfacial bonding strength, resulting in an enhanced compressive strength of up to 1531 MPa. In addition, a gradual transition of microhardness was observed at the interface. According to Zhang and Bandyopadhyay,[45] who fabricated Ti6Al4V/Al12Si multi-material parts using LDED technology, the interface obtained Ti$_3$Al IMCs with a high microhardness value, resulting in a relatively lower compressive strength of 507.8 MPa. In addition, researchers have attempted to improve the mechanical properties of multi-material parts by constructing multi-material systems, including Ti6Al4V/W7Ni3Fe,[46] Ti6Al4V/SS316,[47] and Al12Si/SS316.[48] Although most of these systems achieved high microhardness in multi-material parts, they often exhibited low compressive strength due to the formation of cracks and brittle IMCs at the interface. It is also worth mentioning that due to the presence of cracks commonly found at interfaces, Ti6Al4V/AlMgScZr-graded multi-material samples may not meet the tensile requirements. Therefore, further process optimization and investigation are required in further studies. Tensile and fatigue tests should be conducted to determine whether these functionally graded materials meet the functional requirements.

This study demonstrated that LPBF-processed Ti6Al4V/AlMgScZr-graded multi-material parts enable effective control of density behavior, interfacial metallurgical reactions, and mechanical properties. These desired characteristics are achieved through a graded interface that connects the two different materials with a composition-graded layer. A well metallurgically bonded-graded multi-material interface was obtained by controlling the laser scanning speed of the graded layer, thereby improving the overall mechanical properties of the multi-material samples. This study also established a relationship between laser processing parameters, interface microstructure, and mechanical properties.

4. Conclusion

This paper presents a methodology for incorporating a composition-graded layer (25wt% Ti6Al4V + 75wt% AlMgScZr) into the interface of Ti6Al4V/AlMgScZr multi-material fabricated through the LPBF process. In the study, the influence mechanism of the graded layer's laser scanning speed on crack formation, metallurgical reaction, and microstructure evolution were investigated. The following conclusions are drawn:

(i) As the scanning speed increased from 2400 mm/s to 3000 mm/s, significant changes were observed in the surface morphologies of the graded layer in Ti6Al4V/AlMgScZr-graded multi-material. Initially, a rough interface with cracks and pores was evident, which then transitioned into a relatively smoother surface with increasing scanning speeds. At higher scanning speeds, cracks resulted from unmelted powders were observed. The increase in scanning speed led to a decrease in residual thermal stress, which prevented crack formation. On the other hand, when the scanning speed was too high, insufficient laser energy input hindered the complete melting of powders at the edge of the molten pool. Notably, at a scanning speed of 2800 mm/s, the maximum density (3.24 g/cm^3) and minimum crack area (0.067 mm^2) were observed.

(ii) The $TiAl_3$ was generated through a metallurgical reaction, resulting from the diffusion of Ti and Al elements through the graded layer under the influence of Marangoni convection. With an increase in scanning speed, decreased laser energy input prevented the complete melting of Ti powders and their reaction with Al, leading to a gradual decrease of $TiAl_3$ content. The morphology of $TiAl_3$ was determined by the atomic ratio of Al and Ti in the melt pool. When the atomic ratio of Al to Ti approached 3, coarse dendrites formed. However, an insufficient amount of either Al or Ti atoms constrained dendrite growth, leading to the development of rod-like or finer dendritic structures.

(iii) When the scanning speed was 2800 mm/s, a gradual decrease in microhardness from the Ti6Al4V layer to the AlMgScZr layer was observed. Microhardness values exhibited a stable and continuous variation without any significant abrupt changes, attributed to the presence of a strong metallurgical bond at the interface. The compressive strength and densification behavior of LPBF-processed Ti6Al4V/AlMgScZr-graded multi-materials at different scanning speeds exhibited a consistent pattern of variation, initially increasing and then decreasing with increasing scanning speed. Notably, at a scanning speed of 2800 mm/s, the Ti6Al4V/AlMgScZr-graded multi-material achieved a maximum compressive strength of 1531 MPa, demonstrating excellent compressive performance.

Acknowledgments

None.

Funding

The authors gratefully acknowledge the funding support from National Key Research and Development Program (No. 2023YFB4603300 and 2023YFB4603304), the National Natural Science Foundation of China (No. 52225503), the Key Research and Development Program of Jiangsu Province (No. BE2022069 and No. BE2022069-1), and the National Natural Science Foundation of China for Creative Research Groups (Grant No. 51921003).

Conflict of interest

The authors declare that they have no (potential) conflicts or competing interests with any institutes, organizations, or agencies that might influence the integrity of results or objective interpretation of their submitted works to disclose.

Author contributions

Conceptualization: Dongdong Gu
Formal analysis: Hong Liu, He Sun
Funding acquisition: Dongdong Gu
Investigation: Guangjing Huang, Kaijie Lin
Methodology: Guangjing Huang
Project administration: Dongdong Gu, Kaijie Lin
Supervision: Dongdong Gu, Kaijie Lin
Validation: Rui Wang, He Sun
Visualization: Hong Liu
Writing – original draft: Hong Liu
Writing – review & editing: Guangjing Huang, Dongdong Gu

Ethics approval and consent to participate

Not applicable.

Consent for publication

Not applicable.

Availability of data

If required, the original data will be provided as per the submission guidelines.

Further disclosure

The authors hereby confirm that this original research article is an original research work and has not been presented in conference previously and is not uploaded to any preprint server. It has the full consent of all authors.

References

1. Tyagi SA, Manjaiah M. Laser additive manufacturing of titanium-based functionally graded materials: A review. *J Mater Eng Perform*. 2022;31(8):6131-6148.

   doi: 10.1007/s11665-022-07149-w

2. Yan L, Chen Y, Liou F. Additive manufacturing of multi-material structures. *Mater Sci Eng R Rep.* 2018;129:1-16.

   doi: 10.1016/j.mser.2018.04.001

3. Yao L, Xiao Z, Huang S, *et al*. The formation mechanism of metal-ceramic interlayer interface during laser powder bed fusion. *Virtual Phys Prototy*. 2023;18:2235324.

   doi: 10.1080/17452759.2023.2235324

4. Mehrpouya M, Tuma D, Vaneker T, Afrasiabi M, Bambach M, Gibson I. Multimaterial powder bed fusion techniques. *Rapid Prototyp J*. 2022;28(11):1-19.

   doi: 10.1108/RPJ-01-2022-0014

5. Heidarzadeh A, Mironav S, Kaibyshev R, *et al*. Friction stir welding/processing of metals and alloys: A comprehensive review on microstructural evolution. *Prog Mater Sci*. 2021;117:100752.

   doi: 10.1016/j.pmatsci.2020.100752

6. Gu D, Shi X, Poprawe R, Bourell DL, Setchi R, Zhu J. Material-structure-performance integrated laser-metal additive manufacturing. *Science*. 2021;372(6545):eabg1487.

   doi: 10.1126/science.abg1487

7. Zhai X, Jin L, Jiang J. A survey of additive manufacturing reviews. *Mater Sci Addit Manuf*. 2022;1(4):21.

   doi: 10.18063/msam.v1i4.21

8. Wei C, Li L, Zhang X, *et al*. 3D printing of multiple metallic materials via modified selective laser melting. *CIRP Ann*. 2018;67(1):245-248.

   doi: 10.1016/j.cirp.2018.04.096

9. Sing SL, Huang S, Goh GD. Emerging metallic systems for additive manufacturing: *In-situ* alloying and multi-metal processing in laser powder bed fusion. *Prog Mater Sci*. 2021;119:100795.

   doi: 10.1016/j.pmatsci.2021.100795

10. Liu Y, Sing SL. A review of advances in additive manufacturing and the integration of high-performance polymers, alloys, and their composites. *Mater Sci Addit Manuf*. 2023;2(3):1587.

    doi: 10.36922/msam.1587

11. Zhang C, Chen F, Huang ZF, *et al*. Additive manufacturing of functionally graded materials: A review. *Mat Sci Eng A Struct*. 2019;764:138209.

    doi: 10.1016/j.msea.2019.138209

12. Yan L, Chen Y, Liou F. Additive manufacturing of functionally graded metallic materials using laser metal deposition. *Addit Manuf*. 2020;21:100901.

    doi: 10.1016/j.addma.2019.100901

13. Chen WY, Zhang X, Li M. Laser powder bed fusion of Inconel 718 on 316 stainless steel. *Addit Manuf*. 2020;36:101500.

    doi: 10.1016/j.addma.2020.101500

14. Chen J, Yang Y, Song C. Interfacial microstructure and mechanical properties of 316L/CuSn10 multi-material bimetallic structure fabricated by selective laser melting. *Mater Sci Eng A Struct*. 2019;752:75-85.

    doi: 10.1016/j.msea.2019.02.097

15. Zhang Y, Bandyopadhyay A. Direct fabrication of compositionally graded Ti-Al2O3 multi-material structures using Laser Engineered Net Shaping. *Addit Manuf*. 2018;21:104-111.

    doi: 10.1016/j.addma.2018.03.001

16. Wei C, Liu L, Cao H, *et al*. Cu10Sn to Ti6Al4V bonding mechanisms in laser-based powder bed fusion multiple material additive manufacturing with different build strategies. *Addit Manuf*. 2022;51:102588.

    doi: 10.1016/j.addma.2021.102588

17. Sing SL, Huang S, Goh GD. Additive manufacturing of multiple materials by selective laser melting: Ti alloy to stainless steel via a Cu-alloy interlayer. *Addit Manuf*. 2020;31:100970.

    doi: 10.1016/j.addma.2019.100970

18. Zhang J, Wang X, Gao J. Additive manufacturing of Ti-6Al-4V/Al-Cu-Mg multi-material structures with a Cu interlayer. *Int J Mech Sci*. 2023;256:108477.

    doi: 10.1016/j.ijmecsci.2023.108477

19. Tan C, Chew Y, Bi G, *et al*. Additive manufacturing of steel-copper functionally graded material with ultrahigh bonding strength. *J Mater Sci Technol*. 2021;72:217-222.

    doi: 10.1016/j.jmst.2020.07.044

20. Wei C, Zhao Z, Tang J, *et al*. Effect of interface-layer process parameters on forming quality of 316L/CuSn10 bimetals fabricated via laser powder bed fusion. *Mater Lett*. 2023;336:133896.

    doi: 10.1016/j.matlet.2023.133896

21. Demir AG, Kim J, Caltabissetta F, *et al*. Enabling multi-material gradient structure in laser powder bed fusion. *J Mater Process Technol*. 2022 301: 117439.

doi: 10.1016/j.jmatprotec.2021.117439

22. Huang S, Kumar P, Yeong WY, Narayan RL, Ramamurty U. Fracture behavior of laser powder bed fusion fabricated Ti41Nb via *in-situ* alloying. *Acta Mater*. 2022;225:117593.

    doi: 10.1016/j.actamat.2021.117593

23. Blakey-Milner B, Gradl P, Snedden G, *et al*. Metal additive manufacturing in aerospace: A review. *Mater Des*. 2021;209:110008.

    doi: 10.1016/j.matdes.2021.110008

24. Kagerer S, Hudak OE, Schloffer M, Riedl H, Mayrhofer PH. TGO formation and oxygen diffusion in Al-rich gamma-TiAl PVD-coatings on TNM alloys. *Scr Mater*. 2022;210:114455.

    doi: 10.1016/j.scriptamat.2021.114455

25. Hotz H, Zimmermann M, Gerco S, Kirsch B, Aurich JC. Additive manufacturing of functionally graded Ti-Al structures by laser-based direct energy deposition. *J Manuf Process*. 2021;68:1524-1534.

    doi: 10.1016/j.jmapro.2021.06.068

26. Jing Z, Liu X, Li L, Wang W, Xu G, Chang L. Microstructure and mechanical properties of transition zone in laser additive manufacturing of TC4/AlSi12 bimetal structure. *Mater Res Express*. 2022;9(1):016513.

    doi: 10.1088/2053-1591/ac47c8

27. Wu X, Zhang D, Yi D, *et al*. Interfacial characterization and reaction mechanism of Ti/Al multi-material structure during laser powder bed fusion process. *Mater Charact*. 2022;192:112195.

    doi: 10.1016/j.matchar.2022.112195

28. Liu Y, Liu C, Liu W, *et al*. Microstructure and properties of Ti/Al lightweight graded material by direct laser deposition. *Mater Sci Technol*. 2018;34(8):945-951.

    doi: 10.1080/02670836.2017.1412042

29. Kothari K, Radhakrishnan R, Wereley NM. Advances in gamma titanium aluminides and their manufacturing techniques. *Prog Aerosp Sci*. 2012;55:1-16.

    doi: 10.1016/j.paerosci.2012.04.001

30. Kattner UR, Lin JC, Chang YA. Thermodynamic assessment and calculation of the Ti-Al system. *Metall Trans A*. 1992;23(8):2081-2090.

    doi: 10.1007/BF02646001

31. Tian Y, Shen J, Hu S, *et al*. Effect of deposition layer on microstructure of Ti-Al bimetallic structures fabricated by wire and arc additive manufacturing. *Sci Technol Weld Join*. 2022;27(1):22-32.

    doi: 10.1080/13621718.2021.1996850

32. Cook PS, Ritchie DJ. Determining the laser absorptivity of Ti-6Al-4V during laser powder bed fusion by calibrated melt pool simulation. *Opt Laser Technol*. 2023;162:109247.

    doi: 10.1016/j.optlastec.2023.109247

33. Li Y, Tang X, Lu F, *et al*. Dual beam laser fusion-brazed Ti6Al4V/AA7075 dissimilar lap joint: Crack inhibition via inoculation with TiC nanoparticles. *Mater Charact*. 2022;191:112127.

    doi: 10.1016/j.matchar.2022.112127

34. Gerold U, Herzig C. Titanium self-diffusion and chemical diffusion in bcc Ti-Al alloys. *Defect Diffus Forum*. 1997;143:437-442.

    doi: 10.4028/www.scientific.net/DDF.143-147.437

35. Shi Q, Zhong G, Sun Y, Politis C, Yang S. Effects of laser melting plus remelting on interfacial macrosegregation and resulting microstructure and microhardness of laser additive manufactured H13/IN625 bimetals. *J Manuf Process*. 2021;71:345-355.

    doi: 10.1016/j.jmapro.2021.09.036

36. Yao L, Huang S, Ramamurty U, Xiao Z. On the formation of "Fish-scale" morphology with curved grain interfacial microstructures during selective laser melting of dissimilar alloys. *Acta Mater*. 2021;220:117331.

    doi: 10.1016/j.actamat.2021.117331

37. Xie H, Lv J. Precipation of TiAl3 in remelting Al-5Ti-1B and the grain refinement of 7050 alloy. *Mater Res Express*. 2021;8(6):066513.

    doi: 10.1088/2053-1591/ac0559

38. Liu ZQ, Zhu XO, Yin GL, Zhou Q. Direct bonding of bimetallic structure from Ti6Al4V to Ti48Al2Cr2Nb alloy by laser additive manufacturing. *Mater Sci Technol*. 2022;38(1):39-44.

    doi: 10.1080/02670836.2021.2023287

39. Xi L, Ding K, Zhang H, Gu D. *In-situ* synthesis of aluminum matrix nanocomposites by selective laser melting of carbon nanotubes modified Al-Mg-Sc-Zr alloys. *J Alloy Compd*. 2022; 891:162047.

    doi: 10.1016/j.jallcom.2021.162047

40. Huang S, Kumar P, Lim CWJ, Radhakrishnan J, Ramamurty U. Fracture behavior of PH15-5 stainless steel manufactured via directed energy deposition. *Mater Des*. 2023;235:112421.

    doi: 10.1016/j.addma.2019.100970

41. Karimi J, Antonov M, Kollo L, Prashanth KG. Role of laser remelting and heat treatment in mechanical and tribological properties of selective laser melted Ti6Al4V alloy. *J Alloy Compd*. 2022;897:163207.

    doi: 10.1016/j.jallcom.2021.163207

42. Jiao Z, Ma C, Fu J, *et al*. The effects of Zr contents on microstructure and properties of laser additive manufactured Ti-6.5Al-3.5Mo-0.3Si-xZr alloys. *J Alloy Compd*. 2018;745:592-598.

    doi: 10.1016/j.jallcom.2018.02.079

43. Bi J, Lei Z, Chen Y, *et al*. Microstructure and mechanical properties of a novel Sc and Zr modified 7075 aluminum alloy prepared by selective laser melting. *Mat Sci Eng A Struct*. 2019;768:138478.

    doi: 10.1016/j.msea.2019.138478

44. Casati R, Lemke JN, Alarcon AZ, Vedani M. Aging behavior of high-strength Al alloy 2618 produced by selective laser melting. *Metall Mater Trans A*. 2017;48(2):575-579.

    doi: 10.1007/s11661-016-3883-y

45. Zhang Y, Bandyopadhyay A. Direct fabrication of bimetallic Ti6Al4V+Al12Si structures via additive manufacturing. *Addit Manuf*. 2019;29:100783.

    doi: 10.1016/j.addma.2019.100783

46. Zhang Y, Groden C, Nyberg E, *et al*. W7Ni3Fe-Ti6Al4V bimetallic layered structures via directed energy deposition. *Virtual Phys Prototyp*. 2023;18(1):e2137048.

    doi: 10.1080/17452759.2022.2137048

47. Onuike B, Bandyopadhyay A. Functional bimetallic joints of Ti6Al4V to SS410. *Addit Manuf*. 2020;31:100931.

    doi: 10.1016/j.addma.2019.100931

48. Zhang Y, Bandyopadhyay A. Influence of compositionally graded interface on microstructure and compressive deformation of 316L stainless steel to Al12Si aluminum alloy bimetallic structures. *ACS Appl Mater Interfaces*. 2021;13(7):9174-9185.

    doi: 10.1021/acsami.0c21478

ACCSCIENCE PUBLISHING

Materials Science in Additive Manufacturing

ORIGINAL RESEARCH ARTICLE

Effects of heat treatment on microstructure and mechanical properties of 17-4PH/IN625 bimetallic parts fabricated through extrusion-based sintering-assisted additive manufacturing

Yulin Liu, Dayue Jiang, and Fuda Ning*

Department of Systems Science and Industrial Engineering, State University of New York at Binghamton, Binghamton, New York, United States of America

Abstract

The mechanical properties of bimetallic composites are significantly influenced by their interfacial morphologies. This study delves into the impact of various heat treatment conditions on the microstructure and mechanical attributes of steel/nickel bimetallic (17-4PH/IN625) components produced through extrusion-based sintering-assisted additive manufacturing (ES-AM). The bimetallic composites were annealed at 1150°C for 1, 4, and 8 h, followed by an aging treatment at 482°C for samples annealed for 8 h. After annealing, microstructural heterogeneities, including variations in grain size and elemental distribution within the transition zone close to the interface, were observed. It was found that in the diffusion transition zone between the two alloy layers, the diffusion of iron (Fe) and nickel (Ni) elements increased with longer holding times, as corroborated by microhardness tests and quantified through theoretical parabolic diffusion law. The transition zone exhibited two distinct areas: an Fe-predominant zone and a Ni-predominant zone, with the latter containing oxides and molybdenum (Mo)- and niobium (Nb)-rich precipitates. No new phases emerged post-heat treatment; however, shifts in peak due to stress relaxation and the emergence of precipitates were identified through X-ray diffraction (XRD) observations. Microhardness within the transition zone increased following heat treatment, peaking at 186 $HV_{1.0}$ after a 4-h annealing. The optimal heat treatment condition was identified as 1150°C for 4 h, which facilitated the development of uniform microstructures and improved bonding strength. This study demonstrates an enhanced interfacial bonding strength in 17-4PH and IN625 bimetallic parts manufactured through ES-AM, suggesting their wide-ranging potential applications in industry.

Keywords: Bimetallic composites; Extrusion-based sintering-assisted additive manufacturing; ES-AM; Heat treatment; Interface bonding; Diffusion zone

***Corresponding author:**
Fuda Ning
(fning@binghamton.edu)

Citation: Liu Y, Jiang D, Ning F. Effects of heat treatment on microstructure and mechanical properties of 17-4PH/IN625 bimetallic parts fabricated through extrusion-based sintering-assisted additive manufacturing. *Mater Sci Add Manuf*. 2024;3(2):3281. doi: 10.36922/msam.3281

Received: March 27, 2024

Accepted: April 29, 2024

1. Introduction

The demand for hybrid structures containing a combination of varied metal materials has increased to address the requirements of multiple industrial applications.[1] Bimetallic structures offer several advantages, such as superior structural robustness, improved mechanical strength, and improved economic efficiency compared to components manufactured from a single metal alloy.[2] Additive manufacturing (AM) techniques, categorized into fusion-state and solid-state AM methods, have been utilized to produce bimetallic parts. Fusion-based processes such as directed energy deposition (DED) and powder bed fusion (PBF) utilize high-energy sources such as electrons, wire arcs, and lasers to rapidly melt feedstocks, which then solidify on the substrate to form the desired part.[3] However, due to the varying thermal coefficients of bimetallic parts, the intense energy input and rapid melting and solidification processes often result in cracks and brittle failures.[4] Hybrid cold spray AM is a solid-state AM technique where micron-sized particles are accelerated to high velocities by high-pressure, low-temperature gas, impacting a substrate and undergoing plastic deformation to form a coating layer by layer.[5] Extrusion-based sintering-assisted additive manufacturing (ES-AM) employs a printing-debinding-sintering process, utilizing sintering temperatures lower than the melting point to handle bimetallic parts.[6] This approach allows for sufficient element diffusion during the sintering process, typically resulting in smoother interface surfaces and fewer intermetallic phases.[7] In addition, ES-AM offers benefits such as ease of operation, reduced risk, and an environmentally friendly manufacturing process.[8-10]

Several researchers have investigated the fabrication of bimetallic parts with fewer defects and cracks in the interface using ES-AM. Bimetallic components comprising low- and high-carbon steel have been synthesized through ES-AM; yet, the quality of the resultant part was compromised due to suboptimal optimization of process parameters, particularly in the co-sintering process.[11] Employing a copper infiltration technique, a composite structure featuring a high carbon steel exterior and a copper channel was engineered to fulfill the requirements of an injection mold, necessitating adequate mechanical strength, stiffness, and wear resistance, coupled with superior thermal conductivity.[12] In prior investigations, 17-4PH and IN625 were processed through ES-AM to fabricate a bimetallic component with a smooth interface and cohesive bonding devoid of conspicuous cracks.[7] 17-4PH stainless steel (SS) boasts high strength, hardness, and relatively good corrosion resistance, although it may have reduced elongation and temperature stability.[13] Meanwhile, IN625, a nickel-based superalloy, excels in corrosion resistance and high-temperature performance with reduced strength, commonly employed in aerospace and industrial sectors.[14] By combining these two materials in a bimetallic structure, the aim is to enhance mechanical properties, corrosion resistance, and temperature stability, catering to a broad spectrum of applications ranging from engine components to structural parts in harsh environments.[15] In addition, the thermal expansion coefficients of IN625 and 17-4PH are relatively close, with IN625 nickel-based superalloy at approximately 12.8×10^{-6}/°C[16] and 17-4PH SS at about $10.8 - 11.0 \times 10^{-6}$/°C.[17] This similarity in thermal expansion coefficients means that these two materials tend to expand and contract at similar rates in response to temperature changes, thereby reducing interface stress and minimizing the likelihood of cracks and defects. The co-sintering process in ES-AM is utilized to establish interface bonding, concurrently minimizing thermal stress and the development of intermetallic phases, due to its operation at relatively low temperatures. These lower temperatures can impede atomic diffusion, leading to pore formation and reduced interface bonding strength. The interface thus emerges as a critical factor in determining the structural integrity of dissimilar metal materials, acting as an essential conduit for the transfer of electricity, heat, damping, and other properties.[9,18-20]

Numerous studies have investigated the microstructure of interfaces and the mechanical properties of bimetallic parts made from SS and Inconel alloy, which were fabricated using various AM techniques. In a bimetallic part fabricated through hybrid DED and thermal milling, consisting of IN718 and 316L, diffusion layers were observed with a significant width of 450 mm, featuring a microstructural transition from columnar to equiaxed dendrites. Niobium (Nb) and molybdenum (Mo) precipitates were identified in the Inconel near the interface, with no other phases detected.[21] In the interface of a 304SS/IN738L bimetal fabricated by DED, an architecture featuring soft and stiff lamellae with inherent interfacial defects was observed, resulting from partial solute mixing and intricate fluid dynamics in the melt pool during rapid solidification.[22] In bimetallic materials composed of 316L and IN625, printed using DED, two types of interfaces were identified: one showing a gradual compositional change with IN625 grains growing epitaxially on 316L grains, and the other exhibiting a sudden compositional shift that encourages bidirectional nucleation and grain growth, leading to a high susceptibility to cracking.[23] In a bimetallic SS/nickel (Ni) alloy manufactured through PBF, no intermediate softening from ferrite phase formation occurred, but a decrease in hardness at the 316L side was noted, resulting from the thermal effects of manufacturing nickel alloy. In addition, MC carbides form in Ni-based superalloys during slow solidification due to the strong affinity of carbon for these metallic elements.[24] Bimetallic parts made of IN718 and high-carbon steel have been produced using ES-AM, which revealed a layered microstructure in partially sintered high-carbon steel and IN718 particles due to the diffusion of Ni and chromium (Cr) toward the steel granules.[25]

Heat treatment techniques are utilized to enhance bimetallic bonding by increasing the thickness of the diffusion zone and refining the intermetallic phase composition. The bimetallic assembly comprising SS316L and IN625, fabricated through arc welding, was heated to 970°C to facilitate the transformation of δ-ferrite into the austenite phase in SS316L, thereby improving the bond strength over the as-fabricated sample.[26] The process of normalizing applied to the IN625/carbon steel bimetallic joint resulted in the recrystallization of the constituent materials, along with the emergence of a diffusion zone and the precipitation within IN625.[27] After heat treatment, the bimetallic parts made of Ni-based superalloy and SS exhibited a secondary phase (Nb-rich phase) near the fusion boundary in the heat-affected zone on the Inconel side with higher hardness values.[28] Heat treatment effectively diminishes residual stresses and improves the toughness of aluminum (Al) bronze-steel bimetallic structures produced through AM, resulting in a sample with reoriented grains and a more uniform microstructure.[29] Varying the temperature or duration of heat treatment led to different levels of bonding strength at the interface. A continuous layer of titanium aluminide ($TiAl_3$) intermetallic was formed in the interface of Al/Ti bimetallic during specific heat treatment conditions, and the shear strength was governed by the strength of Al, with minimal impact from changes in the interlayer thickness.[30] The bonding behavior of a copper (Cu)/Al/Cu clad composite was investigated under different heat treatment temperatures, uncovering significant formation of intermetallic layers following specific heat treatment cycles, such as annealing at 500°C, leading to higher ductility and relatively high strength.[31] For a bimetallic part consisting of SS and carbon steel, the diffusion transition zone exhibited a rising trend with increasing annealing temperature, resulting in enhanced interfacial shear strength and improved ductility; however, it had a less pronounced effect on impeding fatigue crack propagation along the interface.[32] Heat treatment between 800°C and 1100°C for 30 min to 2 h significantly improved the properties of a bimetallic low-carbon steel and austenitic-SS structure, increasing its ultimate tensile strength by 35% and elongation by 250%.[33]

Nevertheless, there is insufficient research on the effects of heat treatment on the microstructure and mechanical properties of 17-4PH/IN625 bimetals produced through ES-AM. The co-sintering process, conducted at relatively low temperatures, results in pore formation and weaker bonding strength, necessitating heat treatment to enhance bonding strength and overall material properties. Consequently, this study aimed to investigate 17-4PH/IN625 bimetallic composites fabricated via ES-AM. It presents a comparative analysis elucidating the effects of heat treatment on the interfacial characteristics of bimetallic composites, with a focus on elemental diffusion, transition zone thickness, and microhardness evolution. To facilitate the expansion of the diffusion zone, specific heat treatment conditions were explored, including a homogenization treatment at 1150°C, with varying dwell times and cooling rates, followed by an aging treatment to establish an optimized heat treatment procedure for superior interfacial bonding strength.

2. Materials and methods

2.1. Materials and fabrication procedures

In this study, 17-4PH SS and IN625 filaments were procured from Markforged Corporation., (USA) consisting of metal powders combined with a consistent binder system comprised of wax and polyethylene. These filaments were fabricated using a dual-nozzle desktop 3D printer (F350, Creatbot, China) with a heated nozzle capable of reaching temperatures up to 450°C. An illustrative diagram of the manufacturing process is presented in Figure 1A. The 17-4PH SS filament was on the left and first extruded through a heated nozzle to reach a thickness of 2 mm with a layer thickness of 0.1 mm. Then, IN625 was printed using the right nozzle to deposit onto 17-4PH parts with a thickness of 0.1 mm. Finally, the overall size of parts is 15 × 15 × 4 mm^3, as shown in Figure 1D. The material properties for each filament and specific printing settings employed for each material are documented in Table 1. The processes of binder removal and solid-state sintering were carried out utilizing the Markforged production equipment (Metal X™ System, USA). A tailored sintering profile for IN625 alloy was applied due to its lower melting point compared to 17-4PH, with the entire procedure lasting 29 h. To achieve a denser structure during sintering, a smaller component with a thickness of 2 mm was placed on top of the bimetallic part. The printed and sintered bimetallic parts are presented in Figure 1B and C. The alloy compositions for 17-4PH and IN625 feedstocks are listed in Table 2. In addition, the properties of single metals are listed in Table 3 for comparison with bimetallic parts.

The heat treatments were conducted at a steady temperature of 1150°C and a heating rate of 10°C/min, with durations of 1, 4, and 8 h, labeled as HT1, HT4, and HT8, respectively. The utilization of this high constant temperature and extended holding time was aimed at effectively broadening the transition zone.[32] Typically, a homogenization temperature exceeding 1000°C is required for 17-4PH to attain complete supersaturation

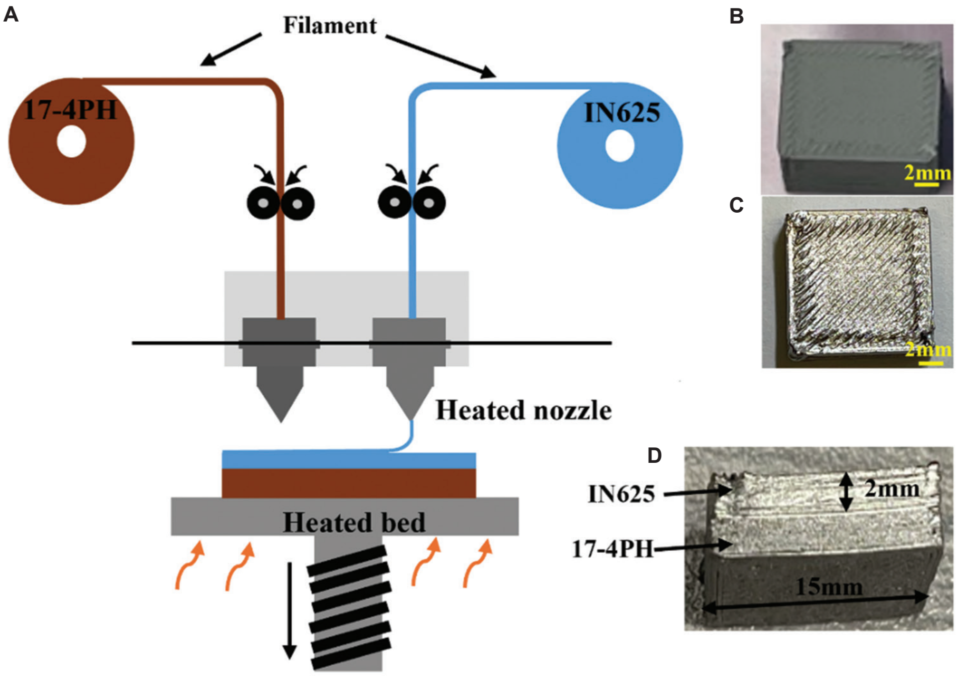

Figure 1. The illustration of the ES-AM process and the fabricated 17-4PH/IN625 bimetal part. (A) An illustration ES-AM process with a dual nozzle system (B) A bimetallic material after printing. (C) The top perspective of the sintered component. (D) Profile of the sintered component, showcasing geometrical details. Scale bars: 2 mm.
Abbreviation: ES-AM: Extrusion-based sintering-assisted additive manufacturing.

Table 1. Material properties for 17-4PH and IN625 filament and optimized printing parameters for 17-4PH/IN625 bimetallic green part

Parameters	17-4PH	IN625
Filament		
Version	V2	-
Diameter	1.75 mm	1.75 mm
Specification	400 cc/spool	200 cc/spool
Composition	20 vol.% wax, 20 vol.% polyethylene, and 60 vol.% powder	
Optimized printing parameters		
Nozzle temperature	230°C	210°C
Bed temperature	80°C	80°C
Chamber temperature	60°C	60°C
Nozzle size	0.4 mm	0.4 mm
Layer thickness	0.1 mm	0.1 mm
Infill density	100%	100%
Speed	40 mm/s	40 mm/s
Infill orientation	45°	135°

of martensite. Considering factors such as the presence of NbC and oxides, as well as the dimensions of prior austenite grain and martensite lath, the homogenization temperature was set at 1150°C to ensure adequate uniformity.[34] One of the recommended heat treatment procedures for the IN625 alloy involves subjecting it to a solutionizing operation at 1150°C. This thermal processing step serves to eliminate compositional inhomogeneities, eliminate secondary phases present, trigger recrystallization phenomena, and promote grain coarsening.[35] The aging temperature and duration were adjusted for specific applications to balance strength and toughness while controlling tempered martensite and precipitation. In addition, an aging heat treatment was employed (482°C for 1 h holding time), following HT8 to enhance hardness. Rapid cooling through water quenching was implemented for the samples to promote expedited heat extraction and mitigate the potential for carbide precipitation, especially within the temperature regime of 1150°C sustained for 8 h. Figure 2 illustrates the heat treatment conditions used during the experiments.

2.2. Microstructure characterizations and mechanical properties

To investigate the microstructure and microhardness, bimetallic samples were prepared in both as-sintered and heat-treated states. Pore distribution and grain morphology were analyzed using optical microscopy (OM; Olympus DSX 510, Olympus, Japan) and scanning electron microscopy (SEM; Supra 55-VP, Zeiss, Germany).

Table 2. The alloy composition of the 17-4PH and IN625 feedstocks

Weight %	Cr	Fe	Ni	Nb	Mo	Mn	Si	C	Cu	Co	Other elements
17-4PH	15 – 17.5	Balance	3 – 5	0.15 – 0.45	-	1	1	0.07	3 – 5	-	0.07
IN625	20 – 23	5	Balance	3.15 – 4.15	8 – 10	0.5	0.5	0.1	-	1	0.82

Table 3. Material properties of 17-4PH and IN625

Material properties	17-4PH V2	IN625
Relative density	>96.5%	>96.5%
Hardness (HRC)	36	7
Ultimate tensile strength (MPa)	1180	765
0.2% yield strength (MPa)	710	334
Elongation at break	7%	42%
Corrosion	Good	Excellent
Thermal coefficient	10.8×10^{-6}/°C[16]	12.8×10^{-6}/°C[17]

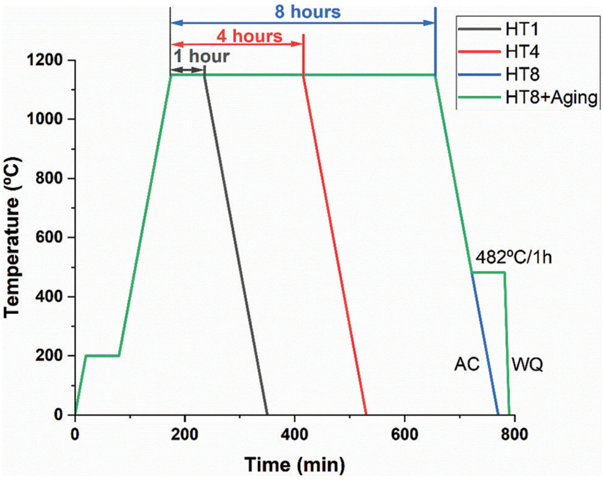

Figure 2. Schematic overview of heat treatment conditions. Abbreviations: AC: Air cooling; WQ: Water quenching.

Initially, the samples were sectioned transversely relative to the building direction and embedded in epoxy to ensure secure fixation. The process involved grinding and polishing, culminating in a final polish utilizing an alumina suspension with a particle size of 0.25 µm. After polishing, the samples underwent microstructural characterization utilizing an SEM integrated with an energy-dispersive X-ray spectroscopy (EDS) system to analyze the elemental distribution across the interfacial region. Meanwhile, internal porosity was assessed using OM at ×40 magnification, followed by the analysis of the polished internal surfaces of cut samples using ImageJ software (National Institutes of Health, USA). To reveal the grain structure, chemical etching was performed using Marble's and Kalling's 2 reagents (ES Laboratory, LCC, USA), followed by observation through OM. XRD analyses were employed to identify the phase constituents present in the bimetallic samples. Microindentation hardness testing following ASTM E384 guidelines was conducted utilizing a Vickers hardness tester (LM-310AT, LECO, USA). The test was conducted with a load of 1.0 kg, an approach speed of 60 µm/s, and a measurement period lasting 10 s.

3. Results and discussion

3.1. Interface characterization

The microstructure of the interface between 17-4PH and IN625 after heat treatment reveals metallurgical bonding, as depicted in Figure 3. Figure 3A-D depicts the variation in pore population and dimensions across the polished surface subjected to distinct heat treatment conditions. The grain morphology of 17-4PH after surface etching with Marble's reagent is presented in Figure 3A1-D1. Small pores (dark pores) were distributed within the 17-4PH parts due to insufficient densification when employing the sintering profiles for IN625. Nevertheless, with an increase in holding time, the pore size decreased owing to the heat contribution facilitating densification to a certain extent.[36] Typical martensitic and ferrite phases were observed on the 17-4PH side of the interface, resulting from the precipitation hardening process.[37] Concurrently, the grain size of 17-4PH initially decreased and subsequently increased with increasing holding time, a phenomenon attributable to recrystallization and grain growth induced by excessive heat input.[32] The chemical etching process did not reveal the phase composition of IN625; however, subsequent XRD analysis confirmed the presence of the austenitic phase, corroborating the findings reported in the literature.[38]

No evident intermetallic phases were formed at the interface under different heat treatment conditions, which aligns with the findings in the relevant literature.[5] In Figure 3A-D, the interface is marked by a band with a lighter appearance, which lacks visible grain structure, suggesting an absence of grain development in this transition zone. Figure 3 illustrates that the thickness of the interfacial white bands did not significantly vary with extended holding times, maintaining an approximate width of 60 µm in both as-sintered and heat-treated states. Significantly, the precipitation of minute particulates, visible as black dots in Figure 3, was localized within the IN625 alloy region. Meanwhile, as time increases, the porosity of the entire part decreases, as depicted in Figure 4, which uses images from OM taken at three different locations along the interface.

SEM analysis revealed a comparable phenomenon occurring at the interface, irrespective of whether heat treatment was applied or not, as shown in Figure 4. To

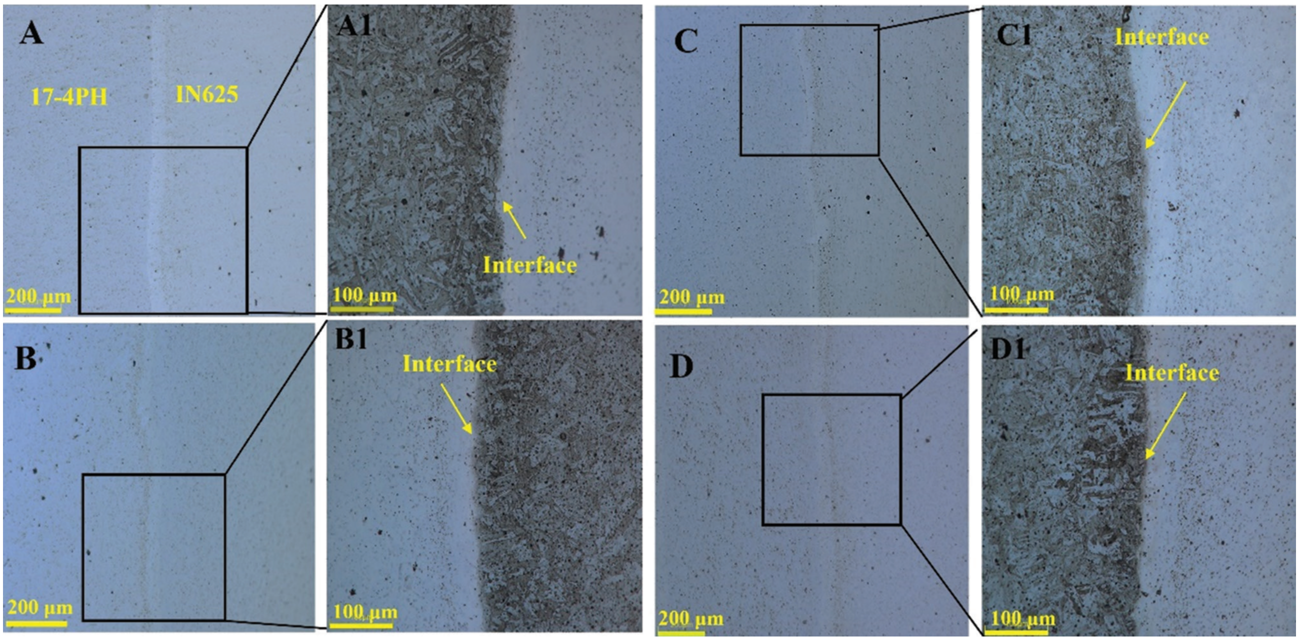

Figure 3. Optical micrographs of the bimetallic part at different dwell times. (A) 1 h, (B) 4 h, (C) 8 h, and (D) 8 h + aging, all at 482°C/h. Scale bars: 200 µm; magnification: ×222. The enlarged images (A1, B1, C1, and D1) represent chemically etched surfaces after polishing. Scale bars: 100 µm; magnification: ×555.

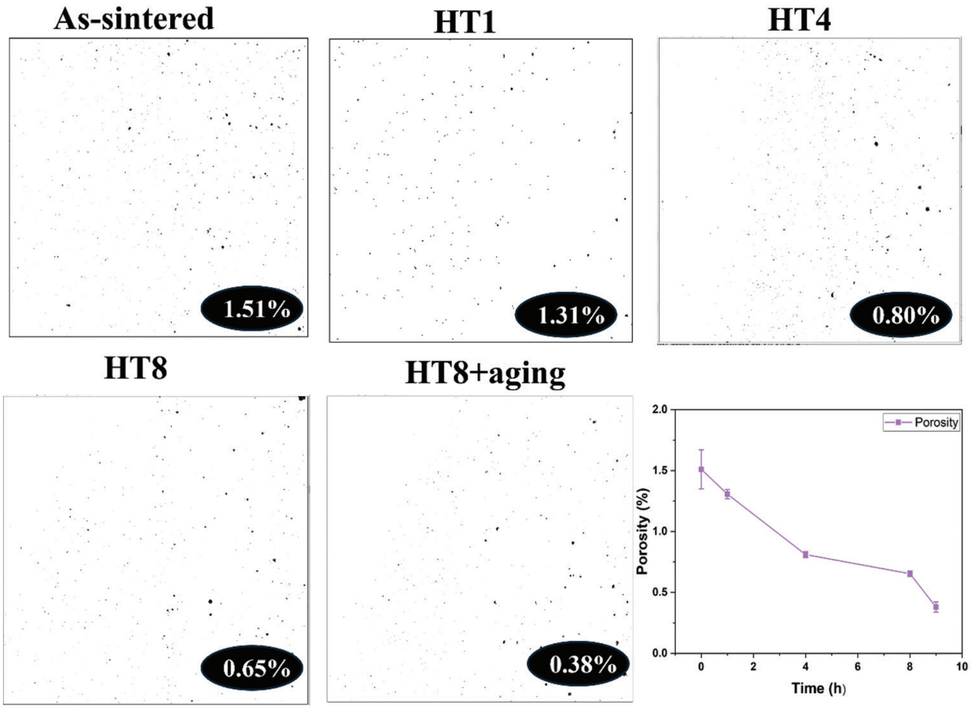

Figure 4. Internal porosity of samples at different heat treatment conditions.
Note: Images were processed using ImageJ software.

further delineate the specific transition zone within the interface, an EDS line scan analysis was conducted to investigate the elemental variations. The EDS line scan data, as depicted in Figure 5F, reveal that the white bands observed in the OM images (Figure 3) and the precipitate accumulations (Figure 5A-E) correspond to regions where iron (Fe) and Ni constituents undergo interdiffusion in opposite directions. Within these areas, the concentrations of Fe and Ni elements are diminished in comparison to their respective pure forms, accompanied by a depletion of Nb and Mo relative to pure Inconel. Conversely, Cr exhibits a uniform distribution since both 17-4PH and IN625 alloys contain this element.

These white bands are characterized by reduced porosity, exhibiting either smaller pores or an absence of pores altogether, as evident from Figure 5A-E. The white band region, dominated by the Fe element, is referred to as the Fe-predominant zone. With increasing holding time, the thickness of these bands remains relatively unchanged, a phenomenon vividly illustrated in Figure 3. It measures almost 60 µm under both as-sintered and heat-treated conditions, consistent with our previous research.[39] Another region is primarily characterized by Ni elements, termed the Ni-predominant zone, as illustrated in Figure 5F. The segregation of precipitates and inclusions within this region undergoes modifications as the holding time increases. During heat treatment, precipitates form during heat treatment as carbon diffuses from steel into the Inconel alloy, containing elements (Cr, Mo, Nb) with a strong affinity for carbon.[40] After 1 h of heat treatment, the size and distribution of precipitates and inclusions diminish in comparison to the as-sintered condition. Similarly, the 4-h holding time yields the smallest precipitates and inclusions relative to the other holding times investigated. However, an excessively prolonged holding time of 8 h promotes grain growth, resulting in larger precipitate sizes. In addition, elongated precipitates are observed in the sample subjected to the 8-h holding time.

3.2. Element diffusion at the interface

The behavior of element diffusion at the interface between 17-4PH and IN625 is critical for the bonding quality and strength of the bimetallic composite. Previous observations indicate that a larger distance of alloy diffusion correlates with increased interfacial shear strength.[32,41] This study highlights significant variations in the chemical compositions of 17-4PH and IN625, particularly in the elements Fe, Ni, Mo, and Nb. These variations in elemental concentrations between two materials initiate diffusion during heat treatments, detectable through EDS analysis. SEM images and EDS maps illustrating the distribution of Fe and Ni elements near the interface post-annealing at varied durations of 1, 4, and 8 h are presented in Figure 6.

The primary constituents of the diffusion zone, Fe and Ni, exhibit marked variations in their concentrations within this region. Notably, the concentration of Ni sharply

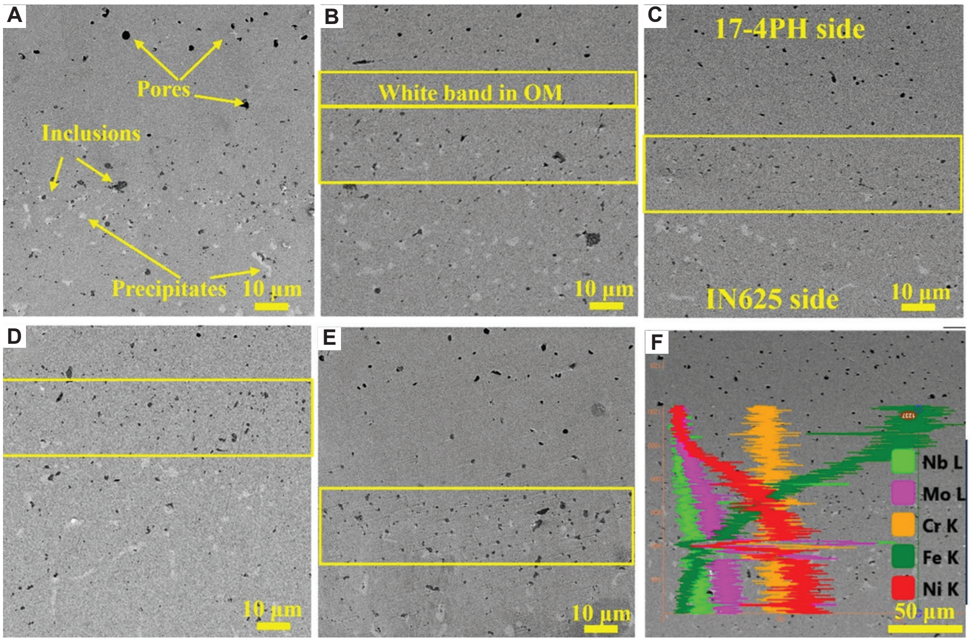

Figure 5. Scanning electron microscopy analysis of the interface following different heat treatment conditions. (A) As-sintered; (B) heat-treated at 1150°C for 1 h; (C) 4 h; (D) 8 h; (E) 8 h + aging; and (F) energy-dispersive X-ray spectroscopy line scanning of the interface highlighting five primary elements. Scale bars: (A-E) 10 µm, magnification: ×1280; (F) 50 µm, magnification: ×862.
Note: In all panels, the top part is the 17-4PH side, and the bottom part is the IN625 side. Abbreviation: OM: Optical microscopy.

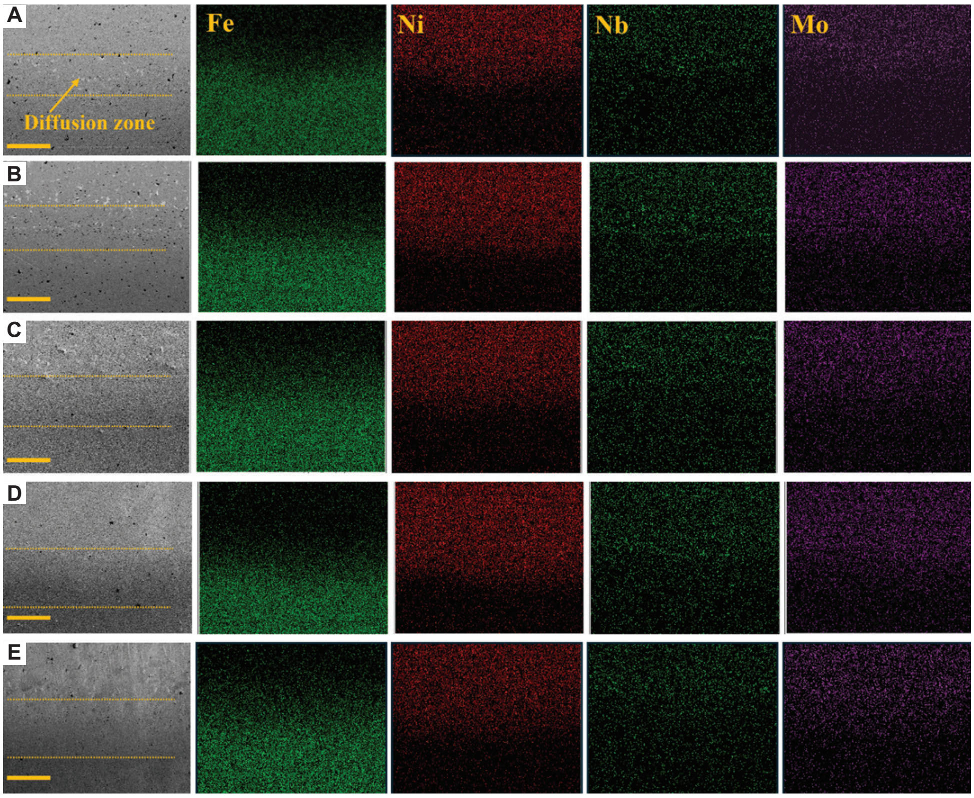

Figure 6. Scanning electron microscopic images and energy-dispersive X-ray spectroscopy maps of Fe, Ni, Nb, and Mo adjacent to the interface following different annealing durations. (A) As-sintered; (B) 1 h; (C) 4 h; (D) 8 h; and (E) 8 h + aging at 482°C for 1 h. Scale bars: 100 µm, magnification: ×543).

declines at the boundary of the diffusion zone, while that of Fe correspondingly surges. In the diffusion zone between two layers, the boundary of Ni and Fe elements is not distinct after 1 h and 4 h, as shown in Figure 6; however, a gradient distribution of these elements becomes noticeable after 8 h. In addition, Nb and Mo elements segregate near the diffusion zone, leading to the formation of delta phase or precipitates in IN625, which is characterized by increased brittleness, consistent with another previous publication.[42] Furthermore, the Nb- and Mo-rich zone, depicted in Figure 6A as a light area, becomes less pronounced and diminishes in size as the holding time is extended.

To measure the diffusion distance of the alloy, profile curves depicting the diffusion of elements in various states (Figure 7A-E) were plotted along the scan line shown in Figure 7. The transition zone for diffusion between the two steel layers expands as the holding time is prolonged. This result is aligned with the findings reported by Li *et al.*[32] and Jiang *et al.*,[43] who noted a similar trend. The expansion of the transition zone is believed to follow a parabolic law, allowing its thickness to be quantified as Equation I:

$$\delta = \sqrt{K_0 \exp\left(\frac{-Q}{RT}\right) * t} \tag{I}$$

where δ denotes the thickness (m), t stands for annealing duration (s), K_0 represents the factor (m^2/s), Q signifies the activation energy (J·mol) required for interface diffusion, R is the universal gas constant (8.3145 J/(mol·k)), and T indicates the absolute temperature (Kelvin).

Figure 7 presents the EDS line scanning across the interfaces of 17-4PH/IN625 bimetals fabricated under varying solution times. It reveals distinct concentrations of Fe and Cr elements at the interfaces, indicating a high-quality metallurgical bond. In addition, it demonstrates that the thickness of the reaction layer significantly increases with extended heat treatment times, correlating with related research on diffusion zone thickness.[43] Initially, a 1-h solution time slightly thickens the reaction layer compared to the as-sintered state, with the diffusion zone measuring 105 µm compared to 75 µm for the as-sintered sample, as shown in Figure 7A. Extending the solution time to 4 h results in the reaction layer thickening to approximately 160 µm, a 52% increase over the 1-h solution time sample, as detailed in Figure 7B. Nevertheless, there are holes within the reaction layer. According to Equation I, $\delta_3 = \sqrt{2}\,\delta_2 = 2\sqrt{2}\,\delta_1$, where δ_1, δ_2, δ_3 represent the diffusion zone thicknesses under heat treatment for 1, 4, and 8 h, respectively. At an 8-h solution time in Figure 7C, the transition zone reaches nearly 220 µm,

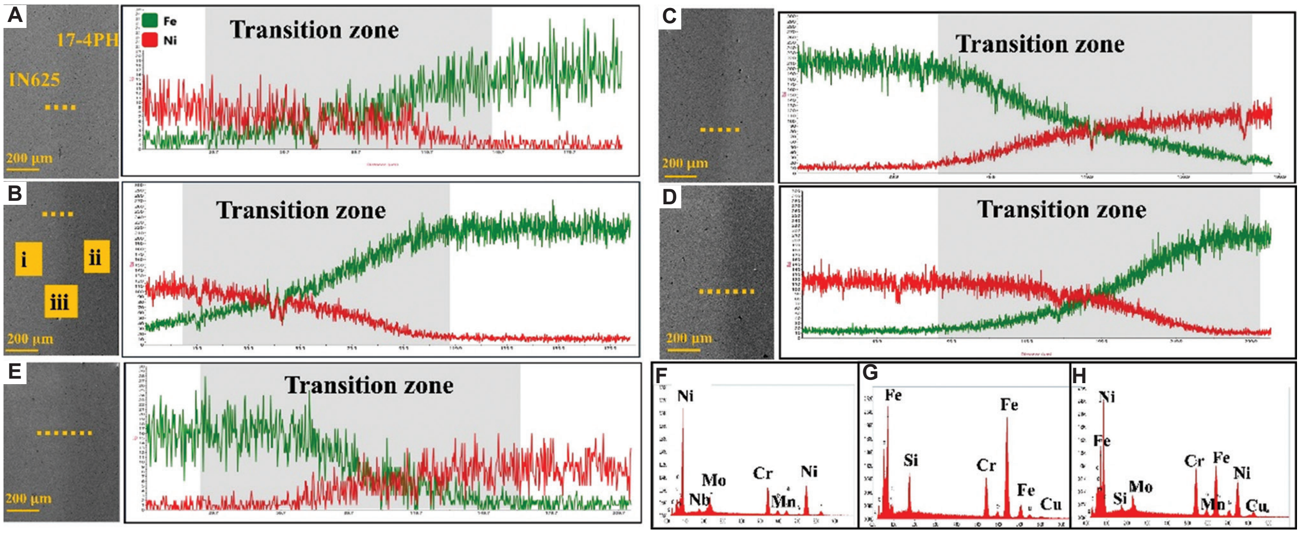

Figure 7. Scanning electron microscopic images and transition zones across different heat treatment conditions. (A) As-sintered; (B) treated at 1150°C for 1 h; (C) 4 h; (D) 8 h; and (E) 8 h + aging. Scale bars: 200 μm, magnification: ×200. Elemental composition analysis at specific locations in (B): (F) Element at point A, (J) element at point B, and (K) element at point C.

about 2.1 times the thickness at 1 h, aligning closely with the calculated value of approximately 2.8 times. Prolonged solution times, while increasing the reaction layer thickness, also enhance the risk of cracking and excessive growth of grain size, as shown in Figure 3. Additional EDS analyses at the interfaces of 17-4PH/IN625 bimetals for different solution times, as illustrated in Figure 7, indicate that solution time does not alter the composition of interface phases within the reaction layer. In addition, Figure 7F and G present EDS point scan analyses at points i and ii in Figure 7B, corresponding to the 17-4PH and IN625 alloys, respectively. Figure 7H illustrates elemental distribution at point iii in Figure 7B, identifying Fe, Ni, Co, Si, and Mn in the specified area.

3.3. Interface microstructure analysis

To delve deeper into the characteristics of the diffusion zone, a focused examination of a select region was conducted to analyze the distribution of elements and identify the presence of precipitates, as illustrated in Figure 8. This investigation employed linear analysis and mapping techniques to scrutinize the chemical composition of the white band observed in Figure 3 and the precipitates found within the diffusion zone.

Figure 8A illustrates the characteristic structure observed at the interface, which features a black zone encircled by a lighter zone. Elemental mapping reveals that the darker oxides are composed of oxygen (O), manganese (Mn), and Cr, while Nb and Mo constitute the lighter secondary phase. These zones are characterized as Ni-predominant areas, as corroborated by EDS analyses referenced in Figure 8A, C, and E. Furthermore, examination of Figure 8F and J reveals that the Fe-predominant zone comprises Fe, Cr, and Mn elements exclusively, devoid of any other discernible phases, thus aligning with earlier findings outlined in Section 3.1.

The emergence of oxidized regions and the formation of carbides are anticipated outcomes during the debinding and sintering stages, largely attributable to the accumulation of impurities. Within the comprehensive microstructure of the material, carbides, characterized by a blocky appearance, were observed both internally and at the grain boundaries in parts manufactured through ES-AM.[4] Further SEM analyses highlighted a homogeneously distributed secondary phase within the material (Figure 7A, B, and D), which was predominantly composed of Mo, Nb, and Si (Figure 7B). A comparative analysis of its EDS spectrum with that of the matrix revealed a marginal increase in carbon content within this secondary phase, which also exhibited a reduction in Ni, Fe, and Cr in comparison to the matrix, as outlined in Table 4. Heat-treated samples, as contrasted with as-sintered ones, demonstrated the presence of elongated carbides, as illustrated in Figure 3. These carbides were arranged in semi-continuous sequences along the grain boundaries, consistent with the literature.[35] In other studies, a similar phenomenon was observed in heat-treated IN625 produced using PBF and DED methods.[44] These carbides are classified into two types: NbC and Cr23C7.[45] Among the two, NbC typically has a higher dissolution temperature (above 1200°C) and remains incompletely dissolved during heat treatment under 1150°C.[29] Cr23C7 usually forms during the solid-phase transition process due to a

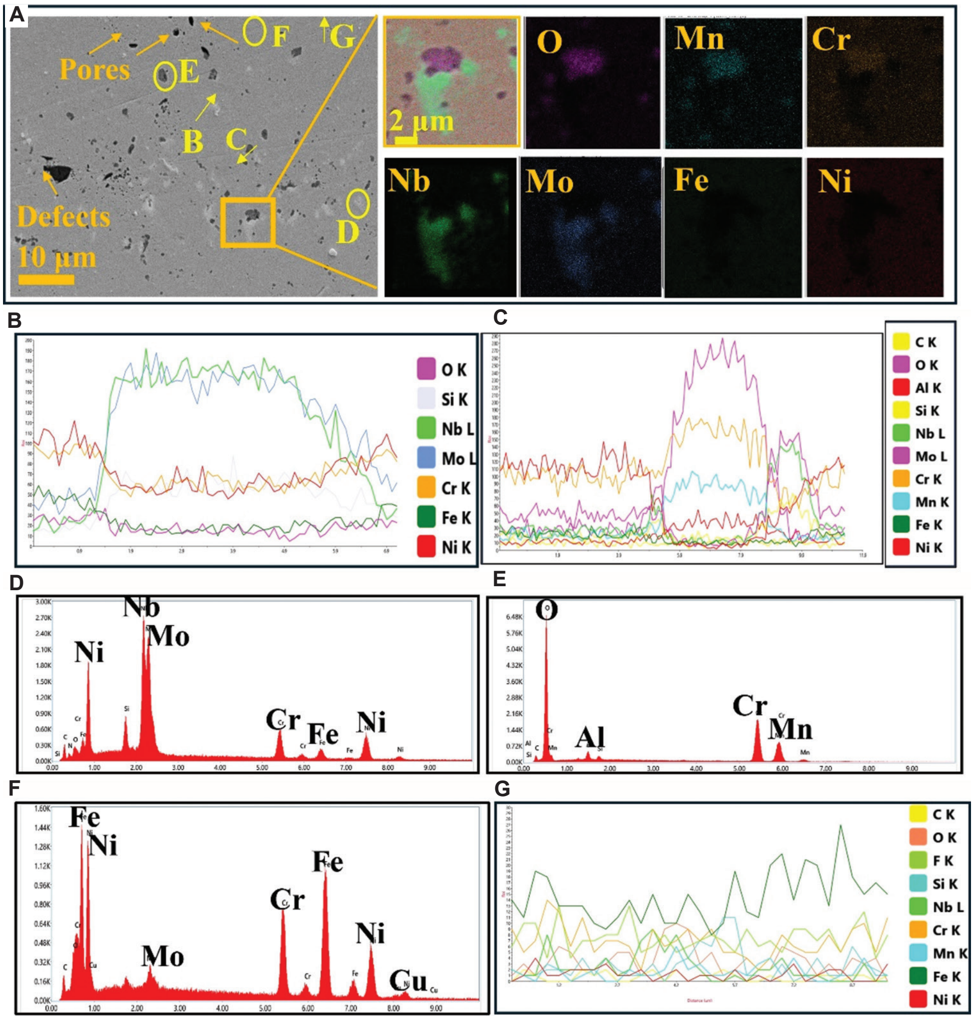

Figure 8. Microstructural analysis of interfaces. (A) Elemental mapping covering an oxide inclusion and secondary phase. Scale bars: 10 μm, magnification: ×3678; Scale bars: 2 μm, magnification: ×3678. Energy-dispersive X-ray spectroscopy (EDS) line scans for light (B) and dark (C) areas; elemental analyses for specific spots: (D) analysis at spot D, (E) analysis at spot E; (H) EDS line scans for white band.

Table 4. Element distribution in the interface of bimetal

Weight %	Cr	Fe	Ni	Nb	Mo	Mn	Si	C	O
Precipitates	9.7	5.1	20.9	25.8	15.9	-	2.1	16.5	2.3
Oxides	39.5	-	-	-	-	19.5	0.5	8.7	30.4
White bands	14.8	51.9	14.6	-	1.4	-	0.3	10.6	-
17-4PH	12.6	57.6	3.1	-	-	0.4	2.8	9.1	7.0
IN625	18.5	5.8	52.0	2.6	7.0	-	0.6	11.6	1.9

slower cooling rate.[46] The elongated morphology of these carbides is due to the slow cooling rates experienced at the conclusion of the heat treatment process, a detail that aligns with the observed structural characteristics.

The XRD patterns of phases present at the 17-4PH/IN625 composite, both in as-sintered and heat-treated states, were analyzed to assess changes in intermetallic phases, as depicted in Figure 9A. The primary phases in 17-4PH are the α-phase (martensitic and ferritic phases), whereas in IN625, the dominant phase is the γ-phase (austenitic phase). No additional phases were discovered following the heat treatments, which were under 1150°C for various durations, with or without subsequent aging, of 17-4PH, with only austenite and martensite peaks detected.[20] Both direct aging and aging following Hot Isostatic Pressing (HIP) of 17-4PH fabricated through PBF showed no formation of other phases.[31,47] Furthermore, the absence of additional peaks suggests the absence of reactive phase formation within the bimetallic structure of SS316L and IN718 alloy.[48] Similarly, further XRD patterns corroborate the observation in our research that no new intermetallic phases form within the diffusion zone following heat treatment, aligning with the findings from EDS analyses. Independent of

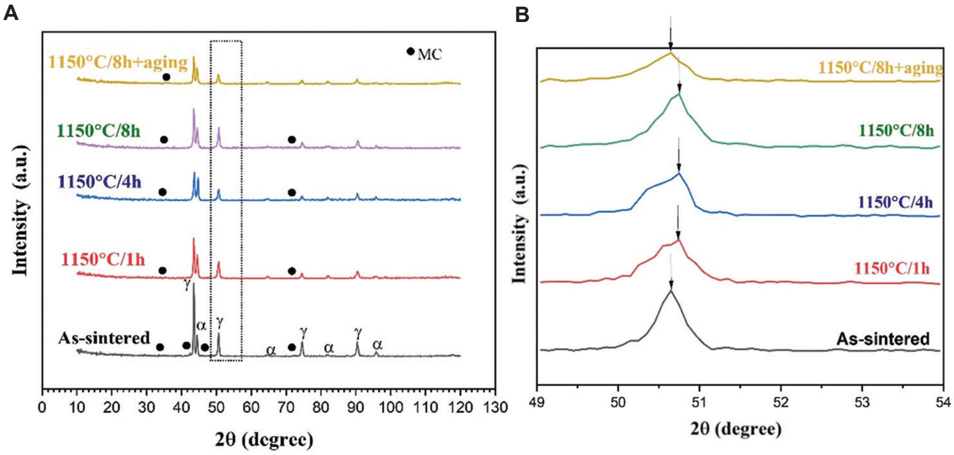

Figure 9. The X-ray diffraction (XRD) patterns of 17-4PH/IN625 bimetallic samples under different heat treatment conditions: (A) Overall XRD patterns; (B) The XRD peak shift at specific location. (A) The XRD patterns and (B) the XRD peak shift at the specific locations of 17-4PH/IN625 bimetallic samples under different treatment conditions.

whether they underwent heat treatment, the reaction layers predominantly consist of oxides and precipitates exhibiting a high concentration of Nb and Mo elements. In addition to the Ni matrix, peaks indicative of MC carbides were also identified.[49] Similarly, MC carbides were found in IN625 treated under 1150°C.[50] The heat treatment process appears to diminish the presence of carbides, as evidenced by Figure 4, showing a reduction in both the size and quantity of carbides. Simultaneously, as the duration increases, the peak position shifts due to stress relaxation and precipitate formation,[35] as depicted in Figure 9B. As IN625 alloy and 17-4PH possess different coefficients of thermal expansion, the stress level escalates with prolonged time. Previous literature has reported similar observations regarding the behavior of IN625 under various heat treatment conditions, especially when compared to stress-free powder materials.[50]

3.4. Effects of heat treatment on microhardness

The impact of heat treatment on the microhardness of 17-4PH/IN625 bimetallic parts was determined through microhardness testing. Figure 10 presents the microhardness distributions along the bimetallic interfaces under both as-sintered and heat-treated states.

The microhardness of the bimetal improves uniformly across all areas, including both the 17-4PH side and the IN625 side, as well as the interface, after undergoing heat treatment. In the case of 17-4PH steel, there is an initial increase in hardness, peaking at 367 $\mathrm{HV}_{1.0}$, followed by a subsequent decline. This observation aligns with other studies wherein a peak hardness value of approximately 360 $\mathrm{HV}_{1.0}$ was noted following solution heat treatment.[34] The enhancement in hardness can be attributed to the reduction in porosity and the diminution of pore size. However, over time, an enlargement in grain size is discernible, as indicated in Figure 3, adversely affecting hardness. The predominant phases in 17-4PH consist of ferrite and martensite. Slower cooling rates or extended heating periods facilitate the migration of carbon and other alloying elements, leading to a reversal from martensite to ferrite. An increase in the proportion of ferrite, at the expense of martensite, typically results in a diminished hardness, given the inherent softness of ferrite compared to martensite.[51] A comparable trend was observed in the microhardness of 17-4PH manufactured through PBF as time progressed, manifesting a decrease. This trend is attributed to the presence of samples consisting of fine lath martensite lacking distinct preferred orientations, coupled with the elimination of delta-ferrite following homogenization.[34] Meanwhile, through aging followed by homogenization, fine particles (precipitates) form and impede dislocation movement, thereby augmenting hardness compared to the material devoid of aging, as illustrated in Figure 10. For IN625, the microhardness initially experiences a marginal increase from 208 $\mathrm{HV}_{1.0}$ to 209 $\mathrm{HV}_{1.0}$, before subsequently decreasing to 205 $\mathrm{HV}_{1.0}$. The strengthening of IN625 alloy mainly ensues through solid solution hardening facilitated by Cr, Mo, and Nb.[49] However, during heat treatment, the segregation of these elements within the transition zone forms precipitates, thereby reducing the strengthening effect in IN625. In alternative bimetallic structures consisting of IN625 and Ti6Al4V, the absence of Cr- and Mo-enriched phases within the Ni matrix on the IN625 side culminates in a reduced hardness gradient.[52] With prolonged holding time, the enlargement of

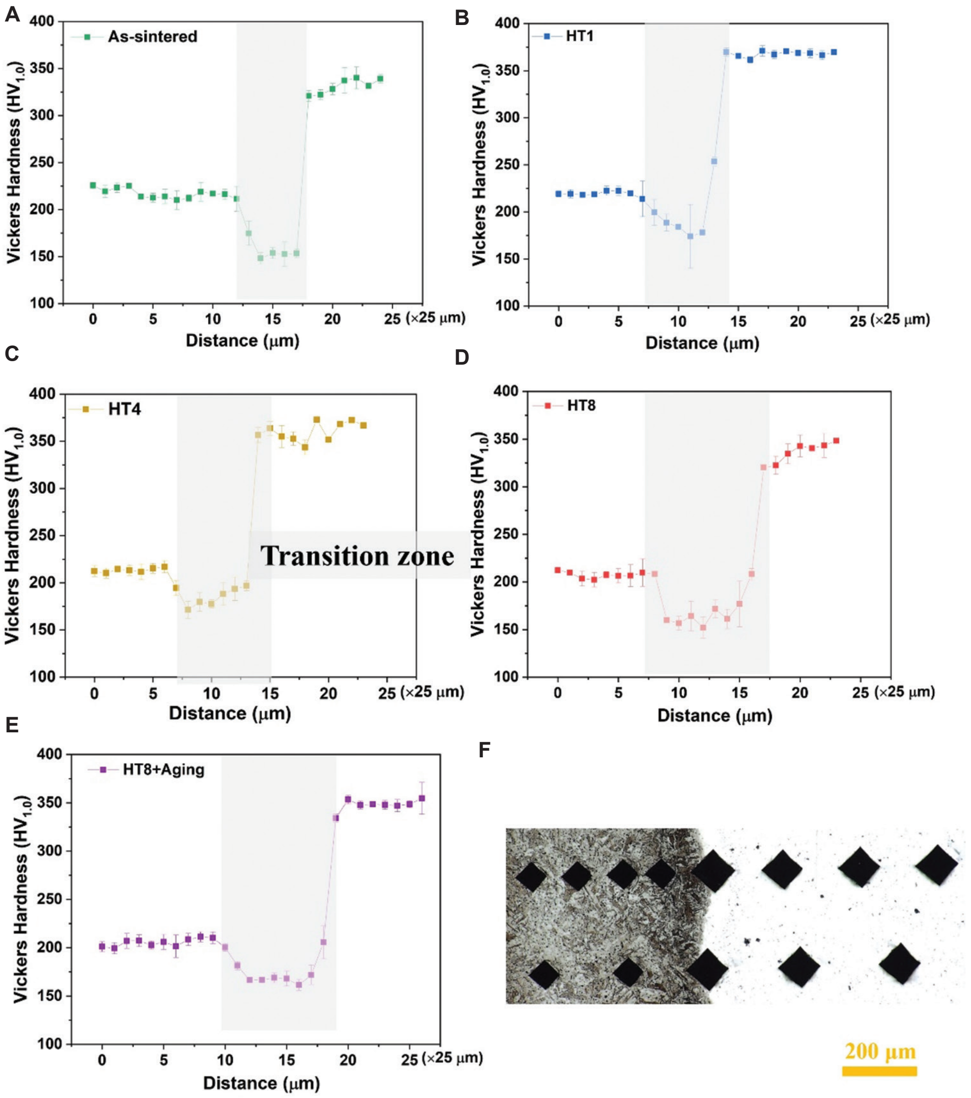

Figure 10. Microhardness profiles across bimetal interfaces. (A) As-sintered and heat-treated at 1150°C for (B) 1 h, (C) 4 h, (D) 8 h, and (E) 8 h + aging. (F) Optical microscopic image showing indentations. Scale bar: 200 µm; magnification: ×264.

Table 5. Thickness of the diffusion zone across various treatment conditions

Diffusion zone (µm)	As-sintered	HT1	HT4	HT8	HT8+aging
EDS line scan analysis (µm)	75	105	160	220	200
Results derived from Equation I	-	a	2 a	2.8 a	2.8 a
Microhardness measurements (µm)	100	150	188	250	250

Abbreviation: EDS: Energy-dispersive X-ray spectroscopy.

grain size and the reduction in the spread of elongated precipitates on the IN625 side (Figure 5) lead to reduced microhardness.

The microhardness distributions, regardless of whether in the as-sintered or heat-treated state, exhibit a consistent pattern, wherein the microhardness of the reaction layers is markedly lower than that of the matrices, particularly evident in the steel matrix, as depicted in Figure 10. The indentations on the interface appear larger compared to those in Inconel alloy and SS, as depicted in Figure 10F. This significant decrease in microhardness within the diffusion zone is attributed to the presence of pores and the absence of secondary phases.

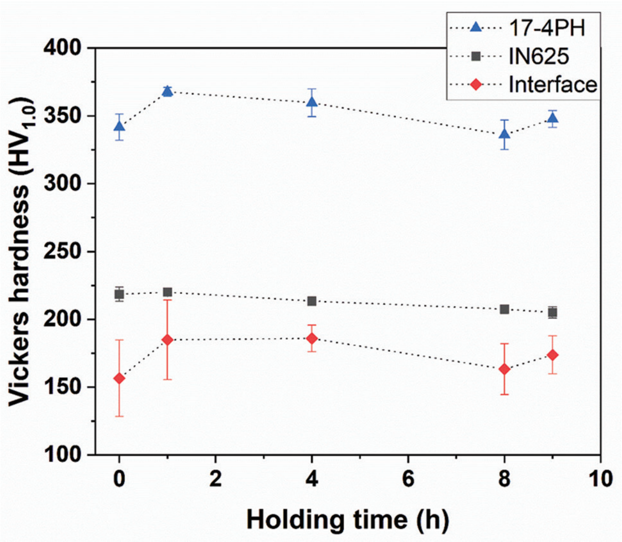

Figure 11. Microhardness changes along the bimetallic interfaces under various conditions.

With an increase in holding time, the microhardness of the transition zone initially rises, and then decreases after 4 h, as shown in Figure 11. Heat treatment for 4 h yields the highest microhardness value, approximately 186 $HV_{1.0}$, compared to the lowest value of 156 $HV_{1.0}$ observed in samples without heat treatment. This observed increase represents a nearly 20% post-treatment enhancement, closely aligning with the microhardness on the IN625 side. With the increase in time, the size of pores reduces, and the occurrence of pores decreases. During heat treatment, oxides and carbides form in the transition zone, creating an intermetallic compound that is both hard and brittle. Excessively long dwell times typically result in larger grain sizes, which are detrimental to the hardness of the interface. Notably, microhardness measurements also allow us to determine the thickness of the transition zone in Figure 10A-D. These values are consistent with results calculated using Equation I and EDS scan line analysis results from Table 5.

4. Conclusion

This study investigated the effects of various heat treatment approaches on the microstructure and mechanical properties of 17-4PH/IN625 bimetallic components fabricated through the ES-AM process. The key findings are summarized below.

(i) The 17-4PH/IN625 bimetallic composite exhibited excellent interfacial bonding after heat treatment, with few pores at the interface and uniform elemental distribution without delamination. The diffusion zone could be separated into two regions: an Fe-rich zone and a Ni-rich zone (containing oxides and Mo-, Nb-rich precipitates). Significant Nb segregation was observed in the transition zone.

(ii) With extended dwell time, overall porosity decreased. Simultaneously, carbides, an intermetallic compound (a hard and brittle phase), exhibited a more uniform and finer distribution after 4 h of heat treatment.

(iii) The thickness of the transition zone increased with prolonged dwell times, resulting in enhanced bonding strength for the bimetallic components. Empirical data on microhardness and the theoretical parabolic diffusion law provided supporting evidence for the observed phenomenon.

(iv) No new phases were detected after heat treatment; however, XRD peak shifts occurred due to stress relaxation and precipitate formation.

(v) The microhardness of the transition zone increased with heat treatment, reaching a maximum of 186 $HV_{1.0}$ after a 4-h holding time. The optimized heat treatment condition was determined to be 1150°C for 4 h to attain uniform microstructures and high bonding strength.

Future studies could involve complementary computational efforts involving modeling and simulations to acquire insights into the mechanisms facilitating interfacial bonding. Particular attention should be paid to elucidating the role of elemental segregation and diffusion phenomena.

Acknowledgments

The authors extend their sincere gratitude to the anonymous reviewers for their valuable comments and suggestions, which have greatly contributed to the improvement of this paper. This work was funded by the United States National Science Foundation through the award CMMI-2224309.

Funding

This work was funded by the United States National Science Foundation through the award CMMI-2224309.

Conflict of interest

The authors declare that they have no competing interests.

Author contributions

Conceptualization: Yulin Liu and Fuda Ning
Formal analysis: Yulin Liu and Dayue Jiang
Investigation: Yulin Liu
Methodology: Yulin Liu and Dayue Jiang
Writing – original draft: Yulin Liu
Writing – review & editing: All authors
All authors have read and agreed to the published version of the manuscript.

Ethics approval and consent to participate

Not applicable.

Consent for publication

Not applicable.

Availability of data

Data are available from the corresponding author on reasonable request.

References

1. Bandyopadhyay A, Zhang Y, Onuike B. Additive manufacturing of bimetallic structures. *Virtual Phys Prototyp.* 2022;17(2):256-294.

   doi: 10.1080/17452759.2022.2040738

2. Zhang B, Zhang W, Xiao H, Yang H, Wang Y, Chen B. QCr0. 8 Cu alloy/S06 stainless steel bimetal structure via In718 multi-interlayer fabricated by laser powder hybrid additive manufacturing. *J Mater Res Technol.* 2023;24:1034-1042.

   doi: 10.1016/j.jmrt.2023.03.073

3. Jiménez A, Bidare P, Hassanin H, Tarlochan F, Dimov S, Essa K. Powder-based laser hybrid additive manufacturing of metals: A review. *Int J Adv Manuf Technol.* 2021;114:63-96.

   doi: 10.1007/s00170-021-06855-4

4. Sahasrabudhe H, Harrison R, Carpenter C, Bandyopadhyay A. Stainless steel to titanium bimetallic structure using LENS^{TM}. *Addit Manuf.* 2015;5:1-8.

   doi: 10.1016/j.addma.2014.10.002

5. Wu H, Xie X, Liu S, *et al.* Bonding behavior of Bi-metal-deposits produced by hybrid cold spray additive manufacturing. *J Mater Process Technol.* 2022;299:117375.

   doi: 10.1016/j.jmatprotec.2021.117375

6. Jiang D, Ning F. Physical-mechanical behaviors of stainless steel plate-lattice built by material extrusion additive manufacturing. *J Mater Process Technol.* 2022;309:117739.

   doi: 10.1016/j.jmatprotec.2022.117739

7. Jiang D, Ning F. Reprint of: Bi-metal structures fabricated by extrusion-based sintering-assisted additive manufacturing. *J Manuf Process.* 2023;100:20-26.

   doi: 10.1016/j.jmapro.2023.05.101

8. Zhang Y, Bandyopadhyay A. Influence of compositionally graded interface on microstructure and compressive deformation of 316L stainless steel to Al12Si aluminum alloy bimetallic structures. *ACS Appl Mater Interfaces.* 2021;13(7):9174-9185.

   doi: 10.1021/acsami.0c21478

9. Wei C, Liu L, Gu Y, *et al.* Multi-material additive-manufacturing of tungsten-copper alloy bimetallic structure with a stainless-steel interlayer and associated bonding mechanisms. *Addit Manuf.* 2022;50:102574.

   doi: 10.1016/j.addma.2021.102574

10. Ergene B, Yalçın B. Investigation on mechanical performances of various cellular structures produced with fused deposition modeling (FDM). *J Fac Eng Archit Gazi Univ.* 2023;38:201-207.

    doi: 10.17341/gazimmfd.945650

11. Mousapour M, Salmi M, Klemettinen L, Partanen J. Feasibility study of producing multi-metal parts by Fused Filament Fabrication (FFF) technique. *J Manuf Process.* 2021;67:438-446.

    doi: 10.1016/j.jmapro.2021.05.021

12. Seleznev M, Roy-Mayhew JD. Bi-metal composite material for plastic injection molding tooling applications via fused filament fabrication process. *Addit Manuf.* 2021;48:102375.

    doi:10.1016/j.addma.2021.102375

13. Sun Y, Hebert RJ, Aindow M. Effect of heat treatments on microstructural evolution of additively manufactured and wrought 17-4PH stainless steel. *Mater Des.* 2018;156:429-440.

    doi: 10.1016/j.matdes.2018.07.015

14. Karmuhilan M, Kumanan S. A review on additive manufacturing processes of inconel 625. *J Mater Eng Perform.* 2021;31:2583-2592.

    doi: 10.1007/s11665-021-06427-3

15. Jagtap BM, Kakandikar GM, Jawade SA. Mechanical behavior of inconel 625 and 17-4 PH stainless steel processed by atomic diffusion additive manufacturing. In: Dave HK, Dixit US, Nedelcu D, editors. *Recent Advances in Manufacturing Processes and Systems.* Berlin: Springer Nature Singapore; 2022. p. 583-594.

    doi: 10.1007/978-981-16-7787-8

16. Mattli MR, Khan A, Matli PR, *et al.* Effect of Inconel625 particles on the microstructural, mechanical, and thermal properties of Al-Inconel625 composites. *Mater Today Commun.* 2020;25:101564.

    doi: 10.1016/j.mtcomm.2020.101564

17. Dash A, Bandyopadhyay A. 17-4 PH and SS316L bimetallic structures via additive manufacturing. *Virtual Phys Prototyp.* 2024;19(1):e2292695.

    doi: 10.1080/17452759.2023.2292695

18. Du Plessis A, Razavi N, Benedetti M, *et al.* Properties and applications of additively manufactured metallic cellular materials: A review. *Prog Mater Sci.* 2022;125:100918.

    doi: 10.1016/j.pmatsci.2021.100918

19. Li G, Jiang W, Guan F, Zhu J, Yu Y, Fan Z. Effect of different Ni interlayers on interfacial microstructure and bonding properties of Al/Mg bimetal using a novel compound casting. *J Manuf Process.* 2020;50:614-628.

    doi: 10.1016/j.jmapro.2020.01.017

20. Wu B, Qiu Z, Pan Z, *et al.* Enhanced interface strength in

steel-nickel bimetallic component fabricated using wire arc additive manufacturing with interweaving deposition strategy. *J Mater Sci Technol*. 2020;52:226-234.

doi: 10.1016/j.jmst.2020.04.019

21. Li P, Gong Y, Xu Y, Qi Y, Sun Y, Zhang H. Inconel-steel functionally bimetal materials by hybrid directed energy deposition and thermal milling: Microstructure and mechanical properties. *Arch Civ Mech Eng*. 2019;19:820-831.

    doi: 10.1016/j.acme.2019.03.002

22. Dang X, Li Y, Chen K, Luo S, Liang X, He W. Insight into the interfacial architecture of a hybrid additively-manufactured stainless steel/Ni-based superalloy bimetal. *Mater Des*. 2022;216:110595.

    doi: 10.1016/j.matdes.2022.110595

23. Chen N, Khan HA, Wan Z, *et al*. Microstructural characteristics and crack formation in additively manufactured bimetal material of 316L stainless steel and Inconel 625. *Addit Manuf*. 2020;32:101037.

    doi: 10.1016/j.addma.2020.101037

24. Fan H, Shi Q, Wang C, Tian Y, Zhou K, Yang S. Laser powder bed fusion of bimetallic stainless steel/Nickel-based superalloy: Interface and mechanical properties. *Mater Sci Eng A*. 2023;877:145193.

    doi: 10.1016/j.msea.2023.145193

25. Ferro P, Fabrizi A, Elsayed H, Berto F, Savio G. Creating IN718-high carbon steel Bi-metallic parts by fused deposition modeling and sintering. *Procedia Struct Integr*. 2023;47:535-544.

    doi: 10.1016/j.prostr.2023.07.071

26. Ahsan MR, Fan X, Seo GJ, *et al*. Microstructures and mechanical behavior of the bimetallic additively-manufactured structure (BAMS) of austenitic stainless steel and Inconel 625. *J Mater Sci Technol*. 2021;74:176-188.

    doi: 10.1016/j.jmst.2020.10.001

27. Kosturek R, Wachowski M, Śnieżek L, Gloc M. The influence of the post-weld heat treatment on the microstructure of inconel 625/carbon steel bimetal joint obtained by explosive welding. *Metals*. 2019;9(2):246.

    doi: 10.3390/met9020246

28. Gope DK, Chattopadhyaya S. Dissimilar welding of nickel based superalloy with stainless steel: Influence of post weld heat treatment. *Mater Manuf Process*. 2022;37(2):136-142.

    doi: 10.1080/10426914.2021.1945095

29. Liu J, Miao Y, Wang Z, Zhao Y, Wu Y, Li C. Effect of heat treatment on microstructure and properties of additively manufactured aluminum bronze-steel bimetallic structures. *Mater Charact*. 2024;207:113462.

    doi: 10.1016/j.matchar.2023.113462

30. Miriyev A, Levy A, Kalabukhov S, Frage N. Interface evolution and shear strength of Al/Ti bi-metals processed by a spark plasma sintering (SPS) apparatus. *J Alloys Compd*. 2016;678:329-336.

    doi: 10.1016/j.jallcom.2016.03.137

31. Wang Y, Song R, Yanagimoto J, Li H. Effect of heat treatment on bonding mechanism and mechanical properties of high strength Cu/Al/Cu clad composite. *J Alloys Compd*. 2019;801:573-580.

    doi: 10.1016/j.jallcom.2019.06.132

32. Li Z, Zhao J, Jia F, *et al*. Interfacial characteristics and mechanical properties of duplex stainless steel bimetal composite by heat treatment. *Mater Sci Eng A*. 2020;787:139513.

    doi: 10.1016/j.msea.2020.139513

33. Ahsan MR, Tanvir ANM, Seo GJ, *et al*. Heat-treatment effects on a bimetallic additively-manufactured structure (BAMS) of the low-carbon steel and austenitic-stainless steel. *Addit Manuf*. 2020;32:101036.

    doi: 10.1016/j.addma.2020.101036

34. Li K, Zhan J, Yang T, *et al*. Homogenization timing effect on microstructure and precipitation strengthening of 17-4PH stainless steel fabricated by laser powder bed fusion. *Addit Manuf*. 2022;52:102672.

    doi: 10.1016/j.addma.2022.102672

35. Parizia S, Marchese G, Rashidi M, *et al*. Effect of heat treatment on microstructure and oxidation properties of Inconel 625 processed by LPBF. *J Alloys Compd*. 2020;846:156418.

    doi: 10.1016/j.jallcom.2020.156418

36. Zhang Q, Liang S, Zou J, Yang Q. Interfacial microstructure of CuCr/1Cr18Ni9Ti bi-metal materials and its effect on bonding strength. *Sci China Technol Sci*. 2015;58(5):825-831.

    doi: 10.1007/s11431-015-5791-6

37. Lashgari H, Adabifiroozjaei E, Kong C, Molina-Luna L, Li S. Heat treatment response of additively manufactured 17-4PH stainless steel. *Mater Charact*. 2023;197:112661.

    doi: 10.1016/j.matchar.2023.112661

38. Gonzalez J, Mireles J, Stafford S, Perez M, Terrazas C, Wicker R. Characterization of Inconel 625 fabricated using powder-bed-based additive manufacturing technologies. *J Mater Process Technol*. 2019;264:200-210.

    doi: 10.1016/j.jmatprotec.2018.08.031

39. Jiang D, Ning F. Bi-metal structures fabricated by extrusion-based sintering-assisted additive manufacturing. *J Manuf Process*. 2023;98:216-222.

    doi: 10.1016/j.jmapro.2023.05.025

40. Kumar N, Pandey C, Kumar P. Dissimilar welding of inconel

alloys with austenitic stainless-steel: A review. *J Press Vessel Technol*. 2023;145(1):011506.

doi: 10.1115/1.4055329

41. Bina MH, Dehghani F, Salimi M. Effect of heat treatment on bonding interface in explosive welded copper/stainless steel. *Mater Des*. 2013;45:504-509.

    doi: 10.1016/j.matdes.2012.09.037

42. Liu X, Fan J, Zhang P, *et al*. Influence of heat treatment on Inconel 625 superalloy sheet: Carbides, γ", *δ* phase precipitation and tensile deformation behavior. *J Alloys Compd*. 2023;930:167522.

    doi: 10.1016/j.jallcom.2022.167522

43. Jiang W, Li G, Wu Y, Liu X, Fan Z. Effect of heat treatment on bonding strength of aluminum/steel bimetal produced by a compound casting. *J Mater Process Technol*. 2018;258:239-250.

    doi: 10.1016/j.jmatprotec.2018.04.006

44. Marchese G, Lorusso M, Parizia S, *et al*. Influence of heat treatments on microstructure evolution and mechanical properties of Inconel 625 processed by laser powder bed fusion. *Mater Sci Eng A*. 2018;729:64-75.

    doi: 10.1016/j.msea.2018.05.044

45. Floreen S, Fuchs GE, Yang WJ. The metallurgy of alloy 625. *Superalloys*. 1994;718(625):13-37.

46. Hu Y, Lin X, Li Y, *et al*. Influence of heat treatments on the microstructure and mechanical properties of Inconel 625 fabricated by directed energy deposition. *Mater Sci Eng A*. 2021;817:141309.

    doi: 10.1016/j.msea.2021.141309

47. Sabooni S, Chabok A, Feng SC, *et al*. Laser powder bed fusion of 17–4 PH stainless steel: A comparative study on the effect of heat treatment on the microstructure evolution and mechanical properties. *Addit Manuf*. 2021;46:102176.

    doi: 10.1016/j.addma.2021.102176

48. Wen Y, Gao J, Narayan RL, *et al*. Microstructure-property correlations in as-built and heat-treated compositionally graded stainless steel 316L-Inconel 718 alloy fabricated by laser powder bed fusion. *Mater Sci Eng A*. 2023;862:144515.

    doi: 10.1016/j.msea.2022.144515

49. Carrozza A, Lorenzi S, Carugo F, *et al*. A comparative analysis between material extrusion and other additive manufacturing techniques: Defects, microstructure and corrosion behavior in nickel alloy 625. *Mater Des*. 2023;225:111545.

    doi: 10.1016/j.matdes.2022.111545

50. Li C, White R, Fang XY, Weaver M, Guo YB. Microstructure evolution characteristics of Inconel 625 alloy from selective laser melting to heat treatment. *Mater Sci Eng A*. 2017;705:20-31.

    doi: 10.1016/j.msea.2017.08.058

51. An S, Eo DR, Sohn I, Choi K. Homogenization on solution treatment and its effects on the precipitation-hardening of selective laser melted 17-4PH stainless steel. *J Mater Sci Technol*. 2023;166:47-57.

    doi: 10.1016/j.jmst.2023.04.055

52. Vinod A, Warghane S, Murugan A, Balashanmugam N, Venkaiah N. Microstructure and interfacial characteristics of inconel 625-Ti6Al4V bimetallic structures produced by directed energy deposition. *J Mater Eng Perform*. 2023;33:1-12.

    doi: 10.1007/s11665-023-08250-4

ACCSCIENCE PUBLISHING

Materials Science in Additive Manufacturing

ORIGINAL RESEARCH ARTICLE

Effects of aging heat treatment on the mechanical properties of NiTi triply periodic minimal surface

Jinwei Li[1], Mingkang Zhang[1]*, Jie Chen[2], Chang Liu[1], Wenbin Liu[1], and Mingjian Deng[1]

[1]Additive Manufacturing Laboratory, School of Mechanical and Energy Engineering, Guangdong Ocean University, Yangjiang, Guangdong, China

[2]Institute of Intelligent Manufacturing, Guangdong Academy of Sciences, Guangzhou, Guangdong, China

(This article belongs to the *Special Issue: In-situ strengthening in metal additive manufacturing*)

***Corresponding author:**
Mingkang Zhang
(zhangmk@gdou.edu.cn)

Citation: Li J, Zhang M, Chen J, Liu C, Liu W, Deng M. Effects of aging heat treatment on the mechanical properties of NiTi triply periodic minimal surface. *Mater Sci Add Manuf*. 2024;3(2):3137. doi: 10.36922/msam.3137

Received: March 11, 2024

Accepted: April 22, 2024

Abstract

This study investigated the impact of aging heat treatment time on the mechanical properties of NiTi triply periodic minimal surface structures fabricated through laser powder bed fusion. X-ray diffraction analysis results indicate that with increasing aging time, the $NiTi_2$ phase precipitates while the content of the B19′ phase decreases. At 10 h of aging time, the Ni_4Ti_3 phase becomes evident in the sample. The differential scanning calorimeter results show that R phase transformation occurs, and the phase transformation temperature increases when the aging time reaches 6 h. Microhardness increases with aging time, peaking at 477.8 HV after 10 h. Compression experiment results reveal a maximum elastic modulus of 1262.82 MPa for the gyroid sheet-shaped structure achieved after 2 h. In addition, the superelasticity test indicates the highest recoverable strains at 2%, 4%, and 6% compressive strain for the gyroid rod-shaped structure after aging for 10 h. In cyclic compression experiments, the ratio of shape memory recovery increases from 40% at 0 h to 97% at 6 h. Fracture analysis results show that the transition in the fracture mechanism from brittle fracture to quasi-cleavage fracture occurs after aging heat treatment.

Keywords: NiTi alloy; Laser powder bed fusion; Aging heat treatment; Triply periodic minimal surface; Shape memory effect

1. Introduction

Shape memory alloys (SMAs) constitute a family of metallic materials capable of reverting to their original shape on heating after deformation by external forces.[1] SMAs include Cu-based, NiTi-based, and Fe-based variants.[2] Among these variants, NiTi-based SMAs exhibit excellent shape memory properties, characterized by high shape recovery ratios, hyperelastic strain capacities, excellent corrosion resistance, biocompatibility, and superior damping properties.[3] Compared with traditional NiTi alloy components, NiTi alloy porous structures, such as minimal surface structure and lattice structure,[4-8] offer distinct advantages, including lightweight construction, low density, large specific area, and high specific strength.[9] These attributes render them applicable across diverse domains such as biomedicine, aerospace, automotive engineering, shock absorption systems, and propulsion devices, capitalizing on the characteristics of NiTi alloy.[10] For example, porous biomaterials enable adjustments of elastic modulus, while the biocompatibility of NiTi alloy enhances implant integration with host bone tissue and improves bone tissue regeneration. In addition, the porous structure increases surface area, facilitating the functionalization of biomaterials.[11,12] Due to their lightweight nature, extensive contact area, and excellent transmission characteristics, minimal surface structures offer great advantages in aerospace thermal management technologies.[13,14]

The triply periodic minimal surface (TPMS) structure represents a form of porous architecture characterized by smooth surfaces devoid of sharp edges, thus mitigating stress concentration. Fundamental properties of TPMS, such as the type, size, and porosity of monomer cells, are controllable through adjustment of functional parameters, with significant implications for mechanical properties. Stress in the NiTi sheet gyroid structure primarily localizes at the joint of inclined surfaces under compressive loading. As the volume fraction increases, mechanical properties such as compression modulus and ultimate yield strength improve.[15] Research by Shi *et al.*[16] highlights that gyroid, diamond, and I-graph-wrapped package (IWP) structures are prone to shear failure, coupled with flexural and torsional coupling deformation. Primitive deformation predominantly involves stretching, manifesting in layer-by-layer collapse. Gyroid and IWP structures exhibit heightened energy absorption among the four TPMS lattices. Axial loading results in a notable increase in effective stress and martensite volume fraction with rising relative density of TPMS cells, with the diamond structure exhibiting superior mechanical properties.[17] In cyclic compression experiments, the residual strain of the gyroid structure escalates with the number of cycles. A rise in maximum strain from 4% to 8% corresponds to an increase in residual strain from 1% to 4%, indicative of favorable superelasticity.[18] Jin *et al.*[19] similarly affirm the superior superelastic properties of Ni-Ti gyroid TPMS lattice structure. In addition, the gyroid structures exhibit superior static mechanical properties and fatigue resistance compared to traditional octahedral minimum trabecular lattice structures at equivalent volume fractions.[20] In addition to mechanical research, TPMS structures find applications in sound absorption,[21-23] heat dissipation,[24,25] catalysis,[26,27] and other fields. However, traditional machining methods encounter challenges in forming TPMS structures due to the high work hardening and strength characteristics of NiTi SMA,[28,29] resulting in poor processing ability.

Laser powder bed fusion (LPBF) technology offers a viable approach for manufacturing metallic porous structures. LPBF uses laser spots to selectively melt metal powder on a powder bed to form metal parts with complex shapes.[30] However, the LPBF process applied to NiTi SMA can result in residual thermal stress and the formation of Ni-rich precipitates in the sample, due to the high thermal cycling, substantial thermal gradient, and rapid cooling rate involved.[31] Heat treatment serves as a means to alleviate residual stress, dissolve precipitates, adjust Ni content, control precipitate existence and distribution, and consequently affect microstructure, phase transformation characteristics, and mechanical properties.[32] Given the apparent over-solid solubility of the B2 phase relative to Ni, Ni-rich NiTi alloy lends itself to solid solution heat treatment to dissolve the second phase, resulting in uniform microstructure, high plasticity, elimination of residual stress, and reduction of dislocation density.[33] However, the solution temperature generally tends to be relatively high, which can promote grain growth.[34] Subsequent aging heat treatment is often necessary after the solution heat treatment. Aging heat treatment facilitates the precipitation of the Ni_4Ti_3 phase with uniform size and dispersed distribution, thereby altering phase transformation behavior and enabling controlled adjustments of mechanical properties, shape memory effect (SME), and superelasticity.[35]

The mechanical properties of NiTi alloy are influenced by varying aging temperatures and durations. For example, the residual strain in samples aged at 350°C was significantly lower compared to those aged at 450°C. This disparity arises from a slight increase in dislocation formation during the loading process in samples aged at 350°C, resulting in a significantly lower content of retained stable martensite.[36] After aging heat treatment at 600°C, the tensile strength of NiTi alloy could reach 729 MPa, with a strain recovery ratio of 92.85%. This enhancement is attributed to the gradual formation of Ni_4Ti_3 and $NiTi_2$ precipitates, which affects the adjustments of properties and microstructure.[37] As the aging temperature increases to 700°C, particle aggregation, dislocation formation, and strain-induced boundary migration occur.[38] Yan *et al.*[39] concluded that aging at 750°C for 5 h could improve the mechanical strength of NiTi alloy, with the effect of aging temperature on the hardness of NiTi alloy surpassing that of aging time. These studies underscore the significant impact of aging temperature on microstructure characteristics and thermal properties such as phase transformation process, temperature, and rate. Moreover, increasing aging time leads to uneven precipitation of Ni-rich intermetallic compounds such as Ni_4Ti_3 and Ni_3Ti from the matrix.[40] In addition, the type, volume fraction, size, and distribution of precipitated phases within the matrix after LPBF can affect phase transformation behavior and mechanical properties, thus complicating the effect of aging on the mechanical properties of NiTi alloy.

In this study, sheet-shaped gyroid cellular structure (SGCS) and rod-shaped gyroid cellular structure (RGCS) were designed and manufactured using LPBF with NiTi alloy powder. Subsequently, the effects of aging heat treatments on the microstructure and phase transformation behavior of NiTi cellular structures were investigated through metallographic microscopy and X-ray diffraction (XRD) analyses. Furthermore, the influence of aging heat treatments on the mechanical properties, superelasticity, and SME of NiTi cellular structures was analyzed using an electronic universal testing machine and digital image correlation (DIC) technique. Finally, the fracture mechanism of NiTi cellular structures was elucidated through detailed examination employing scanning electron microscopy (SEM).

2. Materials and methods

2.1. Design of gyroid surface structure

All models in this study were designed using MATLAB software (MathWorks Inc, America), employing the implicit function of the gyroid structure expressed in Equation I:

$$F_{Gyroid} = \sin(2\pi x/a)\cos(2\pi y/a) + \sin(2\pi y/a)\cos(2\pi z/a) + \sin(2\pi z/a)\cos(2\pi x/a) - t(x,y,z) \quad \text{(I)}$$

where a denotes the size of the cell body in millimeters (mm), and $t(x,y,z)$ represents the relative density variation parameter controlling the structure of minimal surfaces. Utilizing this function, samples of SGCS and RGCS with a volume fraction of 15% were designed. The dimensions of the cell body were set at 3 mm × 3 mm × 3 mm, and the overall size of the structure was 15 mm × 15 mm × 15 mm, as illustrated in Figure 1A. For SGCS, the surface thickness was set as 0.15 mm, while the minimum rod diameter for RGCS was set as 0.64 mm.

2.2. Manufacturing

The RGCS and SGCS samples were printed using the Dimetal-100H laser selective melting manufacturing equipment (Guangzhou Laseradd Additive Technology Co., LTD., China). The powder employed was $Ni_{50.67}Ti_{49.33}$ (Shenzhen MINATECH CO., LTD., China), with a particle size distribution range of 15 – 53 μm (D_{10}=17.8 μm, D_{50}=33.6 μm, D_{90}=55.8 μm). Given the known benefits of laser remelting in effectively increasing sample density, refining surface roughness, reducing defects, and optimizing microstructure through multiple laser scans applied to each layer of slices,[41,42] the remelting process was deemed suitable for this study. The pertinent forming process parameters are detailed in Table 1. Subsequently, based on these process parameters, the RGCS and SGCS were prepared using LPBF technology, as illustrated in Figure 1B.

2.3. Aging heat treatment

Before aging heat treatment, the manufactured samples underwent solution heat treatment. They were placed into quartz tubes and sealed with argon of 99.9% purity, then kept in a furnace at 1000°C for 2 h, followed by water quenching. Different aging times were designed, as outlined in Table 2. The heating rate for both heat treatments was set at 10°C/min. The designation "A0" denoted no heat treatment, while samples subjected to 2 h of aging heat treatment were labeled by SGCS-A2 and RGCS-A2.

2.4. Characterization of microstructure

The aged samples were cold-set and coarsely ground using sandpaper ranging from 120 grit to 2000 grit. Subsequently, mechanical polishing was conducted using a 50 nm diamond abrasive paste. The polished surface was then etched using an etching solution (HF: HNO_3:H_2O in a volume ratio of 1:2:5) for 120 s. The samples were then thoroughly washed with water and alcohol. The phase structure was observed using a metallographic microscope, and photographic documentation was performed. Analysis of the crystalline phases presented in the samples before and after the aging process was conducted using XRD patterns with Cu-Kα radiation, with a scanning angle ranging 20 – 90° and a scanning speed of 10°/min.

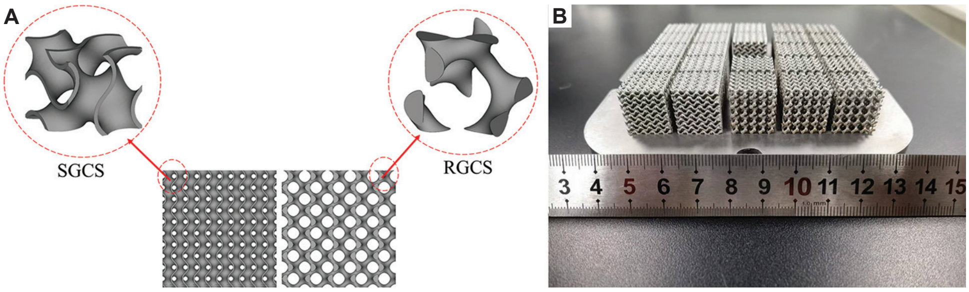

Figure 1. NiTi alloy porous structures. (A) Illustrations of sheet-shaped gyroid cellular structure (SGCS) and rod-shaped gyroid cellular structure (RGCS) structures, and (B) the structures fabricated through laser powder bed fusion.

Table 1. The processing parameter for laser powder bed fusion

Parameters	Value
Laser power (W)	240
Laser speed (mm/s)	600
Hatch spacing (mm)	0.1
Layer thickness (mm)	0.03
Remelting power (W)	60
Remelting speed (mm/s)	200

Table 2. Process parameters of aging heat treatment

Sample no.	Shape	Temperature (°C)	Aging time (h)	Cooling method
RGCS-A0	Rod-shape	-	-	-
RGCS-A2	Rod-shape	400	2	Air cooling
RGCS-A4	Rod-shape	400	4	Air cooling
RGCS-A6	Rod-shape	400	6	Air cooling
RGCS-A8	Rod-shape	400	8	Air cooling
RGCS-A10	Rod-shape	400	10	Air cooling
SGCS-A0	Sheet-shape	-	-	-
SGCS-A2	Sheet-shape	400	2	Air cooling
SGCS-A4	Sheet-shape	400	4	Air cooling
SGCS-A6	Sheet-shape	400	6	Air cooling
SGCS-A8	Sheet-shape	400	8	Air cooling
SGCS-A10	Sheet-shape	400	10	Air cooling

Abbreviations: RGCS: Rod-shaped gyroid cellular structure; SGCS: Sheet-shaped gyroid cellular structure.

Furthermore, the phase transformation temperatures of the aged sample were measured using a differential scanning calorimeter (DSC) operating with a heating and cooling rate of 10°C/min in a helium atmosphere within a temperature range of 0 – 80°C.

2.5. Mechanical properties and functional properties test

Compression test was conducted using a CMT5105 testing machine (SUST Co., Ltd., China) at room temperature. The superelasticity test was conducted in an electronic universal testing machine equipped with a high-temperature test chamber (CMT5105GD, SUST Co., Ltd., China). The temperature was raised above the end temperature of reverse martensitic transformation, and the recoverable strain and unrecoverable strain were determined based on the stress-strain curve obtained from loading the sample from 0% to 8% strain with a 2% strain increment. The SME test involved loading the sample to a 6% strain at room temperature and unloading it for 15 cycles. After the cycles, the sample was heated in a water bath at 100°C for 3 min. The ratio of height changes before and after heating to the original height was measured, and the shape memory recovery ratio (η) was calculated using Equation II. The loading and unloading speeds were both set at 0.5 mm/min.

$$\eta = (h_3 - h_2)/(h_2 - h_1) \times 100\% \quad \text{(II)}$$

where h_1 is the height of the sample before testing, h_2 is the height of the sample after the end of the cycle, and h_3 is the height of the sample after heating, all in mm.

Microhardness of the aged samples was measured using a Vickers microhardness tester (HV-1000, CVOK Co., Ltd., China) with a 1000 gf load applied for 15 s.

2.6. DIC test

The deforming behavior of the gyroid structure was analyzed using VIC-3D (Related Solutions Co. Ltd., United States of America). A white paint was sprayed on the surface as a background in advance, and random black spots were sprayed after drying for DIC data acquisition and analysis. During the static compression test, deformation was captured by a data acquisition camera (camera resolution=3376 × 2704 pixels), with a camera sampling frequency of 1 Hz. Subsequently, the collected images during the structural deformation process were calculated and analyzed using DIC software. To achieve a more accurate analysis of the deformation of the Gyroid structure, the non-interest region of the gyroid's internal holes was removed from the initial image to identify the region of interest (ROI), and the strain cloud diagram of the maximum principal strain was obtained.

2.7. Fracture morphology

The fracture morphology of RGCS and SGCS was analyzed using SEM (TESCAN CLARA, TESCAN, Czech Republic) with an acceleration voltage of 10 kV.

3. Results and discussion

3.1. Effect of aging time on microstructure and phase transformation behavior

The metallographic structure of the NiTi minimum surface structure after different aging times in the X–Z direction is depicted in Figure 2. The figure illustrates that the microstructures of the samples exhibited coarse columnar crystals. During the LPBF process, samples were printed layer by layer from bottom to top, resulting in significant temperature gradient changes that facilitated vertical grain growth and columnar crystal formation. The crystal size of sample A0, as measured using ImageJ software, was 56.46 ± 10.92 µm. In contrast, samples aged for 2 h, 4 h, 6 h, 8 h, and 10 h exhibited sizes of 31.11 ± 3.67 µm, 26.81 ± 1.89 µm, 46.77 ± 4.16 µm, 39.17 ± 4.57 µm, and 44.63 ± 6.03 µm, respectively. These results indicated a decrease in grain size and an increasing trend of columnar crystals after aging treatment.

The XRD and semi-quantitative analysis results are presented in Figure 3. The untreated samples exhibited the B2 parent phase, with three primary peaks corresponding to the crystal plane index of (100), (110), and (200), respectively, with the highest intensity observed for the diffraction peak of (200). On aging heat treatment, the samples exhibited the presence of the B2 phase, B19' phase, and $NiTi_2$ phase. This phenomenon was attributed to the decrease in Ni content due to evaporation during

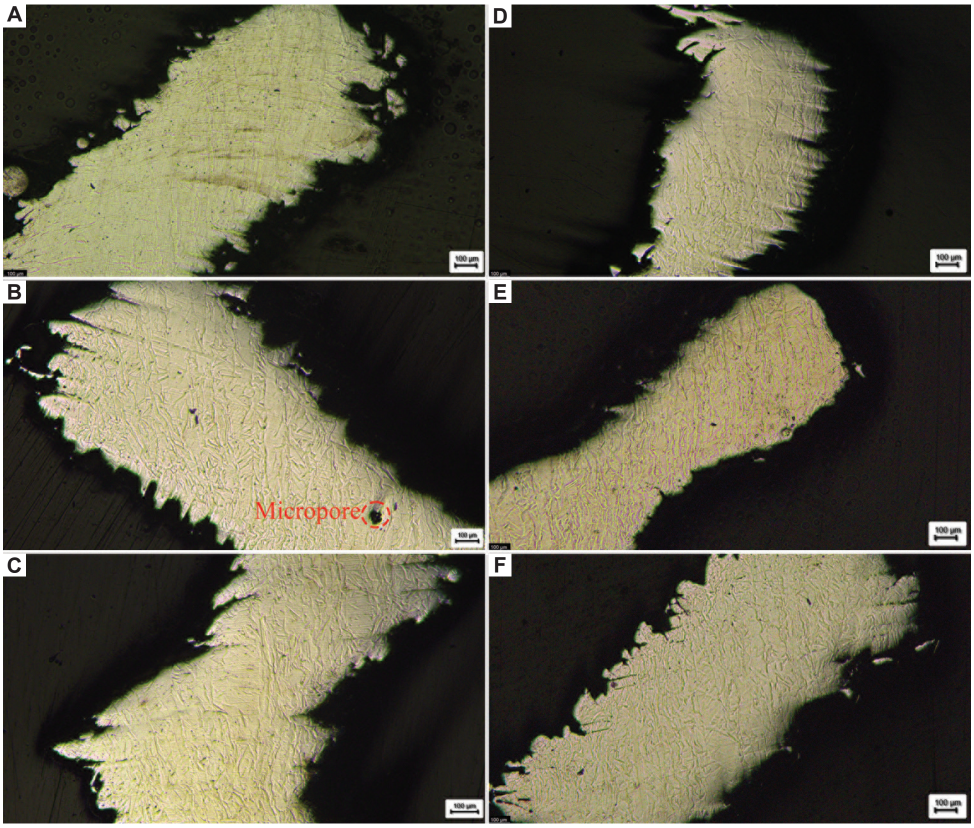

Figure 2. The microstructure of the X–Z plane of the sample treated with different aging times. (A) 0 h; (B) 2 h; (C) 4 h; (D) 6 h; (E) 8 h; and (F) 10 h. Scale bars: 100 µm; magnification: ×5.

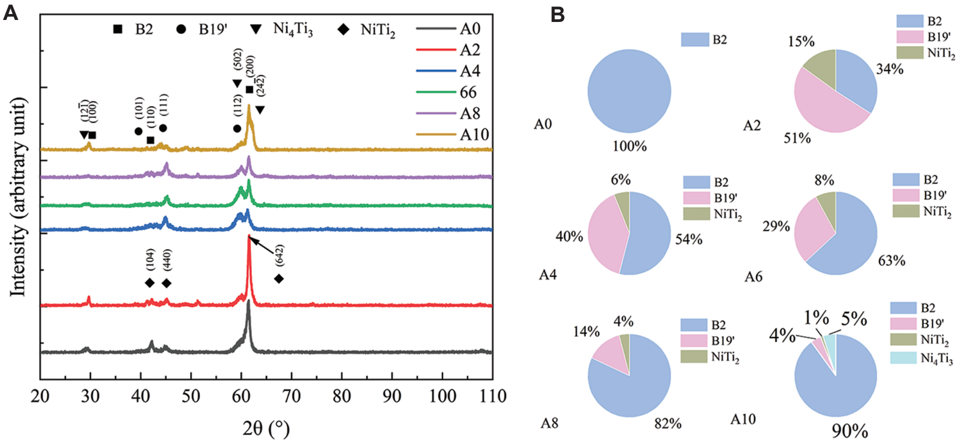

Figure 3. Phase analysis of laser powder bed fusion samples with aging heat treatment. (A) X-ray diffraction pattern. (B) Semi-quantitative analysis results.

the LPBF process, leading to excessive Ti precipitation in the form of the $NiTi_2$ phase. The appearance of the B19’ phase is a result of changes in the Ni/Ti ratio after aging heat treatment. The intensity of the highest peak of the B2 phase started decreasing after aging for more than 2 h, with some overlapping peaks observed with the $NiTi_2$ phase. It is worth noting that when the aging time reached 10 h, a diffraction peak for the Ni_4Ti_3 phase was revealed. Semi-quantitative analysis indicated that aged samples were mainly composed of B2 and B19’ phases, with a small amount of $NiTi_2$ phases present. In the LPBF process, the content of the B2 phase is the highest because the high cooling rate inhibits the transition of B19’ phase, while the $NiTi_2$ phase preferentially precipitates due to heat and supercooling.[43] The content of B19’ and $NiTi_2$ phases decreased with aging time. A small amount of the Ni_4Ti_3 phase appeared in the A10 sample, indicating that the second phase was almost completely dissolved, and the Ni_4Ti_3 phase began to precipitate between 8 and 10 h. As a brittle phase, the $NiTi_2$ phase led to the fracture of NiTi alloy in the early stage of plastic deformation, resulting in a sharp decrease in the ductility of the alloy.[44] The precipitation of $NiTi_2$ changed the ratio of Ni/Ti atoms in the matrix, and the phase transformation temperature changed accordingly, inducing uneven microstructure and low ductility. The Ni_4Ti_3 phase is one of the vital precipitated phases in the NiTi alloy. The mechanical properties and shape memory properties of the NiTi alloy were adjusted by controlling their physical properties, such as morphology, size, density, and position distribution.[45] For example, the recoverable strain of the NiTi alloy after stretching is due to the interaction between the dislocation formed under a certain number of stretching cycles and the Ni_4Ti_3 nanoprecipitate.[36] By increasing the laser volume energy density, the content of Ni4Ti3 was markedly reduced, which improved the pseudoelastic recovery behavior of the matrix during nanoindentation to a certain extent.[46]

The DSC curves of the aging samples and the analysis of phase transformation temperatures are depicted in Figure 4. In these curves, M_s and M_f represent the starting and ending temperatures of martensitic transformation, respectively, while A_s and A_f represent the starting and ending temperatures of reverse martensitic transformation, respectively. Figure 4A illustrates a two-step phase transformation behavior in the samples after aging heat treatment. The precipitation of the second phase induced multistep phase transformation behavior in the Ni-rich NiTi alloy. The primary mechanism underlying multistep phase transformation is the non-uniform position distribution of the precipitated phase during the initial stages of aging. Most precipitates form and grow along the grain boundary, resulting in an uneven composition of the matrix. Consequently, different parts of the matrix undergo phase transformation at varying aging temperatures or durations. As the aging time increased, both the endothermic peak and exothermic peak shifted to the right. The width of the martensite transformation peak slightly decreased, while the width of the austenite transformation peak increased. In Figure 4B, it can be observed that M_f decreased from 18.6°C to 7.9°C with increasing aging time, then increased to 16.7°C, while M_s only slightly increased from 22.5°C to 27.9°C. As A_s increased from 32.7°C to 54.9°C, A_f increased and stabilized at about 63°C after decreasing to 58.2°C, with the phase transformation temperature lag gradually increasing. The decrease in M_f and A_f before 6 h may be attributed to the precipitation of the $NiTi_2$ phase, resulting in an increase in Ni content and a decrease in phase transformation temperature. Conversely, after aging heat treatment, the evaporation of Ni and Ni-rich secondary phase led to a low Ni concentration in the matrix, resulting in an increased phase transformation temperature.[47]

The hardness of sample A0 was 278.2 HV and increased with the aging time, as depicted in Figure 5. The maximum

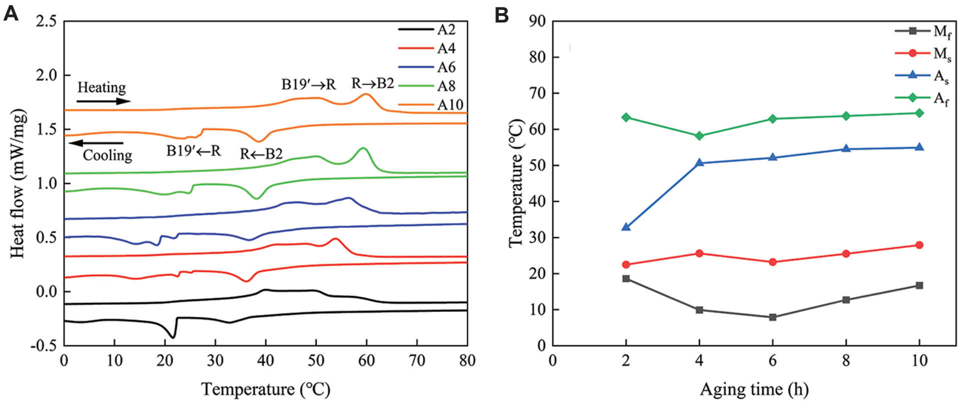

Figure 4. (A) DSC curves of NiTi fabricated by LPBF. (B) Analysis of M_s, M_f, A_s, and A_f.

value recorded was 477.8 HV for A10, representing a 71.74% increase compared to the untreated samples. This notable increase can be attributed to the precipitation of the second phase, which enhances the resistance to plastic deformation. As a result, the critical stress required for slip in the matrix increases, leading to an overall increase in hardness.[48] In addition, the precipitation of the $NiTi_2$ phase also contributes to the improved hardness of the sample. Saedi[49] similarly observed an increase in sample hardness with extended aging time, underscoring the significant influence of aging duration on the hardness of NiTi alloy. Moreover, it is worth noting that the hardness of NiTi alloy is highly dependent on the test environment temperature.

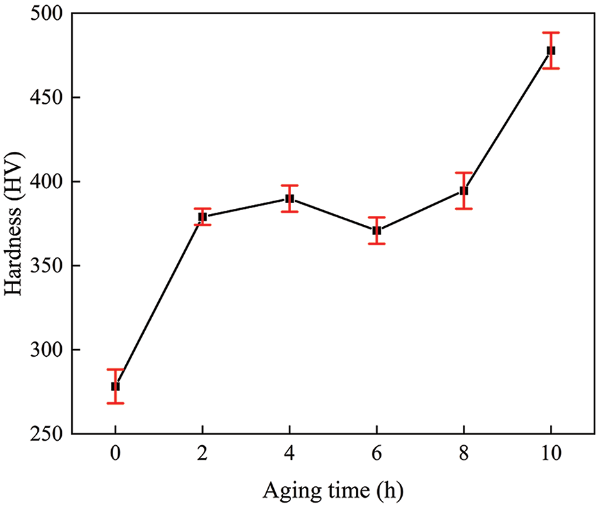

Figure 5. Microhardness of samples with aging heat treatment.

3.2. Effect of aging heat treatment on compressive properties

The compressive stress-strain curves of RGCS and SGCS after different aging times are depicted in Figure 6A and B. Both structures exhibited three classical stages during the compression process: (i) linear elastic stage, (ii) yield stage, and (iii) fracture stage. During the initial stage, RGCS underwent a brief period of linear elastic deformation before transitioning into the yield stage. During the yield stage, stress increased non-linearly until reaching the strength limit, followed by a sharp stress drop leading to sample failure. Following aging heat treatment, the yield plateau of RGCS structures extended, enhancing plasticity

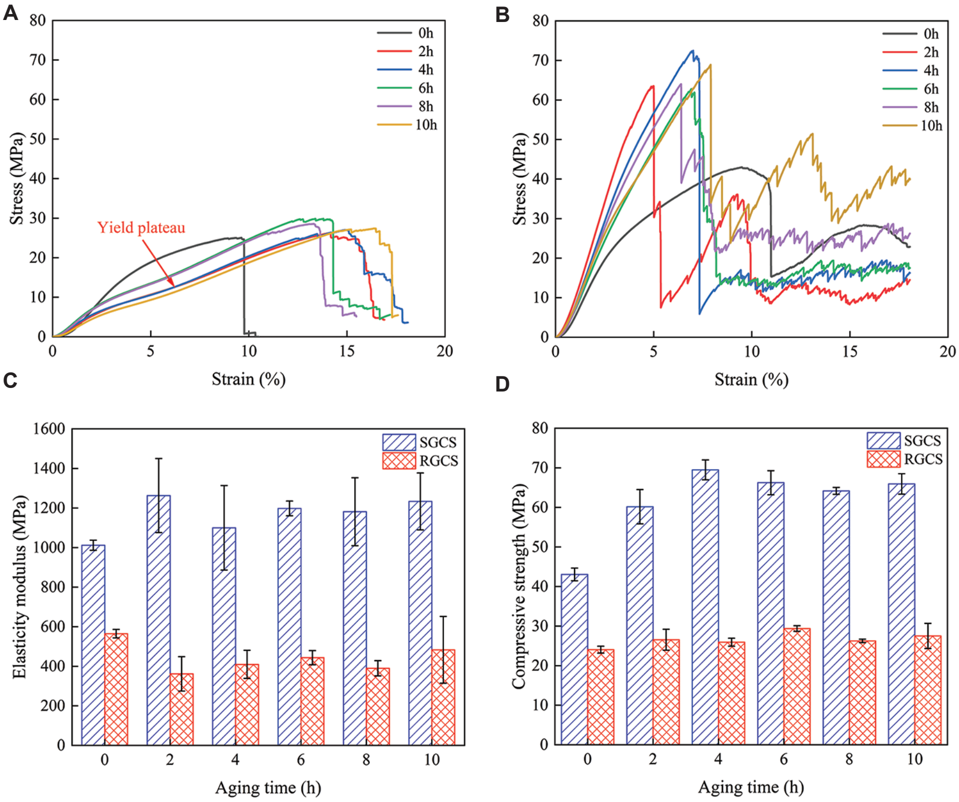

Figure 6. Compression results of samples treated with different aging times. (A) The stress-strain curve of rod-shaped gyroid cellular structure (RGCS). (B) The stress-strain curve of sheet-shaped gyroid cellular structure (SGCS). (C) Elastic modulus. (D) Compressive strength.

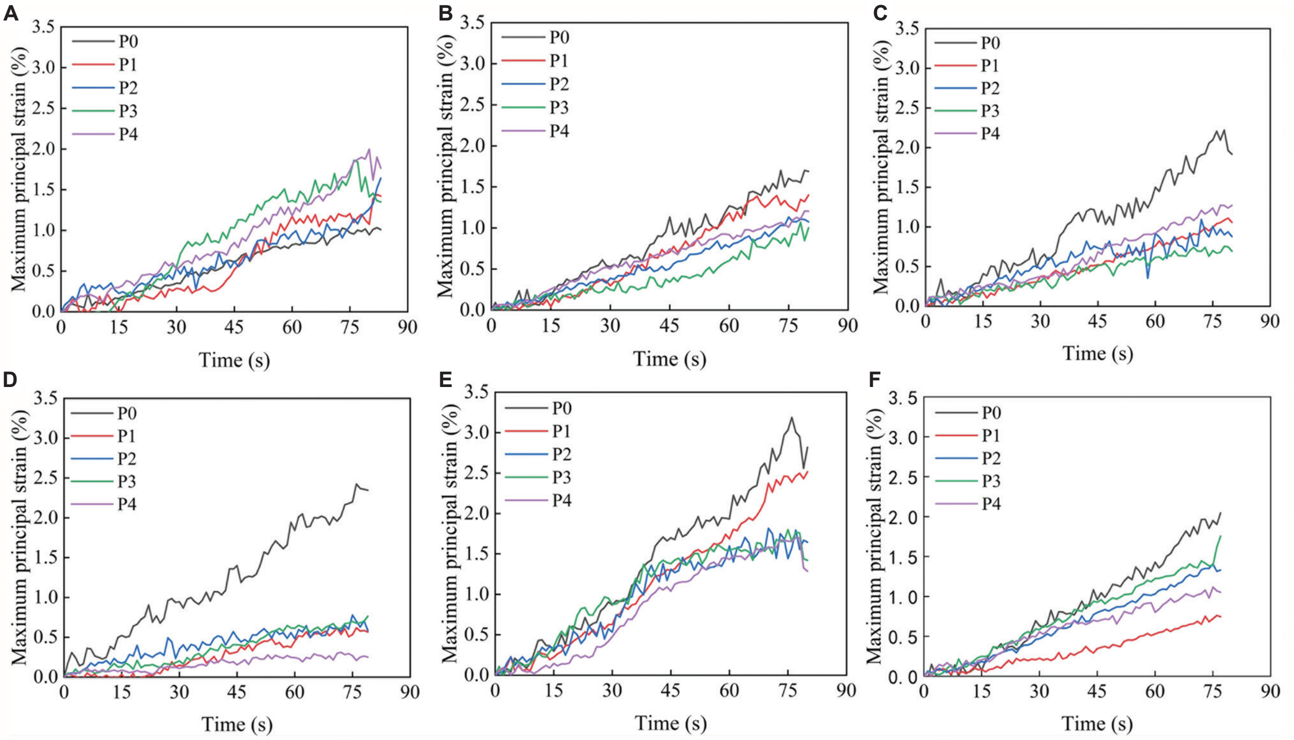

Figure 7. The maximum principal strain of rod-shaped gyroid cellular structure (RGCS) with different aging times. (A) 0 h; (B) 2 h; (C) 4 h; (D) 6 h; (E) 8 h; and (F) 10 h.

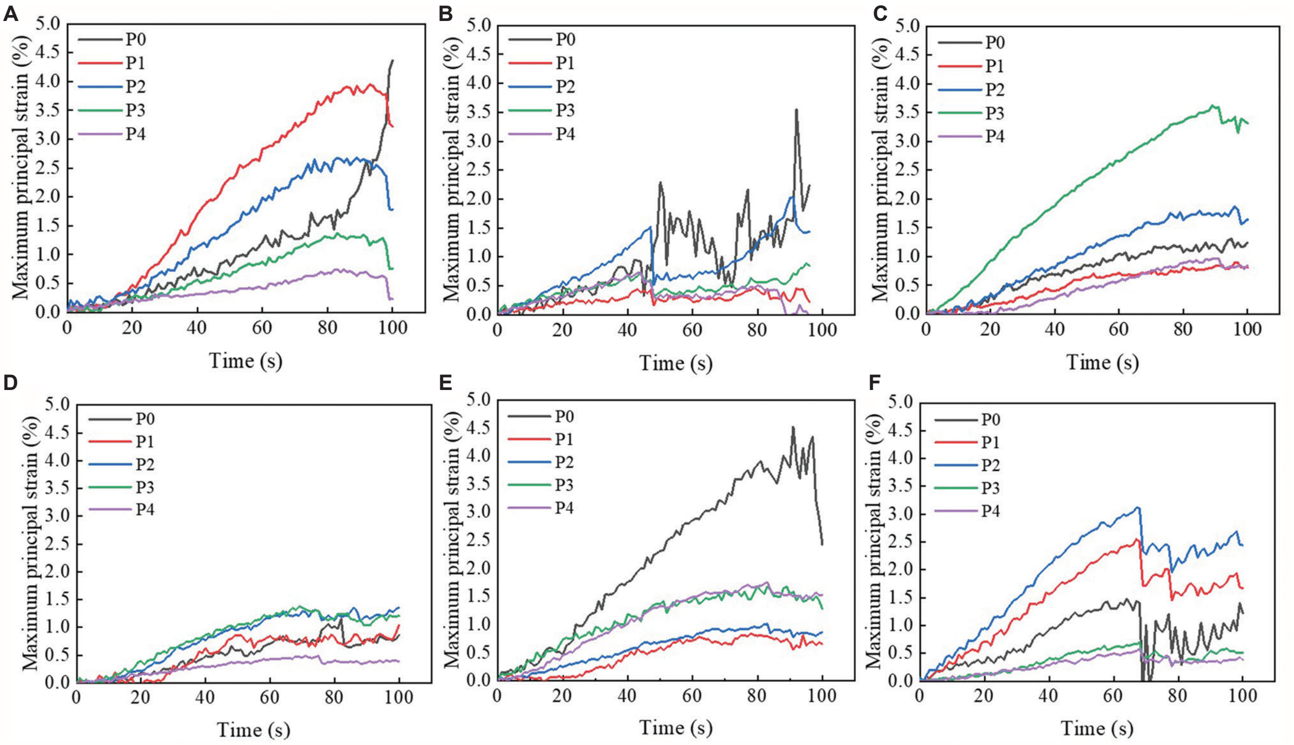

Figure 8. The maximum principal strain of sheet-shaped gyroid cellular structure (SGCS) with different aging times. (A) 0 h; (B) 2 h; (C) 4 h; (D) 6 h; (E) 8 h; and (F) 10 h.

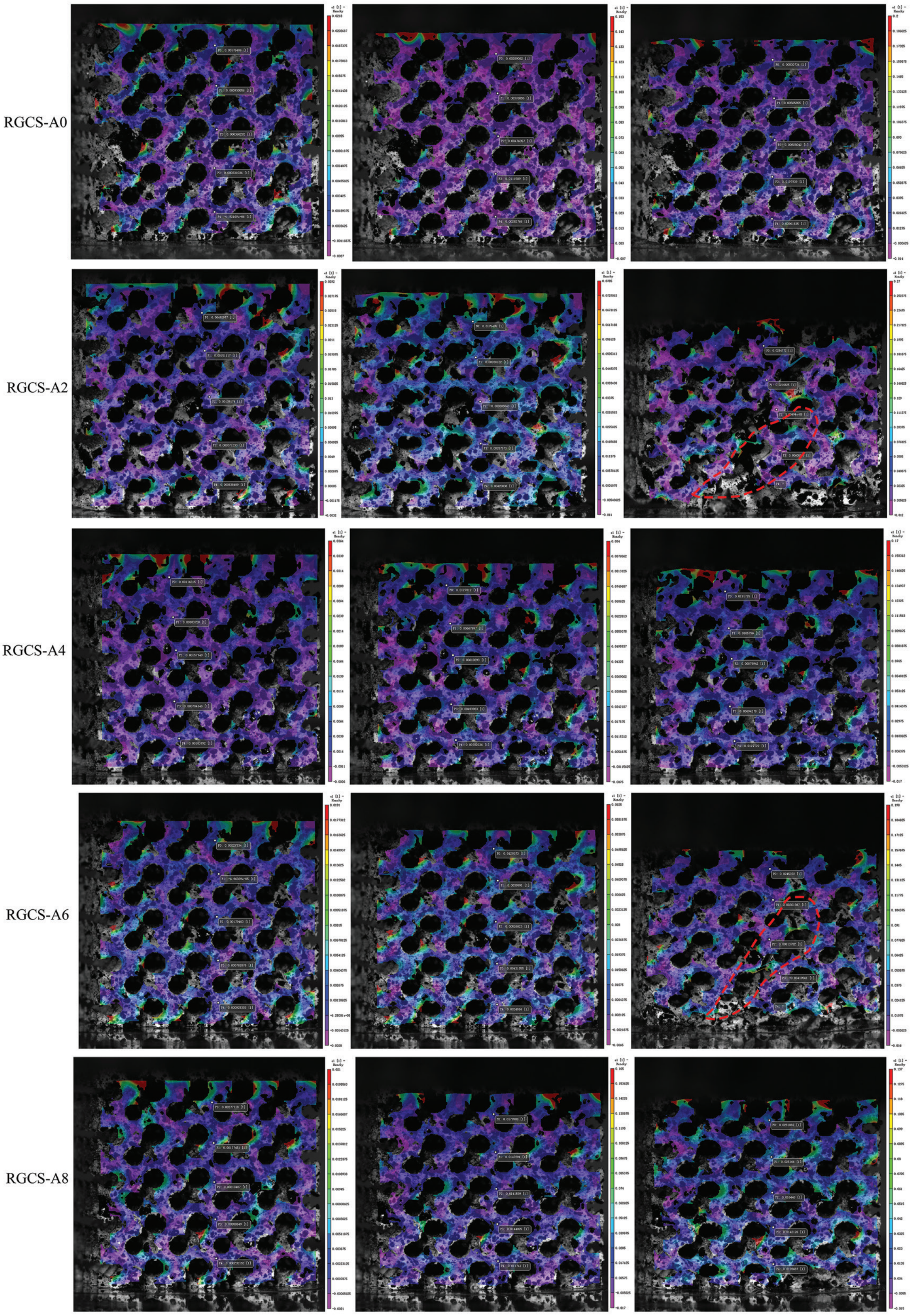

Figure 9. Digital image correlation (DIC) analysis of the compression strain of rod-shaped gyroid cellular structure (RGCS) at different time points after heat treatment with different aging times.

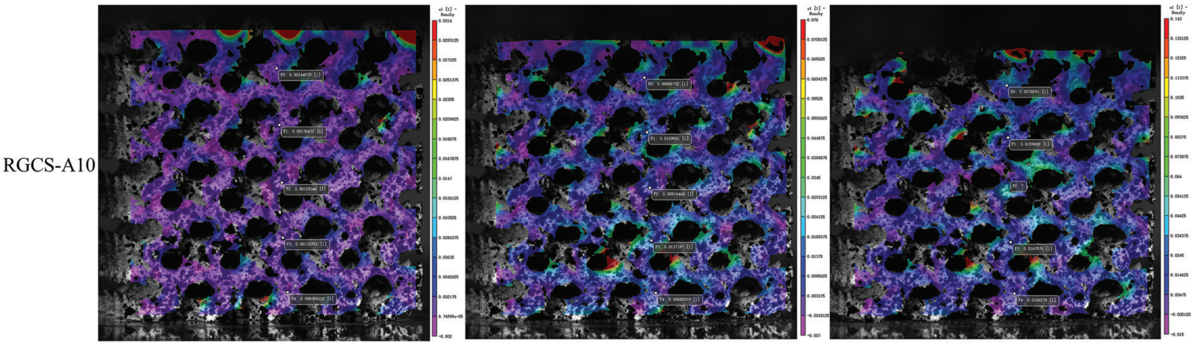

Figure 9. *(Continued).*

while maintaining strength, with RGCS-A6 and RGCS-A8 demonstrating the highest yield strength.

In contrast, the aging heat treatment shortened the yield plateau of SGCS, leading to a rapid transition through the yield stage and prompt initiation of fracture on reaching its strength limit. The failure strain of RGCS increased from 10% to 15%, while that of SGCS decreased from 10% to approximately 5%. These results indicate that aging heat treatment improved the plasticity and strength of RGCS but increased the brittleness of SGCS. Due to age hardening, the strength of SGCS increased while its plasticity and toughness declined, causing it to enter the compression fracture stage more rapidly, consistent with age hardening principles. Figure 3A illustrates the precipitation of the $NiTi_2$ phase in the matrix after aging heat treatment, impeding dislocation movement within the alloy and thereby enhancing both yield strength and compressive strength. Furthermore, the LPBF process introduced sample defects such as micropores, with SGCS exhibiting greater sensitivity to defects compared to RGCS, leading to faster progression to the compression fracture stage. This study demonstrates enhanced plasticity for RGSC after aging heat treatment while maintaining nearly unchanged strength.

The compressive elastic modulus is depicted in Figure 6C. The elastic modulus of RGCS-A0 was 564.89 MPa, while that of SGCS-A0 was 1011.74 MPa. Compared with the untreated samples, the elastic modulus of RGCS decreased, whereas that of SGCS increased after aging heat treatment. At 2 h of aging, the minimum elastic modulus recorded for RGCS-A2 was 361.52 MPa, whereas the maximum elastic modulus observed for SGCS-A2 was 1262.82 MPa.

Figure 6D illustrates the compressive strength. Both RGCS and SGCS demonstrated higher compressive strength after aging heat treatment compared to the untreated samples. The maximum compressive strength of SGCS-A4 reached 69.48 MPa, marking a 61.39% increase over the compressive strength of SGCS-A0. Conversely, the maximum compressive strength of RGCS-A6 only exhibited a modest increase of 22.23%, reaching 29.38 MPa compared to RGCS-A0. These results indicate a significant enhancement in the mechanical properties of rod-shaped gyroid structures due to aging heat treatment.

Five evenly distributed points were extracted from the DIC strain cloud diagram, from top to bottom, to analyze the compression process of the gyroid, as depicted in Figures 7 and 8. Except for RGCS-A0, the strain at point P0 from RGCS-A2 to RGCS-A10 consistently exceeded that of the other four points after 45 s. Notably, the strain at the P0 point of samples A4, A6, and A8 surpassed 2%, as shown in Figure 7. The upper unit of RGCS experienced the most significant compression deformation. Conversely, the strain at the five extraction points of SGCS exhibited a synchronous upward trend within 20 s in Figure 8, indicating that the overall structure underwent rapid, uniform elastic deformation during the compression process. Twenty seconds later, the rate of strain increased more rapidly at points P2, P3, and P4 in the middle compared to the other points, except for SGCS-A8. Figures 9 and 10 display the strain contours of the two structures analyzed using DIC. The compressive shear failure of RGCS was attributed to the significant stress near the diagonal of the structure. Zhang[50] discovered that the initial fracture of the uniform gyroid rod structure occurred on the diagonal rod at the corner with higher stress and strain levels. The first fractures occurred at the bottom of the cell and then extended to the upper layer. Most fractures were observed on the diagonal rod, while very few occurred on the horizontal rod. Chen[51] discovered that the homogeneous gyroid structure developed a 45° shear band along the cube diagonal and fractured due to the localized shear stress aligned with the loading direction at a 45° angle. The text explained that the uniform gyroid structure was prone to failure when diagonal yield deformation occurred. However, the angle of the fracture zone of RGCS was slightly larger than 45°, and the position showed an offset near the diagonal. The RGCS-A2 and RGCS-A6 displayed a 45°

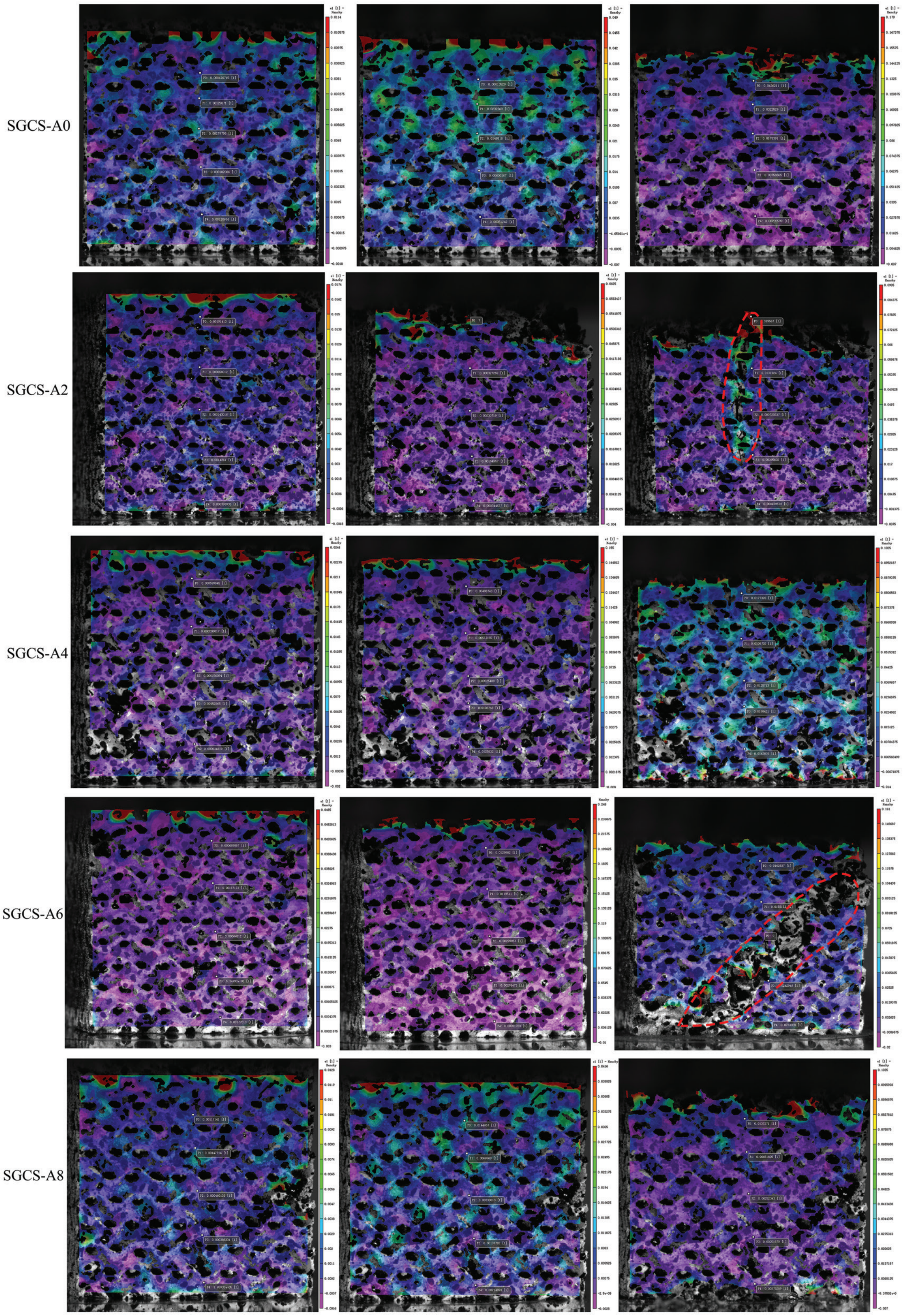

Figure 10. Digital image correlation (DIC) analysis of the compression strain of sheet-shaped gyroid cellular structure (SGCS) at different time points after heat treatment with different aging times.

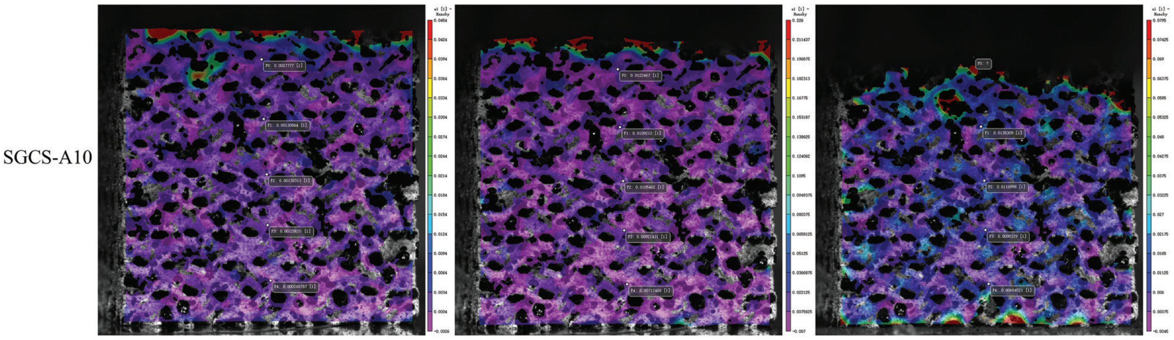

Figure 10. *(Continued).*

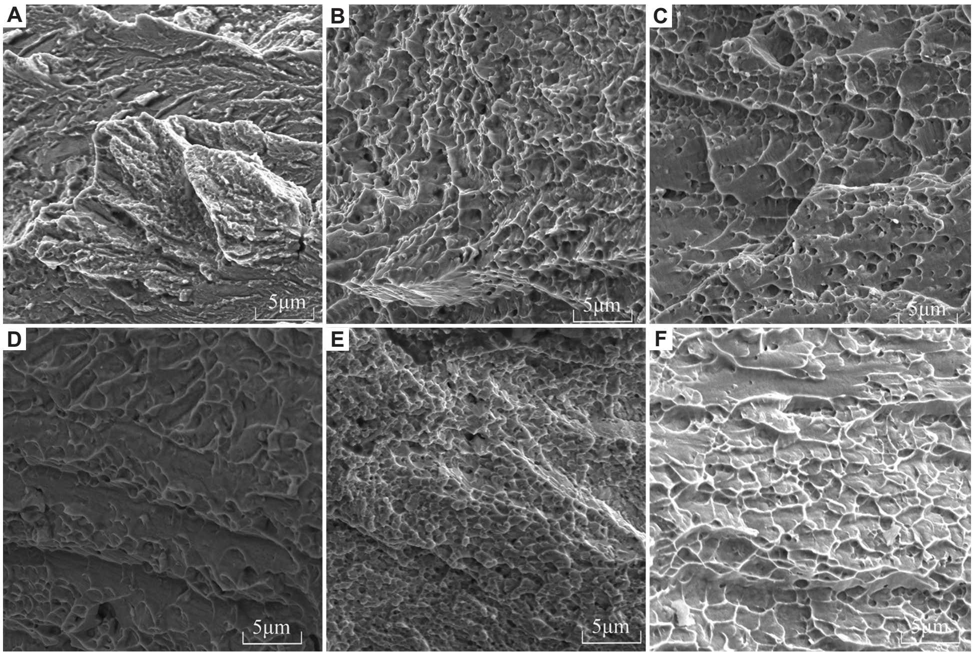

Figure 11. Fracture morphology of rod-shaped gyroid cellular structures (RGCS) with different aging times. (A) 0 h; (B) 2 h; (C) 4 h; (D) 6 h; (E) 8 h; and (F) 10 h.

fracture zone around t=80 s. At the base of the structure, the micro-rod was bent upward due to compressive stress.

The initial collapse, as depicted in Figure 10, occurred at the upper edge of the structure, resulting in fragment formation under pressure. This collapse primarily stemmed from the stress exerted on the uppermost layer of SGCS reaching a local maximum and leading to the compaction of fragments and the formation of voids. Subsequently, this stress-induced fracturing propagated to the successive layer, demonstrating the strain ratio of the lower layer. Figure 10 further illustrates that while the upper layer of SGCS suffered damage, the bottom structure retained a certain level of integrity. The collapse of SGCS proceeded layer by layer, elucidating the serrated stress-strain curve of SGCS depicted in Figure 6B after reaching the failure strain. In addition, SGCS-A2 exhibited a vertical downward fault zone in the middle at t=100 s, whereas SGCS-A6 exhibited a 45° fault. Sun *et al.*[52] proposed that SGCS reaches its initial ultimate stress after undergoing elastic deformation and subsequently collapsed, losing a substantial portion of its strength. After the initial collapse, the remaining structure partially regained its strength and experienced a cascading collapse during the subsequent process, ultimately displaying an upward trend. This abrupt collapse exemplifies the typical failure behavior observed in brittle minimal surface structures under minimal deformation.

Figure 11 illustrates the fracture morphology of RGCS after the compression test. For RGCS-A0 without heat treatment, the fracture morphology exhibited the typical river patterns and multiple cleavage steps, accompanied by

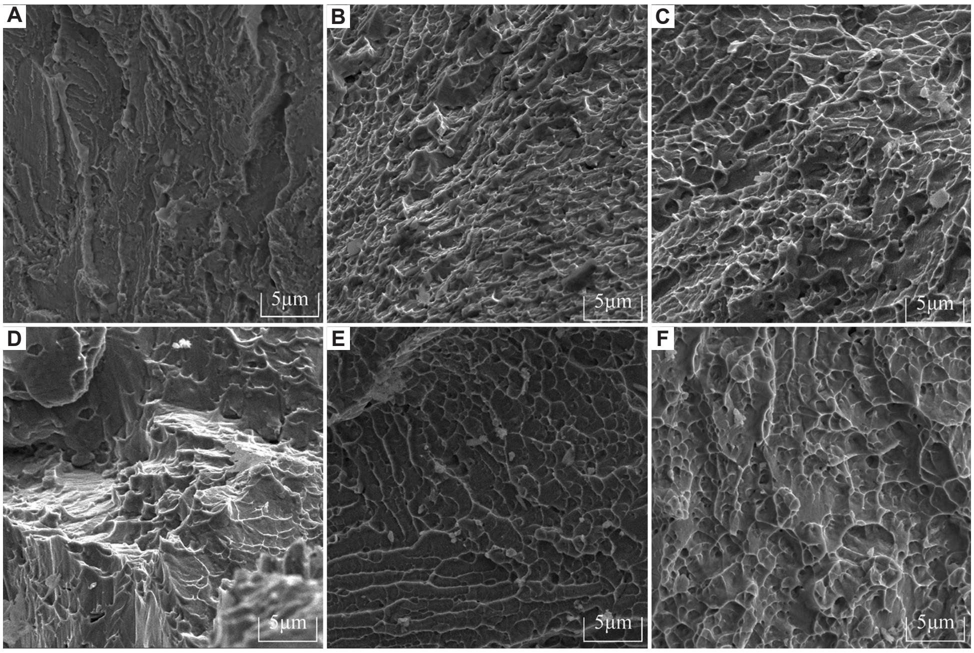

Figure 12. Fracture morphology of sheet-shaped gyroid cellular structures (SGCS) with different aging times. (A) 0 h; (B) 2 h; (C) 4 h; (D) 6 h; (E) 8 h; and (F) 10 h.

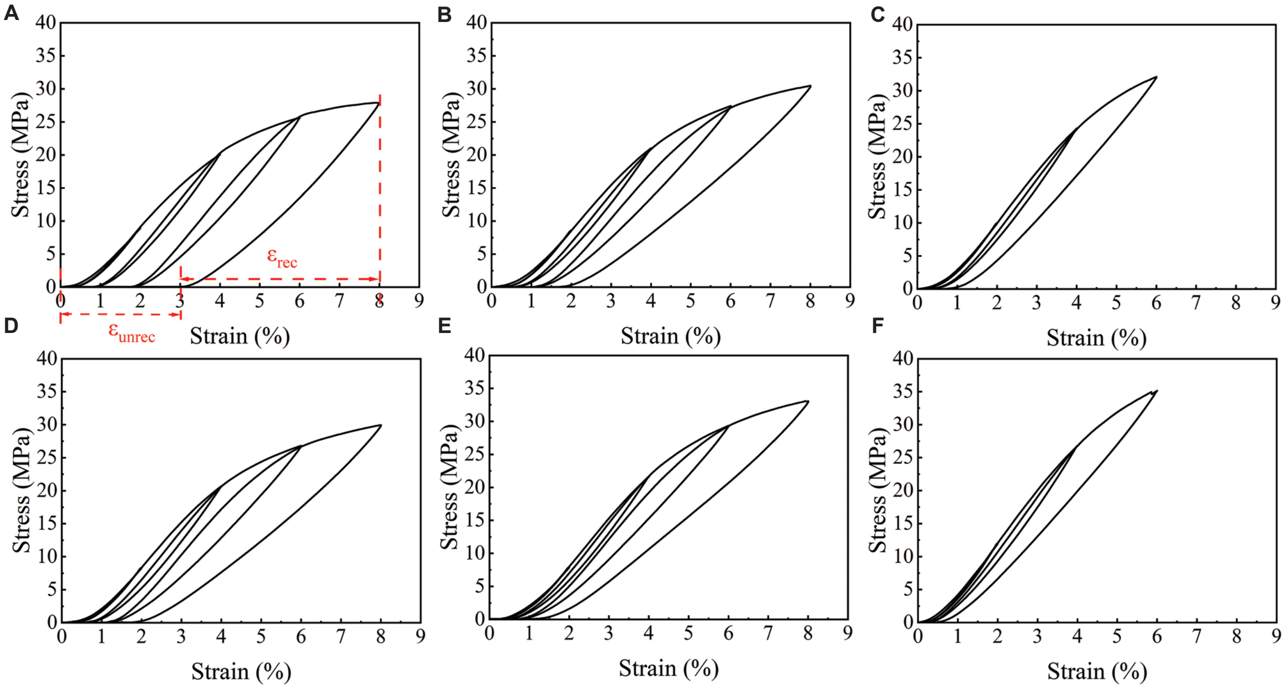

Figure 13. Superelasticity behavior of rod-shaped gyroid cellular structure (RGCS) under different strains after different aging times. (A) 0 h; (B) 2 h; (C) 4 h; (D) 6 h; (E) 8 h; and (F) 10 h.

a small number of dimples in localized areas, indicative of brittle fracture mechanisms. Conversely, after aging heat treatment, RGCS-A2 displayed a plethora of dimples on its fracture section, signaling a transition to ductile fracture behavior. As the aging time extended beyond 4h, the dimples in RGCS (Figure 11C-E) became shallower than RGCS-A2, with tear ridges featuring planes also observed in RGCS-A4 to RGCS-A10. This result underscores a shift

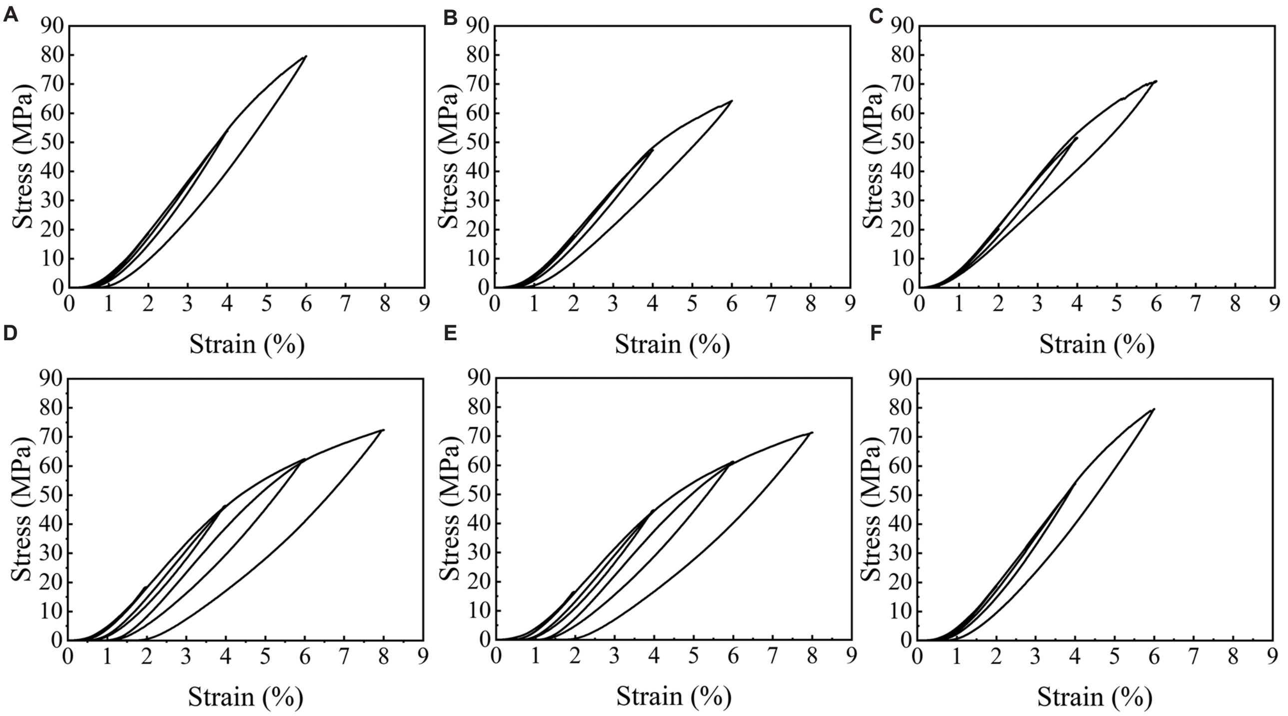

Figure 14. Superelasticity behavior of sheet-shaped gyroid cellular structure (SGCS) under different strains after different aging times. (A) 0 h; (B) 2 h; (C) 4 h; (D) 6 h; (E) 8 h; and (F) 10 h.

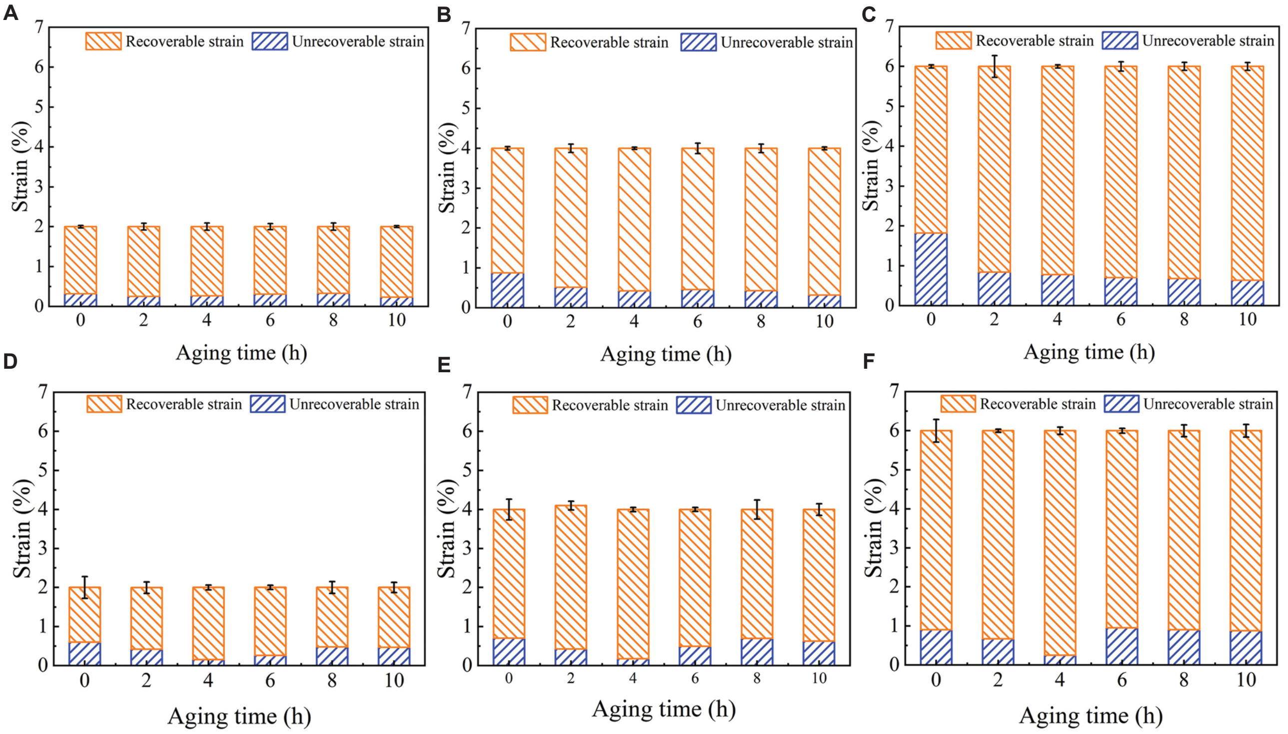

Figure 15. The recoverable and unrecoverable strain of the gyroid cellular structures. Rod-shaped gyroid cellular structure (RGCS) with compressive strain at (A) 2%, (B) 4%, and (C) 6% and sheet-shaped gyroid cellular structure (SGCS) with compressive strain at (D) 2%, (E) 4%, and (F) 6%.

toward quasi-cleavage fracture mechanisms in RGCS-A4, RGCS-A6, RGCS-A8, and RGCS-A10.

Figure 12 depicts the fracture morphology of SGCS after the compression test. Similar to RGCS-A0, the fracture morphology of SGCS-A0 exhibited characteristics typical of river patterns and cleavage steps, without evident macroscopic plastic deformation. This observation suggests that brittle fracture is the primary fracture mechanism. After aging heat treatment, numerous dimpled fractures were observed in SGCS-A2 and SGCS-A4, indicating a shift toward ductile fracture mechanisms in these samples. With aging time exceeding 6 h, the dimples in SGCS became shallower and fewer in number. Notably, the tear ridge observed in SGCS-A6 was significantly higher than in SGCS-A8 and SGCS-A10. These results suggest that quasi-cleavage fracture was the fracture mechanism in SGCS-A6, SGCS-A8, and SGCS-A10.

Yan[39] observed a significant presence of ductile dimples on the fracture surface of samples treated with a solid solution, indicating the dominance of ductile fracture. After compression, the fracture pattern resembled a river-like formation, indicating rapid crack propagation speed. This phenomenon was attributed to the absence of a plastic zone in the NiTi sample to prevent crack propagation during compression. Bhardwaj[53] noted that after aging heat treatment at 350°C, the density of dimple and tear ridge in the NiTi alloy increased, accompanied by the appearance of micro-cracks, indicative of ductile fracture. Subsequent heat treatment at 450°C resulted in the emergence of substantial microcracks, with the cleavage surface becoming predominant. In addition, grain refinement was observed after solution treatment, leading to a decrease in the average particle size from 52.43 μm to 15.45 μm.

3.3. Effect of aging heat treatment on the superelasticity

Superelasticity is an important characteristic of NiTi SMA, denoting its capacity to undergo significant deformation on the application of stress to the austenite phase, exceeding its elastic limit strain, and subsequently automatically reverting to its original shape during unloading.[54] Figures 13 and 14 depict the stress-strain curves of RGCS and SGCS subjected to 2%, 4%, 6%, and 8% compressive strain at 100°C, respectively. RGCS-A0, RGCS-A2, RGCS-A6, and RGCS-A8 exhibited the capability to withstand a compressive strain of 8%, accompanied by a reduction in unrecoverable strain from 3.12% to 1.27% with increasing aging time. Conversely, SGCS exhibited commendable superelasticity up to 6% compressive strain, with a maximum unrecoverable strain not exceeding 1.35%. However, only the SGCS-A6 and SGCS-A8 samples

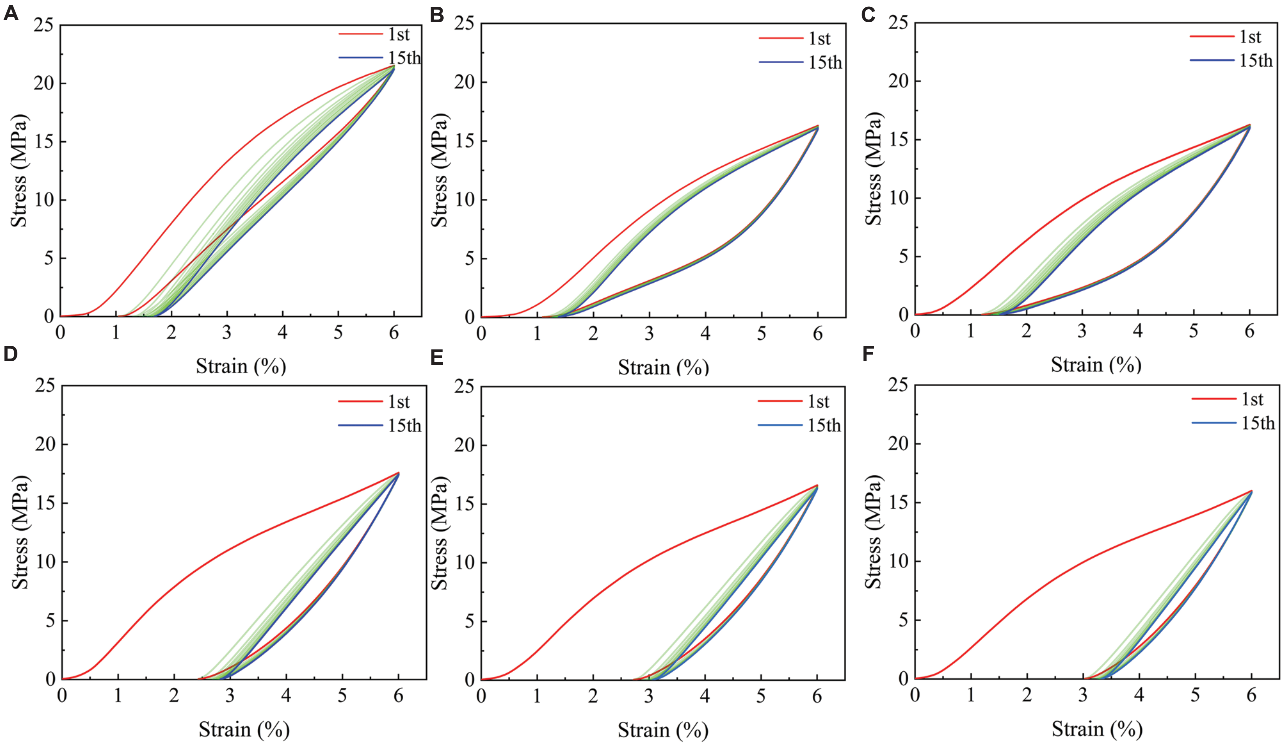

Figure 16. Shape memory behavior of rod-shaped gyroid cellular structure (RGCS) under different strains with different aging times. (A) 0 h; (B) 2 h; (C) 4 h; (D) 6 h; (E) 8 h; and (F) 10 h.

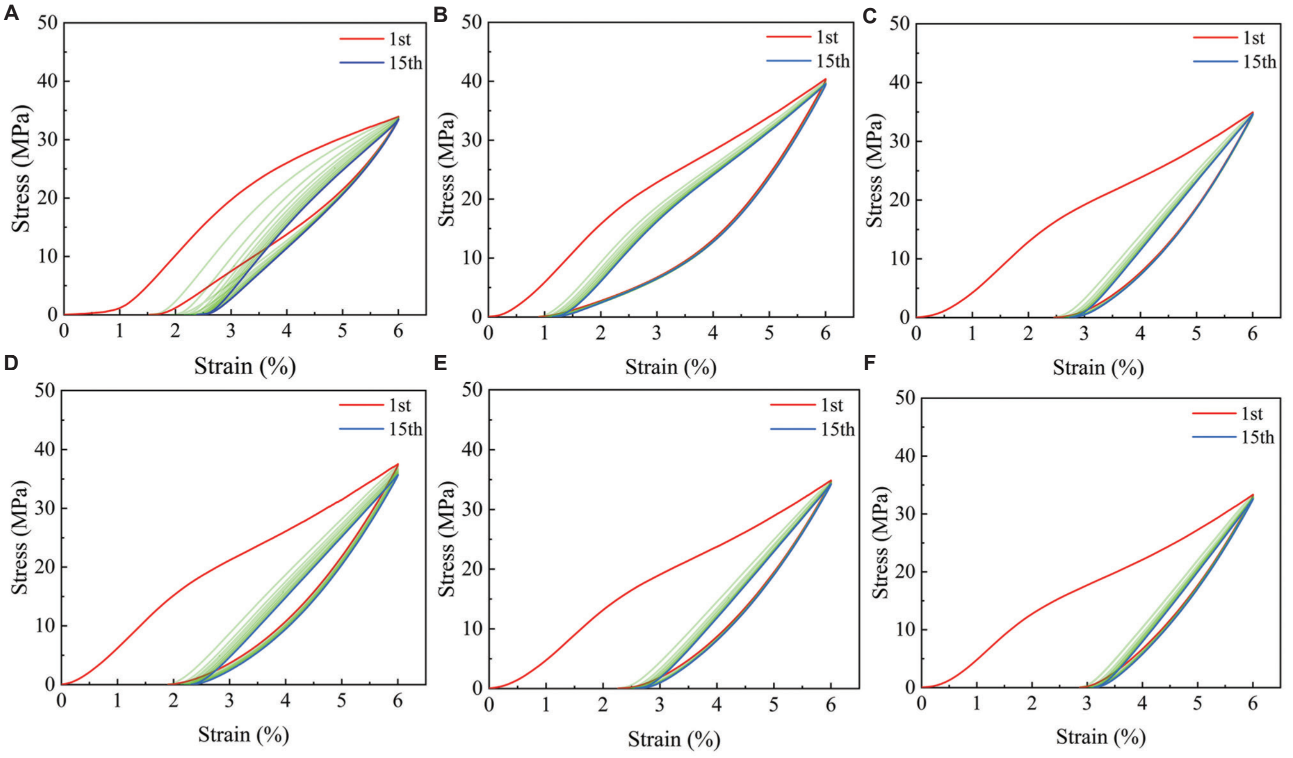

Figure 17. Shape memory behavior of sheet-shaped gyroid cellular structure (SGCS) under different strains with different aging times. (A) 0 h; (B) 2 h; (C) 4 h; (D) 6 h; (E) 8 h; and (F) 10 h.

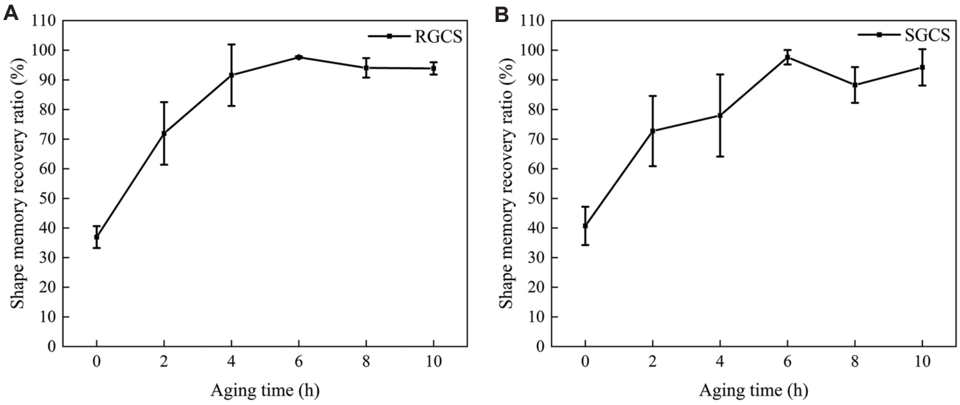

Figure 18. Shape memory recovery ratio of samples treated with different aging times. (A) Rod-shaped gyroid cellular structure (RGCS); (B) Sheet-shaped gyroid cellular structure (SGCS).

withstood an increase to 8% compressive strain, while the SGCS-A0, SGCS-A2, SGCS-A4, and SGCS-A10 fractured before reaching 8% compressive strain, resulting in a sharp decline in stress. The superelasticity range of SGCS appeared relatively narrow, spanning between 2% and 4% compressive strain. Notably, the stress-strain curves of SGCS exhibited a slight jagged change at 6% strain, suggesting the onset of compression fracture. The superelastic response of SGCS outperformed that of RGCS, likely attributed to the increased elastic modulus and compressive strength of SGCS after aging heat treatment. In addition, as compressive strain increased, irreversible plastic deformation ensued, due to the accumulation of unrecoverable strain resulting from minor defects such as microcracks and microvoids in the LPBF process. On reaching a strain level of 8%, SGCS attained its maximum compressive strength. The internal collapse of the structure resulted in a significant reduction in elastic strain, causing permanent deformation of the structure.

The recoverable and unrecoverable strains of RGCS and SGCS under various compressive strains are depicted in Figure 15. The recoverable strain of RGCS remained relatively consistent under 2% compressive strain. However, as the compressive strain reached 4% and 6%, an expected increase in recoverable strain was observed, with a slight augmentation noted with prolonged aging time. Among these rod-shaped structures, RGCS-A10 exhibited the largest recoverable strain, measuring at 1.77%, 3.68%, and 5.36%, following compression strains of 2%, 4%, and 6%, respectively. Conversely, within the sheet-shaped structures, the SGCS-A4 sample exhibited the highest recoverable strain, measuring 1.84%, 3.82%, and 5.75% after undergoing 2%, 4%, and 6% compression strain, respectively. The aging heat treatment exerted a positive effect on enhancing the superelasticity of the NiTi-TPMS structures. Moreover, maintaining a constant aging temperature while appropriately increasing the aging time significantly enhanced superelasticity.

3.4. Effect of aging heat treatment on shape memory

The SME is an important functional characteristic of SMA, denoting its capability to restore its original shape after deformation induced by applied stress. This phenomenon hinges on the reversible transformation between the martensite phase and the austenite phase.[55] The results obtained from DSC and XRD analyses indicated that the samples predominantly existed in the B2 phase at room temperature. The recovery of deformation after compression primarily stemmed from martensitic transformation induced by stress excitation. The cyclic compression curves of RGCS and SGCS samples subjected to aging heat treatments are illustrated in Figures 16 and 17. It was observed that the stress hysteresis of both RGCS and SGCS peaked during the initial cycle. Subsequent cycles witnessed a decline in stress hysteresis, suggesting a reduction in energy dissipation during the deformation process. The recoverable strain during the first cycle was measured at 4.96% for RGCS and 4.46% for SGCS. Over 15 cycles, the total irrecoverable strain decreased to 4.3% for RGCS and 3.6% for SGCS. With increasing aging time, the overall recoverable strain of both RGCS and SGCS gradually decreased, while the total unrecoverable strain increased. By the time the aging time reached 10 h, the recoverable strain decreased to 2.67% for RGCS and 2.88% for SGCS.

The shape memory recovery ratios of the samples after cyclic compression and heating in a water bath are presented in Figure 18. On heating the samples above the A_f temperature, the formation of the martensite phase, induced by residual stress, underwent re-transformation into the austenite phase, leading to partial recovery of residual deformation. The irreparable deformation primarily stemmed from internal structural fractures under stress. For RGSC-A0, the shape recovery ratio was measured at 36.93%, while for SGCS-A0, it stood at 40.7%. The recovery ratio of SGCS and RGCS structures gradually increased with aging time. Specifically, the shape recovery ratio of RGCS-A6 and SGCS-A6 increased to 97.63% and 97.62%, respectively. Notably, between 4 h and 6 h of aging time, the enhancement of SMEs was more pronounced, with the recovery ratio reaching its peak. Sun *et al.*[52] measured the recovery strain of the NiTi gyroid structures compressed by 4%, 8%, and 12% strain following immersion in a silicone oil bath at 150°C. The recorded recovery strains were 1.65%, 4.19%, and 5.91%, respectively. Yang *et al.*[56] reported an overall shape recovery ratio of NiTi gyroid structures with varying volume fractions and unit sizes, ranging from 96.5% to 98.8% after heating under compressive strain. Therefore, NiTi alloy samples fabricated through LPBF can undergo aging heat treatment to enhance the recovery ratio and improve the SME.

4. Conclusion

This study investigates the effects of various aging times on the microstructure, phase transformation behavior, mechanical properties, and functional properties of NiTi-TPMS structures after LPBF remelting. The main conclusions drawn from this study are as follows:

(i) The microstructure of the samples manifested as coarse columnar crystals. On aging heat treatment, precipitation of the B19' phase and $NiTi_2$ phase occurred. With increasing aging heat treatment time, M_f initially decreased and then increased, M_s increased from 22.5°C to 27.9°C, and A_s rose from 32.7°C to 54.9°C. Notably, from sample A0 to sample A10, the microhardness value increased from 278.2 HV to 477.8 HV, representing a 71.74% increase.

(ii) The plasticity of RGCS was enhanced after aging heat treatment, while the strength remained almost unchanged. Due to the aging hardening effect, the strength of SGCS increased while the plasticity and toughness declined. When aging time reached 2 h, the minimum elastic modulus of RGCS-A2 was 361.52 MPa, and the maximum elastic modulus of SGCS-A2 was 1262.82 MPa. The maximum compressive strength of SGCS-A4 reached 69.48 MPa, which was 61.39% higher than the compressive strength of SGCS-A0. Compared with RGCS-A0, the maximum compressive strength of RGCS-A6 only increased by 22.23%, reaching 29.38 MPa. In addition, after aging heat treatment, a plethora of dimples appeared in the fractures of RGCS-A2, SGCS-A2, and SGCS-A4, indicating that the fracture mechanism was ductile.

(iii) Under a 6% compressive strain, SGCS exhibits excellent superelasticity. The superelastic response of SGCS is superior to that of RGCS. The shape recovery ratio of RGCS-A0 was 36.93%, while the shape recovery ratio of SGCS-A0 was 40.7%. With the extension of aging time, the recovery ratio of both SGCS and RGCS increased gradually. Specifically, the shape recoveries of RGCS-A6 and SGCS-A6 were increased to 97.63% and 97.62%, respectively.

Acknowledgments

None.

Funding

This research was funded by the Guangdong Natural Science Foundation (No. 2023A1515012704), Guangdong Basic and Applied Basic Research Foundation-Youth Fund Project (No. 2021A1515110033), Program for scientific research start-up funds of Guangdong Ocean University (360302022201), and GDA's Project of Science and Technology Development (2022GDASZH-2022010107).

Conflict of interest

The authors declare that they have no competing interests.

Author contributions

Conceptualization: Mingkang Zhang
Formal analysis: Jinwei Li, Chang Liu, Wenbin Liu
Funding acquisition: Mingkang Zhang, Jie Chen
Investigation: Jinwei Li, Mingkang Zhang
Methodology: Jinwei Li, Wenbin Liu
Project administration: Mingkang Zhang
Supervision: Mingjian Deng
Visualization: Chang Liu, Wenbin Liu
Writing – original draft: Jinwei Li
Writing – review & editing: Mingkang Zhang, Mingjian Deng, Jie Chen

All authors have read and agreed to the published version of the manuscript.

Ethics approval and consent to participate

Not applicable.

Consent for publication

Not applicable.

Availability of data

The authors confirm that the data supporting the findings of this study are available within the article.

References

1. Mohamed OA, Masood SH, Xu W. Nickel-titanium shape memory alloys made by selective laser melting: A review on process optimisation. *Adv Manuf*. 2022;10(1):24-58.

   doi: 10.1007/s40436-021-00376-9

2. Wei S, Zhang J, Zhang L, *et al*. Laser powder bed fusion additive manufacturing of NiTi shape memory alloys: A review *Int J Extreme Manuf.* 2023;5(3):032001.

   doi: 10.1088/2631-7990/acc7d9

3. Zhang Y, Attarilar S, Wang L, Lu W, Yang J, Fu Y. A review on design and mechanical properties of additively manufactured NiTi implants for orthopedic applications. *Int J Bioprint*. 2021;7(2):340.

   doi: 10.18063/ijb.v7i2.340

4. Feng J, Fu J, Yao X, He Y. Triply periodic minimal surface (TPMS) porous structures: From multi-scale design, precise additive manufacturing to multidisciplinary applications. *Int J Extreme Manuf.* 2022;4(2):022001.

   doi: 10.1088/2631-7990/ac5be6

5. Farber E, Orlov A, Borisov E, *et al*. TiNi alloy lattice structures with negative Poisson's ratio: Computer simulation and experimental results. *Metals*. 2022;12(9):1476.

   doi: 10.3390/met12091476

6. Li S, Hassanin H, Attallah MM, Adkins NJ, Essa K. The development of TiNi-based negative Poisson's ratio structure using selective laser melting. *Acta Mater.* 2016;105:75-83.

   doi: 10.1016/j.actamat.2015.12.017

7. Pan C, Han Y, Lu J. Design and optimization of lattice structures: A review. *Appl Sci*. 2020;10(18):6374.

   doi: 10.3390/app10186374

8. Maconachie T, Leary M, Lozanovski B, *et al*. SLM lattice structures: Properties, performance, applications and challenges. *Mater Des*. 2019;183:108137.

   doi: 10.1016/j.matdes.2019.108137

9. Du Plessis A, Razavi SM, Benedetti M, *et al*. Properties and applications of additively manufactured metallic cellular materials: A review. *Prog Mater Sci.* 2022;125:100918.

   doi: 10.1016/j.pmatsci.2021.100918

10. Elahinia M, Moghaddam NS, Andani MT, Amerinatanzi A, Bimber BA, Hamilton RF. Fabrication of NiTi through additive manufacturing: A review. *Prog Mater Sci.* 2016;83:630-663.

    doi: 10.1016/j.pmatsci.2016.08.001

11. Bobbert FS, Lietaert K, Eftekhari AA, *et al*. Additively manufactured metallic porous biomaterials based on minimal surfaces: A unique combination of topological, mechanical, and mass transport properties. *Acta Biomater.* 2017;53:572-584.

    doi: 10.1016/j.actbio.2017.02.024

12. Yuan B, Zhu M, Chung CY. Biomedical porous shape memory alloys for hard-tissue replacement materials. *Materials* (*Basel*). 2018;11(9):1716.

    doi: 10.3390/ma11091716

13. Liu J, Xu MY, Zhang RD, Zhang X, Xi W. Progress of porous/lattice structures applied in thermal management technology of aerospace applications. *Aerospace*. 2022;9(12):827.

    doi: 10.3390/aerospace9120827

14. Riva L, Ginestra PS, Ceretti E. Mechanical characterization and properties of laser-based powder bed-fused lattice structures: A review. *Int J Adv Manuf Technol.* 2021;113(3-4):649-671.

    doi: 10.1007/s00170-021-06631-4

15. Chen Z, Wang X, Tao Y, Wen S, Zhou Y, Shi Y. Volume fraction effect on the mechanical and shape memory properties of NiTi gyroid lattice structure fabricated by laser powder bed fusion. *JOM*. 2024;76(3):1715-1725.

    doi: 10.1007/s11837-024-06372-1

16. Shi X, Liao W, Li P, *et al*. Comparison of compression performance and energy absorption of lattice structures fabricated by selective laser melting. *Adv Eng Mater.* 2020;22(11):2000453.

    doi: 10.1002/adem.202000453

17. Alagha AN, Nguyen V, Zaki W. Effective phase transformation behavior of NiTi triply periodic minimal surface architectures. *J Intell Mater Syst Struct.* 2023;34(6):672-695.

    doi: 10.1177/1045389x221115704

18. Zhang C, Jin J, He M, Yang L. Compressive mechanics and hyperelasticity of Ni-Ti lattice structures fabricated by selective laser melting. *Crystals*. 2022;12(3):408.

    doi: 10.3390/cryst12030408

19. Jin J, Wu S, Yang L, *et al.* Ni-Ti multicell interlacing Gyroid lattice structures with ultra-high hyperelastic response fabricated by laser powder bed fusion. *Int J Mach Tools Manuf.* 2023;195:104099.

    doi: 10.1016/j.ijmachtools.2023.104099

20. Speirs M, Van Hooreweder B, Van Humbeeck J, Kruth JP. Fatigue behaviour of NiTi shape memory alloy scaffolds produced by SLM, a unit cell design comparison. *J Mech Behav Biomed Mater.* 2017;70:53-59.

    doi: 10.1016/j.jmbbm.2017.01.016

21. Zhang M, Liu C, Deng M, Li Y, Li J, Wang D. Graded minimal surface structures with high specific strength for broadband sound absorption produced by laser powder bed fusion. *Coatings*. 2023;13(11):1950.

    doi: 10.3390/coatings13111950

22. Li Z, Zhou Y, Kong X, *et al.* Sound absorption performance of a micro-perforated plate sandwich structure based on selective laser melting. *Virtual Phys Prototyp.* 2024;19(1):386-400.

    doi: 10.1080/17452759.2024.2321607

23. Kong XN, Bin L, Li ZH, Peng-Fei Z, Chao S. Research on sound absorption properties of tri-periodic minimal surface sandwich structure of selective laser melting titanium alloy. *Mater Trans.* 2023;64(4):861-888.

    doi: 10.2320/matertrans.MT-M2022164

24. Catchpole-Smith S, Selo RR, Davis AW, Ashcroft I, John Tuck C, Clare AT. Thermal conductivity of TPMS lattice structures manufactured via laser powder bed fusion. *Addit Manuf.* 2019;30:100846.

    doi: 10.1016/j.addma.2019.100846

25. Qu S, Ding J, Song X. Achieving triply periodic minimal surface thin-walled structures by micro laser powder bed fusion process. *Micromachines*. 2021;12(6):705.

    doi: 10.3390/mi12060705

26. Dong L, Zhu Q, Liu X, *et al.* 3D printing Al porous metamaterials with triply periodic minimal surfaces (TPMS) for hydrogen generation from Al-water reaction. *Int J Hydrogen Energy*. 2024;49:1426-1435.

    doi: 10.1016/j.ijhydene.2023.10.047

27. Lei HY, Li JR, Wang QH, *et al*. Feasibility of preparing additive manufactured porous stainless steel felts with mathematical micro pore structure as novel catalyst support for hydrogen production via methanol steam reforming. *Int J Hydrogen Energy*. 2019;44(45):24782-24791.

    doi: 10.1016/j.ijhydene.2019.07.187

28. Khoo ZX, Liu Y, An J, Chua CK, Shen YF, Kuo CN. A review of selective laser melted NiTi shape memory alloy. *Materials*. 2018;11(4):519.

    doi: 10.3390/ma11040519

29. Wang X, Kustov S, Van Humbeeck J. A short review on the microstructure, transformation behavior and functional properties of NiTi shape memory alloys fabricated by selective laser melting. *Materials*. 2018;11(9):1683.

    doi: 10.3390/ma11091683

30. Gao B, Zhao H, Peng L, Sun Z. A review of research progress in selective laser melting (SLM). *Micromachines*. 2023;14(1):57.

    doi: 10.3390/mi14010057

31. Jalali M, Mohammadi K, Movahhedy MR, *et al.* SLM additive manufacturing of NiTi porous implants: A review

of constitutive models, finite element simulations, manufacturing, heat treatment, mechanical, and biomedical studies. *Met Mater Int.* 2023;29(9):2458-2491.

doi: 10.1007/s12540-023-01401-1

32. Speirs M, Wang X, Van Baelen S, *et al*. On the transformation behavior of NiTi shape-memory alloy produced by SLM. *Shape Mem Superelasticity*. 2016;2(4):310-316.

    doi: 10.1007/s40830-016-0083-y

33. Haberland C, Elahinia M, Walker JM, Meier H, Jan F. On the development of high quality NiTi shape memory and pseudoelastic parts by additive manufacturing. *Smart Mater Struct.* 2014;23(10):104002.

    doi: 10.1088/0964-1726/23/10/104002

34. Ma J, Yu L, Yang Q, Liu J, Yang L. High-superelasticity NiTi shape memory alloy by directed energy deposition-arc and solution heat treatment. *Acta Metall Sin* (*Eng Lett*). 2024;37(1):132-44.

    doi: 10.1007/s40195-023-01659-9

35. Saedi S, Turabi AS, Andani MT, Moghaddam NS, Elahinia M, Karaca H. Texture, aging, and superelasticity of selective laser melting fabricated Ni-rich NiTi alloys. *Mater Sci Eng A*. 2017;686:1-10.

    doi: 10.1016/j.msea.2017.01.008

36. Lu HZ, Ma HW, Cai WS, *et al*. Stable tensile recovery strain induced by a Ni4Ti3 nanoprecipitate in a Ni50.4Ti49.6 shape memory alloy fabricated via selective laser melting. *Acta Mater.* 2021;219:117261.

    doi: 10.1016/j.actamat.2021.117261

37. Chen F, Lu J, Liu Y, Zhang H, Zhang C, Shen Q. Microstructure and mechanical properties of NiTi shape memory alloys by laser engineered net shaping. *Adv Eng Mater.* 2023;25(5):2200504.

    doi: 10.1002/adem.202200504

38. Khoo ZX, An J, Chua CK, Shen YF, Kuo CN, Liu Y. Effect of heat treatment on repetitively scanned SLM NiTi shape memory alloy. *Materials*. 2018;12(1):77.

    doi: 10.3390/ma12010077

39. Yan B, Zhang Y, Jiang S, Yu J, Sun D, Tang M. Mechanical properties and fracture mechanisms of martensitic NiTi shape memory alloy based on various thermomechanical-processing microstructures. *J Alloys Compd*. 2021;883:160797.

    doi: 10.1016/j.jallcom.2021.160797

40. Ma C, Gu D, Setchi R, *et al*. A large compressive recoverable strain induced by heterogeneous microstructure in a $Ni_{50.6}Ti_{49.4}$ shape memory alloy via laser powder bed fusion and subsequent aging treatment. *J Alloys Compd*. 2022;918:165620.

    doi: 10.1016/j.jallcom.2022.165620

41. Bayati P, Safaei K, Nematollahi M, *et al*. Toward understanding the effect of remelting on the additively manufactured NiTi. *Int J Adv Manuf Technol.* 2021;112(1):347-360.

    doi: 10.1007/s00170-020-06378-4

42. Zhan JB, Lu YJ, Lin JX. On the martensitic transformation temperatures and mechanical properties of NiTi alloy manufactured by selective laser melting: Effect of remelting. *Acta Metall Sin* (*Engl Lett*). 2021;34(9):1223-1233.

    doi: 10.1007/s40195-021-01212-6

43. Yuan L, Gu D, Lin K, *et al.* Electrically actuated shape recovery of NiTi components processed by laser powder bed fusion after regulating the dimensional accuracy and phase transformation behaviour. *Chin J Mech Eng Addit Manuf Front.* 2022;1(4):100056.

    doi: 10.1016/j.cjmeam.2022.100056

44. Lu HZ, Liu LH, Yang C, *et al* Simultaneous enhancement of mechanical and shape memory properties by heat-treatment homogenization of Ti_2Ni precipitates in TiNi shape memory alloy fabricated by selective laser melting. *J Mater Sci Technol.* 2021;101:205-216.

    doi: 10.1016/j.jmst.2021.06.019

45. Zhu J, Wu HH, Wu Y, *et al*. Influence of Ni4Ti3 precipitation on martensitic transformations in NiTi shape memory alloy: R phase transformation. *Acta Mater.* 2021;207:116665.

    doi: 10.1016/j.actamat.2021.116665

46. Gu DD, Ma CL. *In-situ* formation of Ni_4Ti_3 precipitate and its effect on pseudoelasticity in selective laser melting additive manufactured NiTi-based composites. *Appl Surf Sci.* 2018;441:862-870.

    doi: 10.1016/j.apsusc.2018.01.317

47. Yu H, Qiu Y, Young ML. Influence of Ni_4Ti_3 precipitate on pseudoelasticity of austenitic NiTi shape memory alloys deformed at high strain rate. *Mater Sci Eng A*. 2021;804:140753.

    doi: 10.1016/j.msea.2021.140753

48. Liu G, Chen D, Tan F, *et al*. Effects of annealing on softening and hardening behaviors of 60NiTi alloy. *J Mater Res Technol.* 2022;21:3220-3234.

    doi: 10.1016/j.jmrt.2022.10.093

49. Saedi S, Turabi AS, Taheri Andani M, Haberland C, Karaca H, Elahinia M. The influence of heat treatment on the thermomechanical response of Ni-rich NiTi alloys manufactured by selective laser melting. *J Alloys Compd*. 2016;677:204-210.

    doi: 10.1016/j.jallcom.2016.03.161

50. Zhang M, Li J, Liao X, Xu M, Shi W. Influence of cycle number on the compression behavior of nonlinear periodically gradient porous structures produced by laser powder bed fusion. *Mater Des.* 2022;223:111257.

doi: 10.1016/j.matdes.2022.111257

51. Chen W, Yang Q, Huang S, Kruzic JJ, Li X. Compression behavior of graded NiTi gyroid-structures fabricated by laser powder bed fusion additive manufacturing under monotonic and cyclic loading. *JOM*. 2021;73(12):4154-4165.

    doi: 10.1007/s11837-021-04938-x

52. Sun L, Chen K, Geng P, Zhou Y, Wen S, Shi Y. Mechanical and shape memory properties of NiTi triply periodic minimal surface structures fabricated by laser powder bed fusion. *J Manuf Processes*. 2023;101:1091-100.

    doi: 0.1016/j.jmapro.2023.06.034

53. Bhardwaj A, Ojha M, Garudapalli A, Gupta AK. Microstructural, mechanical and strain hardening behaviour of NiTi alloy subjected to constrained groove pressing and ageing treatment. *J Mater Process Technol*. 2021;294:117132.

    doi: 10.1016/j.jmatprotec.2021.117132

54. Sinha A, Rajak DK, Shaik NB, *et al*. A review on 4D printing of Nickel-Titanium smart alloy processing, the effect of major parameters and their biomedical applications. *Proc Inst Mech Eng E J Process Mech Eng*. 2023.

    doi: 10.1177/09544089231154416

55. Mohd Jani J, Leary M, Subic A, Gibson G. A review of shape memory alloy research, applications and opportunities. *Mater Des* (*1980-2015*). 2014;56:1078-1113.

    doi: 10.1016/j.matdes.2013.11.084

56. Yang X, Yang Q, Shi Y, *et al*. Effect of volume fraction and unit cell size on manufacturability and compressive behaviors of Ni-Ti triply periodic minimal surface lattices. *Addit Manuf*. 2022;54:102737.

    doi: 10.1016/j.addma.2022.102737

ACCSCIENCE PUBLISHING

Materials Science in Additive Manufacturing

ORIGINAL RESEARCH ARTICLE

Developing a sustainable resin for 3D printing in coral restoration

Yukai Jia, Sherin Abdelrahman, and Charlotte A.E. Hauser*

Laboratory for Nanomedicine, King Abdullah University of Science and Technology, Thuwal, Saudi Arabia

Abstract

Coral reefs boast one of the planet's most diversified ecosystems, serving as an essential source of food and revenue for millions of people while providing shelter to a wide variety of marine creatures. However, overfishing, pollution, climate change, and other factors collectively pose an escalating danger to coral reefs. Therefore, coral reef restoration efforts are urgently needed to save corals. In this study, we exploited 3D printing technology based on vat polymerization to fabricate artificial coral plugs, expediting the reef restoration process while minimizing labor costs. We have developed a scalable model through the photoinitiated polymerization of an eco-friendly resin composed of modified soybean oil and calcium carbonate which has the potential to significantly enhance global restoration efforts. Material characterization demonstrated that the printed scaffold was highly cross-linked. Based on cytotoxicity analysis, the printed scaffold exhibited excellent cell adhesion and proliferation characteristics. The coral microfragmentation experiment showed initial signs of coral settlement on the printed coral plugs. This work demonstrates that plant-based material and vat-polymerization-based 3D printing techniques hold promise for coral restoration.

Keywords: Coral restoration; 3D printing; Sustainable resin; Calcium carbonate-based ink; Vat polymerization; Acrylated epoxidized soybean oil

***Corresponding author:**
Charlotte A. E. Hauser
(chauser@age.mpg.de)

Citation: Jia Y, Abdelrahman S, Hauser CAE. Developing a sustainable resin for 3D printing in coral restoration. *Mater Sci Add Manuf.* 2024;3(2):3125. doi: 10.36922/msam.3125

Received: March 9, 2024

Accepted: April 11, 2024

This article has been updated with modifications. See the correction notice (doi: 10.36922/msam.corr081624).

1. Introduction

A coral reef is a diverse underwater ecosystem that provides refuge and protection to a variety of marine species.[1] However, due to pollution, overfishing, climate change, and other factitious factors, coral reefs are now under unprecedented peril.[2,3] Coral bleaching, a process characterized by the loss of vibrant symbiotic algae (*e.g.*, Zooxanthellae), has become increasingly common, rendering corals more vulnerable to disease and mortality.[4] Numerous coral reefs worldwide are experiencing a decline, and by predictions, as much as 90% of coral reefs could vanish by 2050 if conservation measures are not implemented.[5]

Coral reefs are mostly constructed by calcium carbonate skeletons and colonial marine animals known as coral polyps.[6] The coral polys can spread in two-dimensional (2D) areas and three-dimensional (3D) volumes by the secretion of calcium carbonate. The secretion of the calcium carbonate skeleton is very slow and serves as a rate-determining process, with an average vertical extension rate of 1 – 10 cm/year.[7] Thus, many coral restoration projects concentrate on supporting and facilitating the growth of coral skeletons.

The rapid development of 3D printing technology (also known as additive manufacturing) in recent years has offered a promising tool for coral restoration purposes.[8] 3D printing can produce 3D objects by layering materials such as plastic, ceramic, or metal according to the digital design.[9] Artificial reefs that mirror the complexity and morphology of the original coral reefs have been made using this technology, offering coral polyps a substrate to attach and flourish.

3D printing enables exact control over the size and structure of the artificial reef, allowing it to be customized to the unique requirements of various coral species and marine environments with less labor.[10] However, some issues still need to be resolved, such as ensuring the materials/resin used for 3D printing are secure for marine life in the long term, as well as optimizing the structural design. In addition, the cost of the materials and the scalability of the prints are also topics of concern. Despite the challenges, researchers have been actively exploring various 3D printing techniques for coral restoration purposes and have already made some significant progress.

One of the examples is the "Coral Carbonate" project, led by the objects and ideograms design workshop.[11] They created a calcium carbonate-based coral skeleton using binder jetting technique,[12] with the powder ground from natural coral rubble. Paste-based extrusion is another popular technique for coral restoration.[13] Examples of such applications include 3DPARE modules[14] and the Rexcor reef by XtreeE.[15]

Vat polymerization is a widely used 3D printing technique that falls under the category of photopolymerization processes. One of the most common vat polymerization methods is digital light processing (DLP), a technique that utilizes a digital light projector to selectively cure photopolymer resins.[16] In general, DLP offers faster printer speed and different material selection compared to other printing techniques. To the best of our knowledge, coral restoration projects using the vat polymerization technique are rarely reported thus far.

One of the key challenges in 3D printing of coral skeletons is choosing the appropriate materials/resin for printing. Further investigations on many conventional 3D printing materials, such as thermoplastics and metals, are warranted due to their potential to leach harmful chemicals or micro-plastics and their limited degradability over time.[17] As a result, a range of biocompatible and environmentally friendly materials have been explored such as limestone.[18] In addition, ceramic terracotta materials have been utilized to create 3D-printed ceramic tiles,[19] effectively mimicking the morphologies of natural coral structures. In recent years, biodegradable substrates have gained prominence in many applications. Biopolymer-based materials, specifically designed to degrade over time, can provide temporary support for coral growth while promoting natural integration with the surrounding environment.

One of the most common examples is acrylated epoxidized soybean oil (AESO). AESO is a form of acrylate polymer that originates from the chemical transformation of soybean oil. This process involves the initial reaction of soybean oil with hydrogen peroxide to produce epoxidized soybean oil (ESO). Following this, ESO is further processed through a reaction with acrylic acid or methacrylic acid, forming AESO.[20,21] The resulting AESO has a high degree of functionality due to the high double bond concentration from the acrylate group, allowing it to be used as a resin for 3D printing[22-24] and other applications. AESO-based resin affords eco-friendly and sustainable ways to construct biomaterials.[25] The molecular structure of AESO consists of natural fatty acids, which have negligible cytotoxicity.

Previously, our group at the Laboratory for Nanomedicine developed a specialized ink called calcium carbonate-photoinitiated ink (CCP) by mixing 70% commercially available photocurable resin (Anycubic Plant-Based UV Resin, China) with 30% calcium carbonate to fabricate coral skeletons using extrusion-based 3D printing.[26] In this work, the primary objective is to optimize the CCP and modify the current formulation to develop a more sustainable resin formulation for fabricating 3D coral plugs using the DLP printing technique. In addition, we aim to evaluate the biocompatibility of the modified CCP with coral fragments and assess its cytotoxicity to cells. In the subsequent chapter, the resin will be referred to as "modified CCP."

In addition, various material characterizations were conducted to test the scaffold's composition, morphology, glass transition temperature, and wettability. This study advances the coral restoration effort using sustainable plant-based soybean oils and vat photopolymerization method. With continued research and innovation, we hope to see more practical and cost-effective solutions soon that can help protect and preserve coral reefs for generations to come.

2. Experimental methods

2.1. Resin preparation and coral plugs fabrication

The objective of this paper is to print a relatively simple structure, namely, coral plugs for the microfragmentation experiment. These plugs are widely used in the realm of coral restoration.[27] Figure 1 shows an example of commercially

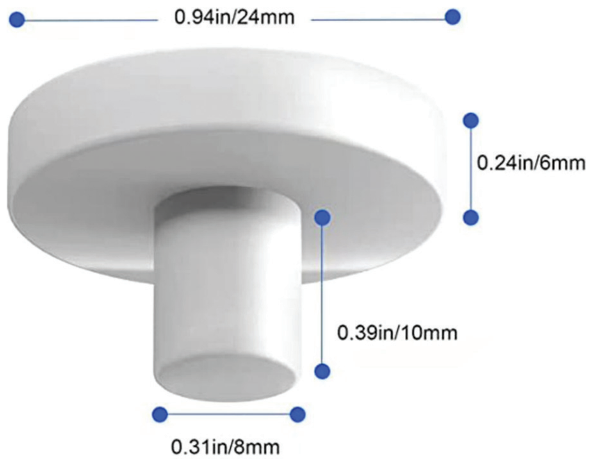

Figure 1. Schematic illustration of commercial coral plugs with dimensions.

available coral plugs that are made of ceramic. Computer-aided design (CAD) software was utilized to design the model for printing.

2.1.1. Preparation of AESO resin

The process of preparing the AESO resin can be described as follows: 80 g of AESO (containing 4000 ppm monomethyl ether hydroquinone as an inhibitor; Sigma-Aldrich, USA) was mixed with 80 mL of acetone (HPLC grade) and 20 g of 1,6-hexanediol diacrylate (Sigma-Aldrich, USA). The mixture was stirred thoroughly to achieve a homogeneous solution. Then, 1.25 g of bis(2,4,6trimethyl benzoyl)-phenylphosphineoxide (Irgacure 819; Sigma-Aldrich, USA) was added to the solution. The mixture was stirred until the photoinitiator was fully dissolved and then placed in a vacuum chamber for 2 days to remove the solvent. The resulting yellow resin can be used for 3D printing (referred to as AESO resin).

2.1.2. Preparation of modified CCP resin

The AESO resin, weighing 100 g, was thoroughly mixed with 43 g of fine calcium carbonate powder (particle size ≤50 µm, with a purity of 98%; Thermo Scientific, USA). The ratio of AESO resin to calcium carbonate is 7:3. The resulting resin, which appeared white/yellowish in color, was utilized for 3D printing. The size of the filler particles (calcium carbonate) needs to be smaller than the height of each printing layer to ensure successful printability. In addition, the selection of the specific calcium carbonate type is significant. It was found that finer calcium carbonate particles facilitate their integration with resin matrix.

2.1.3. 3D printing of CCP and AESO coral plugs

CCP coral plugs were printed through vat polymerization using a tabletop DLP-based printer (ELEGOO Mars 3). The wavelength of the ultraviolet (UV) light source is 405 nm. After polymerization, the coral plugs were lifted off the building platform, soaked, and washed in 70% isopropanol for 30 min to remove unpolymerized ink and photoinitiator. Subsequently, the coral plugs were cured for 60 min at 40°C in the Formlab UV curing machine to enhance the mechanical strength of the structures.

2.2. Material characterizations

2.2.1. Fourier transform infrared (FTIR) spectroscopy

A FTIR spectrometer (FTIR-Nicolet iS50R, Thermo Scientific Instrument, USA) equipped with a built-in wide-range diamond ATR was used to analyze the AESO sample before and after curing. The scan range was between 400 and 3800 cm^{-1} with a resolution of 5 cm^{-1}.

2.2.2. Scanning electron microscopy

The surface morphology of the printed CCP scaffold was analyzed using a scanning electron microscope (SEM; Zeiss Merlin SEM-61-95, Zeiss, Germany) operating under a 5.0 kV accelerating voltage electron beam. Before imaging, the samples were sputter-coated with gold to dissipate the charge that builds up during SEM imaging. The gun vacuum and system vacuum were maintained at 9.26×10^{-10} mbar and 1.37×10^{-5} mbar, respectively. The current probe (I Probe) was set to 100 pA.

2.2.3. Water contact angle

The surface wettability of the printed CCP scaffold was assessed using a contact angle analyzer (DSA100E, Kruss-Scientific, Germany). Approximately 2.2 µL of deionized water was dispensed onto the surface of the samples. The entire process of water deposition and sample absorption was recorded. The first image captured after water deposition was utilized for static water contact angle measurements. The measurements were conducted at room temperature and repeated 6 times for accuracy.

2.2.4. Thermogravimetric analysis (TGA)

The decomposition of the printed AESO and CCP scaffold was analyzed using a TGA analyzer (Discovery TGA 5500, TA Instruments, USA). Initially, the sample was equilibrated at a temperature of 50°C and then heated from 50°C to 900°C at a programmed ramp rate of 10°C/min. The heating process was conducted in a nitrogen atmosphere.

2.2.5. Differential scanning calorimetry

The glass transition temperature (Tg) of the printed AESO scaffold was measured using a differential scanning calorimeter from TA Instruments (Discovery 250) at a programmed ramp rate of 10°C/min. The sample underwent a two-step cycle:

(i) Heating from room temperature to 160°C and holding at 160°C for 1 min.
(ii) Cooling from 160°C to −30°C and holding for another 1 min.

Subsequently, the second cycle was used to determine the Tg:

(i) Heating from −30°C to 160°C.
(ii) Holding at 160°C for 1 min.
(iii) Decreasing from 160°C to room temperature.

2.2.6. Cytotoxicity analysis

The scaffold, as depicted in Figure 2, was 3D-printed using the modified CCP resin. It features a diameter of 5 mm and a minimal height of 0.3 mm, with four holes incorporated to facilitate visualization of the cells. In post-printing, the scaffolds underwent a thorough cleaning process using 95% ethanol to remove any uncured resin. Subsequently, they were cured for 2 h using the Formlab UV curing machine at room temperature. To ensure sterilization, all printed constructs were immersed in 70% ethanol for 30 min. Before cell culturing, the scaffolds were further soaked in phosphate-buffered saline (PBS, 1×) overnight.

Human neonatal dermal fibroblasts (HDFs; Cat. #C0045C, Gibco, USA) were selected as the most suitable cell type to test the cytotoxicity of the printed material and investigate potential biomedical applications. Fibroblasts are integral in synthesizing the extracellular matrix (ECM), playing a pivotal role in wound healing, tissue repair, and tissue homeostasis.[28] Due to their sensitivity to toxic substances, fibroblasts exhibit noticeable cellular responses when exposed to cytotoxic materials, making them suitable indicators of potential harm to cells.[29] Moreover, fibroblasts are readily available from commercial sources and research institutions, facilitating experimentation and ensuring consistency in cell sources.

Given our interest in the potential biomedical applications of the modified CCP resin, a peptide-based hydrogel was employed to establish an ECM environment. This hydrogel, mimicking the collagen structure found in the ECM, has the capacity to create a 3D microenvironment that closely resembles native tissues.[30] Among the various ultrashort self-assembling peptides tested, ultrashort self-assembling peptide IIZK (Ac-Ile-Ile-Cha-Lys-NH_2) was selected. This peptide has previously been successfully utilized in the Laboratory for Nanomedicine to create diverse 3D *in vitro* cellular models.[31-33]

The study utilized a 96-well assay plate (white plate, clear bottom; Corning, USA). The vertical plate layout for the experiment is structured as follows:

(i) The six columns on the left are designated for adenosine triphosphate (ATP) analysis, a method employed to measure cell proliferation by detecting ATP, a biomarker of active cellular metabolism.[34]
(ii) The middle three columns are reserved for the live/dead assay, which is performed to assess cell viability and distinguish between live and dead cells.[35]
(iii) The right three columns are allocated for studying the cytoskeleton, enabling investigation of cell structure and morphology.[36]

This plate layout facilitates efficient analysis of various aspects of cell behavior and responses in a high-throughput manner. Figure 3 offers a visual representation of the plate layout.

The horizontal plate layout for the experiment is structured as follows:

(i) First row: Reserved for printed constructs only.
(ii) Second row: Reserved for printed constructs and IIZK-based hydrogel at 2 mg/mL.
(iii) Third row: Cells cultured in IIZK-based hydrogel at 2 mg/mL (control).
(iv) Fourth row: Cells cultured directly on the well plate in two dimensions (control).

The experimental procedure involved transferring printed constructs from 1× PBS to the first two rows of the 96-well assay plate. Subsequently, the IIZK peptide

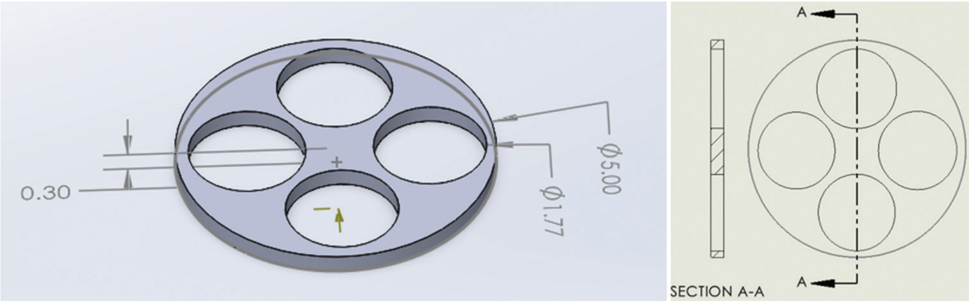

Figure 2. The “button” design of the construct for cytoxicity study.

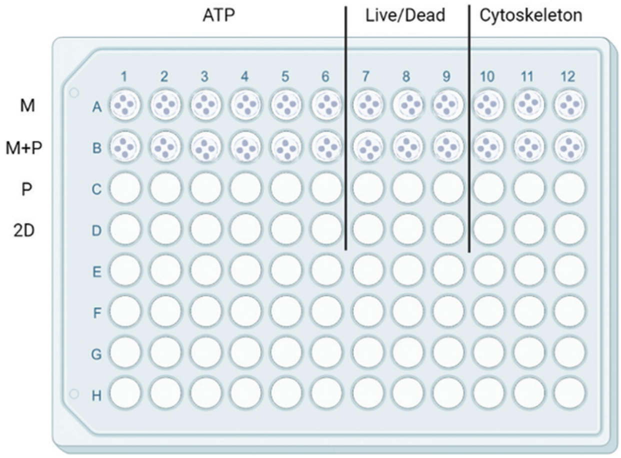

Figure 3. Schematic illustration of the cytotoxicity assay.

powder was weighed to prepare a 2 mg/mL hydrogel. The undissolved peptide powder was sterilized inside the bio-fume hood under UV light for 45 min. Sterile nuclease-free water (Ambion, USA) was used to dissolve the peptide powder. After complete dissolution, 20 μL peptide solution was dispensed into each well. An equal volume (20 μL) of 2× DPBS ($-Ca^{2+}/-Mg^{2+}$) (Gibco, USA) was added to the well plate. Gentle mixing of the peptide with PBS facilitated the self-assembly process of the peptide compound into a hydrogel within 5 min at room temperature.

HDFs obtained from Gibco, USA, at passages 5 – 9, were cultured in Dulbecco's Modified Eagle Medium (DMEM, Gibco, USA) supplemented with 1% penicillin/streptomycin (Gibco, USA) and 10% fetal bovine serum (FBS; Gibco, USA) and in T75 flask (Nunc™ EasYFlask™ Cell Culture Flasks, USA) until reaching 70 – 80% confluency. Subsequently, HDFs were trypsinized, and the cell count was determined using a TC20 automated cell counter (BioRad, USA).

The cells were divided into two groups for the experiments. Each well designated for ATP analysis requires approximately 5000 cells, while each well for the Live/Dead assay and cytoskeleton assay requires around 20,000 cells. To ensure proper cell suspension, complete media was added to achieve a final volume of 200 μL in each well. After seeding the cells, the 96-well assay plates were placed inside the incubator, and the media were replenished every 3 days to maintain cell viability and growth. For this study, a total of three plates were prepared for analysis on days 1, 3, and 7, allowing for multiple time points to assess the cellular responses and behavior to the printed construct over time.

The Live/Dead Kit for mammalian cells (Thermo Fisher Scientific, USA) was utilized across the four mentioned conditions to evaluate the viability of HDFs. This kit enables the discrimination of live cells, which emit vibrant green fluorescence on interaction with calcein (excitation/emission ~494/517 nm). Simultaneously, ethidium homodimer-1 (EthD-1; excitation/emission ~528/617 nm) binds to the DNA of the dead cells with compromised cell membranes and releases red fluorescent light.[37]

The procedure involved replacing the culture media with a mixture of EthD-1 and calcein diluted in 1× PBS. This mixture was then incubated with the cells for 25 min at room temperature. Subsequently, a fluorescence microscope (EVOS M7000 Imaging System) was utilized to capture images of the cells and analyze their viability.

In addition, to evaluate HDF proliferation under four different conditions, the CellTiter- Glo 3D Cell Viability Assay (Promega, USA) was employed. This assay relies on quantifying the luminescent signal resulting from the release of ATP by metabolically active cells. To conduct the assay, half of the media in each well was replaced with the ATP reagent. After a 25-min incubation at room temperature, the released ATP was measured using a BMG Labtech microplate reader (USA) on days 1, 3, and 7 of the cell culture plate. The ATP assay provided valuable quantitative data regarding cell proliferation and metabolic activity in response to the varying conditions, offering critical insights into cell behavior throughout the experiment.

HDF cytoskeleton staining was performed to analyze the cells' morphology by staining the actin fibers and structure. Actin fibers are thin and flexible proteins that provide structural support to the cells.[38] The staining of actin fibers was performed using rhodamine phalloidin (Invitrogen, Thermo Fisher Scientific, USA) with excitation/emission wavelengths of approximately 540/565 nm.[39] The cells were fixed with 4% paraformaldehyde (SantaCruz Biotechnology, USA) for 30 min, followed by washing with 1× PBS. Subsequently, cell permeabilization was achieved through a buffer solution containing 3 mM $MgCl_2$, 300 mM sucrose, and 0.5% Triton X-100 in 1× PBS solution. Each well received 40 μL of the permeabilization buffer. After 5 min of incubation, a blocking buffer consisting of 0.02% sodium azide (Sigma Aldrich, USA), 5% FBS and 0.1% Tween-20 (Sigma Aldrich, USA) in 1× PBS was added (50 μL per well), and the mixture was incubated at room temperature for 25 min.

Next, rhodamine phalloidin was diluted to a ratio of 1:40 in 1× PBS and then added to the cells, followed by incubation at room temperature for 2 h. Cells were washed again with 1× PBS and then incubated for 5 min with 4, 6-diamidino-2-phenylindole (DAPI), which was diluted to a ratio of 1:1500 in sterile nuclease-free water to stain the cells' nuclei.[40] The imaging of the stained cells was conducted using the EVOS M7000 Imaging System, and a confocal microscope (LSM 710 Laser Scanning Confocal Microscope, Germany) was used for higher resolution and Z-stack images.[41]

2.2.7. Microfragmentation on coral plugs

To evaluate the suitability of the materials for coral restoration, healthy coral fragments retrieved from the Red Sea were carefully chosen and fixed onto three printed AESO and modified CCP resin coral plugs. Serving as comparative controls, three ceramic coral plugs (Reefing Art Ceramic Coral Frag Plugs, USA), commonly utilized in the coral restoration field, were included in the experiment. The coral fragments, ranging approximately 1.5–2.5 cm in size, were carefully excised from the same colony to maintain uniformity (*Acropora* species).[42] To securely attach the coral fragments to the plugs, a small quantity of coral glue (Aqua Medic Coral Construct, Switzerland) was applied at the center of the coral plugs. Subsequently, the coral plugs with the attached fragments were affixed to a mesh and placed in an outdoor seawater tank for further observation and growth monitoring before out-planting, as depicted in Figure 4. The seawater tank was maintained at specific environmental conditions, with a pH of 8.2, temperature of 25.7°C, and salinity level of 4.1 g/100 g. The coral plugs within the tank were carefully monitored every week to evaluate the coral growth and development. Regular deep tank cleaning was conducted to mitigate algae overgrowth on coral, thereby maintaining an environment conducive to the growth of the coral fragments.

3. Results and discussion

In this section, we present the results of successfully printing the coral plugs using the novel AESO and modified CCP resin, employing a table-top stereolithography printer (LCD-based, ELEGOO Mars 3), as depicted in Figure 5. The UV light source utilized had a wavelength of 405 nm, facilitating the printing of the coral plugs in good resolution.

3.1. Effect of adding diluent to resin formulation

The impact of the diluent is evident in Figure 6, where the coral plug on the right side, printed without the diluent, appears distorted. In contrast, the plug on the left side, printed with the addition of diluent, displays improved structural integrity. Incorporating a diluent, also known as monomer or thinner, into the resin offers several benefits for 3D printing: Diluents effectively reduce the resin's viscosity, making it less thick and facilitating smoother flow.[43] During the printing process, as each layer is formed, the building platform is lifted, requiring the resin to flow beneath it to ensure adequate resin for the subsequent layer.[44] Moreover, the acrylate diluent reinforces the mechanical strength of the cured AESO resin by promoting a higher level of crosslinking. The AESO molecules, being relatively bulky, face challenges in initiating polymerization through their double bonds. However, introducing a smaller monomer facilitates a more efficient crosslinking process, leading to improved mechanical properties in the final printed object.[45] In addition, the acrylate diluent enhances the solubility of the photoinitiator within the resin. For instance, Irgacure 819 demonstrates relatively good solubility in 1,6-hexanediol diacrylate (HDDA) at 10% w/v.[46] In terms of cost evaluation, diluting the resin with a diluent reduces the consumption of the original, more expensive resin. Reducing material usage helps to minimize waste and lowers production costs, making the 3D printing process more economically viable.

However, excessive dilution can compromise the mechanical properties and final quality of the printed

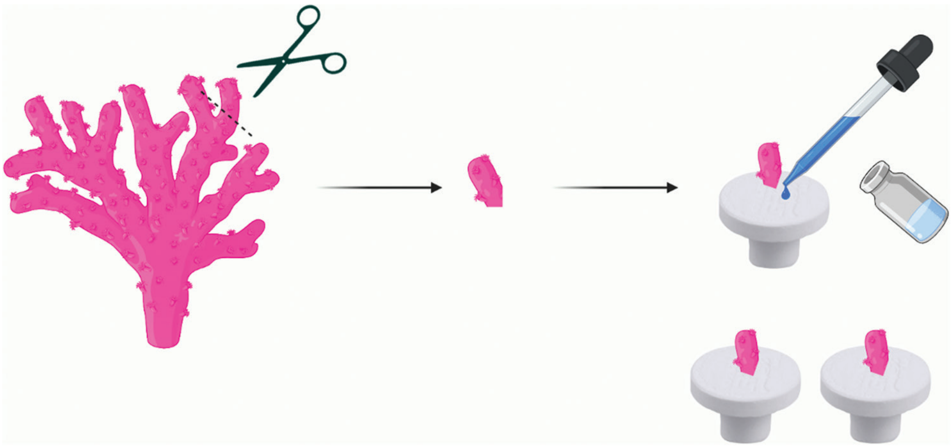

Figure 4. Schematic illustration of coral microfragmentation on coral plug.

object. In this study, the AESO and HDDA diluent ratio of 4:1 was found to achieve an optimal combination of improved flow, reinforced strength of the print, and cost-efficient resin utilization, ensuring successful 3D printing outcomes.

3.2. FTIR analysis

The FTIR analysis provides conclusive evidence of the polymerization of AESO resin after printing (Figure 7). The observed signals at 1635 to 1618 cm^{-1} correspond to the carbon-carbon double bond stretching in the acrylic acid within AESO. These signals display a significant reduction after the reaction, indicating the successful polymerization of the carbon-carbon double bonds. Moreover, the reduction in peaks at 1406 and 810 cm^{-1} further confirms the reduction of double bonds. These signals are associated with the bending of the double bonds. Another noteworthy observation is the shift in signals from 1186 to 1159 cm^{-1} after the polymerization, corresponding to the C-O-C oscillation in the ester group. Given the proximity of the C-O-C group to the double bond, any decrease in the presence of double bonds would influence the oscillation pattern of the C-O-C group.[47]

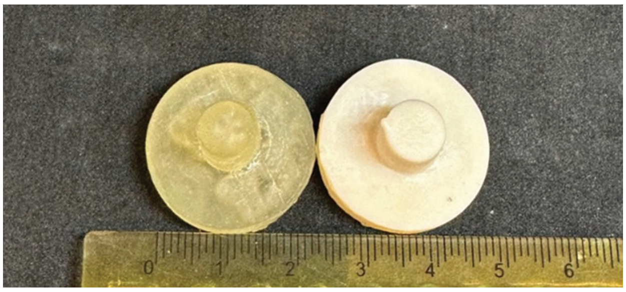

Figure 5. Coral plugs printed in acrylated epoxidized soybean oil resin (left) and modified calcium carbonate-photoinitiated resin (right).

Figure 6. Resin with diacrylate diluent printed coral plug (on the left) and resin without diacrylate diluent printed (on the right).

3.3. TGA analysis

According to the TGA spectra of the printed AESO and CCP scaffold shown in Figure 8, it can be observed from the left spectrum that cured AESO resin starts to decompose at approximately 350°C and completely burns away at 800°C.[48] The right spectrum shows a 70% weight loss at approximately 400°C. This weight loss corresponds to the decomposition of the organic part of the modified CCP resin. On the other hand, calcium carbonate decomposes at 750 °C, producing carbon dioxide and calcium oxide.[49] The weight loss observed corresponds to 12.6% carbon dioxide, indicating that calcium carbonate accounts for approximately 28.7% of the sample's composition.

3.4. Differential scanning calorimetric analysis

The differential scanning calorimetric spectrum (Figure 9) reveals that the glass transition temperature of the printed AESO resin is 48°C. The absence of a distinct sharp melting peak indicates the high degree of crosslinking in the printed AESO scaffold and shows the lack of crystalline domains.[50]

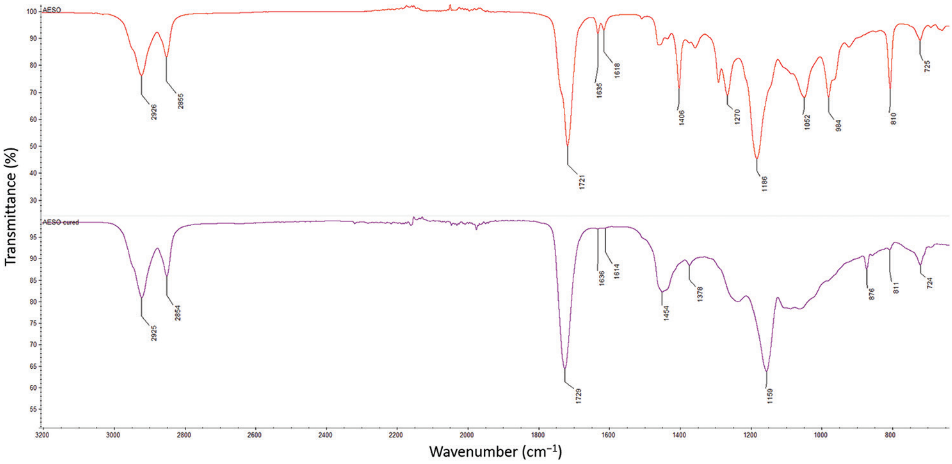

Figure 7. Fourier transform infrared spectra of acrylated epoxidized soybean oil (AESO) resin (top) and printed AESO scaffold (bottom).

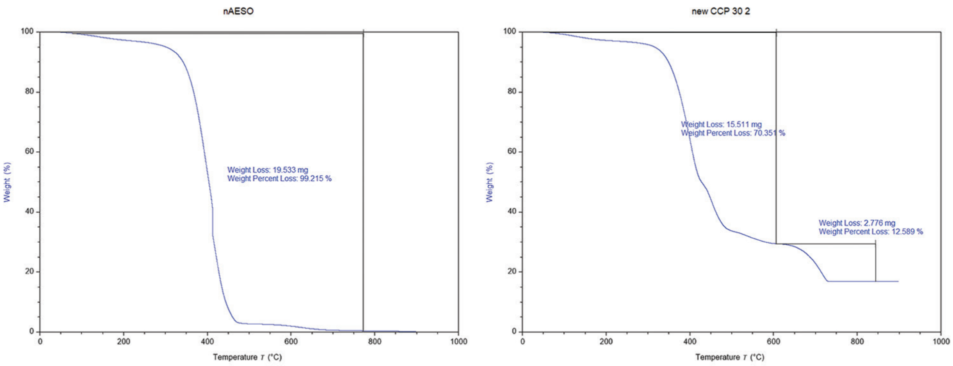

Figure 8. Thermogravimetric analysis spectra of the printed acrylated epoxidized soybean oil scaffold (left) and printed calcium carbonate-photoinitiated scaffold (right), ramp 10°C/min from 50°C to 900°C.

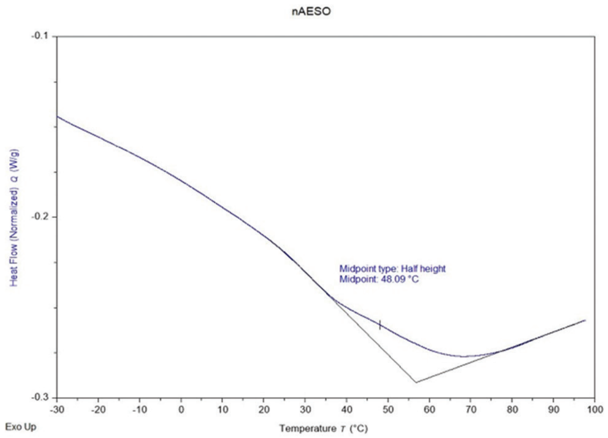

Figure 9. Differential scanning colorimetric analysis of the printed acrylated epoxidized soybean oil scaffold, ramp 10°C/min from −30°C to 100°C.

3.5. Cytoxicity assay

In the fluorescent microscopy images (Figure 10, Live/Dead assay), live cells are stained in vibrant green, while dead cells in red. Notably, on day 1, cells already covered a small part of the construct. By day 3, the cells had substantially spread across the construct, showing rapid growth and colonization. Finally, by day 7, the cells had fully covered the entire area of the construct, indicating successful proliferation and tissue development. Importantly, only a few dead cells were observed in these images, affirming the favorable biocompatibility and suitability of the material for cell culture applications.

Regarding the experimental setup that involves wells containing both the material construct and the peptide hydrogel, cells were observed within the material substrate and the hydrogel matrix. The hydrogel effectively simulates the microenvironment akin to the ECM. This observation highlights the potential of modified CCP resin for biomedical applications beyond its coral restoration context.

The confocal microscopy images, seen in Figure 11, provide a more detailed view of the cells' morphology and structures. Z-stack images show that the cells have spread throughout the entire layer of the constructs, indicating that the printed CCP construct enables good cell attachment and growth. For a more comprehensive understanding, the videos of the Z-stack, taken on days 3 and 7 (Videos S1 and S2, respectively), provide dynamic insights into the cellular behavior and distribution within the constructs. These supplementary confocal videos depict HDFs spreading on the printed CCP construct.

The ATP assay reveals a notable trend in cell proliferation across all four conditions, with ATP luminescence values consistently rising from day 1 to day 7 (Figure 12). Interestingly, the sample featuring solely the printed CCP construct consistently demonstrated the highest ATP levels at all three time points. Following closely is the sample combining the printed CCP construct with the peptide hydrogel. This pattern underscores the potential of the printed CCP construct to enhance cell metabolism and proliferation significantly.

3.6. Water contact angle

Water contact angle measurements provide valuable insights into surface-wetting behavior. The measured water contact angle of the printed CCP construct was 77.4° (*n* = 5, SD = 0.64), indicating its hydrophilic nature. A representative image is shown in Figure 13. This low contact angle value potentially enhances favorable cell attachment, growth, and biocompatibility.[51] Moreover, the composition of AESO resin primarily consists of hydroxyl and ester groups. Both groups are recognized as being biocompatible.[52] The water contact angle for ceramic plugs can vary depending on factors such as the specific type of ceramic material, its surface treatment,

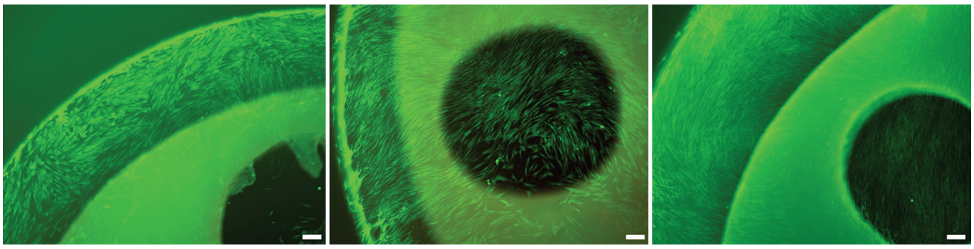

Figure 10. Fluorescent microscopy images of human dermal fibroblasts spreading on the printed calcium carbonate-photoinitiated construct on days 1, 3, and 7, from left to right. Scale bars: 150 μm.

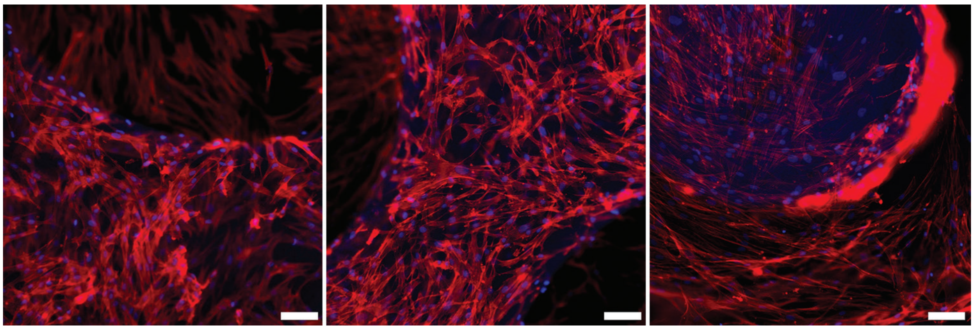

Figure 11. Confocal images of human dermal fibroblasts spreading on the printed calcium carbonate-photoinitiated construct on days 1, 3, and 7, from left to right. Scale bars: 100 μm.

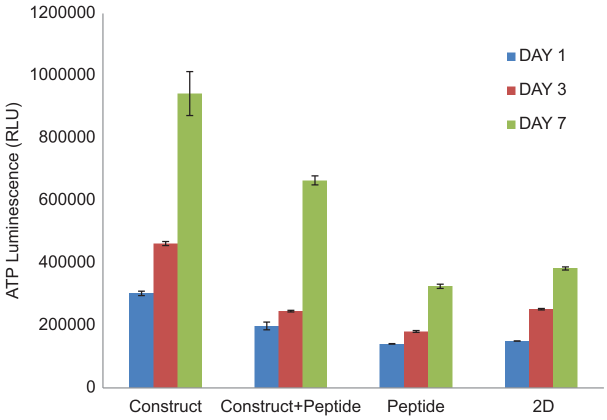

Figure 12. Adenosine triphosphate levels of human dermal fibroblasts cultured in construct, construct + peptide, peptide, and two dimensions measured at days 1, 3, and 7.

and the cleanliness of the surface. In general, ceramic surfaces tend to be also hydrophilic, meaning that they often have a relatively low water contact angle below 90°.

3.7. SEM analysis

The SEM images of the printed CCP scaffold (Figure 14) reveal a well-mixed combination of calcium carbonate and AESO resin. The larger chunks with a smooth surface represent the AESO resin, while the smaller crystalline structures correspond to the calcium carbonate particles.

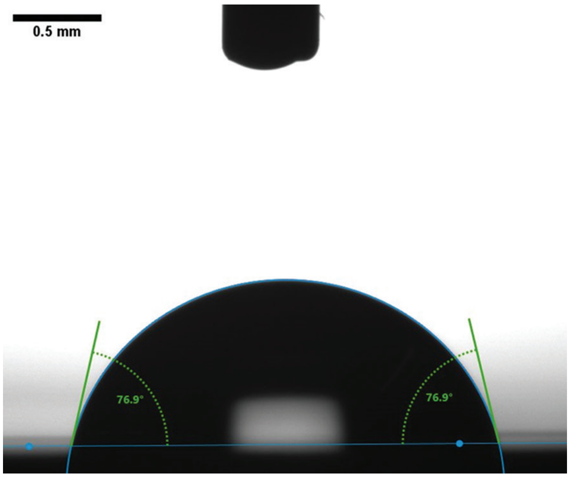

Figure 13. Image of the water contact angle measurement for the printed calcium carbonate-photoinitiated scaffold. The dimension of the needle is 0.51 mm, and the volume of the water is 2.2 μL.

3.8. Microfragmentation on coral plugs

The coral microfragments at day 1 and day 20 are depicted in Figure 15. The coral plugs were randomly distributed inside the water tank to minimize the variables, and they were assembled solely for imaging purposes. After day 7, marine life started settling on the CCP and ceramic plugs. Subsequently, the algae started to accumulate on the coral plugs after around 2 weeks. Interestingly, the algae almost

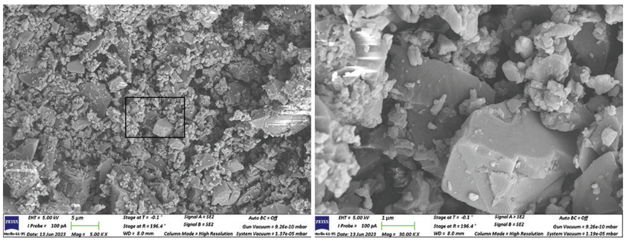

Figure 14. Scanning electron microscope images of the printed calcium carbonate-photoinitiated scaffold. The right picture provides a zoomed-in view of the part circumscribed in the black square on the left image.

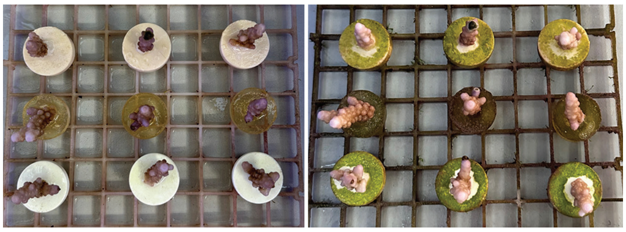

Figure 15. Microfragmentation on different coral plugs at day 1 (left) and day 20 (right). For both images, the first row showcases the calcium carbonate-photoinitiated plugs, the second the acrylated epoxidized soybean oil plugs, and the third the ceramic plugs.

covered the whole coral plugs but not the area around the coral fragments. One of the hypotheses is that coral fragments might release certain chemical compounds or signals during their initial growth or attachment phase that repel or inhibit the settlement and growth of algae.[53-55] This could be a natural defense mechanism of corals to prevent algae overgrowth, which is a positive indication.

At day 25, the purple crustose coralline algae (CCA) was clearly visible on the surface of the modified CCP, AESO, and ceramic plugs (Figure 16). CCA plays a crucial role in the formation and maintenance of coral reefs. CCA deposits calcium carbonate in their cell walls, giving them a hard, crusty appearance. They are often found covering the surfaces of coral reefs, contributing to reef structural integrity, and providing a substrate for coral larvae to settle on.[56]

After 3 months, a notable progression was evident as the coral tissue expanded its coverage on the printed substrate, as illustrated in Figure 17**.** The growth was observed spreading in both dimensions, in two and three dimensions, respectively, indicating successful settlement and adaptation of the corals to the printed substrate.

Figure 16. Microfragments on different coral plugs at day 25. From left to right: Acrylated epoxidized soybean oil, calcium carbonate-photoinitiated, and ceramic plugs. The purple crustose coralline algae can be seen on the side of the surface.

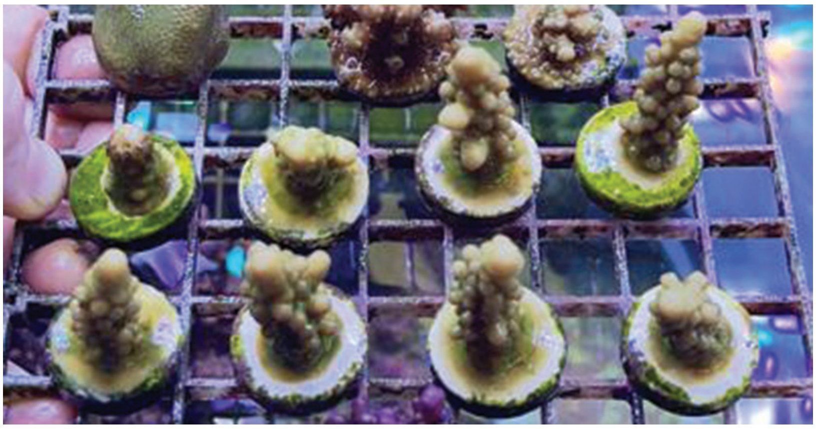

Figure 17. Photo depicting experiment of microfragmentation on calcium carbonate-photoinitiated coral plugs (first row) and ceramic coral plugs (second row) on day 90.

4. Conclusion

The modified CCP resin represents a novel and renewable material suitable for vat polymerization-based 3D printing, fulfilling objectives in both coral restoration and potential biomedical applications. Microfragmentation experiments have demonstrated the successful settlement and expansion of corals on CCP plugs. Moreover, the printed modified CCP construct exhibits high biocompatibility, facilitating cell attachment and proliferation. Material characterization by FTIR and differential scanning calorimetry confirmed that the printed scaffold is highly cross-linked. Furthermore, the CCP plugs exhibit comparable effectiveness to ceramic plugs, which have widely been used in coral restoration. This study contributes to the advancement of printable plant-based renewable materials for fabricating constructs across various applications, thereby supporting sustainability.

Acknowledgments

This work was part of Yukai Jia's Master thesis performed under the guidance of Prof. Charlotte Hauser from KAUST, and Prof. Harm-Anton Klok from EPFL, Lausanne, Switzerland. The authors would like to acknowledge Dr. Panayiotis Bilalis for his support in conducting SEM measurements, Thomas Ressa for his contribution to the microfragmentation experiment, and Aris Konstantinidis for his help in 3D printing and CAD design. We would like to extend our gratitude to Hamed Albalawi, whose preliminary efforts in 3D printing provided insights that served as a guide for the subsequent development of the constructs used in this study. We would like to acknowledge the Visiting Student Research Program (VSRP) at KAUST for supporting the project.

Funding

This work was financially supported by King Abdullah University of Science and Technology (KAUST).

Conflicts of interest

The authors declare no conflicts of interest.

Author contributions

Conceptualization: Charlotte A.E. Hauser and Yukai Jia
Investigation: Yukai Jia and Sherin Abdelrahman
Methodology: Yukai Jia, Sherin Abdelrahman, and Charlotte A.E. Hauser
Formal analysis: Yukai Jia and Sherin Abdelrahman
Writing – original draft: Yukai Jia
Writing – review & editing: Yukai Jia, Sherin Abdelrahman, and Charlotte A.E. Hauser

Ethics approval and consent to participate

Not applicable.

Consent for publication

Not applicable.

Availability of data

Data are available from the authors on reasonable request

References

1. Connell JH. Diversity in tropical rain forests and coral reefs. *Science*. 1978;199(4335):1302-1310.

   doi: 10.1126/science.199.4335.1302

2. Scheffer M, Carpenter S, Foley JA, Folke C, Walker B. Catastrophic shifts in ecosystems. *Nature*. 2001;413(6856):591-596.

   doi: 10.1038/35098000

3. Hoegh-Guldberg O, Mumby PJ, Hooten AJ, *et al*. Coral reefs under rapid climate change and ocean acidification. *Science*. 2007;318(5857):1737-1742.

   doi: 10.1126/science.1152509

4. Hughes TP, Baird AH, Bellwood DR, *et al*. Climate change, human impacts, and the resilience of coral reefs. *Science*. 2003;301(5635):929-933.

   doi: 10.1126/science.1085046

5. Cornwall CE, Comeau S, Kornder NA, *et al*. Global declines in coral reef calcium carbonate production under ocean acidification and warming. *Proc Natl Acad Sci U S A*. 2021;118(21):e2015265118.

   doi: 10.1073/pnas.2015265118

6. Erftemeijer PLA, Riegl B, Hoeksema BW, Todd PA. Environmental impacts of dredging and other sediment disturbances on corals: A review. *Mar Pollut Bull*. 2012;64(9):1737-1765.

   doi: 10.1016/j.marpolbul.2012.05.008

7. Al-Horani FA, Al-Moghrabi SM, De Beer D. The mechanism of calcification and its relation to photosynthesis and respiration in the scleractinian coral *Galaxea fascicularis*. *Mar Biol*. 2003;142(3):419-426.

   doi: 10.1007/s00227-002-0981-8

8. Klinges D. *A New Dimension to Marine Restoration: 3D Printing Coral Reefs*. Vol. 11. California: Mongabay; 2018.

9. Ngo TD, Kashani A, Imbalzano G, Nguyen KTQ, Hui D. Additive manufacturing (3D printing): A review of materials, methods, applications and challenges. *Compos Part B Eng*. 2018;143:172-196.

   doi: 10.1016/j.compositesb.2018.02.012

10. Kim NP, Cho D, Zielewski M. Optimization of 3D printing parameters of Screw Type Extrusion (STE) for ceramics

using the Taguchi method. *Ceram Int*. 2019;45(2):2351-2360.

doi: 10.1016/j.ceramint.2018.10.152

11. Crook L. *Coral Skeletons Crafted from 3D-printed Calcium Carbonate Could Restore Damaged Reefs*. London: Dezeen; 2020.
12. Ziaee M, Crane NB. Binder jetting: A review of process, materials, and methods. *Addit Manuf*. 2019;28:781-780.

    doi: 10.1016/j.addma.2019.05.031
13. Buswell RA, Leal de Silva WR, Jones SZ, Dirrenberger J. 3D printing using concrete extrusion: A roadmap for research. *Cem Concr Res*. 2018;112:37-49.

    doi: 10.1016/j.cemconres.2018.05.006
14. Ly O, Yoris-Nobile AI, Sebaibi N, *et al*. Optimisation of 3D printed concrete for artificial reefs: Biofouling and mechanical analysis. *Constr Build Mater*. 2021;272:121649.

    doi: 10.1016/j.conbuildmat.2020.121649
15. Ikiz SU. 3D-printed artificials reefs to restore coral ecosystems. *Parametric Architecture*. 2022. Available from: https://parametric-architecture.com/3D-printed-artificial-reefs-to-restore-coral-ecosystems. [Last accessed on 2024 Jan 06].
16. Chaudhary R, Fabbri P, Leoni E, Mazzanti F, Akbari R, Antonini C. Additive manufacturing by digital light processing: A review. *Prog Addit Manuf*. 2023;8(2):331-351.

    doi: 10.1007/s40964-022-00336-0
17. Chaudhary B, Li H, Matos H. Long-term mechanical performance of 3D printed thermoplastics in seawater environments. *Results Mater*. 2023;17:100381.

    doi: 10.1016/j.rinma.2023.100381
18. Shokoohi R, Samadi MT, Samarghandi MR, Ahmadian M, Karimaian K, Poormohammadi A. Comparing the performance of granular coral limestone and Leca in adsorbing Acid Cyanine 5R from aqueous solution. *Saudi J Biol Sci*. 2017;24(4):749-759.

    doi: 10.1016/j.sjbs.2016.01.012
19. Lange C, Ratoi L, Co DL. Reformative Coral Habitats - Rethinking Artificial Reef Structures through a Robotic 3D Clay Printing Method. In: *Proceedings of the 25th Conference on Computer Aided Architectural Design Research in Asia (CAADRIA)*. Vol. 2; 2022.

    doi: 10.52842/conf.caadria.2020.2.463
20. Khot SN, Lascala JJ, Can E, *et al*. Development and application of triglyceride-based polymers and composites. *J Appl Polym Sci*. 2001;82(3):703-723.

    doi: 10.1002/app.1897
21. O'Donnell A, Dweib MA, Wool RP. Natural fiber composites with plant oil-based resin. *Compos Sci Technol*. 2004;64(9):1135-1145.

    doi: 10.1016/j.compscitech.2003.09.024
22. Mondal D, Haghpanah Z, Huxman CJ, *et al*. mSLA-based 3D printing of acrylated epoxidized soybean oil-nano-hydroxyapatite composites for bone repair. *Mater Sci Eng C Mater Biol Appl*. 2021;130:112456.

    doi: 10.1016/j.msec.2021.112456
23. Miezinyte G, Ostrauskaite J, Rainosalo E, Skliutas E, Malinauskas M. Photoresins based on acrylated epoxidized soybean oil and benzenedithiols for optical 3D printing. *Rapid Prototyp J*. 2019;25(2):378-387.

    doi: 10.1108/RPJ-04-2018-0101
24. Lebedevaite M, Ostrauskaite J, Skliutas E, Malinauskas M. Photoinitiator free resins composed of plant-derived monomers for the optical μ-3D printing of thermosets. *Polymers* (*Basel*). 2019;11(1):116.

    doi: 10.3390/polym11010116
25. Wang C, Ding L, He M, *et al*. Facile one-step synthesis of bio-based AESO resins. *Eur J Lip Sci Technol*. 2016;118(10):1463-1469.

    doi: 10.1002/ejlt.201500494
26. Albalawi HI, Khan ZN, Valle-Pérez AU, *et al*. Sustainable and eco-friendly coral restoration through 3D printing and fabrication. *ACS Sustain Chem Eng*. 2021;9:12634-12645.

    doi: 10.1021/acssuschemeng.1c04148
27. Roepke LK, Brefeld D, Soltmann U, Randall CJ, Negri AP, Kunzmann A. Antifouling coatings can reduce algal growth while preserving coral settlement. *Sci Rep*. 2022;12(1):15935.

    doi: 10.1038/s41598-022-19997-6
28. Takahashi K, Tanabe K, Ohnuki M, *et al*. Induction of pluripotent stem cells from adult human fibroblasts by defined factors. *Cell*. 2007;131(5):861-872.

    doi: 10.1016/j.cell.2007.11.019
29. Dimri GP, Lee X, Basile G, *et al*. A biomarker that identifies senescent human cells in culture and in aging skin *in vivo*. *Proc Natl Acad Sci U S A*. 1995;92(20):9363-9367.

    doi: 10.1073/pnas.92.20.9363
30. Lee HJ, Lee JS, Chansakul T, Yu C, Elisseeff JH, Yu SM. Collagen mimetic peptide-conjugated photopolymerizable PEG hydrogel. *Biomaterials*. 2006;27(30):5268-5276.

    doi: 10.1016/j.biomaterials.2006.06.001
31. Hauser CAE, Deng R, Mishra A, *et al*. Natural tri-to hexapeptides self-assemble in water to amyloid β-type fiber aggregates by unexpected α-helical intermediate structures. *Proc Natl Acad Sci U S A*. 2011;108(4):1361-1366.

    doi: 10.1073/pnas.1014796108
32. Mishra A, Loo Y, Deng R, *et al*. Ultrasmall natural peptides self-assemble to strong temperature-resistant helical fibers in scaffolds suitable for tissue engineering. *Nano Today*. 2011;6(3):232-239.

    doi: 10.1016/j.nantod.2011.05.001

33. Susapto HH, Alhattab D, Abdelrahman S, *et al*. Ultrashort peptide bioinks support automated printing of large-scale constructs assuring long-term survival of printed tissue constructs. *Nano Lett*. 2021;21(7):2719-2729.

    doi: 10.1021/acs.nanolett.0c04426

34. Heiden MGV, Cantley LC, Thompson CB. Understanding the warburg effect: The metabolic requirements of cell proliferation. *Science*. 2009;324(5930):1029-1033.

    doi: 10.1126/science.1160809

35. Berney M, Hammes F, Bosshard F, Weilenmann HU, Egli T. Assessment and interpretation of bacterial viability by using the LIVE/DEAD BacLight kit in combination with flow cytometry. *Appl Environ Microbiol*. 2007;73(10):3283-3290.

    doi: 10.1128/AEM.02750-06

36. Hall A. Rho GTpases and the actin cytoskeleton. *Science*. 1998;279(5350):509-514.

    doi: 10.1126/science.279.5350.509

37. Hess ST, Girirajan TPK, Mason MD. Ultra-high resolution imaging by fluorescence photoactivation localization microscopy. *Biophys J*. 2006;91(11):4258-4272.

    doi: 10.1529/biophysj.106.091116

38. Ridley AJ, Hall A. The small GTP-binding protein rho regulates the assembly of focal adhesions and actin stress fibers in response to growth factors. *Cell*. 1992;70(3):389-399.

    doi: 10.1016/0092-8674(92)90163-7

39. De La Cruz EM, Pollard TD. Transient kinetic analysis of rhodamine phalloidin binding to actin filaments. *Biochemistry*. 1994;33(48):14387-14392.

    doi: 10.1021/bi00252a003

40. Tarnowski BI, Spinale FG, Nicholson JH. DAPI as a useful stain for nuclear quantitation. *Biotech Histochem*. 1991;66(6):297-302.

    doi: 10.3109/10520299109109990

41. Helmchen F, Denk W. Deep tissue two-photon microscopy. *Nat Methods*. 2005;2(12):932-940.

    doi: 10.1038/nmeth818

42. Mostrales TPI, Rollon RN, Licuanan WY. Evaluation of the performance and cost-effectiveness of coral microfragments in covering artificial habitats. *Ecol Eng*. 2022;184:106770.

    doi: 10.1016/j.ecoleng.2022.106770

43. Luo Y, Le Fer G, Dean D, Becker ML. 3D Printing of poly(propylene fumarate) oligomers: Evaluation of resin viscosity, printing characteristics and mechanical properties. *Biomacromolecules*. 2019;20(4):1699-7108.

    doi: 10.1021/acs.biomac.9b00076

44. Rudawska A, FrigioneM. Effect of diluents on mechanical characteristics of epoxy compounds. *Polymers* (*Basel*). 2022;14(11):2277.

    doi: 10.3390/polym14112277

45. Khalina M, Beheshty MH, Salimi A. The effect of reactive diluent on mechanical properties and microstructure of epoxy resins. *Polym Bull*. 2019;76(8):3905-3927.

    doi: 10.1007/s00289-018-2577-6

46. Green WA. *Industrial Photoinitiators*. Boca Raton: CRC Press; 2010.

    doi: 10.1201/9781439827468

47. Nandiyanto ABD, Oktiani R, Ragadhita R. How to read and interpret ftir spectroscope of organic material. *Indones J Sci Technol*. 2019;4(1):97-118.

    doi: 10.17509/ijost.v4i1.15806

48. Lebedevaite M, Talacka V, Ostrauskaite J. High biorenewable content acrylate photocurable resins for DLP 3D printing. *J Appl Polym Sci*. 2021;138(16):50233.

    doi: 10.1002/app.50233

49. Galan I, Glasser FP, Andrade C. Calcium carbonate decomposition. *J Therm Anal Calorim*. 2013;111(2):1197-1202.

    doi: 10.1007/s10973-012-2290-x

50. Millot C, Fillot LA, Lame O, Sotta P, Seguela R. Assessment of polyamide-6 crystallinity by DSC: Temperature dependence of the melting enthalpy. *J Therm Anal Calorim*. 2015;122(1):307-314.

    doi: 10.1007/s10973-015-4670-5

51. Cassie ABD, Baxter S. Wettability of porous surfaces. *Trans Faraday Soc*. 1944;40:546-551.

    doi: 10.1039/tf9444000546

52. Miao S, Zhu W, Castro NJ, *et al*. 4D printing smart biomedical scaffolds with novel soybean oil epoxidized acrylate. *Sci Rep*. 2016;6:27226.

    doi: 10.1038/srep27226

53. Larson JK, Mccormick MI. The role of chemical alarm signals in facilitating learned recognition of novel chemical cues in a coral reef fish. *Anim Behav*. 2005;69(1):51-57.

    doi: 10.1016/j.anbehav.2004.04.005

54. Whalan S, Abdul Wahab MA, Sprungala S, Poole AJ, De Nys R. Larval settlement: The role of surface topography for sessile coral reef invertebrates. *PLoS One*. 2015;10(2):e0117675.

    doi: 10.1371/journal.pone.0117675

55. Edmunds PJ. Finding signals in the noise of coral recruitment. *Coral Reefs*. 2022;41(1):81-93.

    doi: 10.1007/s00338-021-02204-9

56. Vermeij MJA, Dailer ML, Smith CM. Crustose coralline algae can suppress macroalgal growth and recruitment on Hawaiian coral reefs. *Mar Ecol Prog Ser*. 2011;422:1-7.

    doi: 10.3354/meps08964

ACCSCIENCE PUBLISHING

Materials Science in Additive Manufacturing

ORIGINAL RESEARCH ARTICLE

Compressive properties and fatigue performance of NiTi lattice structures optimized by TPMS

Yunlong Ren[1], Yang Li[1,2], Lei Yang[1,2,3]*, Yun Chen[1,2]*, Chunze Yan[3], Bing Liu[4], Xuan Cai[4], Mingkang Zhang[5], and Yusheng Shi[3]

[1]Department of Mechanical Design and Manufacturing, School of Transportation and Logistics Engineering, Wuhan University of Technology, Wuhan, Hubei, China

[2]Hubei Longzhong Laboratory, Xiangyang, Hubei, China

[3]State Key Laboratory of Materials Processing and Die and Mould Technology, School of Materials Science and Engineering, Huazhong University of Science and Technology, Wuhan, Hubei, China

[4]Wuhan Second Ship Design and Research Institute, Wuhan, Hubei, China

[5]Additive Manufacturing Laboratory and Mechanics Experiment Center, School of Mechanical and Energy Engineering, Guangdong Ocean University, Yangjiang, Guangdong, China

(This article belongs to the *Special Issue: 3D Printing for Structural and Functional Integration*)

Abstract

Nickel titanium (NiTi) lattice structures prepared by laser powder bed fusion (LPBF) have great application potential, due to their unique shape memory effect, superelasticity, and controlled geometry characteristics. In this study, the NiTi I-graph-wrapped package (I-WP) and NiTi body-centered cubic (BCC) lattice structure samples were prepared by the LPBF process. The uniaxial compression properties and cyclic compression properties of NiTi lattice structure samples prepared by LPBF process were studied. The results showed that the surfaces of NiTi lattice structures were very rough and adhered with many powder particles. The sample optimization design through the minimal surface could effectively improve the mechanical properties and deformation resistance and change the surface morphology of fracture surfaces in high cycle fatigue. The I-WP lattice structure had a higher Young's modulus and yield strength. The fatigue strength improved from 1.88 MPa (BCC structure lattice) to 2.08 MPa (I-WP structure lattice). The simulation was performed to investigate the mechanism underlying the improvement in fatigue strength, revealing that optimization of surface stress distribution could be the plausible reason. In general, this study provides valuable guidance for the preparation and design of NiTi lattice structure by the LPBF process.

Keywords: Nickel titanium alloy; Additive manufacturing; Triply periodic minimal surface; Laser powder bed fusion; Lattice structure

***Corresponding authors:**
Lei Yang
(lei.yang@whut.edu.cn)
Yun Chen
(chenyunhbwh@whut.edu.cn)

Citation: Ren Y, Li Y, Yang L, *et al*., 2024, Compressive properties and fatigue performance of NiTi lattice structures optimized by TPMS. *Mater Sci Add Manuf*. doi: 10.36922/msam.3380

Received: 22 May 2024

Accepted: 01 June 2024

1. Introduction

Nickel titanium (NiTi) alloys possess distinctive shape memory effect, superelasticity, biocompatibility, superior fatigue life[1], and other characteristics and have outstanding performance in shock absorption, justifying their extensive applications in aerospace, biomedical, automotive, construction engineering, and other fields.[2,3] In addition, the alloys can safely prevent excessive swaying of the piers, as demonstrated by Fang *et al.* who introduced NiTi washer springs into seismic bridge design.[4] To explore its use in orthopedic applications, Xie *et al.* treated the surface of NiTi alloy to improve surface hardness and antibacterial properties.[5]

The NiTi porous structure features high specific strength and stiffness, as well as remarkable mechanical properties in low-density structures. The internal structure of conventionally made NiTi porous structure is composed of randomly distributed pores with different shapes, giving a random microstructure that leads to local performance differences and affects the structure's applications. However, the development of additive manufacturing technology has enabled the precise fabrication of NiTi porous structures with regular shapes inside.[6,7] Laser powder bed fusion (LPBF) technology is an emerging polymer and metal additive manufacturing technology that uses a laser or electron beam as the energy source to melt or sinter powder materials in a layer-by-layer fashion.[8-11] Hussain *et al.* utilized LPBF to prepare a NiTi triply periodic minimal surface (TPMS) lattice, revealing the effects of process parameters and structural topology on microstructure characteristics.[12]

The service life of NiTi materials is extremely critical in applications such as cardiovascular stents[13] and helical springs.[14] Over the past few decades, many cyclic compression experiments have been conducted on NiTi alloys.[15] Kan *et al.* studied the functional degradation of superelastic NiTi rods in cyclic tension-unloading and compression-unloading experiments,[16] while Safdel *et al.* investigated the tensile-compression asymmetric behavior of NiTi alloys by laser powder bed melting.[17] However, studies on the fatigue properties of NiTi alloys remain scarce.[18] The experiments of Zhang *et al.* showed that rock-like splitting and chipping through nucleation and slow, stable growth of compression-parallel cracks driven by very small stress intensity are the major factors driving fatigue failure of the material.[19] Zhao and Kang showed that the fatigue life of NiTi alloy microtubules would be affected by the loading path and stress level under uniaxial cyclic loading.[20] Most of the previous studies focused on the fatigue performance of the alloy or the structure itself. However, there was no comparison between structural optimization design and fatigue performance.

For the most commonly used strut-based lattice structure, the sharp pillar at the node can lead to higher stress concentration, which adversely affects the mechanical properties and fatigue properties of the sample. Furthermore, the cantilever of strut-based lattice structure is less conducive to additive manufacturing. In contrast, an emerging bionic structure, that is, the TPMS structure, not only reduces the stress concentration at the node but also changes the geometric characteristics of the lattice structure, making its surface smoother and the stress distribution more uniform.[21-23] In this study, the body-centered cubic (BCC) lattice structure and the I-graph-wrapped package (I-WP) lattice structure generated through minimal surface optimization were investigated.[24,25] The I-WP curved surface, commonly referred to as I-WP, is a kind of TPMSs. The "I" denotes the BCC lattice. The "WP" is the abbreviation for "wrapped package," named for the resemblance of finite portions of the I-WP surface to string arrangement on a simply wrapped package.[26]

Therefore, BCC and I-WP structures were selected for experiments to study the forming quality and properties of NiTi lattice structures prepared by LPBF. The applicability of the TPMS optimization design method in the field of metal materials prepared by the LPBF process was also investigated in this study.

2. Methods

2.1. Design and manufacture of lattice structures

2.1.1. Design of BCC and I-WP

As shown in Figure 1, the volume fraction of the sample is 10%. The unit cell is a cube with a side length of 5 mm. The whole sample is composed of unit cells and is a cube with a side length of 20 mm.

The BCC lattice structure was designed by the 3D geometric modeling software Creo (Pro/E), whereas the I-WP lattice structure was parameterized using MATLAB, and their implicit function control equations are as follows:

$$F(x,y,z,t)=2(cos\left(2\pi\frac{x}{L}\right)cos\left(2\pi\frac{y}{L}\right)$$
$$+cos\left(2\pi\frac{y}{L}\right)cos\left(2\pi\frac{z}{L}\right)+cos\left(2\pi\frac{z}{L}\right)cos\left(2\pi\frac{x}{L}\right))-t \tag{I}$$

Where L denotes the unit cell size, which was 5 mm in this study, and t denotes the control volume fraction, which was 10%.

2.1.2. Materials and equipment

NiTi alloy powder with an elemental ratio of 1:1 was prepared by electrode induction melting gas atomization and purchased from Avimetal Powder Metallurgy Technology Co., Ltd. The density of the powder was 6.45 g/cm^3. The BLT-S210 (Xi'an Bright Laser Technologies, Ltd., China) was utilized to conduct the LPBF process.

The process parameters shown in Table 1 were selected for manufacturing. Pre-heating at a temperature of 200°C was required before printing. Before printing the sample, a layer of thin plate was printed with the same parameters for heat accumulation, so that the NiTi powder could efficiently melt and adhere to the substrate. The parameters were optimized by the orthogonal experiment method.[27,28] It is worth noting that the layer thickness was 30 μm and the hatch space was 100 μm in the NiTi sample fabricated by LPBF process. Ge *et al.* have discussed the utilization of different laser powers and scanning speeds for manufacturing.[27] The laser power employed in this study was 125 W, and the scanning speed was 600 mm/s.

It should be noted that the entire LPBF fabrication process was carried out in an inert gas (argon) atmosphere to avoid oxidation of the NiTi powder and the additive-manufactured parts. Upon completion of printing, the sample was cut from the substrate using wire electrical discharge machining and then placed in a 99% alcohol solution for ultrasonic cleaning for 15 min to remove residual powder particles from the surface. Finally, the sample was dried using a high-pressure air gun. The finished sample is shown in (Figure 1E).

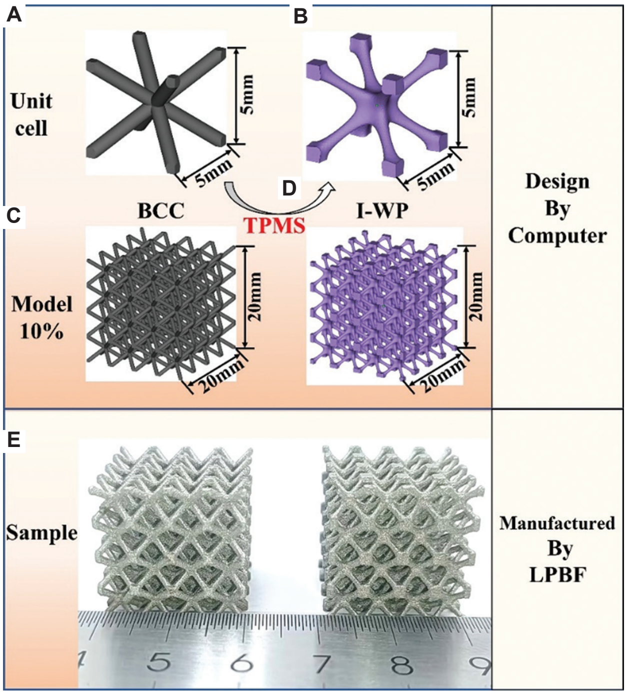

Figure 1. (A-E) The sample design and manufacture of this study.

2.2. Measurement and characterization

2.2.1. Macro- and micro-scopic characterization

The lattice-structured samples prepared by LPBF were measured for their dimensions using a vernier caliper (smallest scale division of 0.01 mm) and weighed using an electronic balance (smallest scale increments of 0.1 mg). The surface and fracture surfaces of the samples were characterized using a Quanta 650 FEG scanning electron microscope (FEI, USA) with a chamber's air pressure of <8 $\times 10^{-3}$ Pa.

2.2.2. Static compression test

Typically, additive-manufactured parts exhibit significant anisotropy, whereas the anisotropy of the compressive mechanical properties of additive-manufactured TPMS lattice structures is relatively small.[29] Therefore, we only attempted to study the compressive mechanical behavior in the printing direction (Z-axis) in the present work. The NiTi samples were tested using a materials high-temperature performance testing machine (AG-IC 100 kN, Shimadzu, Japan). Uniaxial compression tests were conducted at room temperature using two devices with top and bottom loading heads. The compression rate was 0.02 mm/s according to ISO 13314:2011.[30]

2.2.3. Dynamic compression-compression fatigue test

The compression-compression fatigue test was performed at room temperature using an electrohydraulic servo thermal fatigue testing machine (EHF-UK100K2-040-1A, Shimadzu, Japan). The loading frequency was set to 30 Hz; the loading curve took the shape of a sinusoidal waveform; and the load ratio R was set to 0.1. The cycle of the test stop was set to 10^6. The loading stress value of 0.3–0.7 σ_s was selected as the loading condition for the fatigue test. σ_s is defined as a yield strength value of 0.2%. BCC-10% load stress values were 1.71 MPa, 2.28 MPa, 2.86 MPa, 3.43 MPa, and 4.00 MPa, whereas I-WP-10% load stress values were 1.85 MPa, 2.47 MPa, 3.09 MPa, 3.71 MPa, and 4.33 MPa. For each loading condition, two samples were tested.

2.3. Finite element analysis simulation

ABAQUS (2020 version) was used to simulate the static compression test. The boundary conditions were applied to the model, the lower boundary was fixed, and the upper boundary moved downward. General contact and a penalty friction coefficient of 0.1 were utilized as the interaction

Table 1. Process parameter of LPBF

Layer thickness (μm)	Hatch space (μm)	Laser power (W)	Scanning speed (mm/s)	Pre-heating temperature (°C)
30	100	125	600	200

Abbreviation: LPBF: Laser powder bed fusion.

conditions. HyperMesh (2019 version) was used to mesh the I-WP, and the I-WP lattice model was divided into 1387668 elements. The BCC was optimized using Materialise Magics software (Materialise, Belgium), and then, the volume mesh was re-divided using Materialise 3-Matic software (Materialise, Belgium). The BCC lattice model was divided into 230681 elements.

3. Results and discussion

3.1. Surface morphologies and molding accuracy

Figure 2 shows that the surfaces of both BCC and I-WP lattice structures are very rough and covered with many powder particles, which is usually caused by the partial melting of nearby powder by the energy dissipated from the molten pool. By observing the side surface of the two lattice structure pillars from the side view, some stripes caused by the "stair effect" of the addition process can be observed. Furthermore, it can be observed in both BCC and I-WP samples that the lower surface of the node and strut is rougher and has more attached particles than the side surface. During the LPBF process, the node locations acted as cantilevers, and the lower side surfaces lacked support, causing the surface there to adhere more easily to the NiTi powder.[31-33]

As shown in (Figure 2C and D), there are more powder particles adherent to the underside than to the side. It can also be observed that the powder adhesion was more severe at the BCC sample node, where the powders accumulated at the nodes. Despite the larger cantilever area, less powder adhesion was observed at the I-WP sample node than at the BCC sample node, due to the better self-supporting properties of the I-WP TPMS structure.[34,35] Thus, the unit cell type of lattice structures is an important factor affecting fabrication quality. Although the I-WP TPMS is not spared from powder adhesion on the surface of the lower side, it is still superior to the BCC lattice.

The size and weight of the NiTi lattice structure were measured by vernier caliper and electronic balance, respectively. The actual volume fraction was calculated by determining the ratio of the actual mass of the sample to the design mass. As shown in the (Figure 2E and F), the average actual volume fractions of BCC and I-WP lattice structure samples are 12.26% and 12.30%, respectively, which are higher than the design volume fraction. This is because, during the LPBF process, many powder particles are attached to the sample surface, especially at the lower surface. As a result, the actual quality of the sample increases, followed by an enlargement of the actual volume

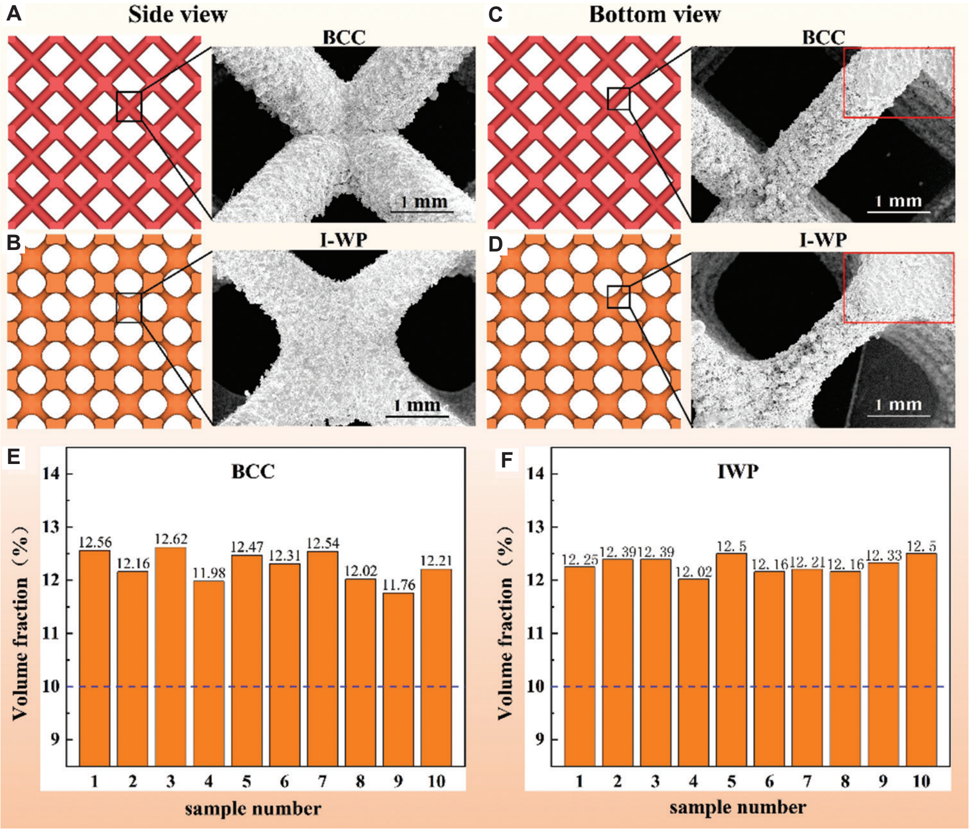

Figure 2. (A-F) Scanning electron microscope images and actual volume fraction of as-built lattices.

fraction, all of these happen because of the excessive adhesion of metal powder particles on the surface of the sample. The occurrence of this phenomenon will become more common if the laser power is too large or the laser scanning speed is too slow.

The LPBF process has similar forming accuracy in the preparation of two lattice structures. Figure 2E and F show that there is not much of a difference in actual volume fraction between the two structures, indicating that TPMS optimization design has little effect on the forming accuracy of additive manufacturing of lattice structures.

3.2. Static compression mechanical results

3.2.1. Stress-strain

The stress–strain curve in (Figure 3A) shows similar behavior. At the initial stage of the compression test, the curves exhibit linear elasticity; then, the curves show a rapid and significant drop in stress due to the applied load exceeding the strength of the lattice structure's struts, which resulted in the collapse of the struts and the flight of some sample fragments out of the test bench. Afterward, the curves show sawtooth fluctuations due to further collapse and damage of the remaining samples.

The compressive mechanical behavior of the NiTi lattice structures exhibited a near 45° "shear" fracture mode, as shown in (Figure 3B). The force-displacement curves of the NiTi lattices published in the study of Chen *et al.*[36] also indicate similar brittle behavior and 45° fracture mode. Yang *et al.*[24] showed that the lattice structure of photosensitive resin samples exhibited densification behavior under high compressive strain. The NiTi lattice structures prepared by Sun *et al.*[37] produced a significant 45° "shear" fracture during uniaxial compression. It can be inferred that the fracture behavior of lattice structures after compression is mainly influenced by the material properties, and different unit cell types of lattice structures also exhibit similar mechanical behavior.

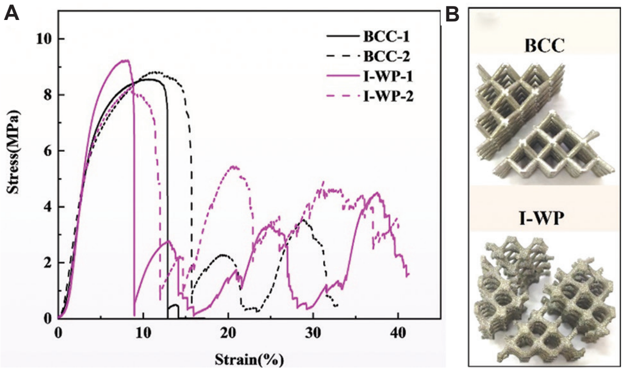

Figure 3. Stress-strain compression of Nickel titanium (NiTi) body-centered cubic (BCC) and I-graph-wrapped package (I-WP) lattice samples: (A) stress-strain curves of NiTi BCC and I-WP lattices; (B) samples after the static compression tests.

The main mechanical properties of NiTi BCC and I-WP lattice structures calculated from Figure 3 are listed in Table 2. The Young's modulus and yield strength of the I-WP lattice structure were higher than those of the BCC lattice structure. According to ISO13314, the gradient of the straight line in (Figure 3A) can be determined within the linear deformation region at the beginning of the compressive stress–strain curve.[30] The quasi-elastic gradient is usually believed to be the modulus of lattice structures.[38,39] In this study, Young's modulus was calculated from the elastic region of (Figure 3A). As shown in Table 2, Young's moduli of the I-WP and the BCC lattice structures were 250.74 MPa and 208.00 MPa, respectively. The yield strength of the I-WP lattice structure was 6.18 MPa, whereas the BCC lattice structure had a yield strength of 5.71 MPa. Therefore, structural optimization of the minimal surface can favorably improve the mechanical properties of the NiTi lattice structures.

3.2.2. Energy absorption

It has been reported that the total energy absorption €, derived from the area under the load-displacement curve of the lattice structure under compression test, can be employed to define the deformation energy per unit volume (EPV) and the specific energy absorption (SEA). The energy absorption efficiency (η) is obtained from the stress–strain curve.[24] *EPV* is defined as the ratio of total energy absorption to the volume of lattice structures[40]; *SEA* is determined by the ratio of total energy absorption to the mass of lattice structures[41]; and η is defined as the ratio of energy absorption to stress value per unit volume under a certain strain.[42]

In this study, the NiTi sample was destroyed under compression, causing a large stress drop in the stress–strain curve, as shown in (Figure 3A). Therefore, while studying the energy absorption capacity of the NiTi lattices, we considered that failure of NiTi lattice structure samples had occurred following the large stress drop, and thus, energy absorption performance parameters of the samples were calculated with reference to this particular position in the curve.

Table 2. Mechanical properties of NiTi BCC and I-WP lattice structures

Mechanical property	BCC	I-WP
Young's modulus (MPa)	208.00	250.74
Yield strength (MPa)	5.71	6.18

Abbreviations: NiTi: Nickel titanium; BCC: Body-centered cubic; I-WP: I-graph-wrapped package.

The strain positions of the flying out of large fragments, ε_1, of the two samples of BCC lattice structures were 12.86% and 15.69%, respectively, while those of I-WP samples were 8.95% and 11.98%, respectively. The ε_1 strain positions of BCC samples were slightly larger than those of I-WP, which may be due to the smaller diameter of the middle positions of the struts of the I-WP lattice structures and the more concentrated stress distribution, which made it easier for the applied load to exceed the strength limit during the compression tests, resulting in the collapse and fracture of I-WP lattices before the BCC lattices.

Figure 4A shows the rise of total energy absorption of these two structures with the increase of strain. At the same strain position, the total energy absorption values were very close. Figure 4C-E show that the values of *E*, *EPV*, and *SEA* of the BCC lattice structure and are higher than those of the I-WP lattice structure at the ε_1 strain position. Although, as shown in (Figure 4A), the total energy absorption of I-WP was not inferior to that of BCC, the value of ε_1 strain of I-WP was smaller, and the strain range that can effectively absorb energy was smaller. Therefore, the total energy absorption of I-WP was lower. The energy absorption per unit strain of these two lattice structures at ε_1 strain was calculated. The values for BCC and I-WP were 0.53 J and 0.48 J, respectively, suggesting that the ability of NiTi BCC to absorb energy is slightly stronger.

Figure 4B presents the energy absorption capacity of two NiTi lattice structures. First, in the linear elastic stage, the stress values of the lattice structures increased uniformly with the gradual increase of strain, and its energy absorption efficiencies also increased uniformly with the increase of strain. Then, it is worth noting that after entering the plateau stage, the pillars of the lattice structures began to yield and deform, and finally break, manifested as a rapid decline in the stress–strain curves. At this strain position, the energy absorption efficiency curves had an inflection point and rose rapidly. According to the definition and formula of the energy absorption

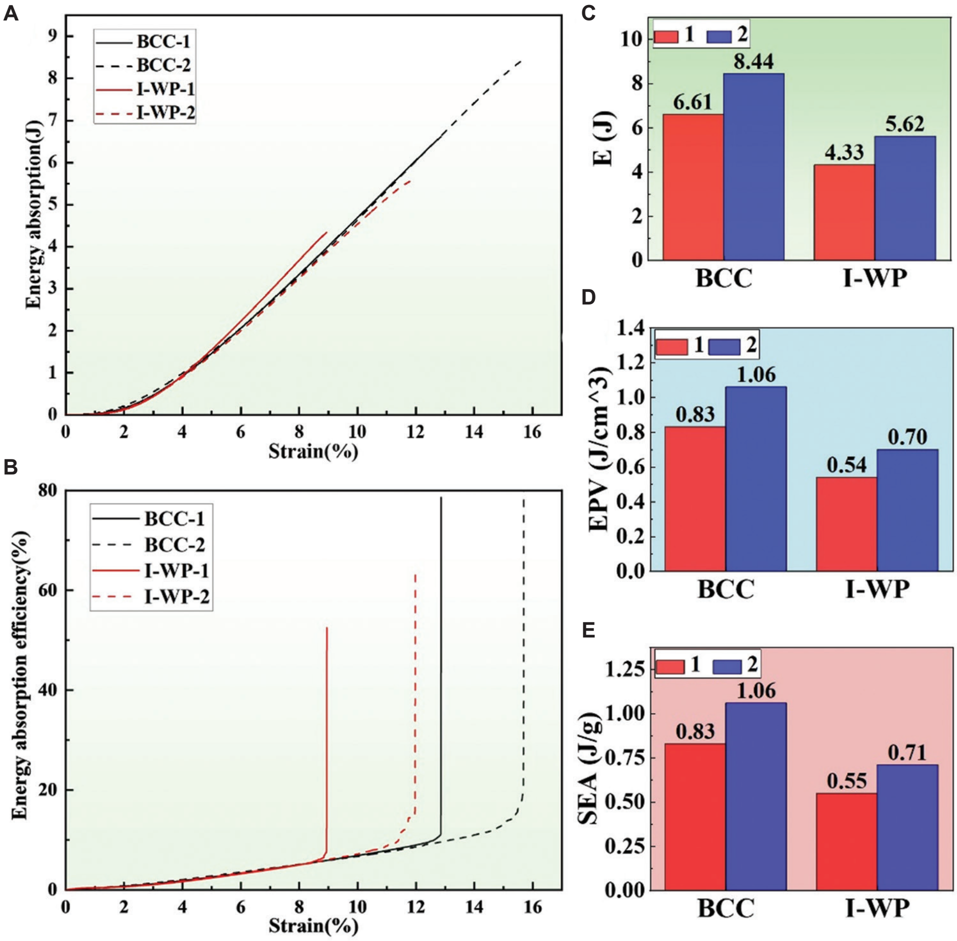

Figure 4. The energy absorption capacity of two Nickel titanium (NiTi) lattice structures: (A) The total energy absorption-strain curves of the NiTi lattice structures; (B) The energy absorption efficiency-strain curves of the NiTi lattice structures; (C) The total energy absorption (*E*); (D) The energy absorption per unit volume (*EPV*); (E) The specific energy absorption (*SEA*).

efficiency,[24] when the lattice structure collapses and breaks, the stress value as the denominator decreases sharply in a small strain range, resulting in an inflection point and a rapid rise in the energy absorption efficiency curve. It can be concluded that during compression, the lattice structures improve the energy absorption efficiency through the deformation of struts.

3.3. Fatigue performance

3.3.1. Strain accumulation

Figure 5A and B show the accumulative strain-cycle curves of the two lattice structures at different stress levels, respectively. The strains of the two structures gradually increased and accumulated with the increase of the cycles, and the compression height of the sample was reduced. The strain accumulation curves can be divided into three stages: the initial strain increase stage ($N < 50$), the constant strain plateau stage, and the rapid strain accumulation stage. As shown in (Figure 5A and B), between the constant strain plateau stage and the rapid strain accumulation stage, the abrupt strain point, N_c can be clearly observed in the strain accumulation curves. As the loading stress increased, the strain value of the abrupt strain point also increased, but the cycle number corresponding to this point decreased, indicating that a smaller load could improve the fatigue life.

The curve bulge observed in the initial stage, as shown in (Figure 5A and B), is attributed to the instability of the fatigue testing machine at the initial stage of operation. Since the load ratio of the fatigue test was set to $R = 0.1$, the minimum value of the load set in the test conditions was too small relative to the working load range of the equipment, so the fatigue test machine was unstable during the initial operation cycles. The changes in applied load and indenter position during the operation of the machine are plotted in (Figure 5C). Between 10 and 100 cycles, the values of the load and indenter position were not stable, and a region of fluctuation in the load and indenter position curves was observed, corresponding to the fluctuations in the strain accumulation curves in (Figure 5A and B).

The accumulative strain per cycle was calculated as shown in (Figure 5D). By calculating the cumulative strain per cycle before the strain mutation point in (Figure 5A and B), we found that the larger the load, the higher the cumulative strain per cycle. In addition, the I-WP exhibited a much lower accumulative strain per cycle than the BCC in high-cycle fatigue (low-stress level),

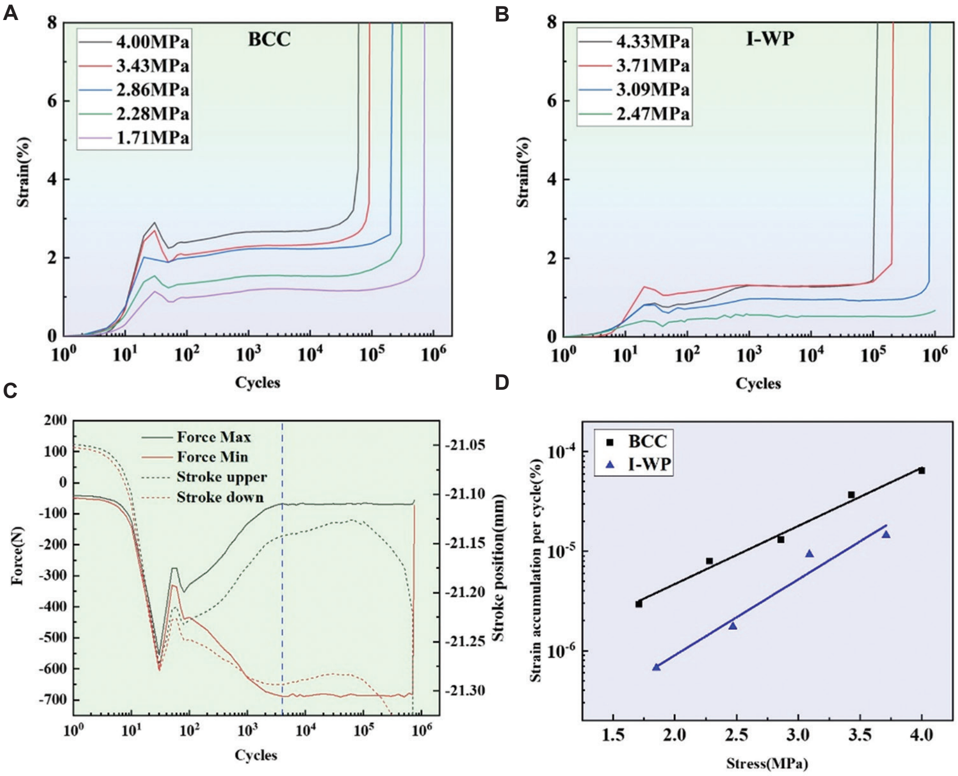

Figure 5. Accumulative strain-cycle curves, as well as changes of force and indenter position during fatigue test. (A and B) Accumulative strain-cycle curves of body-centered cubic (BCC) (A) and I-graph-wrapped package (B). (C and D) Variation of force and indenter position of the fatigue test machine during fatigue tests: BCC1.71 MPa (C), and accumulative strain per cycle (D).

while the accumulative strains per cycle for both lattice structures tended to be close in low-cycle fatigue (high-stress level). It can be inferred that the TPMS design has superior deformation resistance in high-cycle fatigue.

3.3.2. Cyclic responses

Since the fatigue test machine can only operate stably at 4000 cycles, the starting point of the test was set to the 4000th cycle. The hysteresis curves of the BCC and I-WP under the stress condition of $0.3\sigma_s$ (1.71 MPa for BCC and 1.85 MPa for I-WP) are shown in (Figure 6A and B), respectively. Each hysteresis loop moves right along the strain axis, indicating the existence of a cyclic ratchet effect. The hysteresis curves at the initial several cycles were almost parallel to each other. As the fatigue test continued, the tangent modulus of the hysteresis loops decreased with the increase of cycles, which is due to the fatigue crack generation and extension occurring in the struts.[43]

In addition, in (Figure 6A), a "crescent-shaped" hysteresis loop was observed in the BCC lattice structure in the latter cycles, pointing out the superelasticity of the NiTi alloy.[44,45] Compared with the lattice of other materials, the recoverable deformation range of NiTi lattice structure samples is larger.[24,46] During the fatigue test, the cyclic variation of the load applied to the sample was equivalent to loading and unloading, and the BCC structure recovered some of its deformation when the load decreased,[47] resulting in the decrease of the strain value as shown in (Figure 6A). However, this phenomenon is not evident in the I-WP structure because the I-WP is more resistant to deformation and has less deformation under the same stress level conditions. Therefore, the deformation recoverable by the superelasticity is smaller.

The cyclic ratchet strains and fatigue damage strains[48] of the BCC and I-WP lattice structures were calculated and plotted in (Figure 6C and D), respectively. During the low-stress region of the fatigue cyclic loading, the strain values of the NiTi lattice samples were much smaller, even smaller than the strain values of the previous cyclic cycles. This leads to negative values of the cyclic ratchet strains as shown in (Figure 6C and D). In this study, the load and indenter position of the fatigue test machine tended to be constant when the number of cycles was 4000. Therefore, the ratcheting strain curve and the fatigue damage strain curve of the NiTi lattice structure all started with the 4000th cycle. Figure 6A and B show the hysteresis curves of different cycles in the fatigue test. The minimum strain corresponding to the hysteresis curves of these different cycles varies with the number of cycles as the fatigue experiment progresses. The ratcheting strain

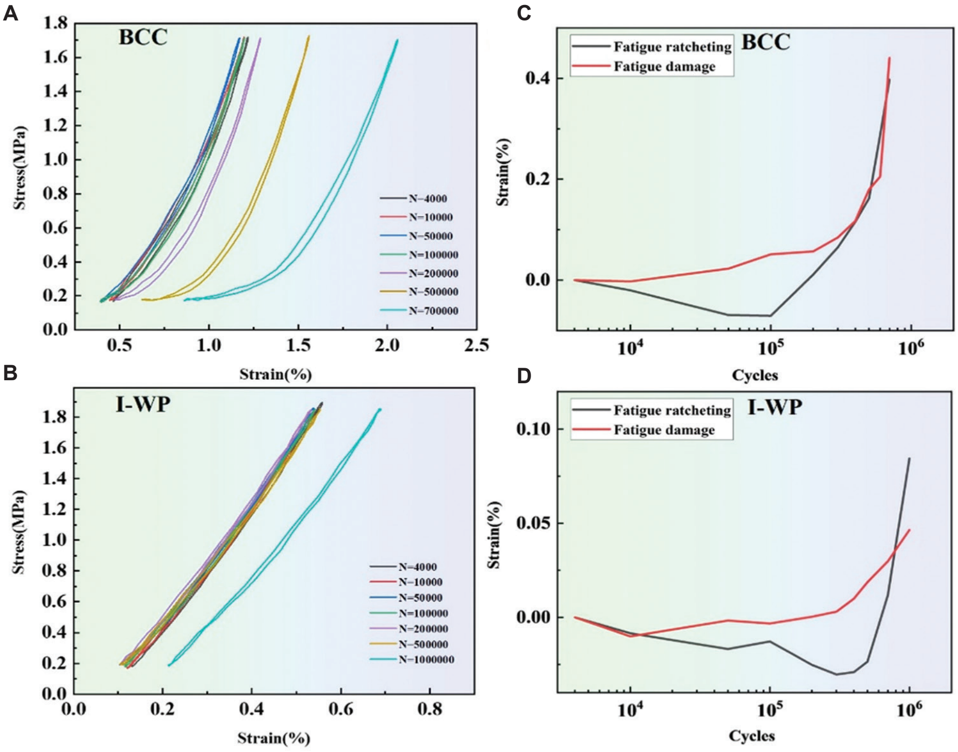

Figure 6. Hysteresis curves, as well as cyclic ratchet strain and fatigue damage strain. (A and B) Hysteresis curves of body-centered cubic (BCC) (A) and I-graph-wrapped package (I-WP) (B) lattice structures. (C and D) Cyclic ratchet strain and fatigue damage strain of BCC (C) and I-WP (D) lattice structures.

is characterized by the change of the minimum strain corresponding to the hysteresis curve of different cycles with the number of cycles. In this study, the 4000th cycle was used as the starting cycle. The ratcheting strain is defined as the difference between the minimum strain of the hysteresis curve of different cycle periods minus the minimum strain of the starting cycle period. The formula for ratcheting strain is given in Equation (II):

$$\varepsilon_{d} = \varepsilon_{min} - \varepsilon_{4000} \quad \text{(II)}$$

Where ε_{d} refers to the ratcheting strain; ε_{min} refers to the minimum strain of the hysteresis curve of different cycle periods; and ε_{4000} refers to the minimum strain of the starting cycle period. In this study, the 4000th cycle was used as the starting cycle period.

The fatigue damage strain is defined as the change in the difference between the maximum and minimum strain of the current cycle with respect to the 4000th cycle. It can be found that the fatigue damage strain played a dominant role in the fatigue failure of NiTi lattice structures. At high cycles, the fatigue damage strain accumulated before failure in I-WP was much lower than that in BCC, indicating that I-WP was more capable of inhibiting crack generation and expansion than BCC. It can be inferred that the TPMS design improves the ability of the BCC lattice structure to resist fatigue cracking, which in turn improves the fatigue performance. In addition, a certain range of negative ratchet strains can be found in both NiTi lattice structures, which was caused by the superelasticity of NiTi alloy recovering a certain amount of deformation.

The fatigue behavior of NiTi lattice structures could be affected by the properties of the NiTi alloy. It can be easily observed that there were "crescent-shaped" hysteresis loops of NiTi lattice structures. The superior superelasticity of NiTi enables a greater range of recoverable deformation of NiTi lattice structure samples than that of lattices with other materials. As a result, during the low-stress region of one cycle of the fatigue cyclic loading, the strain values of the NiTi lattice samples became much smaller, even lower than the strain values of the previous cyclic cycles, leading to negative values of the cyclic ratchet strains as shown in (Figure 6C and D). Therefore, the effect of superelasticity of NiTi lattice structure on fatigue performance was studied using a cyclic compression test.

3.3.3. Fatigue life and fatigue strength

As shown in Figure 5, the fatigue life is defined as the corresponding cycle number.[49] The fatigue strength is defined as the maximum stress at a certain cycle.[50] It can be observed in Figure 5 that for two structures, a greater load is associated with a smaller fatigue life. The number of cycles corresponding to the abrupt strain point decreased with the increase in stress levels.

As shown in Figure 7, the I-WP lattice structure exhibits a higher fatigue strength than the BCC at the same cycles. In addition, the I-WP structure exhibits longer fatigue life when both lattice structures are under the same level of stress conditions. The formulas of life and cycle period fitted by curve are shown in Figure 7.

The fatigue strengths of the NiTi BCC and I-WP at 10^6 cycles were 1.88 MPa and 2.08 MPa (calculated by the curve fitting formula in Figure 7), respectively. The fatigue strength of I-WP was about 1.11 times higher than that of BCC, indicating that the TPMS design is beneficial to the fatigue strength. The fatigue strength ratio is defined as the ratio of the fatigue strength to the yield strength at 10^6 cycles under compression-compression fatigue tests.[51] The fatigue strength ratios of BCC and I-WP were 0.33 and 0.34, respectively. In summary, the fatigue strength ratio of NiTi is constant and unaffected by the structural optimization method of TPMS, which can only enhance the fatigue performance of the material.

3.3.4. Fracture characteristics

The fracture characteristics of the two structures are portrayed in Figure 8. A near 45° shear fracture band can be found in all failed samples. This phenomenon has also been reported by Speirs *et al.*[52] in their study of the fatigue behavior of NiTi structure, which presented identical shear failure characteristics as in the NiTi lattice structure samples shown in Figure 3. The fatigue failure modes of the two NiTi lattice structures did not change with the alteration of loading stress.

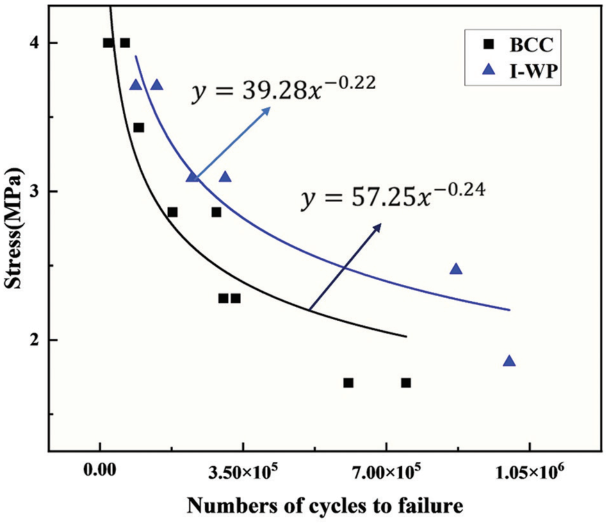

Figure 7. Stress-number of cycles to failure (S-N) curves of Nickel titanium lattice structures.

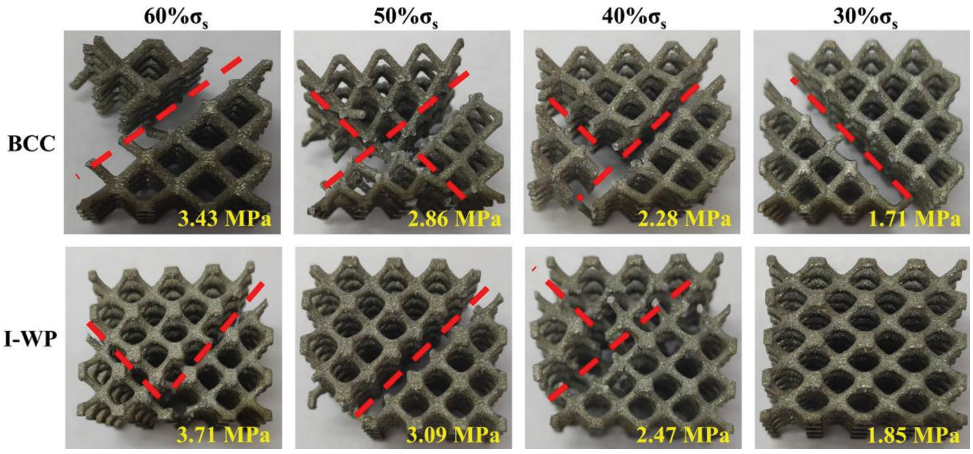

Figure 8. Fracture characteristics of Nickel titanium body-centered cubic and I-graph-wrapped package lattice structure specimens.

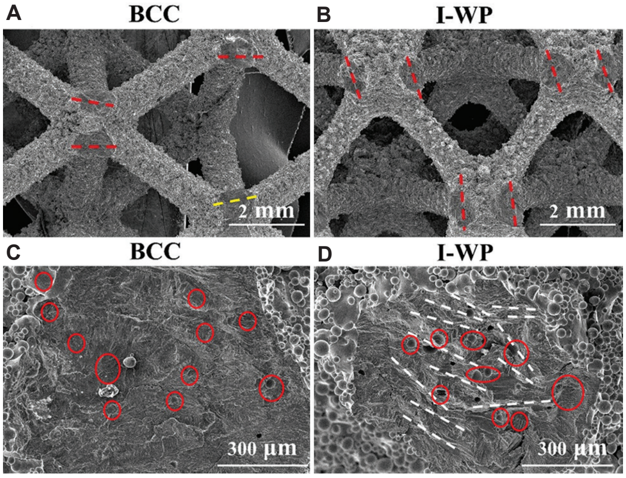

Figure 9. Crack characteristics of Nickel titanium lattice structures: The scale of body-centered cubic (BCC) (A) and I-graph-wrapped package (I-WP) (B) is 2 mm. The scale of BCC (C) and I-WP (D) is 300 µm.

Figure 9 shows the crack characteristics of NiTi lattice structures. As shown in (Figure 9A and B), the red-dotted line indicates that the break occurred near the node, and the yellow dotted line indicates that the break occurred at the node. The fracture of the BCC sample occurred at or near the node location, while the I-WP sample fractured only at the location on the column near the node.

As shown in (Figure 9C and D), differences in the fracture morphology between the two NiTi samples exist. The fracture morphology of the pillar of BCC was flatter. Some river-like streaks can be observed on the upper side of the fracture, indicating the nucleation and growth of the crack. The cracks started from the roots of the particles adhered to the strut surface and the stress concentration area at the nodes of BCC and then spread to the interior of the strut. The lower section was relatively smooth, and it can be inferred that a transient fracture occurred inside the strut after the cracks expanded to a certain area.

Unlike the BCC lattices, the fracture of the pillar of I-WP sample features many "small steps" (the white-dotted lines in Figure 9D), which can be used to determine the direction of crack propagation. Cracks of the I-WP samples were also mainly generated at the root of the metal powder particles attached to the surface. It is worth noting that a certain number of small voids (the red circles in Figure 9) were observed in the cross-sections of the struts of both NiTi lattice samples, which were usually caused by incomplete melting or mixing with impurities due to low laser power or high scanning speed. This phenomenon is conducive to the emergence and expansion of fatigue cracks, which is an unfavorable factor for fatigue strengthening of lattice structures. The research of Zhu *et al.* showed that repeated opening and closing of cracks in the sample will lead to early fatigue damage, which may merge into fatigue steps or form radial ridges.[53] In this study, the same fracture morphology characteristics are found in (Figure 9C and 9D). In addition, the attached particles on the surface of NiTi lattice samples, as shown in Figure 2, acted as crack initiation points during fatigue failure and promoted fatigue crack generation.

3.4. Analysis of compression failure behavior

Figure 10 shows the whole compression process, starting from the initial state to 40% strain. Figure 11 records the changes before and after inducing fractures in BCC and I-WP lattice structures. As shown in Figure 10, the pillars between the two nodes of the BCC structure deviated from the original direction during the compression process. The offset of the pillars between different nodes appeared when the strain was 10%. As the compression progressed, the BCC structure broke along the 45° direction at the joint. After the fracture, the overall structure became unstable, so

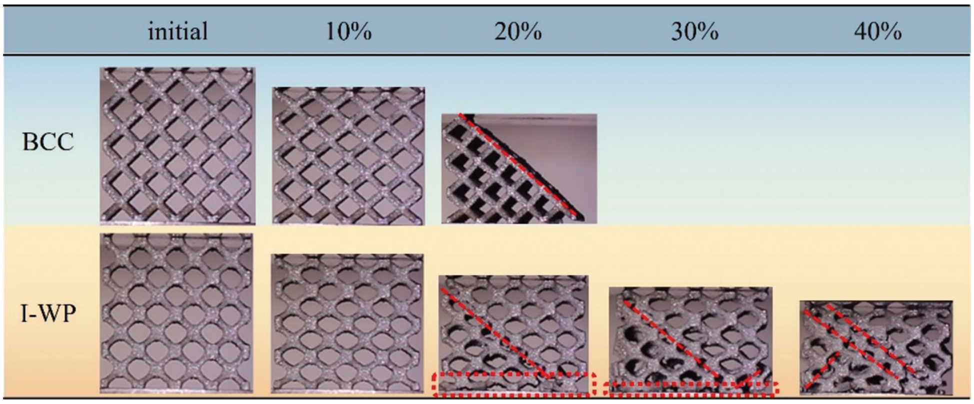

Figure 10. The whole compression process.

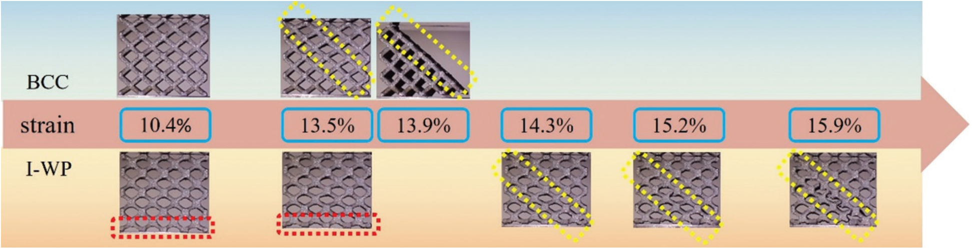

Figure 11. The cracking and failure process.

no pictures were recorded after achieving a strain of 20%. It can be observed that the pillar offset of the BCC structure, enclosed by a yellow dotted-line box in Figure 11, at 13.5% strain was more serious than other parts, and the fracture occurred at the node of this section.

As shown in Figure 10, the pillars between the two nodes of the I-WP structure also deviated from the original direction during the compression process. As the compression progressed, the I-WP fractured along the 45° direction of the strut. Figure 11 shows that the pillar of the I-WP structure enclosed by a yellow dotted-line box bent, and subsequently, the 45° fracture zone occurred at this section. After the fracture, the overall structure remained relatively stable, and the compression process could still continue. Failure appeared, as shown in the red dotted-line box, when the structure was compressed by 20%. The pillars of this unit cell were more easily broken than the other layers. Slight damage can be seen in the region enclosed by the red dotted-line box in Figure 11 when the structure was compressed by 10.4%. When the compression reached 40% for the I-WP structure, a new fracture zone of 45° along the pillar appeared.

Figure 12 presents the static simulation analysis of the two NiTi structures. The stress at the joints of the BCC structure was significantly higher than that of the pillars. As the compression progressed, the pillars between the nodes shifted. The pillar offset aggravated the force at the node, offering an explanation for the fracture at the BCC nodes shown in Figure 11. It is noted that the stress at the joints of the I-WP structure was significantly lower than that of the pillars. The pillars between the nodes exhibited bending as the compression progressed. The bending of the pillar aggravated the stress at the pillar, justifying the occurrence of fracture at the I-WP pillars, as shown in Figure 11.

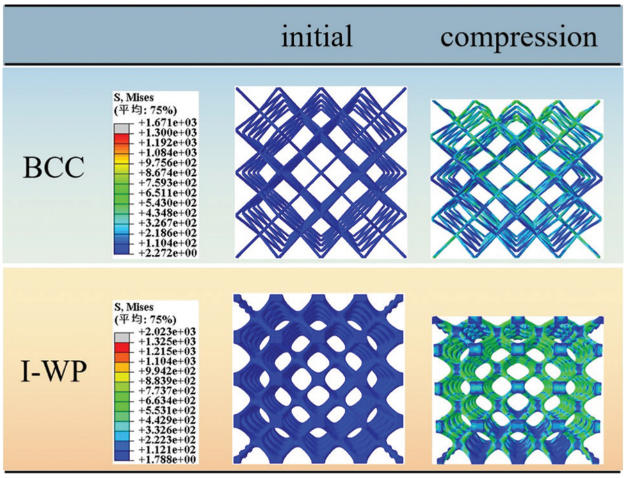

Figure 12. Finite element simulation of body-centered cubic and I-graph-wrapped package lattice structures.

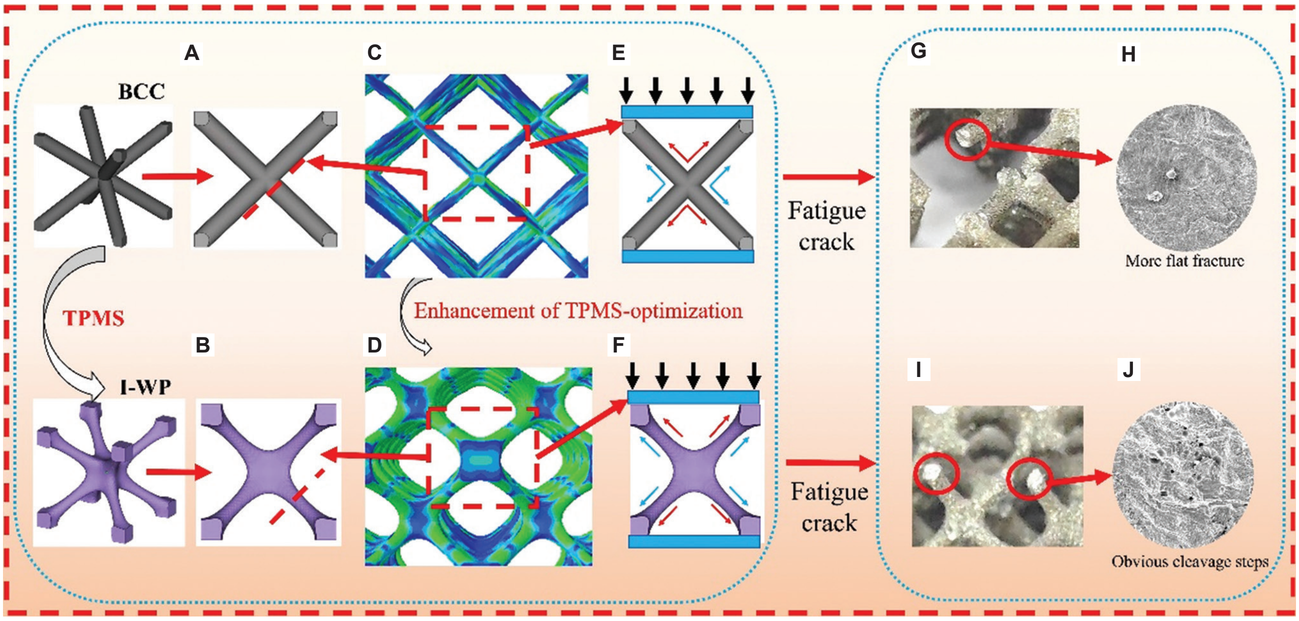

Figure 13. (A-J) Schematic diagram depicting the fatigue fracture mechanism of a Nickel titanium lattice structure.

3.5. Analysis of the fatigue fracture mechanism

A schematic diagram presenting the fatigue fracture mechanism of the two NiTi lattice structures is shown in Figure 13. The red dotted lines in (Figure 13A and B) indicate the location where the sample composed of the two structures is prone to fracture when subjected to uniaxial compression. The BCC structure is prone to fracture at the node, whereas the I-WP structure is prone to fracture at the pillar. This is because the stress distribution of the BCC structure is mainly concentrated at the nodes (Figure 13C), whereas the stress distribution of the I-WP structure is mainly concentrated on the pillars (Figure 13D). In uniaxial compression, as shown in (Figure 13E and F), the red arrows represent tensile stresses and the blue arrows denote compressive stresses. Under compressive loads, the area marked by red arrows produces tensile stress under tension, and the area marked by blue arrows produces compressive stress under compression. When the BCC structure is subjected to cyclic compression, there is a greater stress concentration at the joint. After a certain number of cycles, the joint becomes more susceptible to fatigue fracture. In contrast, when the I-WP structure is subjected to cyclic compression, there is a greater stress concentration at the pillar. After a certain number of cycles, the pillar becomes more vulnerable to fatigue fracture. This proposed mechanism offers some insights into how the fractures resulted in the samples, as shown in Figures 3 and 8, due to compression and fatigue.

It is worth noting that the fracture surfaces of the two metal structures are relatively smooth and bright (Figure 13G and I), characteristic of the cleavage fracture in the fracture analysis of metal materials.[54] However, the morphology of the fracture surface is different for the two structures (Figure 13H and J). As shown in the part enclosed by red dotted lines in (Figure 13C), the stress concentration at the node is more intensive, accelerating the occurrence of fatigue failure at this spot, which allows for the observation of the relatively flat fracture morphology shown in (Figure 13H). The stress concentration at the pillar, as shown in the part circumscribed by red dotted lines in (Figure 13D), is more dispersed, significantly slowing down the occurrence of fatigue failure at this spot, and causing the internal microstructure to break after undergoing longer cyclic loading. These deductions are reflected in the fracture observed in the NiTi lattice structures shown in Figure 8. Obvious cleavage steps formed are shown in (Figure 13J).

4. Conclusion

In this study, NiTi BCC and I-WP lattice structures were prepared by the LPBF process. The microstructure, mechanical properties, and fatigue properties of BCC and I-WP NiTi lattice structures were studied experimentally. The main conclusions stemming from this work are summarized as follows:

(i) The NiTi lattice structure samples prepared by the LPBF process share almost similar forming accuracy. The surfaces of both BCC and I-WP lattice structures produced by LPBF process are very rough, attached with numerous powder particles, especially at the lower surface. The minimal surface of the I-WP lattice structure has a slight benefit in avoiding powder adhesion on the side surface

(ii) The minimum surface optimization design is still applicable to the field of NiTi. The mechanical properties can be improved when the minimum surface optimization design is considered. The I-WP lattice structure has a higher Young's modulus and yield strength

(iii) Fatigue damage stands as the primary factor for the fatigue failure of NiTi lattice structures prepared by the LPBF process. The cracks of NiTi lattice structure samples always occur at the root of metal powder particles attached to the surface. The attached powder particles on the surface of NiTi lattice samples are prepared to act as crack initiation points during fatigue failure and promote the generation of fatigue cracks, which is not conducive to the fatigue performance of the NiTi sample.

(iv) The sample optimization design through the minimal surface can effectively improve the deformation resistance of NiTi lattice structure and change the morphology of fracture surfaces in high cycle fatigue. The fatigue strength improved from 1.88 MPa (BCC lattice structure) to 2.08 MPa (I-WP lattice structure). The enhancement in fatigue strength is attributed to the predominant stress concentration of TPMS lattice structures at the pillar with a more dispersed form and the stress concentration of strut-based lattice structures at the nodes with an intensive form.

Acknowledgments

The authors acknowledge the support provided by the State Key Laboratory of Materials Processing and Die and Mould Technology.

Funding

This study was supported by the National Natural Science Foundation of China (No. 52105396, 52235008, and U2341270) and the Open Fund of Hubei Longzhong Laboratory (2022ZZ-28).

Conflict of interest

The authors declare that they have no known competing financial interests or personal relationships that could have appeared to influence the work reported in this paper.

Author contributions

Conceptualization: Yang Li and Lei Yang
Formal analysis: Yunlong Ren and Yang Li
Funding acquisition: Lei Yang, Yun Chen, Chunze Yan, and Yusheng Shi
Investigation: Yun Chen, Bing Liu, and Xuan Cai
Methodology: Chunze Yan, Yusheng Shi, Lei Yang, and Mingkang Zhang
Writing – original draft: Yunlong Ren and Yang Li
Writing – review & editing: Yunlong Ren and Lei Yang

Ethics approval and consent to participate

Not applicable.

Consent for publication

Not applicable.

Availability of data

Data are available from the corresponding author upon reasonable request.

References

1. Bagheri A, Mahtabi MJ, Shamsaei N. Fatigue behavior and cyclic deformation of additive manufactured NiTi. *J Mater Process Technol*. 2018;252:440-453.

   doi: 10.1016/j.jmatprotec.2017.10.006

2. Gu H, Bumke L, Chluba C, Quandt E, James RD. Phase engineering and supercompatibility of shape memory alloys. *Mater Today*. 2018;21(3):265-277.

   doi: 10.1016/j.mattod.2017.10.002

3. Molod MA, Spyridis P, Barthold FJ. Applications of shape memory alloys in structural engineering with a focus on concrete construction - A comprehensive review. *Constr Build Mater*. 2022;337:127565.

   doi: 10.1016/j.conbuildmat.2022.127565

4. Fang C, Liang D, Zheng Y, Yam MCH, Sun R. Rocking bridge piers equipped with shape memory alloy (SMA) washer springs. *Eng Struct*. 2020;214:110651.

   doi: 10.1016/j.engstruct.2020.110651

5. Xie W, Quinn J, Zhang J, Carson L, Chan CW. Control of laser-gas-material interactions to enhance the surface properties of NiTi for orthopaedic applications. *Surf Coat Technol*. 2021;421:127403.

   doi: 10.1016/j.surfcoat.2021.127403

6. Yang X, Yang Q, Shi Y, *et al*. Effect of volume fraction and unit cell size on manufacturability and compressive behaviors of Ni-Ti triply periodic minimal surface lattices. *Addit Manuf*. 2022;54:102737.

   doi: 10.1016/j.addma.2022.102737

7. Zhang C, Jin J, He M, Yang L. Compressive mechanics and hyperelasticity of Ni-Ti lattice structures fabricated by selective laser melting. *Crystals*. 2022;12(3):408.

   doi: 10.3390/cryst12030408

8. Sefene EM. State-of-the-art of selective laser melting process: A comprehensive review. *J Manuf Syst*. 2022;63:250-274.

   doi: 10.1016/j.jmsy.2022.04.002

9. Liu C, Roux LL, Ji Z, Kerfriden P, Lacan F, Bigot S. Machine learning-enabled feedback loops for metal powder bed fusion additive manufacturing. *Procedia Comput Sci*. 2020;176:2586-2595.

   doi: 10.1016/j.procs.2020.09.314

10. Han Q, Gu Y, Huang J, *et al*. Selective laser melting of hastelloy X nanocomposite: Effects of TiC reinforcement on crack elimination and strength improvement. *Compos B Eng*. 2020;202:108442.

    doi: 10.1016/j.compositesb.2020.108442

11. Zhou SY, Su Y, Wang H, Enz J, Ebel T, Yan M. Selective laser melting additive manufacturing of 7xxx series Al-Zn-Mg-Cu alloy: Cracking elimination by co-incorporation of Si and TiB_2. *Addit Manuf*. 2020;36:101458.

    doi: 10.1016/j.addma.2020.101458

12. Hussain S, Alagha AN, Haidemenopoulos GN, Zaki W. Microstructural and surface analysis of NiTi TPMS lattice sections fabricated by laser powder bed fusion. *J Manuf Process*. 2023;102:375-386.

    doi: 10.1016/j.jmapro.2023.07.055

13. Finazzi V, Berti F, Petrini L, Previtali B, Demir AG. Additive manufacturing and post-processing of superelastic NiTi micro struts as building blocks for cardiovascular stents. *Addit Manuf*. 2023;70:103561.

    doi: 10.1016/j.addma.2023.103561

14. Wang J, Huang B, Gu X, Zhu J, Zhang W. Actuation performance of machined helical springs from NiTi shape memory alloy. *Int J Mech Sci*. 2022;236:107744.

    doi: 10.1016/j.ijmecsci.2022.107744

15. Luo J, Xu K, Li C, Li M, Lin Y. The evolution of dynamic recrystallization and recrystallization texture during isothermal compression of NiTi shape memory alloy. *Mater Sci Eng A*. 2021;820:141424.

    doi: 10.1016/j.msea.2021.141424

16. Kan Q, Zhang Y, Xu Y, Kang G, Yu C. Tension-compression asymmetric functional degeneration of super-elastic NiTi shape memory alloy: Experimental observation and multiscale constitutive model. *Int J Solids Struct*. 2023;280:112384.

    doi: 10.1016/j.ijsolstr.2023.112384

17. Safdel A, Zaker N, Botton GA, Elbestawi MA. The role of texture and restoration mechanisms in defining the tension-compression asymmetry behavior of aged NiTi alloys fabricated by laser powder bed fusion. *Mater Sci Eng A*. 2023;864:144592.

    doi: 10.1016/j.msea.2023.144592

18. Wu Y, Ertekin E, Sehitoglu H. Elastocaloric cooling capacity of shape memory alloys - Role of deformation temperatures, mechanical cycling, stress hysteresis and inhomogeneity of transformation. *Acta Mater*. 2017;135:158-176.

    doi: 10.1016/j.actamat.2017.06.012

19. Zhang K, Kang G, Sun Q. High fatigue life and cooling efficiency of NiTi shape memory alloy under cyclic compression. *Scr Mater*. 2019;159:62-67.

    doi: 10.1016/j.scriptamat.2018.09.012

20. Zhao T, Kang G. Experimental study and life prediction on fatigue failure of NiTi shape memory alloy under multi-axial one-way shape memory cyclic loadings. *Int J Fatigue*. 2022;155:106609.

    doi: 10.1016/j.ijfatigue.2021.106609

21. Jin J, Wu S, Yang L, *et al*. Ni-Ti multicell interlacing Gyroid lattice structures with ultra-high hyperelastic response fabricated by laser powder bed fusion. *Int J Mach Tools Manuf*. 2024;195:104099.

    doi: 10.1016/j.ijmachtools.2023.104099

22. Song W, Mu K, Feng G, *et al*. Mechanical properties of 3D printed interpenetrating phase composites with TPMS architectures. *Thin Walled Struct*. 2023;193:111210.

    doi: 10.1016/j.tws.2023.111210

23. Gado MG, Ookawara S. 3D-printed Triply Periodic Minimal Surface (TPMS) structures: Towards potential application of adsorption-based atmospheric water harvesting. *Energy Convers Manag*. 2023;297:117729.

    doi: 10.1016/j.enconman.2023.117729

24. Yang L, Li Y, Chen Y, Yan C, Liu B, Shi Y. Topologically optimized lattice structures with superior fatigue performance. *Int J Fatigue*. 2022;165:107188.

    doi: 10.1016/j.ijfatigue.2022.107188

25. Zhang C, Qiao H, Yang L, *et al*. Vibration characteristics of additive manufactured IWP-type TPMS lattice structures. *Compos Struct*. 2024;327:117642.

    doi: 10.1016/j.compstruct.2023.117642

26. Fu H, Kaewunruen S. Experimental and DEM investigation of axially-loaded behaviours of IWP-based structures. *Int J Mech Sci*. 2022;235:107738.

    doi: 10.1016/j.ijmecsci.2022.107738

27. Ge J, Yuan B, Chen H, *et al*. Anisotropy in microstructural features and tensile performance of laser powder bed fusion NiTi alloys. *J Mater Res Technol*. 2023;24:8656-8668.

    doi: 10.1016/j.jmrt.2023.05.046

28. Qi Y, Sha P, Yang K, *et al*. Construction and parameter optimization of LPBF-NiTi alloy bionic superhydrophobic surface based on laser processing. *J Mater Res Technol*. 2023;24:9462-9475.

doi: 10.1016/j.jmrt.2023.05.162

29. Yang L, Yan C, Fan H, *et al*. Investigation on the orientation dependence of elastic response in Gyroid cellular structures. *J Mech Behav Biomed Mater*. 2019;90:73-85.

    doi: 10.1016/j.jmbbm.2018.09.042

30. International Organization for Standardization. *ISO 13314:2011, Mechanical Testing of Metals--Ductility Testing--Compression Test for Porous and Cellular Metals*. Geneva: International Organization for Standardization; 2011. p. 1-7.

31. Chen W, Yang Q, Huang S, Kruzic JJ, Li X. Compression behavior of graded NiTi gyroid-structures fabricated by laser powder bed fusion additive manufacturing under monotonic and cyclic loading. *JOM*. 2021;73(12):4154-4165.

    doi: 10.1007/s11837-021-04938-x

32. Yang L, Wu S, Yan C, *et al*. Fatigue properties of Ti-6Al-4V Gyroid graded lattice structures fabricated by laser powder bed fusion with lateral loading. *Addit Manuf*. 2021;46:102214.

    doi: 10.1016/j.addma.2021.102214

33. Jiang H, Wang X, Xi R, *et al*. Size effect on the microstructure, phase transformation behavior, and mechanical properties of NiTi shape memory alloys fabricated by laser powder bed fusion. *J Mater Sci Technol*. 2023;157:200-212.

    doi: 10.1016/j.jmst.2023.02.026

34. Zheng N, Zhai X, Chen F. Topology optimization of Self-supporting porous structures based on triply periodic minimal surfaces. *Comput Aided Des*. 2023;161:103542.

    doi: 10.1016/j.cad.2023.103542

35. Hu J, Wang S, Wang Y, Li F, Luo Z. A lightweight methodology of 3D printed objects utilizing multi-scale porous structures. *Vis Comput*. 2019;35:949-959.

    doi: 10.1007/s00371-019-01672-z

36. Chen W, Gu D, Yang J, Yang Q, Chen J, Shen X. Compressive mechanical properties and shape memory effect of NiTi gradient lattice structures fabricated by laser powder bed fusion. *Int J Extrem Manuf*. 2022;4(4):045002.

    doi: 10.1088/2631-7990/ac8ef3

37. Sun L, Chen K, Geng P, Zhou Y, Wen S, Shi Y. Mechanical and shape memory properties of NiTi triply periodic minimal surface structures fabricated by laser powder bed fusion. *J Manuf Process*. 2023;101:1091-1100.

    doi: 10.1016/j.jmapro.2023.06.034

38. Yang L, Mertens R, Ferrucci M, Yan C, Shi Y, Yang S. Continuous graded Gyroid cellular structures fabricated by selective laser melting: Design, manufacturing and mechanical properties. *Mater Des*. 2019;162:394-404.

    doi: 10.1016/j.matdes.2018.12.007

39. Loginov YN, Koptyug A, Popov VV Jr., *et al*. Compression deformation and fracture behavior of additively manufactured Ti-6Al-4V cellular structures. *Int J Lightweight Mater Manuf*. 2022;5(1):126-135.

    doi: 10.1016/j.ijlmm.2021.11.003

40. Al-Saedi DSJ, Masood SH, Faizan-Ur-Rab M, Alomarah A, Ponnusamy P. Mechanical properties and energy absorption capability of functionally graded F2BCC lattice fabricated by SLM. *Mater Des*. 2018;144:32-44.

    doi: 10.1016/j.matdes.2018.01.059

41. Bian Y, Li P, Yang F, Wang P, Li W, Fan H. Deformation mode and energy absorption of polycrystal-inspired square-cell lattice structures. *Appl Math Mech*. 2020;41(10):1561-1582.

    doi: 10.1007/s10483-020-2648-8

42. Li QM, Magkiriadis I, Harrigan JJ. Compressive strain at the onset of densification of cellular solids. *J Cell Plast*. 2006;42(5):371-392.

    doi: 10.1177/0021955x06063519

43. Prevéy PS, Cammett JT. The influence of surface enhancement by low plasticity burnishing on the corrosion fatigue performance of AA7075-T6. *Int J Fatigue*. 2004;26(9):975-982.

    doi: 10.1016/j.ijfatigue.2004.01.010

44. Nemat-Nasser S, Guo WG. Superelastic and cyclic response of NiTi SMA at various strain rates and temperatures. *Mech Mater*. 2006;38(5):463-474.

    doi: 10.1016/j.mechmat.2005.07.004

45. Gall K, Maier HJ. Cyclic deformation mechanisms in precipitated NiTi shape memory alloys. *Acta Mater*. 2002;50(18):4643-4657.

    doi: 10.1016/S1359-6454(02)00315-4

46. Sun ZP, Guo YB, Shim VPW. Deformation and energy absorption characteristics of additively-manufactured polymeric lattice structures - Effects of cell topology and material anisotropy. *Thin-Walled Struct*. 2021;169:108420.

    doi: 10.1016/j.tws.2021.108420

47. Otsuka K, Ren X. Physical metallurgy of Ti-Ni-based shape memory alloys. *Prog Mater Sci*. 2005;50(5):511-678.

    doi: 10.1016/j.pmatsci.2004.10.001

48. Yang L, Yan C, Cao W, *et al*. Compression-compression fatigue behaviour of gyroid-type triply periodic minimal surface porous structures fabricated by selective laser melting. *Acta Mater*. 2019;181:49-66.

    doi: 10.1016/j.actamat.2019.09.042

49. Zhao S, Li SJ, Wang SG, *et al*. Compressive and fatigue behavior of functionally graded Ti-6Al-4V meshes fabricated by electron beam melting. *Acta Mater*. 2018;150:1-15.

    doi: 10.1016/j.actamat.2018.02.060

50. International Organization for Standardization. *Metallic Materials--Fatigue Testing--Axial Force-controlled Method*. Geneva: International Organization for Standardization; 2006.

51. Li SJ, Murr LE, Cheng XY, *et al*. Compression fatigue behavior of Ti-6Al-4V mesh arrays fabricated by electron beam melting. *Acta Mater*. 2012;60(3):793-802.

    doi: 10.1016/j.actamat.2011.10.051

52. Speirs M, Van Hooreweder B, Van Humbeeck J, Kruth JP. Fatigue behaviour of NiTi shape memory alloy scaffolds produced by SLM, a unit cell design comparison. *J Mech Behav Biomed Mater*. 2017;70:53-59.

    doi: 10.1016/j.jmbbm.2017.01.016

53. Zhu ML, Jin L, Xuan FZ. Fatigue life and mechanistic modeling of interior micro-defect induced cracking in high cycle and very high cycle regimes. *Acta Mater*. 2018;157:259-275.

    doi: 10.1016/j.actamat.2018.07.036

54. Swain MV, Lawn BR, Burns SJ. Cleavage step deformation in brittle solids. *J Mater Sci*. 1974;9(2):175-183.

    doi: 10.1007/BF00550939

ACCSCIENCE PUBLISHING

Materials Science in Additive Manufacturing

ORIGINAL RESEARCH ARTICLE

Accelerating hybrid lattice structures design with machine learning

Chenxi Peng[1,2], Phuong Tran[3]*, and Erich Rutz[1,2,4,5,6,7]*

[1]Department of Paediatrics, The University of Melbourne, Parkville, Victoria, Australia

[2]Murdoch Children's Research Institute, Parkville, Victoria, Australia

[3]RMIT Centre for Additive Manufacturing, School of Engineering, RMIT University, Melbourne, Victoria, Australia

[4]Bob Dickens Chair Paediatric Orthopaedic Surgery, The University of Melbourne, Parkville, Victoria, Australia

[5]Department of Orthopaedics, The Royal Children's Hospital Melbourne, Parkville, Victoria, Australia

[6]The Hugh Williamson Gait Analysis Laboratory, The Royal Children's Hospital Melbourne, Parkville, Victoria, Australia

[7]Medical Faculty, The University of Basel, Basel, Switzerland

Abstract

Lattice structures inspired by triply periodic minimal surfaces (TPMS) have attracted increasing attention due to their lightweight properties and high mechanical performance. Recent research showed that hybrid structures based on the topology of two or more types of TPMS can present interesting multifunctional properties. However, the complexity of TPMS-based lattice designs presents challenges in both design and evaluation. To address these challenges, this study was designed to explore the integration of the machine learning method to predict the mechanical properties of hybrid lattice structures inspired by TPMS based on their patterns. A back propagation neural network (BPNN) was designed and trained on a dataset generated through finite element (FE) simulations and homogenization methods. The BPNN demonstrated robustness in predicting elastic modulus and Poisson's ratio of TPMS hybrid lattice structures, offering rapid and efficient predictions. Validation against FE simulations confirmed the accuracy and reliability of the BPNN predictions, proving its potential as a valuable tool for accelerating the design and evaluation of complex hybrid lattice structures.

Keywords: Lattice structures; Triply periodic minimal surfaces; Elastic modulus; Poisson's ratio; Machine learning

***Corresponding authors:**
Phuong Tran
(jonathan.tran@rmit.edu.au)
Erich Rutz
(erich_rutz@hotmail.com)

Citation: Peng C, Tran P, Rutz E. Accelerating hybrid lattice structures design with machine learning. *Mater Sci Add Manuf.* 2024;3(2):3430 doi: 10.36922/msam.3430

Received: April 16, 2024

Accepted: June 03, 2024

1. Introduction

Lattice structures are attracting increasing attention from researchers as they present promising multifunctional properties, such as exceptional specific modulus and strength and energy absorption capabilities.[1,2] Thus, these structures have the potential to meet the requirements of various applications, for example, thermal management,[3] bone tissue engineering,[4] energy absorption,[5-7] heat dissipation,[8,9] and structural components.[10-12] The base material and cell topology are the two dominant factors affecting the properties of lattice structures.[13] Efforts were made by researchers to investigate different cell topologies to improve the mechanical responses of lattice structures.[14-19]

Lattice structures inspired by triply periodic minimal surfaces (TPMS) have captured increasing attention within the research community due to their promising combination of lightweight properties and high mechanical performance.[20-22] Mathematically, TPMS is characterized by zero mean curvature, three dimensionally periodic, and smooth topology, which is achieved through the minimization of an area within defined surface boundaries. In practical terms, structures with TPMS-like topologies can be modeled using level-set approximation methods.[23] Two primary strategies are employed in generating a TPMS-based lattice. In the network phase TPMS structures, one sub-domain of the space isolated by the surface is filled with a solid material, while the matrix phase is formed by assigning thickness to the TPMS surface.[20] Evaluation of the mechanical properties of TPMS-based lattices has been carried out using various materials such as stainless steel,[24] aluminum alloy,[25] polymer[26,27] and concrete,[28,29] illustrating superior properties to conventional strut-based structures. Furthermore, the geometry of TPMS-based structures can be tailored locally, as it is controlled by mathematical equations.[30,31] For instance, Maskery *et al.* demonstrated the feasibility of designing TPMS-based lattices with graded relative density, resulting in customized collapse behaviors and enhanced energy absorption under compression.[32] Al-Ketan *et al.* proposed a novel class of stochastic cellular structures inspired by TPMS, presenting superior mechanical responses at high relative densities.[31] Recently, Maskery and Ashcroft proposed the concept of designing honeycomb-like structures based on TPMS.[33] Peng *et al.* investigated the multifunctional properties of hybrid honeycomb-like lattices based on TPMS, revealing exceptional mechanical properties and tunable responses.[34] These TPMS-based honeycomb-like structures presented superior mechanical properties compared to traditional honeycomb structures. Meanwhile, hybrid structures can be designed based on different unit cells to exhibit distinct properties that are not possible with monolithic structures. However, the complexity of these structures presents challenges in their design and property evaluations.

In recent years, there has been a notable surge in interest regarding the application of artificial intelligence (AI) and machine learning in the designs of metamaterials.[35-38] Notably, neural networks and evolutionary algorithms have emerged as prominent examples, offering expedited problem-solving capabilities with reduced computational costs. Particularly beneficial for addressing high-complexity challenges characterized by a multitude of design parameters, such as those encountered in the architecture design of lattice structures, AI algorithms excel due to their rapid and reliable nature.[39] Research indicates that machine learning algorithms have significantly accelerated the process of lattice structure design compared to conventional methods, such as trial-and-error or analytical physics-based approaches.[39] Moreover, the advance of new technologies has not only facilitated quicker solutions but has also enabled the discernment of previously unseen correlations between design parameters and mechanical performance.[40] The growing demand for novel structures with distinctive functionalities serves as a driving force for researchers to explore innovative approaches aimed at accelerating the development and discovery of novel architectures. Efforts toward automating the design process and enhancing the evaluation rate of new structures have been underscored in recent literature.[41,42] This necessitates the establishment of frameworks that utilize various AI techniques to streamline these processes. Indeed, the pivotal role of AI in advancing the field of metamaterials is becoming increasingly evident; as it facilitates the automation of labor-intensive discovery processes and unveils previously unnoticed patterns.[43-46]

With the aim of accelerating the design of hybrid lattice structures inspired by TPMS, this work explores the potential of predicting the mechanical properties of complex hybrid lattice structures using machine learning methods. First, the strategy to design hybrid lattices with TPMS-like unit cells, the homogenization method to generate datasets for training, and the architecture of artificial neural networks are introduced in the paper. Then, the dataset evaluation, performance of the model, and further validation by finite element (FE) modeling are discussed. Finally, the key findings of this work are presented.

2. Materials and methods

2.1. Design of TPMS honeycomb cell

Mathematically, minimal surfaces are surfaces with zero mean curvature at a given point $H = 0$ (I)

where $H=(k_1 + k_2)/2$; and k_1 and k_2 represent the principal curvatures in orthogonal planes.[47]

The normal unit vector of the surface maintains a zero divergence across all points, and the Gaussian curvature of the surface is expressed as follows:

$$K = k_1 k_2 \tag{II}$$

When a minimal surface is replicated infinitely and periodically throughout three-dimensional (3D) space, it is referred to as a TPMS. TPMS exhibits distinct geometric characteristics, notably smooth surfaces devoid of sharp corners. These surfaces are prevalent in numerous biological systems, including soap films,[48] block copolymers,[49] wings of butterflies,[50,51] and the skeleton of sea urchins.[52]

Various methods are utilized to model TPMS structures, including parametric, implicit, and boundary functions. The level-set approximation method is mainly employed in modeling TPMS-based honeycomb structures. TPMS in 3D space can be represented by a Fourier summation:

$$\Psi(r) = \sum_k F(k)\cos\left[2\pi k \cdot r - \alpha(k)\right] = 0 \tag{III}$$

where k represents the reciprocal vector, $\alpha(k)$ denotes the phase shift, and $F(k)$ represents the amplitude for vector k.[53] Equation III can be simplified by truncating it to a trigonometric function, φ, which satisfies:

$$\phi(x,y,z) = c \tag{IV}$$

where c is the iso-value controlling offset from the zero level-set. Then, lattice structures based on TPMS can be created using:

$$\phi^2(x,y,z) = c^2 \tag{V}$$

where the intervals [−c,c] specify the fraction of the solid region of the structure. The TPMS gyroid and primitive surfaces can be modeled using the following equations:

$$f_{gyroid}(x,y,z) = \cos(w_x x)\sin(w_y y) + \cos(w_y y)\sin(w_z z) + \cos(w_z z)\sin(w_x x) \tag{VI}$$

$$f_{primitve}(x,y,z) = \cos(w_x x) + \cos(w_y y) + \cos(w_z z) \tag{VII}$$

where x, y, and z represent coordinates in the 3D Cartesian coordinate system. The variable w defines the periodicities of the TPMS function:

$$w_i = 2\pi \frac{n_i}{L_i} fori = x,y,z \tag{VIII}$$

where n_i controls the number of unit cells along each direction. L_i defines the dimensions of the lattice along each direction.

To introduce new two-dimensional (2D) structures, the z periodicity in Equations VI and VII can be eliminated by substituting $z = 0$ and then inserting them into Equation V:

$$U_{G-Honeycomb} = \left(\cos(w_x x)\sin(w_y y) + \sin(w_x x)\right)^2 - c^2 \tag{IX}$$

$$U_{P-Honeycomb} = \left(\cos(w_x x) + \cos(w_y y)\right)^2 - c^2 \tag{X}$$

Equations IX and X define honeycomb-like structures based on TPMS Gyroid and Primitive. The relative density of each cell is approximately 0.25. Examples of unit cells based on TPMS-Gyroid and TPMS-Primitive are illustrated in Figure 1A and B, respectively.

2.2. Hybrid lattice design

As depicted in Figure 1C and D, G-Honeycomb and P-Honeycomb cells exhibit distinct stiffness, with the P-Honeycomb cell being approximately four times stiffer than the G-Honeycomb cell. By combining these hard and soft cells within larger hybrid lattices, a broad spectrum of tunable mechanical responses can be achieved. In this study, a 10 by 10 lattice (100 mm by 100 mm) was designed, incorporating a total of 100 randomly distributed G-Honeycomb and P-Honeycomb cells, as shown in Figure 2A and B, respectively. Figure 2C illustrates an example design of the hybrid lattice, where cells are color-coded: red representing P-Honeycomb (hard) and blue representing G-Honeycomb (soft). To streamline dataset preparation and reduce complexity, the hybrid lattice is further simplified into a binary matrix representation. Figure 2D presents the simplified binary matrix, wherein 0 represents a hard cell (P-Honeycomb), and 1 represents a soft cell (G-Honeycomb).

2.3. FE simulation

To validate the results obtained from the homogenization method, FE analysis was conducted utilizing a pre-validated numerical model.[34] ABAQUS/Explicit 2020 was employed to predict compressive responses of the structure. To enhance computational efficiency, uniform G-Honeycomb, and P-Honeycomb structures were modeled under the plane strain assumption, given their 2D surface-based origins. The lattice structures were discretized using 2,437 CPE4R four-node bilinear plane strain elements with reduced integration and hourglass control for each unit cell. The material behaviors of the base material were simplified to be elastic and perfectly plastic, in line with testing data obtained from 3D-printed tensile samples in literature,[34] as summarized in Table 1. Two platens were modeled, with the bottom platen fixed, while displacement was applied to the top platen to load the structure. Contact behaviors were characterized by a hard formulation along the normal direction and the penalty method with a friction coefficient of 0.3 along the tangential direction. The elastic modulus was determined as the slope of the stress-strain curve in the linear elastic region, while Poisson's ratio was approximated as the ratio between the horizontal displacement of the midpoint on the edge and the applied vertical displacement. In terms of the computational cost, the 2D FE model took about 20 min to calculate the elastic modulus and Poisson's ratio of a lattice running on six cores Intel® I7-8700K CPU at 3.7 GHz.

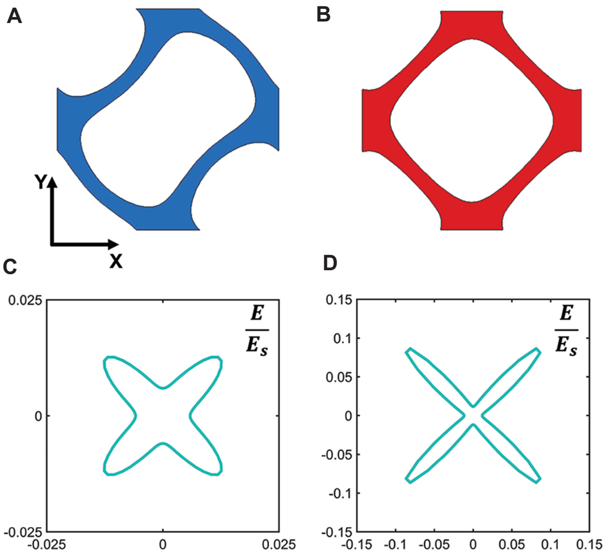

Figure 1. Elastic responses of triply periodic minimal surfaces (TPMS)-based honeycomb-like lattice unit cell. (A and B) The geometry of unit cell based on TPMS-gyroid (A) and TPMS-primitive (B). (C and D) Normalized spatial dependence of homogenized elastic moduli of TPMS-gyroid (C) and TPMS-primitive (D).

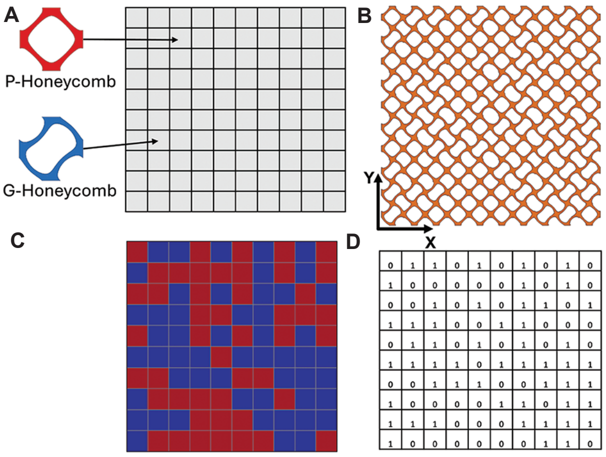

0	1	1	0	1	0	1	0	1	0
1	0	0	0	0	0	1	0	1	0
0	0	1	0	1	0	1	1	0	1
1	1	1	0	0	1	1	0	0	0
0	1	1	0	1	0	1	0	1	0
1	1	1	1	0	1	1	1	1	1
0	0	1	1	1	0	0	1	1	1
1	0	0	0	0	1	1	0	1	1
1	1	1	0	0	0	1	1	1	1
1	0	0	0	0	0	0	1	1	0

Figure 2. Hybrid lattice generation and simplification to binary matrix. (A) Process of hybrid lattice generation. (B) Example of hybrid lattice. (C) Simplified representation of the lattice. (D) Binary matrix representation of the hybrid lattice.

2.4. Homogenization method

The elastic modulus and Poisson's ratio of the hybrid lattice were calculated based on the homogenization method. According to homogenization theory, the elasticity tensor of a periodic structure can be determined by:

$$E^{H}_{ijkl} = \frac{1}{|\Omega|}\int E_{pqrs}\left(\varepsilon^{0(ij)}_{pq} - \varepsilon^{(ij)}_{pq}\right)\left(\varepsilon^{0(ij)}_{rs} - \varepsilon^{(ij)}_{rs}\right)d\Omega \qquad \text{(XI)}$$

where E_{pqrs} is the locally varying stiffness tensor, $|\Omega|$ is the area of the domain, $\varepsilon^{0(ij)}_{pq}$ refers to the applied strain fields at the macroscopic scale, and $\varepsilon^{(ij)}_{pq}$ refers to the locally varying strain fields given by:

$$\varepsilon^{(ij)}_{pq} = \varepsilon_{pq}\left(\chi^{ij}\right) = \frac{1}{2}\left(\chi^{ij}_{p,q} + \chi^{ij}_{q,p}\right) \qquad \text{(XII)}$$

χ^{ij} is the displacement field that can be determined based on applied macroscopic strain:

$$\int_{\Omega} E_{ijpq}\varepsilon_{ij}\left(v\right)\varepsilon_{pq}\left(\chi^{kl}\right)d\Omega = \int_{\Omega} E_{ijpq}\varepsilon_{ij}\left(v\right)\varepsilon^{0(kl)}_{pq}dV\forall v \in \Omega \qquad \text{(XIII)}$$

where v represents the virtual displacement field. The elastic modulus and Poisson's ratio of the hybrid lattice can then be calculated based on the elastic tensor E^{H}_{ijkl}.

Each hybrid lattice was first discretized into a voxel model. Then, the homogenized elastic tensor was calculated based on the code developed by Dong *et al.*[54] Finally, the elastic modulus and Poisson's ratio of the hybrid lattice were determined according to the elasticity tensor. The material behavior is based on the same material as used in the 2D FE model. As presented in Figure 3, a good agreement was achieved between the homogenization method and the 2D FE model. Since a large number of data was required to train the artificial neural network, the homogenization method was used to obtain the elastic modulus and Poisson's ratio of the hybrid lattice to reduce computational costs.

2.5. Data set preparation

A Python script was developed to randomly arrange G-Honeycomb and P-Honeycomb cells within a 10 × 10 hybrid lattice and export it as a stereolithography file, facilitating input for the homogenization model. In

Table 1. Material properties in finite element model

	Elastic modulus (MPa)	Yield strength (MPa)	Poisson's ratio	Strain at break	Density (g/cm^3)
Properties	2400	61	0.35	0.25	1.2

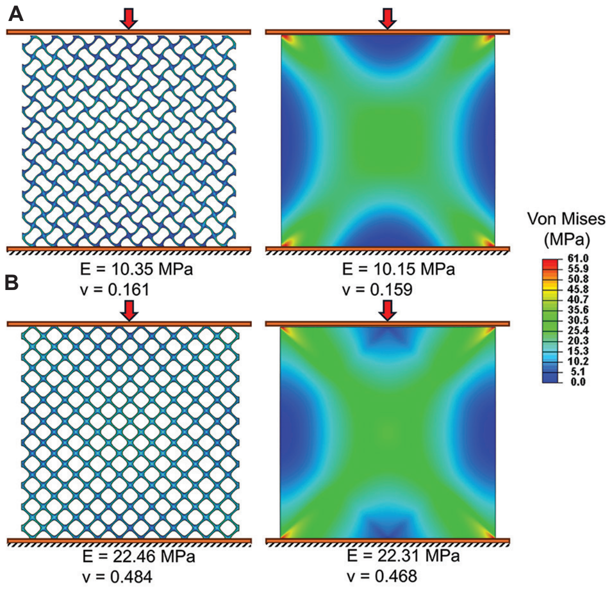

Figure 3. Comparison between modulus and Poisson's ratio obtained from finite element simulation and homogenization method: (A) G-Honeycomb and (B) P-Honeycomb.

addition, a binary matrix is generated for each lattice to serve as input data. Following topology creation, elastic modulus and Poisson's ratio values along both the X- and Y-directions were computed for each lattice using the homogenization method. Each data point comprised a 10 × 10 binary matrix representing the lattice topology, along with corresponding labels: elastic modulus along the X-direction (E_x), elastic modulus along the Y-direction (E_y), Poisson's ratio along the X-direction (v_{xy}), and Poisson's ratio along the Y-direction (v_{yx}). In total, 3000 random lattices were generated using this approach. Figure 4 presents examples of randomly generated hybrid lattices, providing visual insight into the diversity and complexity of the lattice structures produced.

2.6. Architecture of artificial neural network

A back propagation neural network (BPNN) was designed to train the dataset, utilizing TensorFlow and Keras frameworks.[55] The architecture of the network unfolds sequentially, including an input layer, several hidden layers, and an output layer, as presented in Figure 5. Commencing with a flattening layer to process input 10 × 10 binary matrix, subsequent layers include three densely connected layers with 128, 64, and 32 neurons, respectively. In the BPNN, the information from the input layer propagates as follows:

$$Z^{(l)} = A^{(l-1)} \cdot W^{(l)} + b^{(l)} \tag{XIV}$$

$$A^{(l)} = f^{(l)}\left(Z^{(l)}\right) \tag{XV}$$

where l is the layer number, A is the activation signal, Z is the output signal, W is the weight, b is the bias, and f is the activation function of a given layer.

Rectified linear unit (ReLU) activation function was used for each neuron:

$$f(x) = x^{+} = \max(0,x) = \frac{x+|x|}{2} = \begin{cases} xifx > 0 \\ 0otherwise \end{cases} \tag{XVI}$$

where x represents the input to the neuron.

To enhance generalization and mitigate overfitting, dropout layers were strategically positioned between dense layers, with dropout rates of 30% and 20%. The output layer comprises four neurons with a linear activation function, which quantifies E_x, E_y, v_{xy} and v_{yx} of the hybrid lattice. The model was trained utilizing the mean squared error (MSE) loss function:

$$MSE = \frac{1}{N}\sum_{i=1}^{N}\left\{\begin{matrix} \left(E_x^{(i)} - \hat{E}_x^{(i)}\right)^2 + \left(E_y^{(i)} - \hat{E}_y^{(i)}\right)^2 \\ +\left(v_{xy}^{(i)} - \hat{v}_{xy}^{(i)}\right)^2 + \left(v_{yx}^{(i)} - \hat{v}_{yx}^{(i)}\right)^2 \end{matrix}\right\} \tag{XVII}$$

where N is the number of points in the dataset; $E_x^{(i)}, E_y^{(i)}, v_{xy}^{(i)}$ and $v_{yx}^{(i)}$ are the properties predicted by the model; and $\check{E}_x^{(i)}, \check{E}_y^{(i)}, \check{v}_{xy}^{(i)}$ and $\check{v}_{yx}^{(i)}$ are the target properties.

An Adam optimizer with a learning rate of 0.001 was used to train the model. A batch size of 64 and 100 epochs was set for the training process. Key callbacks, including Early Stopping and Model Checkpoint, were integrated to enhance training efficiency and prevent overfitting.[56] Input data were reprocessed to improve model performance before training. Duplicated entries were removed, and normalization was applied to standardize input features, ensuring a well-conditioned dataset with zero mean and unit standard deviation.

3. Results and discussion

3.1. Dataset analysis

The properties of randomly generated hybrid lattices are analyzed in this section. Figure 6 illustrates the probability density of P-Honeycomb and G-Honeycomb cells across the entire dataset. It is evident that both cell types exhibited similar probability densities within the dataset, and their distributions can be effectively approximated using a normal distribution. The result confirmed the achievement of a robust randomization process during the generation of the hybrid lattices.

The mechanical properties of all designs were evaluated using the previously mentioned homogenization method.

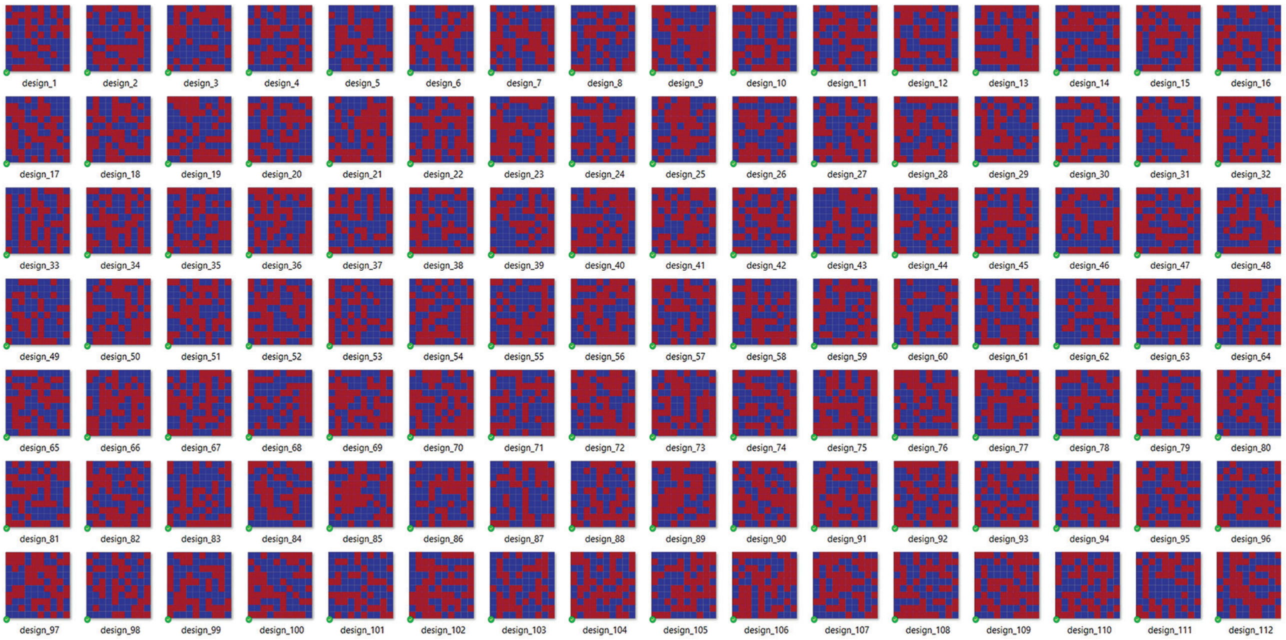

Figure 4. Examples of hybrid lattice configurations (red color represents P-Honeycomb cell and blue color represents G-Honeycomb cell).

Figure 7 provides a visual representation of the 3,000 randomly created hybrid lattices within the property space. Specifically, the elastic modulus along the X- and Y-directions ranged from 10 MPa to 24 MPa, while Poisson's ratio spans from 0.22 to 0.34. Remarkably, the hybrid lattice designs demonstrated the capability to exhibit isotropic behavior across the entire range of elastic modulus values while also offering a high degree of anisotropy within the dataset (Figure 7C). Furthermore, it is observed that for a given elastic modulus along the X- or Y-direction, the lattice could show varying Poisson's ratios (Figure 7D). The randomly generated hybrid lattice structures show a broad spectrum of mechanical properties. Consequently, the dataset generated for the training of the BPNN can provide comprehensive insights into the properties and behaviors of the hybrid lattices.

3.2. Training and validation of BPNN

A total of 3000 random hybrid lattices were generated, with 80% of the dataset (2,400) allocated for training and the remaining 20% (600) for validation. The MSE loss function was employed to quantify the model prediction error. Early stopping was implemented to improve training efficiency and prevent overfitting. Figure 8 illustrates the evolution of model loss for both the training and validation sets throughout the training process, demonstrating the convergence status of the model. Notably, as the total iterations increase, the model loss exhibits a significant reduction. Around 20 epochs into training, the model loss for the validation set reaches a state of convergence.

Subsequently, both the training and validation set losses become below 0.05 after 80 epochs, indicating robust prediction capabilities regarding the properties of hybrid lattices. To validate the training outcomes further, the target and predicted properties for the validation set were extracted. Figure 9 compares the target and predicted values of E_x, E_y, v_{xy} and v_{yx} for the hybrid lattices within the validation set. Overall, a good agreement was observed between the actual and predicted properties. However, it is notable that the model slightly underestimated the elastic modulus of the hybrid lattice. Moreover, the predictive accuracy varied across different properties: the model performed better in predicting the modulus along the Y-direction compared to the X-direction, whereas it demonstrated higher accuracy in predicting the Poisson's ratio along the X-direction. The trained model was saved for future predictions of properties based on the lattice configuration.

3.3. Performance of BPNN

The performance of trained BPNN was tested by the dataset prepared using the homogenization method. The randomly generated lattice patterns were simplified to binary matrix and input into the trained BPNN. Elastic modulus along the X- and Y-direction and Poisson's ratio

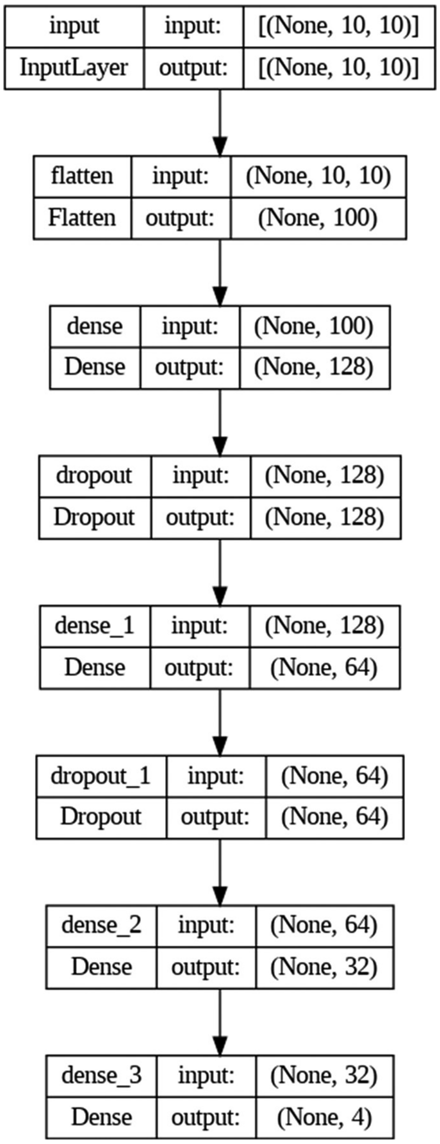

Figure 5. Architecture of the back propagation neural network.

along the X- and Y-direction were then predicted based on the hybrid lattice design. Figure 10 depicts the correlation between the actual properties of the hybrid lattice and the predictions made by the BPNN model.

Notably, the model exhibited optimal performance in predicting the modulus along the X-direction within a mid-range of values, suggesting a robust capability to capture moderate variations in material stiffness. However, it showed tendencies to overestimate modulus values below 12 MPa and underestimate those exceeding 20 MPa, highlighting potential limitations in accurately predicting extreme values (Figure 10A). Similarly, for the modulus along the Y-direction, the model demonstrated overestimations for low values and underestimations for high values, indicating a systematic bias in some areas of the property space (Figure 10C). Regarding Poisson's ratio predictions, the model showed improved accuracy within a mid-range of values, aligning with its proficiency in capturing moderate variations (Figure 10B and 10C). Nonetheless, slight underestimations and overestimations were detected for low and high values, respectively, suggesting regions for refinement in accurately predicting extreme ratios.

These findings proved the performance of the BPNN model and provided valuable insights into its strengths and limitations in predicting the mechanical properties of hybrid lattice structures based on their topologies. Further analysis and refinement of the model may enhance its predictive capabilities and broaden its applicability in material design and engineering.

3.4. Validation of BPNN

To further validate the capability of the trained BPNN, a dataset comprising five random hybrid lattices was generated. The mechanical properties of these lattices

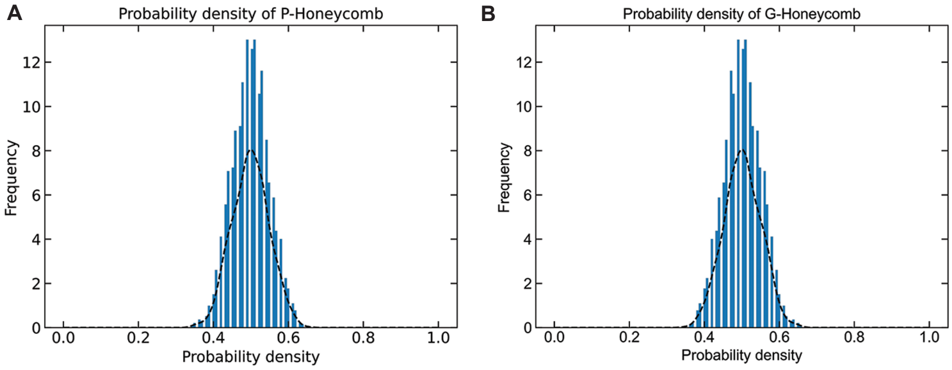

Figure 6. Probability density of (A) P-Honeycomb cell and (B) G-Honeycomb cell in the dataset.

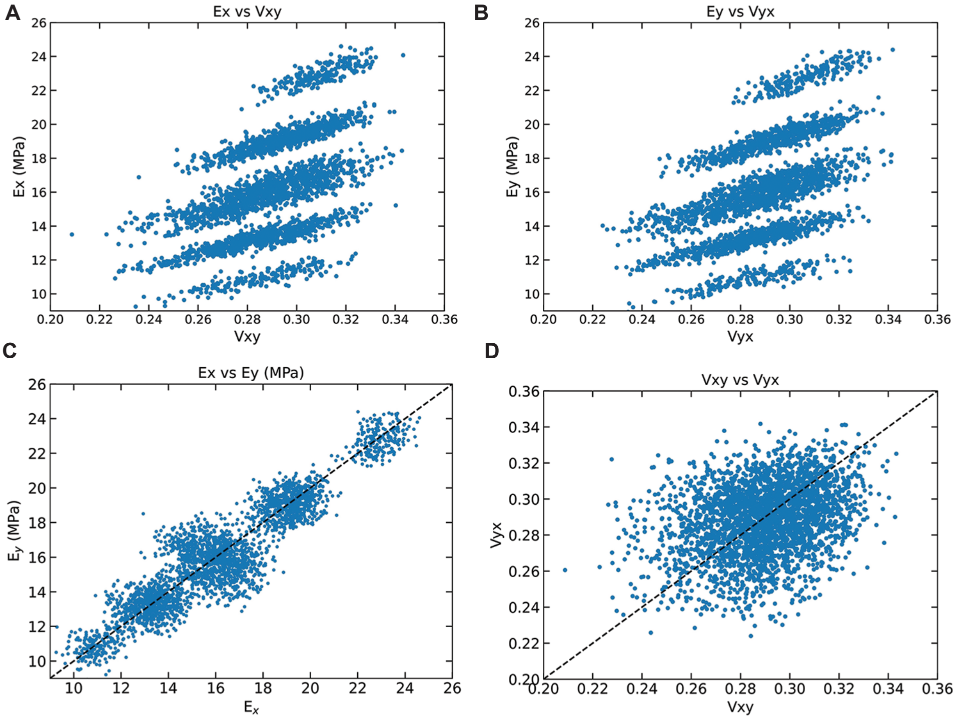

Figure 7. Dataset for artificial neural network training. Distribution of properties in the dataset for training. (A) Correlation between modulus Ex and Poisson's ratio Nu_xy, (B) Correlation between modulus Ey and Poisson's ratio Nu_xy, (C) Correlation between modulus Ey and modulus Ex and (D) Correlation between Poisson's ratio Nu_xy and Nu_yx.

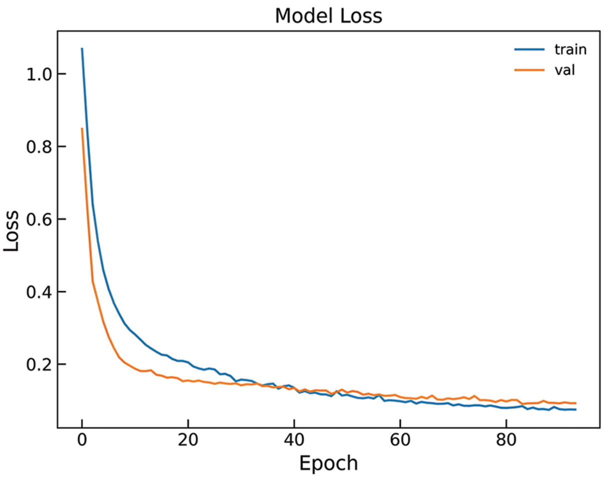

Figure 8. Model loss for the training set and validation set during the training process.

were evaluated through 2D FE simulations. In addition, predictions of lattice properties based on the trained BPNN and lattice configurations were conducted. Figure 11 presents a comparison between the modulus and Poisson's ratio of the lattice as predicted by the BPNN and the results obtained from FE simulations. The deformation and stress contours of the lattice, acquired through FE simulation, are also depicted. The findings indicate a close agreement between the elastic modulus and Poisson's ratio calculated via FE simulations and those predicted by the BPNN based on lattice configurations, which further affirms the robust performance of the trained BPNN. It is worth noting that the dataset used for training the BPNN was generated based on the homogenization method, resulting in slight variations from the FE results. The prediction of mechanical responses of the hybrid lattices conducted with 2D FE simulations took about 30 min. By comparison, the trained BPNN can provide rapid predictions of the elastic modulus and Poisson's ratio for a given topology of the hybrid lattices.

Moreover, the unique deformation behaviors achievable through the design of hybrid lattices using G-Honeycomb (soft) and P-Honeycomb (hard) cells were demonstrated by the deformations and stress contours observed in FE simulations. Overall, the concordance observed between FEM simulation and BPNN predictions provides further confirmation that the proposed BPNN model serves as a reliable tool for predicting the mechanical responses of hybrid lattices.

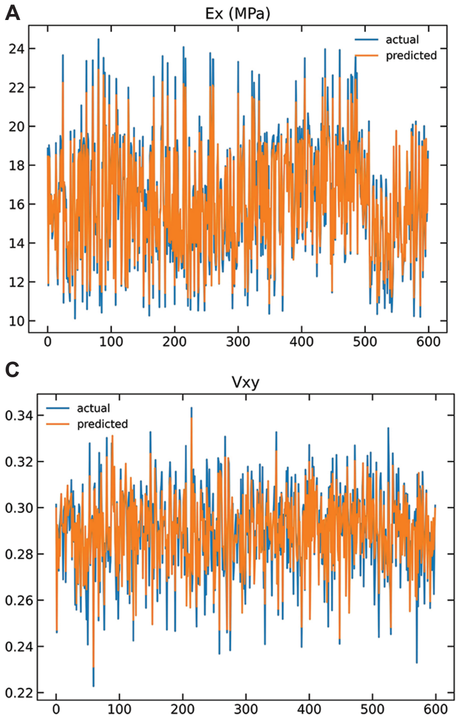

Figure 9. Comparison between the actual and predicted properties of the hybrid lattice in the validation set: (A) E_x, (B) E_y, (C) ν_{xy}, and (D) ν_{yx}.

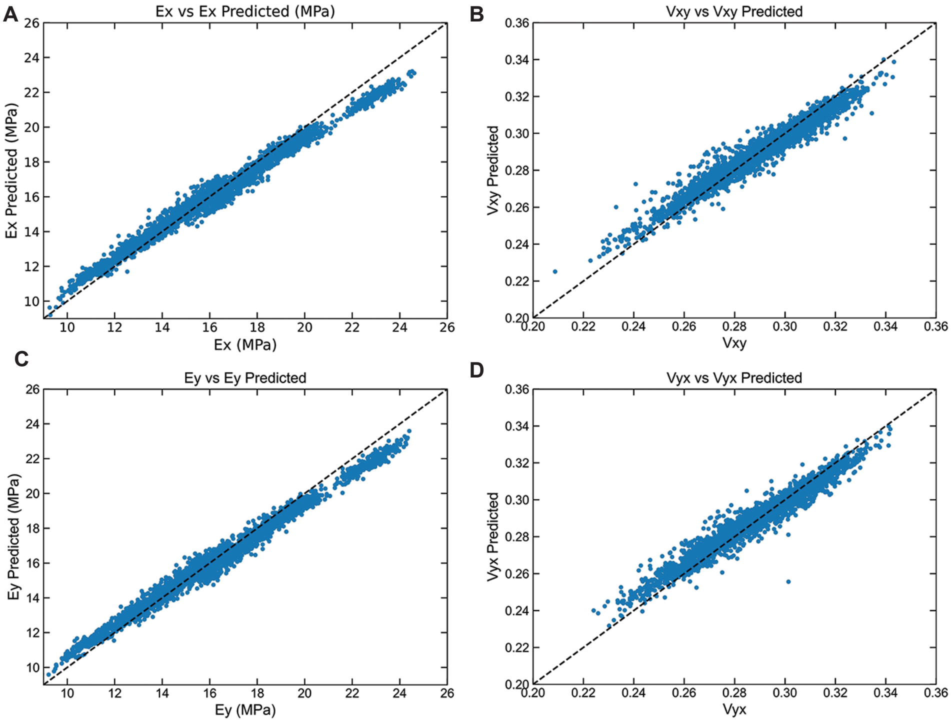

Figure 10. Comparison between user input and back propagation neural network-predicted properties: (A) E_x, (B) E_y, (C) ν_{xy}, and (D) ν_{yx}.

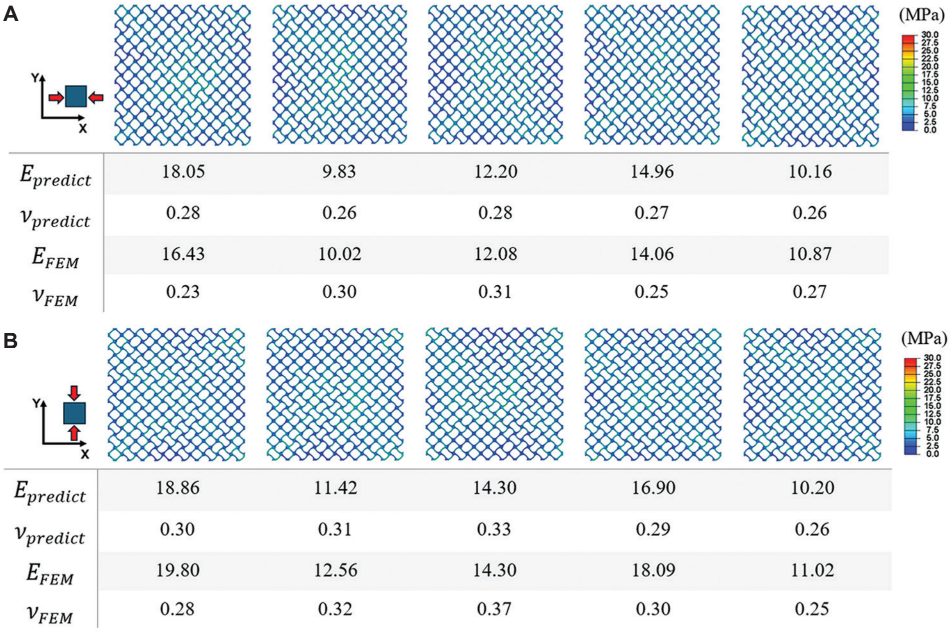

A

$E_{predict}$	18.05	9.83	12.20	14.96	10.16
$\nu_{predict}$	0.28	0.26	0.28	0.27	0.26
E_{FEM}	16.43	10.02	12.08	14.06	10.87
ν_{FEM}	0.23	0.30	0.31	0.25	0.27

B

$E_{predict}$	18.86	11.42	14.30	16.90	10.20
$\nu_{predict}$	0.30	0.31	0.33	0.29	0.26
E_{FEM}	19.80	12.56	14.30	18.09	11.02
ν_{FEM}	0.28	0.32	0.37	0.30	0.25

Figure 11. Validation of back propagation neural network prediction using FE simulation results: (A) Loading along X-direction and (B) Y-direction.

4. Conclusion

In this study, we presented a comprehensive exploration of hybrid lattice structures inspired by TPMS and the integration of machine learning to predict their mechanical properties. Through a combination of FE simulations, homogenization methods, and BPNN training, the efficacy of machine learning techniques in accelerating the design and evaluation process of complex hybrid lattice structures was demonstrated. The results indicated that the trained BPNN exhibited robust capabilities in predicting elastic modulus and Poisson's ratio of hybrid lattice structures, offering a rapid and efficient alternative to traditional simulation methods. Compared to 2D FE simulations, trained BPNN can significantly reduce the computational time to determine the mechanical properties of hybrid lattices based on their topologies, accelerating the design process of novel multifunctional lattice structures. The validation against direct FE simulations further confirmed the accuracy and reliability of the BPNN predictions, indicating its potential as a valuable tool for engineers and researchers in material design and engineering.

Acknowledgments

This research is supported by The Lorenzo and Pamela Galli Medical Research Trust. The authors acknowledge the support from the Digital Construction laboratory at RMIT University.

Part of this work was completed at RMIT University when the first author (Chenxi Peng) conducted his research as a PhD candidate.

Funding

Not applicable.

Conflicts of interest

The authors declare that they have no competing interests.

Author contributions

Conceptualization: Chenxi Peng and Phuong Tran
Formal analysis: Chenxi Peng
Investigation: Chenxi Peng and Phuong Tran
Methodology: Chenxi Peng
Supervision: Phuong Tran and Erich Rutz
Writing – original draft: Chenxi Peng
Writing – review and editing: Phuong Tran and Erich Rutz

Ethics approval and consent to participate

Not applicable.

Consent for publication

Not applicable.

Availability of data

The data that support the findings of this study are available from the corresponding author on reasonable request.

References

1. Ashby MF, Evans AG, Fleck NA, Gibson LJ, Hutchinson JW, Wadley HN. *Metal Foams: A Design Guide*. London: Butterworth-Heinemann; 2000.

2. Peng C, Tran P, Nguyen-Xuan H, Ferreira AJ. Mechanical performance and fatigue life prediction of lattice structures: Parametric computational approach. *Compos Struct*. 2020;235:111821.

   doi: 10.1016/j.compstruct.2019.111821

3. Wong M, Owen I, Sutcliffe CJ, Puri A. Convective heat transfer and pressure losses across novel heat sinks fabricated by Selective Laser Melting. *Int J Heat Mass Tran*. 2009;52(1-2):281-288.

   doi: 10.1016/j.ijheatmasstransfer.2008.06.002

4. Zhang XY, Fang G, Zhou J. Additively manufactured scaffolds for bone tissue engineering and the prediction of their mechanical behavior: A review. *Materials (Basel)*. 2017;10(1)50.

   doi: 10.3390/ma10010050

5. Tran P, Peng C. Triply periodic minimal surfaces sandwich structures subjected to shock impact. *J Sandwich Struct Mater*. 2020;23(6):2146-2175.

   doi: 10.1177/1099636220905551

6. Peng C, Tran P. Bioinspired functionally graded gyroid sandwich panel subjected to impulsive loadings. *Compos Part B Eng*. 2020;188:107773.

   doi: 10.1016/j.compositesb.2020.107773

7. Nguyen-Van V, Peng C, Hazell PJ, Lee J, Nguyen-Xuan H, Tran P. Performance of meta concrete panels subjected to explosive load: Numerical investigations. *Struct Concr*. 2023;25:1590-1619.

   doi: 10.1002/suco.202200749

8. Catchpole-Smith S, Sélo RR, Davis AW, Ashcroft IA, Tuck CJ, Clare A. Thermal conductivity of TPMS lattice structures manufactured via laser powder bed fusion. *Addit Manuf*. 2019;30:100846.

   doi: 10.1016/j.addma.2019.100846

9. Aremu AO, Brennan-Craddock JP, Panesar A, *et al*. A voxel-based method of constructing and skinning conformal and functionally graded lattice structures suitable for additive manufacturing. *Addit Manuf*. 2017;13:1-13.

   doi: 10.1016/j.addma.2016.10.006

10. Peng C, Fox K, Qian M, Nguyen-Xuan H, Tran P. 3D printed sandwich beams with bioinspired cores: Mechanical performance and modelling. *Thin Walled Struct*. 2021;161:107471.

    doi: 10.1016/j.tws.2021.107471

11. Wickramasinghe S, Peng C, Ladani R, Tran P. Analysing fracture properties of bio-inspired 3D printed suture structures. *Thin Walled Struct*. 2022;176:109317.

    doi: 10.1016/j.tws.2022.109317

12. Wu C, Peng C, Le TC, Das R, Tran P. Tunable 3D printed composite metamaterials with negative stiffness. *Smart Mater Struct*. 2023;32(12):125010.

    doi: 10.1088/1361-665X/ad06df

13. Ashby MF. The properties of foams and lattices. *Philos Trans A Math Phys Eng Sci*. 2006;364(1838):15-30.

    doi: 10.1098/rsta.2005.1678

14. Rashed MG, Ashraf M, Mines RA, Hazell PJ. Metallic microlattice materials: A current state of the art on manufacturing, mechanical properties and applications. *Mater Des*. 2016;95:518-533.

    doi: 10.1016/j.matdes.2016.01.146

15. Wang Y, Zhang L, Daynes S, Zhang H, Feih S, Wang MY. Design of graded lattice structure with optimized mesostructures for additive manufacturing. *Mater Des*. 2018;142:114-123.

    doi: 10.1016/j.matdes.2018.01.011

16. Wang P, Yang F, Li P, Zheng B, Fan H. Design and additive manufacturing of a modified face-centered cubic lattice with enhanced energy absorption capability. *Extreme Mech Lett*. 2021;47:101358.

    doi: 10.1016/j.eml.2021.101358

17. Daynes S, Feih S, Lu WF, Wei J. Optimisation of functionally graded lattice structures using isostatic lines. *Mater Des*. 2017;127:215-223.

    doi: 10.1016/j.matdes.2017.04.082

18. Cao X, Zhang D, Liao B, *et al*. Numerical analysis of the mechanical behavior and energy absorption of a novel P-lattice. *Thin Walled Struct*. 2020;157:107147.

    doi: 10.1016/j.tws.2020.107147

19. Lan T, Tran P. Multiscale topology optimization of lattice structure using 3D moving hollow morphable bars. *JOM*. 2021;73(12):4141-4153.

    doi: 10.1007/s11837-021-04917-2

20. Al-Ketan O, Abu Al-Rub RK. Multifunctional mechanical metamaterials based on triply periodic minimal surface lattices. *Adv Eng Mater*. 2019;21(10):1900524.

    doi: 10.1002/adem.201900524

21. Han L, Che S. An overview of materials with triply periodic minimal surfaces and related geometry: From biological structures to self-assembled systems. *Adv Mater*. 2018;30(17):e1705708.

    doi: 10.1002/adma.201705708

22. Lan T, Peng C, Fox K, Do T, Tran P. Triply periodic minimal

surfaces lattice structures: Functional graded and hybrid designs for engineering applications. *Mater Sci Addit Manuf*. 2023;2(3):1753.

doi: 10.36922/msam.1753

23. Maskery I, Aboulkhair NT, Aremu AO, Tuck CJ, Ashcroft IA. Compressive failure modes and energy absorption in additively manufactured double gyroid lattices. *Addit Manuf*. 2017;16:24-29.

doi: 10.1016/j.addma.2017.04.003

24. Li X, Xiao L, Song W. Compressive behavior of selective laser melting printed Gyroid structures under dynamic loading. *Addit Manuf*. 2021;46:102054.

doi: 10.1016/j.addma.2021.102054

25. Yan C, Hao L, Hussein A, Young P, Huang J, Zhu W. Microstructure and mechanical properties of aluminium alloy cellular lattice structures manufactured by direct metal laser sintering. *Mater Sci Eng A*. 2015;628:238-246.

doi: 10.1016/j.msea.2015.01.063

26. Cao X, Yang H, Ren X, *et al*. Mechanical performance and defect analysis of the imperfect micro smooth gyroid cylinder shell structure. *Compos Struct*. 2021;273:114320.

doi: 10.1016/j.compstruct.2021.114320

27. Peng C, Tran P, Mouritz AP. Compression and buckling analysis of 3D printed carbon fibre-reinforced polymer cellular composite structures. *Compos Struct*. 2022;300:116167.

doi: 10.1016/j.compstruct.2022.116167

28. Nguyen-Van V, Liu J, Peng C, Zhang G, Nguyen-Xuan H, Tran P. Dynamic responses of bioinspired plastic-reinforced cementitious beams. *Cement Concr Compos*. 2022;133:104682.

doi: 10.1016/j.cemconcomp.2022.104682

29. Nguyen-Van V, Tran P, Peng C, Pham L, Zhang G, Nguyen-Xuan H. Bioinspired cellular cementitious structures for prefabricated construction: Hybrid design and performance evaluations. *Autom Construct*. 2020;119:103324.

doi: 10.1016/j.autcon.2020.103324

30. Plocher J, Panesar A. Effect of density and unit cell size grading on the stiffness and energy absorption of short fibre-reinforced functionally graded lattice structures. *Addit Manuf*. 2020;33:101171.

doi: 10.1016/j.addma.2020.101171

31. Al-Ketan O, Lee DW, Abu Al-Rub RK. Mechanical properties of additively-manufactured sheet-based gyroidal stochastic cellular materials. *Addit Manuf*. 2021;48:102418.

doi: 10.1016/j.addma.2021.102418

32. Maskery I, Aremu AO, Parry L, Wildman RD, Tuck CJ, Ashcroft IA. Effective design and simulation of surface-based lattice structures featuring volume fraction and cell type grading. *Mater Des*. 2018;155:220-232.

doi: 10.1016/j.matdes.2018.05.058

33. Maskery I, Ashcroft IA. The deformation and elastic anisotropy of a new gyroid-based honeycomb made by laser sintering. *Addit Manuf*. 2020;36:101548.

doi: 10.1016/j.addma.2020.101548

34. Peng C, Marzocca P, Tran P. Triply periodic minimal surfaces based honeycomb structures with tuneable mechanical responses. *Virtual Phys Prototyp*. 2022;18(1):e2125879.

doi: 10.1080/17452759.2022.2125879

35. Cerniauskas G, Sadia H, Alam P. Machine intelligence in metamaterials design: A review. *Oxford Open Mater Sci*. 2024;4(1):itae001.

doi: 10.1093/oxfmat/itae001

36. Meng L, McWilliams B, Jarosinski W, *et al*. Machine learning in additive manufacturing: A review. *JOM*. 2020;72: 2363-2377.

doi: 10.1007/s11837-020-04155-y

37. Jiao P, Alavi AH. Artificial intelligence-enabled smart mechanical metamaterials: Advent and future trends. *Int Mater Rev*. 2021;66(6):365-393.

doi: 10.1080/09506608.2020.1815394

38. Bastek JH, Kochmann DM. Inverse design of nonlinear mechanical metamaterials via video denoising diffusion models. *Nat Mach Intell*. 2023;5(12):1466-1475.

doi: 10.1038/s42256-023-00762-x

39. Nadell CC, Huang B, Malof JM, Padilla WJ. Deep learning for accelerated all-dielectric metasurface design. *Opt Express*. 2019;27(20):27523-27535.

doi: 10.1364/OE.27.027523

40. Liu TW, Chan CT, Wu RT. Deep-learning-based acoustic metamaterial design for attenuating structure-borne noise in auditory frequency bands. *Materials* (*Basel*). 2023;16(5):1879.

doi: 10.3390/ma16051879

41. Li W, Chen P, Xiong B, *et al*. Deep learning modeling strategy for material science: From natural materials to metamaterials. *J Phys Mater*. 2022;5(1):014003.

doi: 10.1088/2515-7639/ac5914

42. Peng H, Liu A, Huang J, Cao L, Liu J, Lu L. PH-Net: Parallelepiped microstructure homogenization via 3D convolutional neural networks. *Addit Manuf*. 2022;60:103237.

doi: 10.1016/j.addma.2022.103237

43. Gu GX, Chen CT, Richmond DJ, Buehler MJ. Bioinspired hierarchical composite design using machine learning:

Simulation, additive manufacturing, and experiment. *Mater Horizons*. 2018;5(5):939-945.

doi: 10.1039/C8MH00653A

44. Zheng X, Chen TT, Guo X, Samitsu S, Watanabe I. Controllable inverse design of auxetic metamaterials using deep learning. *Mater Des*. 2021;211:110178.

    doi: 10.1016/j.matdes.2021.110178

45. Sui F, Guo R, Zhang Z, Gu GX, Lin L. Deep reinforcement learning for digital materials design. *ACS Mater Lett*. 2021;3(10):1433-1439.

    doi: 10.1021/acsmaterialslett.1c00390

46. Wilt JK, Yang C, Gu GX. Accelerating auxetic metamaterial design with deep learning. *Adv Eng Mater*. 2020;22(5):1901266.

    doi: 10.1002/adem.201901266

47. Do Carmo MP. *Differential Geometry of Curves and Surfaces*. 2nd ed. New York: Springer Cham; 2016.

48. Schoen AH. *NASA Technical Note D-5541*; 1970.

49. Matsen MW, Bates FS. Origins of complex self-assembly in block copolymers. *Macromolecules*. 1996;29(23):7641-7644.

    doi: 10.1021/ma960744q

50. Pouya C, Overvelde JT, Kolle M, *et al*. Characterization of a mechanically tunable gyroid photonic crystal inspired by the butterfly parides sesostris. *Adv Opt Mater*. 2015;4(1): 99-105.

    doi: 10.1002/adom.201500436

51. Michielsen K, Stavenga DG. Gyroid cuticular structures in butterfly wing scales: Biological photonic crystals. *J R Soc Interface*. 2008;5(18):85-94.

    doi: 10.1098/rsif.2007.1065

52. Lai M, Kulak AN, Law D, Zhang Z, Meldrum FC, Riley DJ. Profiting from nature: Macroporous copper with superior mechanical properties. *Chem Commun* (*Camb*). 2007;34:3547-3549.

    doi: 10.1039/b707469g

53. Brakke KA. The surface evolver. *Exp Math*. 1992;1(2): 141-165.

    doi: 10.1080/10586458.1992.10504253

54. Dong G, Tang Y, Zhao YF. A 149 line homogenization code for three-dimensional cellular materials written in matlab. *J Eng Mater Technol*. 2019;141(1):11.

    doi: 10.1115/1.4040555

55. Abadi M, Barham P, Chen J, *et al*. TensorFlow: A System for Large-Scale Machine Learning. In: 12th USENIX Symposium on Operating Systems Design and Implementation. 2016. p. 265-283.

56. Yan H, Yu H, Zhu S, Wang Z, Zhang Y, Guo L. Nonlinear properties prediction and inverse design of a porous auxetic metamaterial based on neural networks. *Thin Walled Struct*. 2024;197:111717.

    doi: 10.1016/j.tws.2024.111717

ACCSCIENCE
PUBLISHING

OUR JOURNALS

International Journal of Bioprinting is an international journal covering the technology, science and clinical application of the broadly defined field of Bioprinting. Bioprinting is defined as the use of 3D printing technology with materials that incorporate viable living cells or biological elements to produce tissue or biotechnological products. We are interested in the scientific topics spanning all stages of bioprinting process from concept creation to fabrication and beyond. Knowledge generated in these researches must be related to bioprinting. *IJB* covers subject areas, including but not limited to the following:

- Information technologies and basic research
- Materials and formulation
- Cell source and biotechnology for additive manufacturing
- 3D Bioprinting technologies
- New design and fabrication paradigm
- Applied research purpose & evaluation of 3D printed products
- Associated social implications

International Journal of AI for Materials and Design is an international, peer-reviewed open-access journal that aims to bridge the cutting-edge research between AI and materials, AI and design. In recent years, the tremendous progress in AI is leading a radical shift of AI research from a mainly academic endeavor to a much broader field with increasing industrial and governmental investments. The maturation of AI technology brings about a step change in the scientific research of various domains, especially in the world of materials and design. Machine learning (ML) algorithms enable researchers to analyze extensive datasets on material properties and accurately predict their behavior in different conditions. This subsequently impact the industry to leverage on big data and advanced analytics to build scientific strategies, scale operational performance of processes and drive innovation. In addition, AI and ML are uniquely positioned to enable advanced manufacturing technologies across the value chain of different industries. Integration of multiple and complementary AI techniques, such as ML, search, reasoning, planning, and knowledge representation, will further accelerate advances in scientific discoveries, engineering excellence and the future of cyber-physical systems manufacturing.

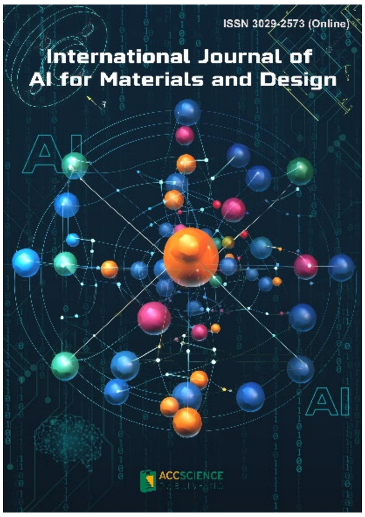

International Journal of AI for Materials and Design covers the following topics: AI or machine learning for material discovery, AI for process optimization, AI and data-driven approaches for product or systems design, application of AI in advanced manufacturing processes such as additive manufacturing, IoT, sensors, robotics, cloud-based manufacturing, intelligent manufacturing for various applications, autonomous experiments, material intelligence, energy intelligence, and AI-linked decarbonization technologies.

Start a new journal

Write to us via email if you are interested to start a new journal with AccScience Publishing. Please attach your CV, professional profile page and a brief pitch proposal in your email. We shall inform you of our decision whether we are interested to collaborate in starting a new journal.

Contact: info@accscience.com

https://accscience.com/journal/MSAM

ACCSCIENCE
PUBLISHING

Access Science Without Barriers

Contact

www.accscience.com
8 Burn Road, #15-03 Trivex, Singapore 369977
E-mail: editorial@accscience.com
Phone: +65 8182 1586